Regional Disaster Events and Environment Simulations

by Atmosphere-Ocean Coupled Model

（大気・海洋結合モデルによる地域環境・災害事象シミュレーション）

Han Soo LEE

September, 2007

Regional Disaster Events and Environment Simulations

by Atmosphere-Ocean Coupled Model

（大気·海洋結合モデルによる地域環境·災害事象シミュレーション）

Han Soo LEE

September, 2007

Abstract

An atmosphere-ocean coupled model was developed based on a preexisting non-hydrostatic mesoscale atmosphere model (MM5) and non-hydrostatic ocean circulation model (MITgcm). This model together with a pre-established wind-wave-currents coupled model was applied to a number of regional environmental issue and disaster events to reproduce the present status and past situations and to help our understanding of the physical processes of such problems in terms of atmosphere-ocean interactions including the sea surface waves in the interface between air and sea. The disaster events and environmental issue studied in this thesis are follows.

1) Storm surge induced by Hurricane Katrina in the Gulf coast of USA in 2005.

2) Extreme high waves at Hara coast, Suruga Bay in Japan caused by the super-Typhoon TIP in 1979.

3) Positive and negative feedbacks in typhoon-ocean interaction in case of Typhoon ETAU in 2003.

4) Thermal water circulation in a dam-made lake (Yachiyo Lake) in Hiroshima, Japan concerning on the hydrodynamics in the lake.

5) Reanalysis of the past 47 storms that caused disasters in West Kyushu, Japan.

6) Wave overtopping simulation over through the submerged offshore breakwater and enhance seawall.

The Regional Environment and Disaster Prevention Simulator is proposed and constructed based on the regional atmosphere-ocean coupled model in this thesis of which the objective was improvement of the numerical assessment method to disaster events and environment problems by introducing the coupling effects between different systems.

ACKNOWLEDGEMENTS

Contents

List of Figures

V

List of Tables

Chapter 1

Introduction

Disaster is one of the most difficult words to find its definition since it can be too broad or too narrow depending on the problems we face. Some of them are "Disasters are exceptional events which suddenly kill or injure large number of people" by Red Cross, and "An occurrence causing widespread destruction and distress" by American Heritage Dictionary. However, the definitions of disaster have a common aspect that disasters are coming from natural and/or man-made hazards. Natural disasters are the consequence when the natural hazards, such as earthquake, volcano, typhoon, landslide, etc human activities cause a negative impact in human society. Man-made disasters are the results of the man-made hazards which are threats caused by human intent, negligence, error or involving a failure of a system.

A typical natural disaster resulted from the atmosphere and ocean interaction is typhoon which is normally accompanied by strong wind, heavy rainfall, high waves and sea level rise (storm surge) at the coast, wave overtopping, flooding, inundation, etc. Recent advanced technology of numerical modeling with available observations makes it possible to reproduce the natural structure of severe storm events called hurricane, cyclone and typhoon. It is now well agreed that the coupling of atmosphere and earth surface of ocean and land is the key to simulate the long-term climate changes as well as the relatively short-term and strong intensity changes in natural disaster events.

1.1 Global Ocean-Atmosphere Coupled Model

Combining ocean and atmosphere, researches for general circulation models (GCM) started in the late 1960's (Manabe and Bryan, 1969) to mainly simulate global climate changes. These coupled models had very simplified physical parameterization in ocean and atmosphere, therefore it was difficult to simulate the climate changes precisely. However, those coupled models have been steadily improved (Boville and Gent, 1998; Manabe et al., 1979; Washington

1

et al., 1980) and now widely being used to simulate the climate changes including global warming due to anthropogenic greenhouse gases (Manabe et al., 1990, 1992) and to provide the operational forecast of global state of the atmosphere. Neelin et al. (1992) investigated 17 coupled ocean-atmosphere models being used in different organization at that time and summarized that the simplified physical processes included in air-sea interaction could amplify the tendency called climate drift emphasizing the special attention on the coupling processes. Mechoso et al. (1995) reported on the progresses over the climate drift of 11 coupled models.

1.2 Regional Ocean-Atmosphere Coupled Model

In early 1980's, the need for predicting the genesis and evolution of ENSO events probably triggered the development of the regional ocean and atmosphere coupled model and the simple regional coupled models proved to be useful since the ENSO is mainly due to the local air-sea interactions and internal variability in the tropical Pacific waveguide (Bjerknes, 1969). It is now agreed that the sea surface temperature (SST) anomalies in the waveguide act to either reinforce or weaken the trade winds, which in turn modify the SST anomalies over certain internal oceanic dynamical timescales, leading to a self-sustained oscillation in the system which is called ENSO (Kantha and Clayson, 2000). Also for the local thermodynamic processes related to air-sea interactions and local processes in coastal ocean such as coastal upwelling, the regional coupled models are meaningful and useful. In the early stage of regional coupled models, the regional coupled models started from the shallow-water models being forced by wind forcing to ocean general circulation model (OGCM) coupled to a simple atmospheric model (Barnett et al., 1993).

In late of 1990's, the comprehensive regional ocean and atmosphere coupled models were developed combining the sophisticated ocean and atmosphere models including not only the oceanic feedback but the atmospheric response to ocean. These models are very useful to study the local processes in coastal regions and marginal seas and somewhat localized basin-scale processes such as the monsoons and cyclones in the Indian Ocean. One of the well-known examples is the Coupled Ocean Atmosphere Mesoscale Prediction System (COAMPS) at Naval Research Laboratory (NRL) in U.S. for the operational purpose for the coastal regions. This system uses the three-dimensional hydrostatic sigma coordinate ocean model coupled to nonhydrostatic atmosphere model (Hodur, 1997). Some of other related works using regional ocean and atmosphere coupled models are listed below. Dickinson et al., (1989) developed a regional climate model that consisted of National Center for Atmospheric Research (NCAR) global community climate model (CCM1), NCAR mesoscale model version 4 (MM4) and Bioshpere Atmospheric Transfer Scheme (BATS). They applied this model to the western

2

U.S. for the climate modeling without considering the ocean states in early stage of regional climate model. And more recently, regional coupled models were developed and applied to regional climate issues. Rummukainen et al., (2001) developed a regional climate model that comprised of Rossby Centre regional Atmospheric model (RCA), a regional Baltic Sea Ocean model and an inland lake modeling system and applied it to regional climate in northern Europe showing improvement in their results compared to GCMs. In the work of Doscher et al., (2002) introduced a regional coupled ocean-atmosphere-ice model for climate study in northern Europe and conducted 5 years hindcast experiments with good agreements with observations. A number of early works of coupled atmosphere and ocean model and their detailed applications on global scale modeling and characteristics are summarized by Neelin et al., (1994). Early work of regional coupled model in Japan explored by Endoh et al. (1991) at Meteorological Research Institute using a 5-level atmospheric GCM (Tokioka et al., 1984) and a primitive equation ocean model with 4000m flat bottom.

Those regional coupled models require the conditions for open boundaries of atmospheric and oceanic domains that are almost provided by the global GCM results for the atmosphere and at least basin-scale models for the ocean, therefore the regional climate models are substantially affected by the biases in global GCM simulations. The initial state of ocean is also often unknown that needs spin-up to get the ocean state as close as the real before the coupling processes (baroclinic simulation) or assumes homogeneous state in temperature and salinity (barotropic simulation). And the regional models are rather lack of information of sea surface states especially surface waves.

1.3 Boundary Layer Processes

Coupling ocean and atmosphere models is achieved through the atmospheric surface layer and marine boundary layer. And the intermediate wave boundary layer on the sea surface plays very important role in the interaction of the systems through the boundary layer processes.

In the atmosphere, the kinetic energy of the large-scale atmospheric circulations cascades down to mesoscale and smaller motions through shear instability, which is generally dominant in the atmospheric boundary layer due to the strong velocity shear by frictional drag. Eddies, then, are introduced to describe these atmospheric circulations from mesoscale to microscale motions and their kinetic energy is dissipated through the viscosity effects. Therefore the atmospheric boundary layer is often defined as the layer near surface that is almost continuously turbulent due to eddies (Edson et al., 1999). In this turbulent boundary layer, the vertical flux of momentum due to the turbulent mixing is particularly important in the ocean and atmosphere interaction and the parameterization of the momentum flux at a given height is

normally related to the local shear stress, which is proportional to the wind shear, τ, and eddy viscosity, K_m, (i.e., $\tau = K_m \left(\partial U / \partial z \right)$). Additionally, mesoscale motions can also be driven by direct thermal circulations within the atmospheric boundary layer. These thermally driven motions are known to mix effectively the boundary layer at mid-level which is called the mixed-layer. These buoyancy-driven circulations in the mixed-layer also enhance the shear-driven motions in convective conditions and suppress it under thermal stratifications. The description of atmospheric boundary layer is generally based on the inland/overland measurements and experiments which naturally bring questions on the validation over the ocean surface where the ever-changing surface waves play important role.

In light winds when the viscous dissipation is dominant and suppresses the short capillary and capillary-gravity waves, the ocean surface stays in mirror-like conditions, then if the wind blows fast, gravitational wind waves are generated and make the ocean surface rough that affects the air-sea interaction (i.e., momentum and heat flux transfer). And these waves also affect the boundary layer structures in both air and sea. In very high winds, such conditions get enhanced correspondingly. In addition, the wave breaking modifies the adjacent ocean surface and boundary layers by introducing the spray into upper air and the air-bubble into the lower water (Edson et al., 1999). These two-phase flows have important effects on momentum, heat and mass transfer, surface mixing, turbulence structure, wave propagation, etc. Therefore the accurate and correct description of wave boundary layer is indispensable in the coupling of ocean and atmosphere and the main issue to be explored thoroughly.

As in the atmospheric boundary layer, analogous processes take place in the ocean boundary layer where the transport of heat and momentum can be driven by direct thermal circulations due to repetitive cooling and heating over the surface, heating by solar radiation, which also modulates the wind-driven transport. These circulations are a result of the removal or addition of fresh water due to surface evaporation, precipitation, river outflow, and runoff. This buoyancy-driven mixing process combines with and enhances the shear-induced mixing to generate an oceanic mixed-layer. In addition, entrainment processes of cool thermocline water at the base of the mixed-layer can also affect the turbulence structure within the mixed-layer and in turn the ocean boundary layer.

1.4 Motivation for this thesis

A regional coupled model generally has been used for the study of regional climate change as its original purpose and short-term local air-sea interactions with strong intensity, such as surges and high waves caused by hurricane, cyclone and typhoon. It is primarily attributed to the simple physical parameterization of atmospheric processes and primitive

equation ocean model. It is now feasible to construct a regional coupled model that is able to deal with from regional and local to small scale processes by coupling the mesoscale meteorological model and nonhydrostatic ocean circulation model with improved physical parameterization.

This thesis has focused on two points. The first is the development of a regional coupled model named Regional Environment and Disaster Events Simulator (REDES). The REDES consists of public domain models mainly for atmospheric and oceanic circulation, ocean wind waves which have been constructed by integrating scientific basic knowledge and technological new findings in many research communities all over the world. To connect the results from regional coupled model to nearshore problem and coastal disasters, 2D direct simulation method for wave deformation and overtopping is also employed in the framework of REDES.

The second part is model verification and applications to make clear the interaction between the related natural phenomena which are the primary and secondary factors of disasters and environmental changes. It has been applied to various scale processes from local air-sea interaction such as typhoon-ocean interaction, storm surge and extreme high waves to small scale processes in thermal circulation in inland lake.

The objectives of this thesis through the REDES are to improve the numerical assessment method to disaster events and environment problems by introducing the coupling effects between different systems through the existing interactions and to enhance our understanding of the physical processes of natural disasters and environmental issues.

1.5 Organization of this thesis

This thesis consists of seven chapters including this first chapter of introduction. In chapter 2, the components models for atmosphere, ocean and ocean waves in REDES are described based on their governing equations and physical parameterization together with the brief explanation of 2D direct simulation method for wave deformation and overtopping. The design concept of REDES is also described. This chapter is largely referred to the manuals and literatures of each model unless mentioned and the detailed citations for numerous formulations are omitted. In the following chapters, the validation and applications of REDES are described. Chapter 3 shows two applications of REDES to disaster events. The first application is storm surge simulation induced by Hurricane Katrina in the United States in 2005 and the second one is extreme high waves simulation at coastal regional caused by Typhoon 7920 (TIP) in Japan. Chapter 4 is about the application to real typhoon-ocean interaction in Typhoon 0310 (ETAU). In this experiment, the baroclinic state of ocean is considered and the mutual responses in

typhoon and ocean are investigated through the two-way momentum, heat, and mass flux transfer. The results of sea surface temperature (SST) changes are validated with the SST observation by Tropical Rainfall Measuring Mission (TRMM) satellite. In chapter 5, REDES is applied to a thermal water circulation in a dam lake. Density stratification due to daily heat budget through the water surface and its evolution in summertime are studied with consideration of river inflow effects as an open boundary condition. The result of thermal structure and its evolution in the lake for one month simulation shows very good agreement with the observation. Chapter 6 contains two applications of REDES for coastal problems. The first one is reanalysis of past major storms in West Kyushu, Japan where a complicated terrain causes difficulty of surface wind simulation in the inland seas, such as Omura Bay, Ariake Sea and Yatsushiro Sea. From the reanalysis results, the wind-induced currents in Ariake Sea are studied, which is important in material transport under storm conditions. An inventory of reanalysis data for the storms simulated by REDES has been available for public use. The second is problem of wave overtopping in the coastal area in which depth-limited wave breaking makes a complicated hydrodynamic zone between ocean and land. Many coastal engineering research subjects have elaborated the modeling in this area as nearshore dynamic models, such as nearshore currents, surf zone dynamics and wave overtopping etc. It is very important research theme to connect ocean model to land model through surf zone model. One effective solution is using a direct simulation method which was conducted in this chapter. Through the experiments, REDES will encompass the coastal disaster simulation caused by strong currents and high waves in nearshore coastal region. Finally this thesis ends up with the concluding remarks in chapter 7.
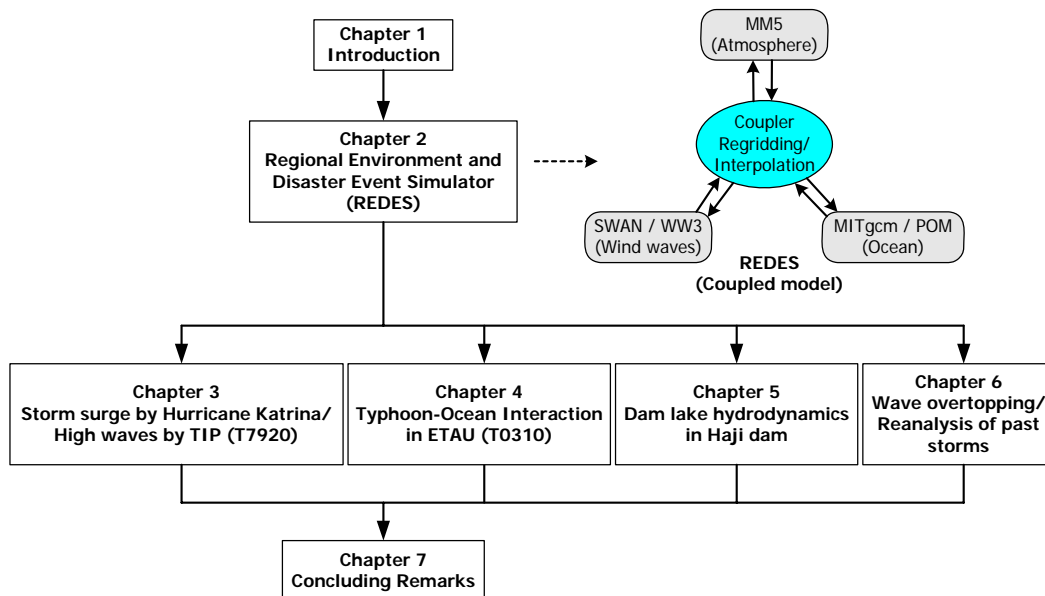
Fig. 1.1 Flowchart of thesis structure.

References

Barnett, T. P., M. Latif, N. Graham, M. Flugel, S. Pazan, and W. White, (1993): ENSO and ENSO-related predictability. Part I. Prediction of equatorial Pacific sea surface temperature with hybrid coupled ocean-atmosphere model, *J. Clim.*, **6**, 1545-1566.

Bjerknes, J., (1969): Atmospheric teleconnections from the equatorial Pacific, *Mon. Wea. Rev.*, **97(3)**, 163-172.

Boville, B. A., and P. R. Gent, (1998): The NCAR climate system model, version one, *J. Clim.*, **11**, 1115-1130.

Dickinson, R. E., R. M. Errico, F. Giorgi, and G. R. Bates, (1989): A regional climate model for the western United States, *Climatic Change*, **15**, 383-422.

Doscher, R., U. Willen, C. Jones, A. Rutgersson, H.E. M. Meier, U. Hansson, and L.P. Graham, (2002): The development of the regional coupled ocean-atmosphere model RCAO,

Edson, J.B., T. Paluskiewicz, L. Vincent, L. Goodman, T. Curtin, J. Hollister, and M. Colton, (1999): Coupled marine boundary layers and air-sea interaction initiative: Combining process studies, simulations, and numerical models, Office of Naval Research, Arlington.

Endoh, M., T. Tokioka, T. Nagai, (1991): Tropical Pacific sea surface temperature variations in a coupled atmosphere-ocean general circulation model, *J. Marine Systems*, **1**, 293-298.

Hodur, R. M. (1997): The Naval Research Laboratory's Coupled Ocean/Atmosphere Mesoscale Prediction system (COAMPS), *Mon. Wea. Rev.*, **125**, 1414-1430.

Kantha, L. H., and C. A. Clayson, (2000): Numerical models of oceans and oceanic processes, Chapter 13. Ocean-atmosphere coupled models, *International Geophysics Series*, V.66, Academic Press.

Manabe, S., and K. Bryan, (1969): Climate calculations with a combined ocean-atmosphere model, *J. Atmos. Sci.*, **26**, 786-789.

Manabe, S., K. Bryan, and M. J. Spelman, (1979): A global ocean-atmosphere climate model

with seasonal variation for future studies of climate sensitivity, *Dyn. Atmos. Oceans*, **3**, 393-426.

Manabe, S., M. J. Spelman, and R. J. Stouffer, (1990): Transient response of a coupled ocean-atmospheremodel to a doubling of atmospheric carbon dioxide, *J. Phys. Oceanogr.*, **20**, 722-749.

Manabe, S., K. Bryan, and M. J. Spelman, (1992): Transient response of a global ocean-atmosphere model to gradual change of atmospheric carbon dioxide. Part II. Seasonal response, *J. Clim.*, **5**, 105-126.

Mechoso, C. R., A. W. Robertson, N. Barth, M. K. Davey, P. Delecluse, P. R. Gent, S. Ineson, B. Kirtman, M. Latif, H. Le Treut, T. Nagai, J. D. Neelin, S. G. H. Philander, J. Polcher, P. S. Schopf, T. Stockdale, M. J. Suarez, L. Terray, O. Thual, and J. J. Tribbia, (1995): The seasonal cycle over the tropical Pacific in coupled ocean-atmosphere general circulation models, *Mon. Wea. Rev.*, **123**, 2825-2838.

Neelin, J. D., et al., (1992): Tropical air-sea interaction in general circulation models, *Clim. Dyn.*, **7**, 73-104.

Neelin, J. D., M. Latif, F-F. Jin, (1994): Dynamics of coupled ocean-atmosphere models: The tropical problem, *Annu. Rev. Fluid Mech.*, **26**, 617-659.

Rummukainen, M., J. Raisanen, B. Bringfelt, A. Ullerstig, A. Omstedt, U. Willen, U. Hansson, and C. Jones, (2001): A regional climate model for northern Europe: model description and results from the downscaling of two GCM control simulations, *Clim. Dyn.*, **17**, 339-359.

Tokioka, T. et al., (1984): A description of the Meteorological Research Institute atmospheric general circulation model (MRI-GCM-I). *Technical Report of the MRI*, **13**, 1-249.

Washington, W. M., A. J. Semtner, Jr., G. A. Meehl, D. J. Knight, and T. A. Mayer, (1980): A general circulation experiment with a coupled atmosphere, ocean, and sea ice model, *J. Phys. Oceanogr.*, **10**, 1887-1908.

Chapter 2

Regional Environment and Disaster Events Simulator

2.1 Introduction

Regional Environment and Disaster Prevention Simulator (REDES) named in this dissertation is a coupled numerical model being used for the studies of natural disasters in coastal and estuarine areas such as storm surge, high waves, flood, inundation, heavy rainfall, etc. This REDES has sub-models that describe the atmospheric and oceanic circulations, wind wave conditions on sea surface, overtopping of waves and estuarine and coastal circulation. The atmospheric circulation in this REDES is represented by non-hydrostatic meso-scale atmospheric model, MM5 and the ocean circulation is described by two ocean models; 1) primitive equation ocean model, POM and 2) non-hydrostatic ocean model, MITgcm. The sea surface wind waves are studied by third-generation wind wave models; 1)WaveWatch III (WW3) and 2)Simulating Waves Nearshore (SWAN). The overtopping of high waves at the coast is described by 2D direct numerical simulation model, CADMAS-SURF and the estuarine and coastal circulation model, ECOMSED is introduced. In this chapter, the governing equations of these sub-models of REDES are described first and then the objectives and design of REDES are followed.

2.2 Basic equations

This section is largely based on the web-based description of extended Navier-Stokes (NS) equations by Cramer, (2002).

The flow motion is known to be described by complete and unapproximated NS equation system that can be written in vector form;

$$\frac{D\rho}{Dt} + \rho \nabla \cdot \mathbf{v} = 0 \tag{2.1}$$

$$\rho \frac{D\mathbf{v}}{Dt} = -\nabla p + \nabla \cdot \mathbf{T}^* + \rho \mathbf{f} \tag{2.2}$$

$$\rho \frac{D\mathrm{e}}{Dt} = -p\nabla \cdot \mathbf{v} + \Phi - \nabla \cdot \mathbf{q} + \rho \mathrm{r} \tag{2.3}$$

where ρ, $\mathbf{v}=[u,v,w]$, p, $\mathbf{f}$, e, and r are the density[mass/volume], three-dimensional velocity vector [length/time], pressure [force/area], body force density [force/mass], internal energy [energy/mass], volumetric energy supply[energy/(time·mass)] and $\Phi(\equiv \mathbf{T}^*)$ is referred to as dissipation function.

Here $\mathbf{T}$ and $\mathbf{q}$ are stress tensor and heat flux vector [energy/area] from constitutive relations and $\mathbf{T}^*$ is the viscous part of the stress tensor as;

$$\mathbf{T} = \left(-p + (\lambda \nabla \cdot \mathbf{v})1\right) + \mu\left(\nabla \mathbf{v} + (\nabla \mathbf{v})^{\mathrm{T}}\right) \tag{2.4}$$

$$\mathbf{q} = -\mathrm{k}\nabla T \tag{2.5}$$

$$\mathbf{T}^* \equiv \lambda(\nabla \cdot \mathbf{v})1 + \mu\left(\nabla \mathbf{v} + (\nabla \mathbf{v})^{\mathrm{T}}\right) \tag{2.6}$$

where λ, 1, μ, k and T are the second viscosity [mass/(length·time)], identity tensor, shear viscosity [mass/(length·time)], thermal conductivity [energy/(time·length·temp)] and temperature[temp] and superscript T is the transpose of the indicate quantity.

The operators, ∇ and $\nabla \cdot (\ )$, are the gradient and the divergence of quantity ( ) respectively and the total derivative;

$$\frac{D(\ )}{Dt} = \frac{\partial(\ )}{\partial t} + \mathbf{v} \cdot \nabla(\ ) \tag{2.7}$$

is the time rate of change of any quantities ( ).

The NS equations given by (2.1) ~ (2.3) can be extended for more familiar form without tensor by simply replacing the (2.5) and (2.6) into the momentum and energy equations and then result in;

$$\frac{D\rho}{Dt} + \rho\nabla \cdot \mathbf{v} = 0 \tag{2.8}$$

$$\rho \frac{D\mathbf{v}}{Dt} = -\nabla p + \nabla\left[\lambda(\nabla \cdot \mathbf{v})\right] + \nabla \cdot \left(\mu\left(\nabla \mathbf{v} + (\nabla \mathbf{v})^{\mathrm{T}}\right)\right) + \rho \mathbf{f} \tag{2.9}$$

$$\rho \frac{D\mathrm{e}}{Dt} = -p\nabla \cdot \mathbf{v} + \Phi + \nabla \cdot \left(\mathrm{k}\nabla T\right) + \rho \mathrm{r} \tag{2.10}$$

The physical meaning of the system of NS equations (2.8) ~ (2.10) are that

1) Equation (2.8) shows that the time rate of density change can be given by the change rate of certain volume called *control volume* of a material due to the conservation of mass. It is called *continuity equation*.

2) Differential equation (2.9) is derived from the Newton's second law following the conservation of mass and showing that the time rate of momentum change is given by the balance of the spatial variation of pressure, viscosity and the body force acting on control volume. It is called *momentum equation*.

3) Equation (2.10) is given by the conservation of energy on control volume showing that the time rate of total (internal and kinetic) energy change is the work done by surface force on volume change and by the stresses by viscosity and heat transfer by conduction through the surface and by the volumetric energy supply. The volumetric energy transfer, r, is the energy supplied by radiation from the sun or any other external sources and by the chemical reaction within the material. It is call *energy equation*.

The complete and unapproximated NS equations are usually applied to many problems in atmospheric and oceanic motions after variable degrees of approximations are made. Two of the common variable approximations are for the inviscid and incompressible flows. In section 2.3 ~ 2.5, the governing equations of MM5, POM and MITgcm are described with the various approximations applied in NS equation system.

2.3 Boundary conditions for NS equations

As the word *boundary* implies, the boundary conditions are the conditions that NS equations should satisfy at boundaries which are interfaces between materials such as the liquid, gas and solid. Even same materials with different properties of ρ, $\mathbf{v}$ or T have the boundary. The boundaries are kinetic boundary condition, dynamic boundary condition, heat flux condition and no-slip condition. Here the boundary/interface can be written in mathematically as;

$$\mathrm{F}\left(\mathbf{x}, t\right) \equiv 0 \tag{2.11}$$

where $\mathbf{x}$ and t are the position in coordinate systems and a certain time

Kinetic boundary condition (KBC)

KBC is a condition on the particles of materials and the analogue of continuity equation (2.8) being held for every boundary/interface. The general expression of KBC is written by

$$\frac{D\mathrm{F}}{Dt} = \frac{\partial \mathrm{F}}{\partial t} + \mathbf{v}\nabla \cdot \mathrm{F} = 0 \qquad \text{where } \mathrm{F}(\mathbf{x},t) = 0 \tag{2.12}$$

which leads to

$$\mathbf{v}\cdot\mathrm{n} = -\left(\partial\mathbf{F}/\partial t\right)\Big/\left|\nabla\mathbf{F}\right| \tag{2.13}$$

where the n is the normal vector to boundary or interface. Thus the KBC states that the normal velocities on the boundary/interface in different materials are same and conserved that the materials are moving together without gap in between.

Dynamic boundary condition (DBC)

DBC is the analogue of the momentum equation (2.9) and holds for all interfaces. The DBC is expressed by

$$\Delta\left(\mathbf{T}^{\mathrm{T}}\mathrm{n}\right) = 0 \qquad \text{where} \qquad \mathrm{F}(\mathbf{x},t) = 0 \tag{2.14}$$

since the $\mathbf{T}^{\mathrm{T}}$n is the force by stresses acting on unit area on the side of interface, the DBC states that the forces acting on both sides of interface should be balanced and continuous. Therefore if one of the materials is described as a rigid boundary, the DBC does not offer useful condition on the stress in the other material.

Heat flux condition (HFC)

HFC is the analogue of the energy equation (2.10) and is described by

$$\Delta\left(\mathbf{q}\cdot\mathrm{n}\right) = 0 \qquad \text{where} \qquad \mathrm{F}(\mathbf{x},t) = 0 \tag{2.15}$$

the HFC states that the normal component of heat flux vector on the boundary or interface

12

should be continuous in materials.

No-slip conditions

The no-slip condition is only valid when one of the materials is a Navier-Stokes fluid which is governed by NS equations in local thermodynamic equilibrium and is written by

$$\mathbf{n} \times \Delta \mathbf{v} = 0 \qquad \text{where} \qquad F(\mathbf{x}, t) = 0 \tag{2.16}$$

where $\times$ indicates the cross product. Therefore the no-slip condition states that the velocity components parallel to the interface is continuous.

2.4 Atmosphere circulation model in REDES

The atmospheric circulation model employed in REDES is the mesoscale meteorological model, MM5. The governing equations and the parameterization of physical processes incorporated in the model are described in following sections of (2.4.1) and (2.4.2).

2.4.1 Governing equations of MM5

MM5 is the fifth-generation atmospheric mesoscale meteorological model developed by Pennsylvania State University (PSU)/National Center for Atmospheric Research (NCAR), which solves hydrostatic and non-hydrostatic governing equations in the vertical sigma (σ) coordinate where σ is defined in terms of pressure as,

$$\sigma = \frac{\left(p_0 - p_{top} \right)}{p*} \tag{2.17}$$

where $p* = p_{sfc} - p_{top}$ and p_0 is reference-state pressure and the σ levels in non-hydrostatic system are fixed in space being closely related to rather height than pressure and the pressure at a certain point, p, is calculated by $p = p*\sigma + p_{top} + p' = p_0 + p'$ where p' is a computed value of pressure perturbation.

When the non-hydrostatic governing equations of the model are solved, other two prognostic equations for the three-dimensional pressure distribution and the vertical momentum are adopted. The equation for pressure tendency is derived from the continuity equation and the law of perfect gas. In addition to the two prognostic equations, the full three-dimensional

Coriolis effects are also retained in non-hydrostatic equations.

The non-hydrostatic governing equations in Cartesian-sigma, (x,y,σ) coordinate system in rotating frame of reference can be written as;

$$\frac{Dp'}{Dt} = \rho_0 gw - \gamma p \nabla \cdot \mathbf{v} + \frac{\gamma p}{T}\left(\frac{\dot{Q}}{c_p} + \frac{T_0}{\theta_0}D_\theta\right) \tag{2.18}$$

$$\frac{Du}{Dt} = -\frac{1}{\rho}\left(\frac{\partial p'}{\partial x} - \frac{\sigma}{p*}\frac{\partial p*}{\partial x}\frac{\partial p'}{\partial \sigma}\right) + fv - ew\cos\Theta - \frac{uw}{r_{earth}} + D_u \tag{2.19}$$

$$\frac{Dv}{Dt} = -\frac{1}{\rho}\left(\frac{\partial p'}{\partial y} - \frac{\sigma}{p*}\frac{\partial p*}{\partial y}\frac{\partial p'}{\partial \sigma}\right) - fu + ew\sin\Theta - \frac{vw}{r_{earth}} + D_v \tag{2.20}$$

$$\frac{Dw}{Dt} = \frac{\rho_0}{\rho}\frac{g}{p*}\frac{\partial p'}{\partial \sigma} - \frac{g}{\gamma}\frac{p'}{p} + g\frac{p_0}{p}\frac{T'}{T_0} - \frac{gR_d}{c_p}\frac{p'}{p} + e\left(u\cos\Theta - v\sin\Theta\right) + \frac{u^2 + v^2}{r_{earth}} + D_w \tag{2.21}$$

$$\frac{DT}{Dt} = \frac{1}{\rho c_p}\left(\frac{\partial p'}{\partial t} + \mathbf{v}\cdot\nabla p' - \rho_0 gw\right) + \frac{\dot{Q}}{c_p} + \frac{T_0}{\theta_0}D_\theta \tag{2.22}$$

where T, ρ, θ, $\dot{Q}$ and $D_{(\ )}$ are the temperature, the density, the potential temperature, the heating rate due to diabatic processes and subgrid-scale eddy viscous terms respectively. The constants g, f, R_d, c_p and γ are the acceleration due to gravity, Coriolis parameter, the gas constant of dry air, the heat capacity of constant pressure of air and the ratio of heat capacity for air at constant pressure to that of constant volume. Here the two new parameters, Θ, which is the angular difference between the y-axis of the grid and the true north and $e = 2\Omega\cos\varphi$ (note with the internal energy, e), are introduced to describe the full three-dimensional Coriolis effects where the Ω and φ are the angular velocity of the earth and the latitude. The Θ can be expressed by

$$\tan\Theta = -\cos\varphi\frac{\partial\lambda/\partial y}{\partial\varphi/\partial y} \tag{2.23}$$

where λ is the longitude. The advection term in equations can be expanded as

$$\mathbf{v}\cdot\nabla A \equiv u\frac{\partial A}{\partial x} + v\frac{\partial A}{\partial y} + \dot{\sigma}\frac{\partial A}{\partial \sigma} \tag{2.24}$$

where the vertical velocity, $\dot{\sigma}$, in σ coordinate is related to modeled values of velocity components by

$$\dot{\sigma} = -\frac{\rho_0 g}{p*}w - \frac{\sigma}{p*}\frac{\partial p*}{\partial x}u - \frac{\sigma}{p*}\frac{\partial p*}{\partial y}v \qquad (2.25)$$

and the divergence term in (2.18) can be expanded in Cartesian-simga coordinate as

$$\nabla \cdot \mathbf{v} = \frac{\partial u}{\partial x} - \frac{\sigma}{p*}\frac{\partial p*}{\partial x}\frac{\partial u}{\partial \sigma} + \frac{\partial v}{\partial y} - \frac{\sigma}{p*}\frac{\partial p*}{\partial y}\frac{\partial v}{\partial \sigma} - \frac{\rho_0 g}{p*}\frac{\partial w}{\partial \sigma} \qquad (2.26)$$

when $p*$ is constant, the second and fourth terms in right hand side will be disappeared. On the surface ($\sigma=0$) and top ($\sigma=1$) levels, the boundaries are considered as rigid conditions such that $\dot{\sigma} = 0$ is applied.

2.4.2 Physical processes parameterization in MM5

In MM5 model, physical mechanisms such as precipitation physics, planetary boundary layer (PBL) processes and atmospheric radiation processes are parameterized and two additional prognostic equations for water vapor and microphysical variables such as cloud and precipitation are also incorporated. These equations include the advection and various source and sink terms. Table 2.1 shows the available physics schemes such as cumulus, explicit moisture, radiation, land surface and Planetary Boundary Layer (PBL) schemes. Figs 2.1 through 2.5 show the simple illustrations of cumulus scheme, PBL processes, micorphysics processes, atmospheric radiation processes, surface processes, respectively. Fig. 2.6, at last, shows the direct interactions of physics parameterizations (refer to Grell et al., 1995 for details).

Table 2.1 Physical parameterizations in MM5

Cumulus parameterization schemes	References	Planetary Boundary Layer (PBL) Schemes and Diffusion	References
Anthes-Kuo scheme		Bulk PBL scheme	
Grell scheme	Grell et al., 1995	High-resolution Blackadar PBL scheme	
Arakawa-Schubert scheme	Grell et al., 1995	Burk-Thompson PBL scheme	Burke and Thompson, 1989
Fritsch-Chappell scheme	Fritsch and Chappell, 1980	Eta PBL scheme	Janjic, 1990 and 1994
Kain-Fritsch scheme	Kain and Fritsch, 1993	MRF PBL scheme	Hong and Pan, 1996
Betts-Miller scheme	Betts and Miller, 1986 and 1993	Gayno-Seaman PBL scheme	Ballard et al., 1991; Shafran et al. 2000
Shallow Cumulus scheme		Pleim-Chang PBL scheme	Pleim and Chang, 1992
		Moist vertical diffusion scheme	
		Thermal roughness length scheme	
		Horizontal diffusion scheme	Zangl, 2002

Table 2.1 continued

Explicit Moisture Schemes	References	Radiation Schemes	References	Surface Schemes	References
Dry scheme		Simple cooling scheme		Force/restore (Blackadar) scheme	
Stable Precip scheme		Surface radiation scheme		Five-Layer Soil model	Dudhia, 1996
Warm Rain scheme		Cloud-radiation scheme		Noah Land-Surface Model	Chen and Dudhia, 2001a and 2001b
Simple Ice (Dudhia) scheme		CCM2 radiation scheme	Hack et al., 1993	Pleim-Xiu Land-Surface Model	Xiu and Pleim, 2000
Mixed-Phase (Reisner 1) scheme	Reisner et al., 1998	RRTM longwave scheme	Mlawer et al., 1997	Bucket Soil Moisture Model	
Goddard microphysics scheme	Lin et al., 1983; Tao et al., 1989 and 1993			Snow Cover Model	
Reisner graupel (Reisner 2) scheme				Polar Mods	Byrd Polar Research Center at Ohio State Univerisity
Schultz microphysics scheme	Schultz, 1995				
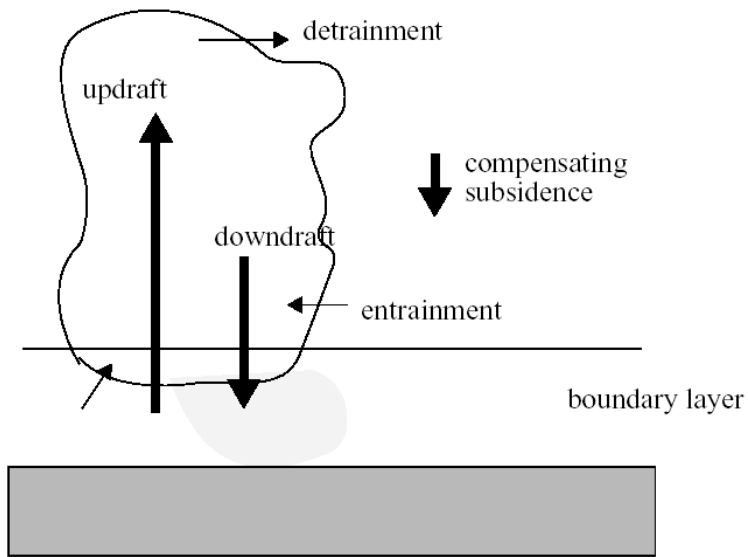
Fig. 2.1 Simple illustration of cumulus scheme (Dudhia et al., 2005)
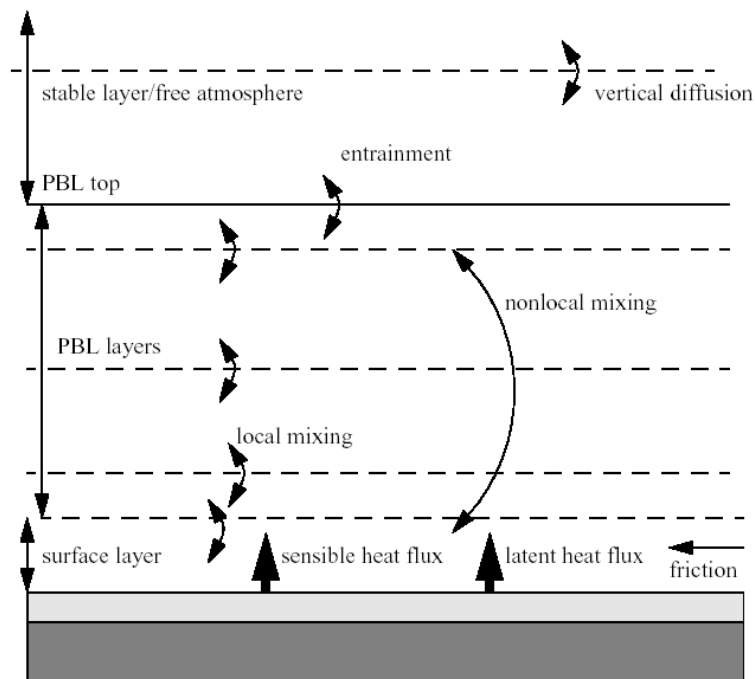
Fig. 2.2 Simple illustration of PBL processes (Dudhia et al., 2005)

18
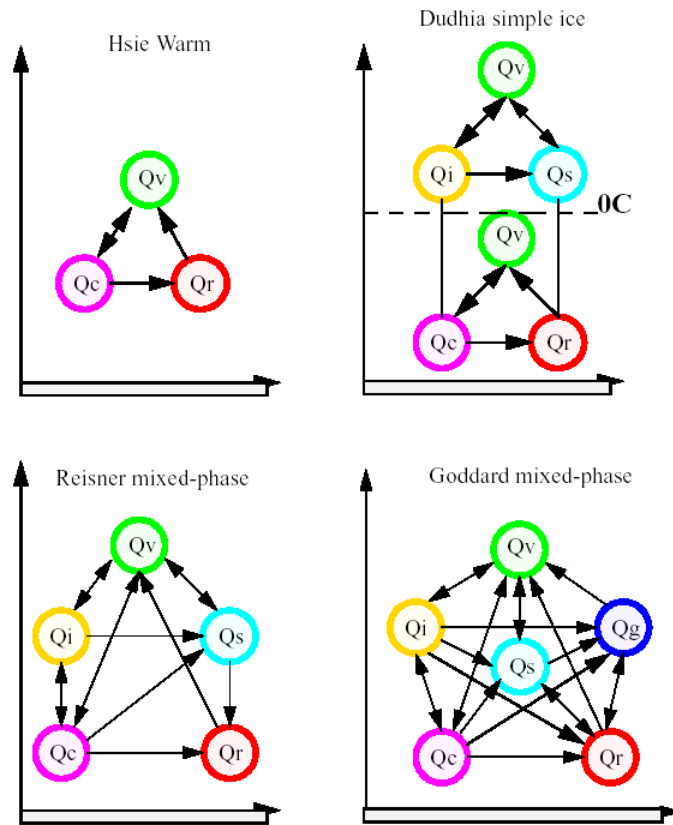
Fig. 2.3 Simple illustration of microphysics processes (Dudhia et al., 2005)
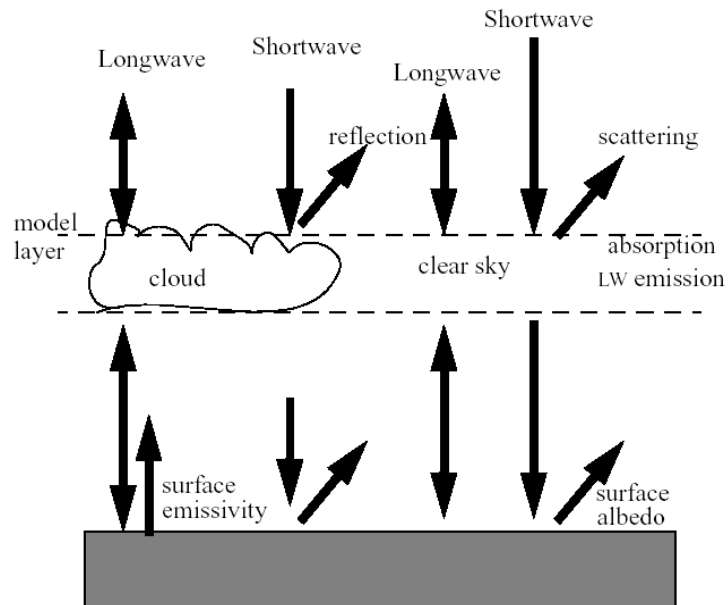
Fig. 2.4 Simple illustration of atmospheric radiation processes (Dudhia et al., 2005)
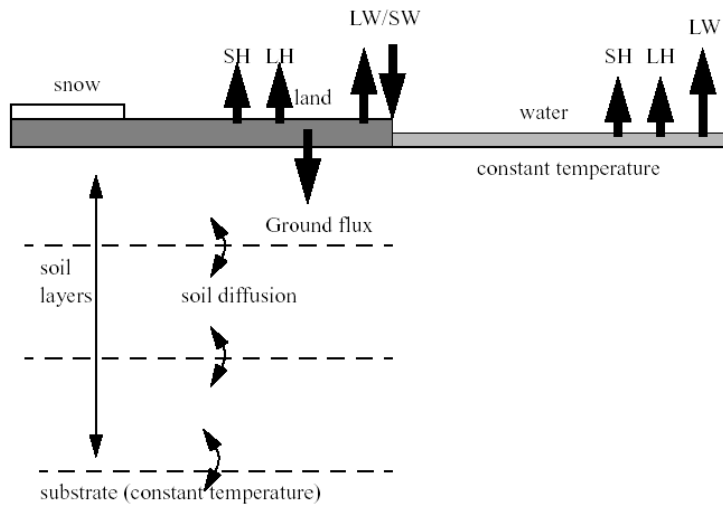
Fig. 2.5 Simple illustration of surface processes (Dudhia et al., 2005)
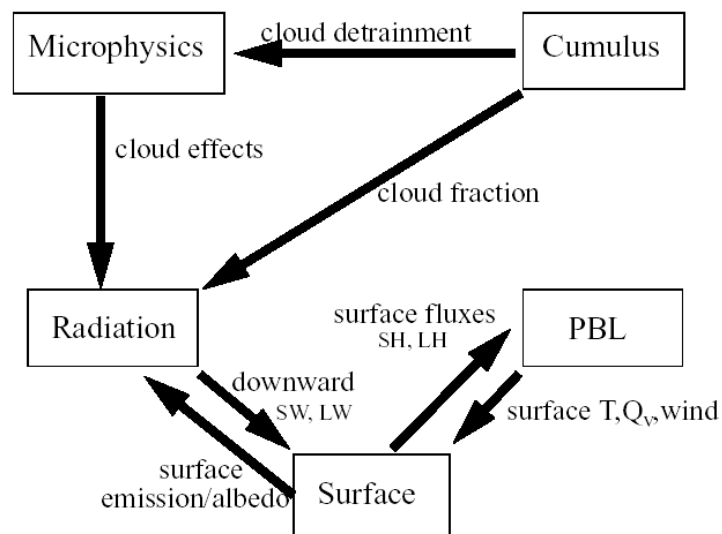
Fig. 2.6 Simple illustration of direct interactions of physics parameterizations (Dudhia et al., 2005)

2.5 Ocean circulation models in REDES

The oceanic circulation part of REDES is described by hydrostatic primitive equation model, POM or MITgcm which has both hydrostatic and non-hydrostatic computations schemes. In the following sections, the governing equations and characteristics of two ocean models are described.

2.5.1 POM

This hydrostatic primitive equation ocean model is developed in Princeton University and applied to many oceanographic problems. The main attributes of this model can be summarized as follow (Mellor, 2004).

1) It contains an imbedded second moment turbulence closure model (Mellor and Yamada, 1982) to calculate vertical mixing coefficients.

2) It is a sigma coordinate model that the vertical coordinate is scaled on water depth.

3) The horizontal grid uses curvilinear orthogonal coordinates and an *Arakawa C* differencing scheme.

4) The horizontal time differencing is explicit whereas the vertical differencing is implicit. The latter eliminates time constraints for the vertical coordinate and permits the use of fine vertical resolution in the surface and bottom boundary layers.

5) This model has a free surface boundary and a split time step in two different modes. The external mode of the model is two-dimensional and uses a short time step based on the CFL condition and the external wave speed. On the other hand, the internal mode of the model is three-dimensional and uses a long time step based on the CFL condition and the internal wave speed.

6) The complete thermodynamics is implemented.

2.5.1.1 Governing equations of POM

Princeton Ocean Model, POM, is based on hydrostatic primitive equations in bottom following, sigma coordinate. The relation between the Cartesian and sigma coordinate is based on the transformation:

$$\sigma = \frac{z - \eta(t)}{D}; \quad D \equiv H(x,y) + \eta(x,y,t) \qquad (2.27)$$

where $H(x,y)$ is bottom topography and $\eta(x,y,t)$ is the surface elevation. Here the simple derivation of governing equations in sigma coordinate is as follows;

Let $\phi(x,y,z,t) = \phi^*(x,y,\sigma,t)$ and then the partial derivative of ϕ using the chain rule becomes

$$\frac{\partial \phi}{\partial x} = \frac{\partial \phi^*}{\partial x} + \frac{\partial \phi^*}{\partial \sigma}\frac{\partial \sigma}{\partial x} = \frac{\partial \phi^*}{\partial x} - \frac{\partial \phi^*}{\partial \sigma}\frac{1}{D}\left(\frac{\partial \eta}{\partial x} + \sigma\frac{\partial D}{\partial x}\right) \tag{2.28}$$

$$\frac{\partial \phi}{\partial y} = \frac{\partial \phi^*}{\partial y} + \frac{\partial \phi^*}{\partial \sigma}\frac{\partial \sigma}{\partial y} = \frac{\partial \phi^*}{\partial y} - \frac{\partial \phi^*}{\partial \sigma}\frac{1}{D}\left(\frac{\partial \eta}{\partial y} + \sigma\frac{\partial D}{\partial y}\right) \tag{2.29}$$

$$\frac{\partial \phi}{\partial z} = \frac{\partial \phi^*}{\partial \sigma}\frac{1}{D} \tag{2.30}$$

$$\frac{\partial \phi}{\partial t} = \frac{\partial \phi^*}{\partial t} + \frac{\partial \phi^*}{\partial \sigma}\frac{\partial \sigma}{\partial t} = \frac{\partial \phi^*}{\partial t} - \frac{\partial \phi^*}{\partial \sigma}\frac{1}{D}\left(\frac{\partial \eta}{\partial t} + \sigma\frac{\partial D}{\partial t}\right) \tag{2.31}$$

Now the continuity equation $\nabla \cdot \mathbf{v} = 0$ in conventional Cartesian coordinate is

$$\frac{\partial u}{\partial x} + \frac{\partial v}{\partial y} + \frac{\partial w}{\partial z} = 0 \tag{2.32}$$

substituting (2.28), (2.29) and (2.30) into continuity equation (2.32) yields

$$\frac{\partial u}{\partial x} - \frac{\partial u}{\partial \sigma}\frac{1}{D}\left(\frac{\partial \eta}{\partial x} + \sigma\frac{\partial D}{\partial x}\right) + \frac{\partial v}{\partial y} - \frac{\partial v}{\partial \sigma}\frac{1}{D}\left(\frac{\partial \eta}{\partial y} + \sigma\frac{\partial D}{\partial y}\right) + \frac{\partial w}{\partial \sigma}\frac{1}{D} = 0 \tag{2.33}$$

using the relation of Cartesian vertical velocity to sigma vertical velocity

$$w = \dot{\sigma} + u\left(\frac{\partial \eta}{\partial x} + \sigma\frac{\partial D}{\partial x}\right) + v\left(\frac{\partial \eta}{\partial y} + \sigma\frac{\partial D}{\partial y}\right) + \frac{\partial \eta}{\partial t} + \sigma\frac{\partial D}{\partial t} \tag{2.34}$$

where $\dot{\sigma}$ is the vertical velocity in sigma coordinate, gives

$$\begin{aligned}
&\frac{\partial u}{\partial x} - \frac{\partial u}{\partial \sigma}\left(\frac{\partial \eta}{\partial x} + \sigma\frac{\partial D}{\partial x}\right) + \frac{\partial v}{\partial y} - \frac{\partial v}{\partial \sigma}\left(\frac{\partial \eta}{\partial y} + \sigma\frac{\partial D}{\partial y}\right) \\
&+ \frac{\partial \dot{\sigma}}{\partial \sigma} + \frac{\partial u}{\partial \sigma}\left(\frac{\partial \eta}{\partial x} + \sigma\frac{\partial D}{\partial x}\right) + \frac{\partial uD}{\partial x} + \frac{\partial v}{\partial \sigma}\left(\frac{\partial \eta}{\partial y} + \sigma\frac{\partial D}{\partial y}\right) + \frac{\partial vD}{\partial y} + \frac{\partial \eta}{\partial t} = 0
\end{aligned} \tag{2.35}$$

that can be simplified as

$$\frac{\partial uD}{\partial x} + \frac{\partial vD}{\partial y} + \frac{\partial \dot{\sigma}}{\partial \sigma} + \frac{\partial \eta}{\partial t} = 0 \tag{2.36}$$

since $D_t = \partial \eta / \partial t$.

 After applying the same procedure to momentum equation and equations for temperature and salinity, the governing equations the model solves are written by

$$\frac{\partial uD}{\partial t} + \frac{\partial u^2 D}{\partial x} + \frac{\partial uvD}{\partial y} + \frac{\partial u\dot{\sigma}}{\partial \sigma} =$$
$$fvD - gD\frac{\partial \eta}{\partial x} - \frac{gD^2}{\rho_r}\int_\sigma^0 \left[\frac{\partial \rho'}{\partial x} - \frac{\sigma'}{D}\frac{\partial D}{\partial x}\frac{\partial \rho'}{\partial \sigma'}\right]\partial \sigma' + \frac{\partial}{\partial \sigma}\left[\frac{K_M}{D}\frac{\partial u}{\partial \sigma}\right] + F_x \tag{2.37}$$

$$\frac{\partial vD}{\partial t} + \frac{\partial uvD}{\partial x} + \frac{\partial v^2 D}{\partial y} + \frac{\partial v\dot{\sigma}}{\partial \sigma} =$$
$$-fuD - gD\frac{\partial \eta}{\partial y} - \frac{gD^2}{\rho_r}\int_\sigma^0 \left[\frac{\partial \rho'}{\partial y} - \frac{\sigma'}{D}\frac{\partial D}{\partial y}\frac{\partial \rho'}{\partial \sigma'}\right]\partial \sigma' + \frac{\partial}{\partial \sigma}\left[\frac{K_M}{D}\frac{\partial v}{\partial \sigma}\right] + F_y \tag{2.38}$$

$$\frac{\partial TD}{\partial t} + \frac{\partial TuD}{\partial x} + \frac{\partial TvD}{\partial y} + \frac{\partial T\dot{\sigma}}{\partial \sigma} = \frac{\partial}{\partial \sigma}\left[\frac{K_H}{D}\frac{\partial T}{\partial \sigma}\right] + F_T - \frac{\partial R}{\partial z} \tag{2.39}$$

$$\frac{\partial SD}{\partial t} + \frac{\partial SuD}{\partial x} + \frac{\partial SvD}{\partial y} + \frac{\partial S\dot{\sigma}}{\partial \sigma} = \frac{\partial}{\partial \sigma}\left[\frac{K_H}{D}\frac{\partial S}{\partial \sigma}\right] + F_S \tag{2.40}$$

$$\frac{\partial q^2 D}{\partial t} + \frac{\partial uq^2 D}{\partial x} + \frac{\partial vq^2 D}{\partial y} + \frac{\partial \dot{\sigma}q^2}{\partial \sigma} =$$
$$\frac{\partial}{\partial \sigma}\left[\frac{K_q}{D}\frac{\partial q^2}{\partial \sigma}\right] + \frac{2K_M}{D}\left[\left(\frac{\partial u}{\partial \sigma}\right)^2 + \left(\frac{\partial v}{\partial \sigma}\right)^2\right] + \frac{2g}{\rho_0}K_H\frac{\partial \tilde{\rho}}{\partial \sigma} - \frac{2Dq^3}{B_1 l} + F_q \tag{2.41}$$

$$\frac{\partial q^2 lD}{\partial t} + \frac{\partial uq^2 lD}{\partial x} + \frac{\partial vq^2 lD}{\partial y} + \frac{\partial \dot{\sigma}q^2 l}{\partial \sigma} =$$
$$\frac{\partial}{\partial \sigma}\left[\frac{K_q}{D}\frac{\partial q^2 l}{\partial \sigma}\right] + E_1 l\left[\frac{K_M}{D}\left(\left(\frac{\partial u}{\partial \sigma}\right)^2 + \left(\frac{\partial v}{\partial \sigma}\right)^2\right)\right] + E_3\frac{g}{\rho_0}K_H\frac{\partial \tilde{\rho}}{\partial \sigma} - \frac{Dq^3}{B_1}\tilde{w} + F_l \tag{2.42}$$

where T and S are temperature and salinity and K_m, K_H are vertical kinetic viscosity and diffusivity respectively and q^2, l are twice the turbulence kinetic energy and turbulence length

scale. $\tilde{w} = 1 + E_2(l/kL)$ where $L^{-1} = (\eta\text{-}z)^{-1} + (H\text{-}z)^{-1}$ and $\partial\tilde{\rho}/\partial\sigma \equiv \partial\rho/\partial\sigma - c_s^{-2}\partial p/\partial\sigma$. Here the $\tilde{\phi} = \Phi + \phi'$ shows that the quantity $\phi = \tilde{\phi}$ is the sum of mean (Φ) and deviation (ϕ') values. The horizontal viscosity and diffusion terms in the momentum equations are defined as:

$$F_x \equiv \frac{\partial}{\partial x}\left(H\tau_{xx}\right) + \frac{\partial}{\partial y}\left(H\tau_{xy}\right) \tag{2.43}$$

$$F_y \equiv \frac{\partial}{\partial x}\left(H\tau_{xy}\right) + \frac{\partial}{\partial y}\left(H\tau_{yy}\right) \tag{2.44}$$

where

$$\tau_{xx} = 2A_M\frac{\partial u}{\partial x}, \quad \tau_{xy} = \tau_{yx} = A_M\left(\frac{\partial u}{\partial y} + \frac{\partial v}{\partial x}\right), \quad \tau_{yy} = 2A_M\frac{\partial v}{\partial y} \tag{2.45}$$

Also,

$$F_\phi \equiv \frac{\partial}{\partial x}\left(Hq_x\right) + \frac{\partial}{\partial y}\left(Hq_y\right) \tag{2.46}$$

where

$$q_x = A_H\frac{\partial\phi}{\partial x}, \quad q_y = A_H\frac{\partial\phi}{\partial y} \tag{2.47}$$

here ϕ represents the T, S, q^2 or q^2l.

As written in the model features, POM include unique technique that the fast moving surface gravity waves and slow moving internal gravity waves are separately dealt with corresponding time steps. The surface gravity waves can be dealt with in the 2D external mode in the model that is governed by the vertically integrated governing equations for continuity and momentum equations where the thermodynamic properties are invariant in time. On the other hand, the 3D internal mode is governed by the hydrostatic primitive equations as described in (2.37) ~ (2.42).

2.5.2 MITgcm

The 3D general circulation model has been developed in Massachusetts Institute of

Technology and has a number of unique features as follows (Marshall et al., 1997a, b).

1) It can be used to study both atmospheric and oceanic phenomena; one hydrodynamical kernel that consists of a set of governing equations is used to drive forward both atmospheric and oceanic models.

2) It has a non-hydrostatic capability as well as hydrostatic one and so can be used to study from small scale like convection to large scale processes such as global thermohaline circulation.

3) Finite volume techniques are employed yielding an intuitive discretization and support for the treatment of irregular geometries using orthogonal curvilinear grids and shaved cells.

4) Tangent linear and adjoint counterparts are automatically maintained along with the forward model, permitting sensitivity and optimization studies.

5) The model is developed to perform efficiently on a wide variety of computational platforms.

2.5.2.1 Governing equations of MITgcm

As written in the first of unique features, this model is based on one hydrodynamical kernel that is a set of equations governing the atmospheric and oceanic circulations and can be used for modeling of both systems. The governing equations of MITgcm are based on the incompressible NS equations with Boussinesq approximation and therefore the Eqs. (2.8) ~ (2.10) can be re-written as:

$$\nabla \cdot \mathbf{v} = 0 \tag{2.48}$$

$$\frac{D\mathbf{v}}{Dt} = -\frac{1}{\rho_r}\nabla\phi - f\mathbf{n}\times\mathbf{v} + b\mathbf{n} + v_h\left(\frac{\partial^2}{\partial x^2} + \frac{\partial^2}{\partial y^2}\right)\mathbf{v} + v_v\frac{\partial^2}{\partial z^2}\mathbf{v} \tag{2.49}$$

$$\frac{D\theta}{Dt} = Q_\theta \tag{2.50}$$

$$\frac{DS}{Dt} = Q_s \tag{2.51}$$

$$b = b(\theta, S, p) \tag{2.52}$$

where $\mathbf{v} = (u, v, \dot{r})$ is the three-dimensional velocity vector in zonal, meridional and vertical directions, r is vertical coordinate, ρ_r is the reference density of water, f is Coriolis parameter, p is the pressure, b is the buoyancy ($-g(\delta\rho/\rho_r)$), θ and S are the potential temperature and salinity, v_h and v_v are the horizontal and vertical viscosity coefficients and Q_θ and Q_s are source and sink term of tracers (potential temperature and salinity). Here $\times$ is

cross product of vector and **n** is the unit vector in vertical direction. The equation of state for water density depends on θ, S and p and takes a form of linear or high-order polynomials.

2.5.2.2 Atmosphere in MITgcm

For the atmospheric circulation in MITgcm, the governing Eqs. (2.48) ~ (2.52) are interpreted as;

$$r = p \quad \text{is the pressure} \tag{2.53}$$

$$\dot{r} = \frac{Dp}{Dt} = w \quad \text{is the vertical velocity in pressure coordinate} \tag{2.54}$$

$$\phi = \rho_r gz \quad \text{is the geopotential height} \tag{2.55}$$

$$b = \frac{\partial \Pi}{\partial p}\theta \quad \text{is the buoyancy} \tag{2.56}$$

$$\theta = T\left(\frac{p_c}{p}\right)^k \quad \text{is the potential temperature} \tag{2.57}$$

$$S = q \quad \text{is the specific humidity} \tag{2.58}$$

where T, p and z are the temperature, pressure and height of pressure level. In the above the buoyancy is expressed in terms of Exner function (Π) which represents the ideal gas law ($p=\rho RT$) and is given by;

$$\Pi(p) = c_p\left(\frac{p}{p_c}\right)^k \tag{2.59}$$

where p_c is a reference pressure where $\theta = T$ and k ($=R/c_p$) with R, the gas constant and c_p is specific heat of air at constant pressure.

2.5.2.3 Ocean in MITgcm

For the oceanic circulation in MITgcm, the governing equations are interpreted as:

$$r = z \quad \text{is the depth from the surface} \tag{2.60}$$

$$\dot{r} = \frac{Dz}{Dt} = w \quad \text{is the vertical velocity in } z \text{ coordinate} \tag{2.61}$$

$$\phi = p \quad \text{is the pressure} \tag{2.62}$$

$$b(\theta, S, r) = \frac{g}{\rho_r}\left(\rho(\theta, S, r) - \rho_r\right) \quad \text{is the buoyancy.} \tag{2.63}$$

where ρ_r is the reference density. When the non-hydrodynamic governing equations are being solved, the full three-dimensional Coriolis effects are retained and a prognostic equation for pressure perturbation, p', can be found by combining the incompressibility condition with the momentum equations. For convenience, first define the vector G to be all the terms of the momentum equations except the local derivative and pressure gradient:

$$G \equiv -\mathbf{v} \cdot \nabla \mathbf{v} - f\mathbf{n} \times \mathbf{v} - F \tag{2.64}$$

where F is the dissipation terms by viscosity and any other forcing terms. Here the momentum equation can be re-written simply by:

$$\frac{\partial v}{\partial t} + \frac{1}{\rho_r} \nabla p' = G \tag{2.65}$$

then substituting the above momentum equation into the incompressibility condition yields the pressure equation as:

$$\frac{1}{\rho_r} \nabla^2 p' = \nabla \cdot G - \frac{\partial}{\partial t} \nabla \cdot \mathbf{v} \tag{2.66}$$

Now together with the mass conservation, momentum equation and equation for temperature and salinity, there are six prognostic equations for p, $\mathbf{v}$, θ and S and one diagnostic relation for ρ.

2.6 Ocean wave simulation models in REDES

Sea surface wind/gravity waves are prevailing everywhere and play a critical role in the interaction between atmosphere and ocean in their interface. Two third-generation wind wave models, WW3 and SWAN, are adopted in REDES for the modeling of wind wave fields and the interactions

2.6.1 WaveWatch III

This third-generation wind wave model is developed at Marine Modeling and Analysis Branch (MMAB) of the Environment Modeling Center (EMC) of the NCEP and based on previous WaveWatch I and WaveWatch II models.

2.6.1.1 Governing equations of WW3

Waves or spectral wave components in water are generally described by several phase and amplitude parameters such as the wave number, k, the wave number vector, $\mathbf{k}$, the direction, θ, and the relative ($\sigma = 2\pi f_r$) and absolute ($\omega = 2\pi f_a$) frequencies. Here the linear wave theory can be applied locally giving a relationship so-called dispersion relation and Doppler type equation to interrelate the phase parameters as:

$$\sigma^2 = gk \tanh kd \tag{2.67}$$
$$\omega = \sigma + \mathbf{k} \cdot \mathbf{v} \tag{2.68}$$

where d is mean water depth and $\mathbf{v} = (u,v)$ is the depth- and time-averaged current velocity. For the irregular wind waves, the variance of the sea surface is described using density spectra, E (also called energy spectra or energy density spectra), and the density spectra depends on all independent parameters, i.e., wave number, frequency, space and time.

In WW3, the basic spectrum is the wave number-direction spectrum $E(k,\theta)$, which has been selected because of its invariance characteristics with respect to physics of wave growth and decay for variable water depth and winds. However, the output of WW3 is more traditional frequency-direction spectrum $E(f_r,\theta)$ which can be calculated from the $E(k,\theta)$ using straightforward Jacobian transformations:

$$E\left(f_r,\theta\right) = \frac{\partial k}{\partial f_r} E\left(k,\theta\right) = \frac{2\pi}{c_g} E\left(k,\theta\right) \tag{2.69}$$

$$E\left(f_a,\theta\right) = \frac{\partial k}{\partial f_a} E\left(k,\theta\right) = \frac{2\pi}{c_g}\left(1 + \frac{\mathbf{k} \cdot \mathbf{v}}{kc_g}\right)^{-1} E\left(k,\theta\right) \tag{2.70}$$

$$c_g = \frac{\partial \sigma}{\partial k} = n\frac{\sigma}{k}, \quad n = \frac{1}{2} + \frac{kd}{\sinh 2kd} \tag{2.71}$$

where c_g is the group velocity.

In the presence of currents in wave fields, the energy density spectra $E(k,\theta)$ is not conserved while the action density spectra, defined as $N(k,\theta) \equiv E(k,\theta)/\sigma$, is conserved, thus the action density spectra appears in the balance equation.

The balance equation in Cartesian coordinate which describes the wave propagation is given by:

$$\frac{\partial N}{\partial t} + \frac{\partial}{\partial x}\left(c_g \cos\theta + u\right)N + \frac{\partial}{\partial y}\left(c_g \sin\theta + v\right)N + \frac{\partial}{\partial k}\dot{k}N + \frac{\partial}{\partial \theta}\dot{\theta}N = \frac{S}{\sigma} \tag{2.72}$$

$$\dot{k} = -\frac{\partial\sigma}{\partial d}\frac{\partial d}{\partial s} - \mathbf{k}\cdot\frac{\partial \mathbf{v}}{\partial s}, \qquad \dot{\theta} = -\frac{1}{k}\left(\frac{\partial\sigma}{\partial d}\frac{\partial d}{\partial m} - \mathbf{k}\cdot\frac{\partial \mathbf{v}}{\partial m}\right) \tag{2.73}$$

where s is a coordinate in the direction θ and m is a coordinate perpendicular to s. The balance equation in spherical coordinate for the application in large-scale is given by:

$$\frac{\partial N}{\partial t} + \frac{1}{\cos\phi}\frac{\partial}{\partial \phi}\dot{\phi}N\cos\theta + \frac{\partial}{\partial \lambda}\dot{\lambda}N + \frac{\partial}{\partial k}\dot{k}N + \frac{\partial}{\partial \theta}\dot{\theta}_g N = \frac{S}{\sigma} \tag{2.74}$$

$$\dot{\phi} = \frac{c_g \cos\theta + \mathbf{v}_\phi}{R}, \qquad \dot{\lambda} = \frac{c_g \sin\theta + \mathbf{v}_\lambda}{R\cos\phi}, \qquad \dot{\theta}_g = \dot{\theta} - \frac{c_g \tan\phi\cos\theta}{R} \tag{2.75}$$

where R is the radius of the earth and $\mathbf{v}_\phi$ and $\mathbf{v}_\lambda$ are current components.

2.6.1.2 Source terms

In the balance equation above, the S $(= S(k,\theta))$ in the right hand side is the source term that describes the wave generation by surface wind (S_{in}), nonlinear interaction between waves (S_{nl}), dissipation by whitecapping (S_{ds}) and dissipation by bottom friction (S_{bot}) in shallow water.

$$S = S_{in} + S_{nl} + S_{ds} + S_{bot} \tag{2.76}$$

Input source term by wind

In WW3, there are two wind source terms incorporated; 1) the wind input source term by Snyder et al. (1981) and Komen et al. (1984) that is input term in WAve prediction Model (WAM) cycles 1 through 3 and SWAN and 2) the wind input source term by Tolman and Chalikov (1996). The former source term is described in (2.5.2.2) in SWAN model.

The latter wind source term in WW3 based on Chalikov and Belevich (1993) and Chalikov (1995) is given by

$$S_{in}(k,\theta) = \sigma \beta N(k,\theta) \qquad (2.77)$$

where β is a non-dimensional wind-wave interaction parameter, that depends on the wind velocity and drag coefficient (Tolman, 2002).

Dissipation term

The dissipation source term in the model consists of two constituents. The first low-frequency component is based on an analogy with energy dissipation due to turbulence,

$$S_{ds,l}(k,\theta) = -2u_* h k^2 \phi N(k,\theta) \qquad (2.78)$$

$$h = 4\left(\int_0^{2\pi} \int_{f_h}^{\infty} F(f,\theta) df d\theta\right)^{1/2} \qquad (2.79)$$

$$\phi = b_0 + b_1 \tilde{f}_{p,i} + b_2 \tilde{f}_{p,i}^{-b_3} \qquad (2.80)$$

where h is a mixing scale determined from the high-frequency energy content of the wave field and ϕ is an empirical function accounting for the development stage of the wave field and u_* is the friction velocity.

The second component of dissipation term is the empirical high-frequency dissipation defined as:

$$S_{ds,h}(k,\theta) = -a_0 \left(\frac{u_*}{g}\right)^2 f^3 \alpha_n^B N(k,\theta) \qquad (2.81)$$

$$B = a_1 \left(\frac{f u_*}{g}\right)^{-a_2}, \qquad \alpha_n = \frac{\sigma^6}{c_g g^2 \alpha_r} \int_0^{2\pi} N(k,\theta) d\theta \qquad (2.82)$$

where α_n is Phillips' non-dimensional high-frequency energy level normalized with α_r and α_0, α_1, α_2 and α_r are empirical constants. The two components of dissipation term are combined using a linear combination as follows:

$$S_{ds}\left(k,\theta\right) = AS_{ds,l}\left(k,\theta\right) + (1-A)S_{ds,h}\left(k,\theta\right) \tag{2.83}$$

$$A = \begin{cases} 1 & \text{for} \quad f < f_2 \\ \left(f - f_2\right)/\left(f_1 - f_2\right) & \text{for } f_1 \le f < f_2 \\ 0 & \text{for } f_2 \le f \end{cases} \tag{2.84}$$

Bottom Friction term

   The bottom friction term in WW3 is based on the simple empirical JONSWAP parameterization (Hasselmann et al., 1973) and can be given by:

$$S_{bot}\left(k,\theta\right) = 2\Gamma\frac{n-0.5}{gd}N\left(k,\theta\right), \qquad \begin{aligned} \Gamma = -0.038 \, {m^2}/{s^3} & \quad \text{for} \quad \text{Swell} \\ \Gamma = -0.067 \, {m^2}/{s^3} & \quad \text{for} \quad \text{Wind seas} \end{aligned} \tag{2.85}$$

where Γ is an empirical constant and n is the ratio of phase velocity to group celerity given by (2.71).

Nonlinear interaction term

   The nonlinear interaction term in WW3 can be calculated in two methods; 1) Discrete Interaction Approximation (DIA) method by Hasselmann et al. (1985) and 2) Webb-Resio -Tracy (WRT) method.

   In *DIA* method, the resonant nonlinear interactions occur between four wave components (quadruplets) with wave number vector $\mathbf{k}_1$, $\mathbf{k}_2$, $\mathbf{k}_3$ and $\mathbf{k}_4$ assuming that $\mathbf{k}_1 = \mathbf{k}_2$. The following conditions must be satisfied in DIA method:

$$\begin{cases} \mathbf{k}_1 + \mathbf{k}_2 = \mathbf{k}_3 + \mathbf{k}_4 \\ \quad\sigma_2 = \sigma_1 \\ \sigma_3 = \left(1 + \lambda_{nl}\right)\sigma_1 \\ \sigma_4 = \left(1 - \lambda_{nl}\right)\sigma_1 \end{cases} \tag{2.86}$$

where λ_{nl} is a constant (=0.25 in SWAN). For these quadruplets, the contribution δS_{nl} to the interaction for each discrete (fr, θ) combination of the spectrum corresponding to $\mathbf{k}_1$ is calculated as

$$
\begin{pmatrix} \delta S_{nl,1} \\ \delta S_{nl,2} \\ \delta S_{nl,3} \end{pmatrix} = D \begin{pmatrix} -2 \\ 1 \\ 1 \end{pmatrix} g^{-4} f_{r,1}^{11} C \times \left[F_1^2 \left(\frac{F_3}{\left(1+\lambda_{nl}\right)^4} + \frac{F_4}{\left(1-\lambda_{nl}\right)^4} \right) - \left(\frac{2F_1 F_3 F_4}{\left(1-\lambda_{nl}^2\right)^4} \right) \right]
\tag{2.87}
$$

where $F_1 = F(f_{r,1}, \theta_1)$, $F_3 = F(f_{r,3}, \theta_3)$ and $F_4 = F(f_{r,4}, \theta_4)$ and $\delta S_{nl,1} = \delta S_{nl}(f_{r,1}, \theta_1)$, $\delta S_{nl,3} = \delta S_{nl}(f_{r,3}, \theta_3)$ and $\delta S_{nl,4} = \delta S_{nl}(f_{r,4}, \theta_4)$ and C is a proportionality constant. The nonlinear interactions are calculated by considering a limited number of combinations (λ_{nl}, C).

In *WRT* method, which is based on the original six-dimensional Boltzmann integral formulation of Hasselmann (1962, 1963a, b) and additional considerations by Webb (1978), Tracy and Resio (1982), those wave numbers from $\mathbf{k}_1$ to $\mathbf{k}_4$ should satisfy the more general resonance conditions

$$
\begin{cases} \mathbf{k}_1 + \mathbf{k}_2 = \mathbf{k}_3 + \mathbf{k}_4 \\ \sigma_1 + \sigma_2 = \sigma_3 + \sigma_4 \end{cases}
\tag{2.88}
$$

and the Boltzmann integral in WRT describes the rate of change of action density of a particular wave number due to resonant interactions between pairs of four wave numbers. The rate of change of action density N_1 at wave number $\mathbf{k}_1$ due to all quadruplet interactions involving $\mathbf{k}_1$ is given by

$$
\frac{\partial N_1}{\partial t} = \iiint G\left(\mathbf{k}_1,\mathbf{k}_2,\mathbf{k}_3,\mathbf{k}_4\right) \delta\left(\mathbf{k}_1 + \mathbf{k}_2 - \mathbf{k}_3 - \mathbf{k}_4\right) \delta\left(\sigma_1 + \sigma_2 - \sigma_3 - \sigma_4\right) \times
$$
$$
\left[N_1 N_3 \left(N_4 - N_2\right) + N_2 N_4 \left(N_3 - N_1\right) \right] d\mathbf{k}_2 d\mathbf{k}_3 d\mathbf{k}_4
\tag{2.89}
$$

where the action density N is defined in terms of the wave number vector $\mathbf{k}$, $N = N(\mathbf{k})$. The term G is a complicated coupling coefficients and to remove the delta function above in the WRT method a number of transformations, which the main idea is to consider the integration space for each ($\mathbf{k}_1$, $\mathbf{k}_3$) combination are made. The main element of the transformations is written by

$$
\frac{\partial N_1}{\partial t} = 2 \int T\left(\mathbf{k}_1, \mathbf{k}_3\right) d\mathbf{k}_3
\tag{2.90}
$$

where the function T is given by

$$T\left(\mathbf{k}_1,\mathbf{k}_3\right) = \iint G\left(\mathbf{k}_1,\mathbf{k}_2,\mathbf{k}_3,\mathbf{k}_4\right)\delta\left(\mathbf{k}_1+\mathbf{k}_2-\mathbf{k}_3-\mathbf{k}_4\right)$$
$$\times\delta\left(\sigma_1+\sigma_2-\sigma_3-\sigma_4\right)\theta\left(\mathbf{k}_1,\mathbf{k}_3,\mathbf{k}_4\right) \qquad (2.91)$$
$$\times\left[N_1 N_3\left(N_4-N_2\right)+N_2 N_4\left(N_3-N_1\right)\right]d\mathbf{k}_2 d\mathbf{k}_4$$

where the function θ is given by

$$\theta\left(\mathbf{k}_1,\mathbf{k}_3,\mathbf{k}_4\right)=\begin{cases}1 & \text{when} \quad \left|\mathbf{k}_1-\mathbf{k}_3\right|\leq\left|\mathbf{k}_1-\mathbf{k}_4\right| \\ 0 & \text{when} \quad \left|\mathbf{k}_1-\mathbf{k}_3\right|>\left|\mathbf{k}_1-\mathbf{k}_4\right|\end{cases} \qquad (2.92)$$

2.6.2 SWAN

SWAN is the third-generation wind wave model and it uses the same formulation of source term with WAM model. However, SWAN incorporated some additional formulations for shallow water. Thus SWAN can be nested in WW3 for the shallow water region taking the boundary conditions from wide domain of WW3. The main differences of SWAN from WW3 are the source term formulations for the wind input and whitecapping dissipation terms.

2.6.2.1 Governing equations of SWAN

The spectrum that is considered in SWAN is the relative frequency-direction spectrum $E(\sigma,\theta)$ that is differ from the basic spectrum of WW3, which is the wave number-direction spectrum $E(k,\theta)$.

The action balance equation in Cartesian coordinate for the random wave generation and propagation in SWAN is given by:

$$\frac{\partial N}{\partial t}+\frac{\partial}{\partial x}c_x N+\frac{\partial}{\partial y}c_y N+\frac{\partial}{\partial \sigma}c_\sigma N+\frac{\partial}{\partial \theta}c_\theta N=\frac{S}{\sigma} \qquad (2.93)$$

where $N=N(\sigma,\theta)$ and c_x, c_y, c_σ and c_θ are the propagation velocities in x, y spaces and frequency, direction spaces. The physical meaning of the action balance equation is that the first term in left hand side is the local rate of change of action density in time, the second and third terms are the wave propagations in x and y spaces and the fourth and fifth terms represents the shifting of relative frequency due to variation of depth and current and depth- and current-induced refraction, the changes in direction, respectively.

The action balance equation can be written in spherical coordinate for the large scale applications as:

$$\frac{\partial N}{\partial t} + \frac{\partial}{\partial \lambda} c_\lambda N + \frac{1}{\cos\phi}\frac{\partial}{\partial \phi} c_\phi N \cos\phi + \frac{\partial}{\partial \sigma} c_\sigma N + \frac{\partial}{\partial \theta} c_\theta N = \frac{S}{\sigma}$$

(2.94)

where λ and ϕ are the longitude and latitude.

2.6.2.2 Source terms

In the balance equation above, the S (= $S(\sigma,\theta)$) in the right hand side is the source term that describes the wave generation by surface wind (S_{in}), nonlinear interaction between waves (S_{nl}), dissipation by whitecapping (S_{ds}), dissipation by bottom friction (S_{bot}) in shallow water and dissipation by depth-induced breaking waves (S_{br}).

$$S = S_{in} + S_{nl} + S_{ds} + S_{bot} + S_{br}$$

(2.95)

Input source term by wind

The wave generation and growth by wind is described by two methods in SWAN, which are the linear growth and the exponential growth by wind and can be given by

$$S_{in}(\sigma,\theta) = A + BE(\sigma,\theta)$$

(2.96)

where A represents the linear wind growth term and $BE(\sigma,\theta)$ describes the exponential wind growth.

The *linear wind growth* term is expressed by

$$A = \frac{1.5 \times 10^{-3}}{2\pi g^2}\left\{U_* \max\left[0, \cos(\theta - \theta_w)\right]\right\}^4 H$$

(2.97)

$$H = \exp\left(-\left(\sigma / \sigma_{PM}^*\right)^{-4}\right) \qquad \text{with} \qquad \sigma_{PM}^* = \frac{0.13g}{28U_*} 2\pi$$

(2.98)

where θ_w is the wind direction, H is the filter for eliminating the wave growth at frequencies lower than the σ_{PM}^* and σ_{PM}^* is the Pierson and Moskowitz frequency that is the peak frequency

of the fully developed sea state. Here the wind friction velocity, U_* has the relation to wind velocity 10m above the surface, U_{10} as

$$U_*^2 = C_D U_{10}^2 \tag{2.99}$$

where C_D is the drag coefficient

$$C_D(U_{10}) = \begin{cases} 1.2875 \times 10^{-3} & \text{for} \quad U_{10} < 7.5 \, m/s \\ \left(0.8 + U_{10} \cdot 0.0065 \, s/m\right) & \text{for} \quad U_{10} \geq 7.5 \, m/s \end{cases} \tag{2.100}$$

The second *exponential wind growth* terms are described in two manners in SWAN. The first description from Komen et al. (1984) is given by

$$B = \max\left[0, 0.25 \frac{\rho_a}{\rho_w}\left(28\frac{U_*}{c_{ph}}\cos(\theta - \theta_w) - 1\right)\right]\sigma \tag{2.101}$$

where c_{ph} is the phase velocity and ρ_a and ρ_w are the density of air and water. The second description of exponential wind growth is from Janssen (1989 and 1991) based on a quasi-linear wind-wave theory and is given by:

$$B = \beta \frac{\rho_a}{\rho_w}\left(\frac{U_*}{c_{ph}}\right)^2 \max\left[0, \cos(\theta - \theta_w)\right]^2 \sigma \tag{2.102}$$

where β is the Miles constant that is estimated from non-dimensional critical height λ

$$\begin{cases} \beta = \frac{1.2}{\kappa^2}\lambda \ln^4 \lambda, & \lambda \leq 1 \\ \beta = 0, & \lambda > 1 \end{cases} \tag{2.103}$$

$$\lambda = \frac{gz_e}{c_{ph}^2}e^r, r = \kappa c / |U \cos(\theta - \theta_w)| \tag{2.104}$$

where κ (=0.41) is Von Karman constant and z_e is the effective surface roughness. The both exponential wind growth terms are functions of so-called wave age, U_* / c_{ph}.

Dissipation term

The whitecapping dissipation in SWAN is described by

$$S_{ds}(\sigma,\theta) = -\gamma \tilde{\sigma} \frac{k}{\tilde{k}} E(\sigma,\theta) \tag{2.105}$$

where $\tilde{\sigma}$ and $\tilde{k}$ are the mean values of frequency and wave number and the wave steepness, γ is given as

$$\gamma = \gamma_{KJ} = C_{ds}\left((1-\delta)+\delta\frac{k}{\tilde{k}}\right)\left(\frac{\tilde{s}}{\tilde{s}_{PM}}\right)^P \tag{2.106}$$

in which C_{ds}, δ and m are tunable coefficients in the model and $\tilde{s}$ is the overall wave steepness and $\tilde{s}_{PM}$ $(=(3.02\times10^{-3})^{-1/2})$ is the $\tilde{s}$ value of Pierson-Moskowitz spectrum.

$$\tilde{s} = \tilde{k}\sqrt{E_{tot}} \tag{2.107}$$

The mean frequency, wave number and total wave energy are defined as

$$\tilde{\sigma} = \left(\frac{\int_0^{2\pi}\int_0^\infty \frac{1}{\sigma} E(\sigma,\theta)d\sigma d\theta}{E_{tot}}\right)^{-1} \tag{2.108}$$

$$\tilde{k} = \left(\frac{\int_0^{2\pi}\int_0^\infty \frac{1}{\sqrt{k}} E(\sigma,\theta)d\sigma d\theta}{E_{tot}}\right)^{-2} \tag{2.109}$$

$$E_{tot} = \int_0^{2\pi}\int_0^\infty E(\sigma,\theta)d\sigma d\theta \tag{2.110}$$

and those tunable coefficients are obtained in the model by closing the energy balance of the waves in idealized wave growth condition of deep water.

Bottom friction term

The dissipation by bottom friction in SWAN model is identical to that of WW3 which is based on the empirical JONSWAP parameterization.

Depth-induced wave breaking

The dissipation by depth-induced breaking waves in shallow water in SWAN which is not considered explicitly in WW3 is described by the bore-based model from Battjes and Janssen (1978). The mean rate of energy dissipation per unit area due to wave breaking, D_{tot} is given as:

$$D_{tot} = -\frac{1}{4}\alpha_{BJ} Q_B \left(\frac{\bar{\sigma}}{2\pi}\right) H_m^2 \quad \text{where} \quad \alpha_{BJ} = 1 \tag{2.111}$$

here H_m is the maximum wave height at given depth and Q_B is the fraction of breaking waves calculated by

$$\frac{1 - Q_b}{\ln Q_b} = -8 \frac{E_{tot}}{H_m^2} \tag{2.112}$$

and the mean frequency, $\bar{\sigma}$ is defined as

$$\bar{\sigma} = \frac{\int_0^{2\pi} \int_0^{\infty} \sigma E(\sigma, \theta) d\sigma d\theta}{E_{tot}} \tag{2.113}$$

the dissipation for a spectral component per unit time is calculated in SWAN model by:

$$S_{br}(\sigma, \theta) = D_{tot} \frac{E(\sigma, \theta)}{E_{tot}} \tag{2.114}$$

Nonlinear interaction term

The SWAN model includes two method to estimate the source term by nonlinear wave-wave interaction; the first is the Discrete Interaction Appproximation (DIA) method and

the second is the Lumped Triad Approximation (LTA) method. The *DIA* in SWAN is identical to that of WW3 which is proposed by Hasselmann et al. (1985).

The *LTA* is a slightly adopted method of DIA and can be expressed in each spectral direction

$$S_{nl,3}(\sigma,\theta) = S_{nl,3}^{-}(\sigma,\theta) + S_{nl,3}^{+}(\sigma,\theta) \tag{2.115}$$

in which

$$S_{nl,3}^{+}(\sigma,\theta) = \max\left[0, \alpha_{EB} 2\pi cc_g J^2 |\sin\beta| \left\{ E^2\left(\frac{\sigma}{2},\theta\right) - 2E\left(\frac{\sigma}{2},\theta\right)E(\sigma,\theta) \right\} \right] \tag{2.116}$$

$$S_{nl,3}^{-}(\sigma,\theta) = -2S_{nl,3}^{+}(2\sigma,\theta) \tag{2.117}$$

where α_{EB} is a tunable proportionality coefficient and the biphase, β is given by

$$\beta = -\frac{\pi}{2} + \frac{\pi}{2}\tanh\left(\frac{0.2}{Ur}\right) \tag{2.118}$$

$$Ur = \frac{g}{8\sqrt{2}\pi^2} \frac{H_s \bar{T}^2}{d^2} \tag{2.119}$$

here Ur is Ursell number and $\bar{T} = 2\pi/\bar{\sigma}$ is the interaction coefficient, J is given by Madson and Sørensen (1993):

$$J = \frac{k_{\sigma/2}^2\left(gd + 2c_{\sigma/2}^2\right)}{k_\sigma d\left(gd + \frac{2}{15}gd^3 k_\sigma^2 - \frac{2}{5}\sigma^2 d^2\right)} \tag{2.120}$$

2.7 Coastal models

The coastal models in REDES consist of two parts such that the overtopping and wave run-up height is calculated by CADMAS-SURF and the estuarine and coastal circulation is simulated by ECOMSED. This thesis shows only the application of CADMAS-SURF.

2.7.1 CADMAS-SURF

CADMAS-SURF is a 2D numerical model designed for the numerical experiments on the wave flume with free water level variation boundary condition developed at Coastal Development Institute of Technology in Japan. The unique features of CADMAS-SURF are

1) This model is governed by the 2D incompressible NS equations and continuity equation,

2) The free surface boundary is described by the Volume-of-Fluid method,

3) The porous medium for bottom and structure boundary is considered,

4) Boundary conditions and obstacles/structures can be specified in any computational cells,

5) The irregular random waves and monochromatic waves can be given for the incident wave boundary condition,

6) The monochromatic waves are generated by six wave generation functions,

7) Sommerfield radiation boundary and the sponge layer effect are adopted for the open boundary conditions.

The governing equations of CADMAS-SURF based on the 2D (x,z) incompressible NS equations (Minami and Notoya, 2003) with consideration of porous medium are given by;

$$\frac{\partial \gamma_x u}{\partial x} + \frac{\partial \gamma_z w}{\partial z} = S_p \tag{2.121}$$

$$\frac{\partial \lambda_v u}{\partial t} + \frac{\partial \lambda_x uu}{\partial x} + \frac{\partial \lambda_z uw}{\partial z} =$$
$$-\frac{\gamma_v}{\rho}\frac{\partial p}{\partial x} + \frac{\partial}{\partial x}\left\{\gamma_x v_e\left(2\frac{\partial u}{\partial x}\right)\right\} + \frac{\partial}{\partial z}\left\{\gamma_z v_e\left(\frac{\partial u}{\partial x}+\frac{\partial w}{\partial z}\right)\right\} - D_x u + S_u - R_x \tag{2.122}$$

$$\frac{\partial \lambda_v w}{\partial t} + \frac{\partial \lambda_x wu}{\partial x} + \frac{\partial \lambda_z ww}{\partial z} =$$
$$-\frac{\gamma_v}{\rho}\frac{\partial p}{\partial z} + \frac{\partial}{\partial x}\left\{\gamma_x v_e\left(\frac{\partial u}{\partial x}+\frac{\partial w}{\partial z}\right)\right\} + \frac{\partial}{\partial z}\left\{\gamma_z v_e\left(2\frac{\partial w}{\partial z}\right)\right\} - D_z w + S_w - R_z - \gamma_v g \tag{2.123}$$

where γ_x, γ_z are the permeability coefficients in horizontal and vertical directions and S_p is the source term by wave generations and t, p, g and ρ are the time, pressure, acceleration due to gravity and density of water, respectively. Here the v_e is the summation of molecular viscosity and eddy viscosity and γ_v is the void ratio and D_x, D_z are the coefficients for wave absorbers. The S_u are S_w are the source terms by wave generations in momentum equations.

$$\begin{cases} \lambda_v = \gamma_v + \left(1 - \gamma_v\right) C_M \\ \lambda_x = \gamma_x + \left(1 - \gamma_x\right) C_M \\ \lambda_z = \gamma_z + \left(1 - \gamma_z\right) C_M \end{cases} \tag{2.124}$$

where C_M is the coefficient of inertial force, thus the λ represents the permeability with consideration of the effects of inertial force by structures and obstacles. The resistance force, R is defined as

$$\begin{cases} R_x = \dfrac{1}{2} \dfrac{C_D}{\Delta x} \left(1 - \gamma_x\right) u \sqrt{u^2 + w^2} \\ R_z = \dfrac{1}{2} \dfrac{C_D}{\Delta z} \left(1 - \gamma_z\right) w \sqrt{u^2 + w^2} \end{cases} \tag{2.125}$$

where C_D is the drag coefficient and Δx and Δz are the grid interval in horizontal and vertical directions.

Volume of Fluid (VOF)

The volume of fluid (VOF) method adopted in CADMAS-SURF is a numerical technique to track the developing free surfaces of liquids in motion. This method can, for example, be applied to compute the liquid flow patterns. The free surface of flow is captured via the volume fraction, F which is convected with the fluid and given;

$$\frac{\partial F}{\partial t} + \mathbf{v} \cdot \nabla F = 0 \tag{2.126}$$

2.7.2 ECOMSED

The ECOMSED is a state-of-the-art hydrodynamic and sediment transport model, which realistically computes water circulation, temperature, salinity, mixing and transport, deposition and resuspension of cohesive and non-cohesive sediments. The complete ECOMSED model consists of several modules, these are hydrodynamic module, wind induced wave module, heat flux module and particle tracking module. The ECOMSED has its origin back to 1980's from POM, thus the hydrodynamic module of ECOMSED is pretty much identical to POM. Since then, the earlier version of POM for shallow water environments such as rivers, bays, estuaries and the coastal region, reservoirs and lakes is called ECOM. The concepts for cohesive

sediment resuspension, settling and consolidation were incorporated within the ECOM modeling framework.
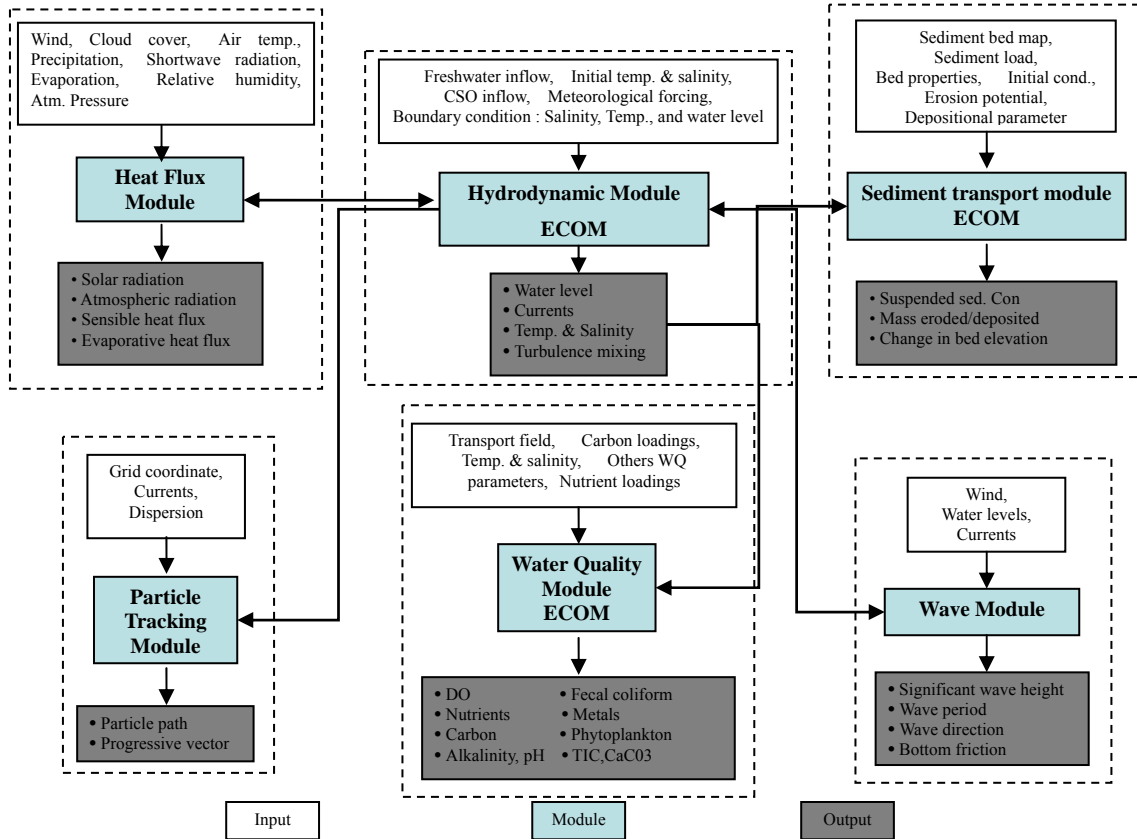
Fig. 2.7 Modeling framework of ECOMSED (Fitri, 2007)

2.8 Design concept of REDES

The REDES system consists of several numerical models as described in the previous sections. The important and difficult task in designing of the coupling framework of REDES is the exchanging information repeatedly between different scale components which simulate various scales of different phenomena simultaneously. The synoptic design concept of coupling the models is given in two steps.

First, the components models, MM5, MITgcm, POM, SWAN, and WW3 are all parallelized through the Massage Passing Interface (MPI) by themselves in Single Process/Program Multiple Data method that is all processors run the same program with their own data. Here the information transfer, regridding to different target domains and computing a diagnostic variable are all conducted by a specially designed program called *coupler*. The

component models including coupler are parallelized as well through the MPI in Multiple Process/Program Multiple Data method exchanging data at every least multiple time-step.

Second, the interactions between the models are very significant and achieved by the data transferred through the coupler. In the case of storm surge simulation with the wind-wave-ocean (MM5-WW3-POM) coupled model, the wind and atmospheric pressure are calculated by MM5 and transferred to the coupler. The information from MM5 is transferred to WW3 and POM by the coupler. The WW3 and POM receive the data from the coupler while provide the water elevation, currents from POM to WW3 and the stress by whitecapping from WW3 to POM through the coupler. Fig. 2.8 shows a synoptic diagram of REDES in which it is used for the simulation of coastal disaster caused by storm surge.

In REDES, there is a wind-wave-current coupled system (Fig. 2.9) established by coupling MM5-WW3-POM (Kim, 2005). This wind-wave-ocean coupled model has been extensively utilized mainly in storm surge and high wave climate simulations. In most of simulations by wind-wave-ocean coupled model, the barotropic ocean states are considered such that the influences of temperature and salinity profiles in the ocean are remained uniform.

Fig 2.10 shows the other atmosphere-ocean coupled model which is developed by the author and comprised of MM5-MITgcm. This coupled model deals with the ocean in accurate baroclinic manner and the element models can be used standalone. The interactions between the systems are achieved through the coupler based on the coupling library, OASIS3 (Valcke, 2006), transferring and regridding the water level, current, surface roughness and surface fluxes such as momentum, heat, and fresh water flux. The preliminary results from an application of atmosphere-ocean (MM5-MITgcm) coupled model are presented in Chapter 4 in the study of real typhoon-ocean interaction.
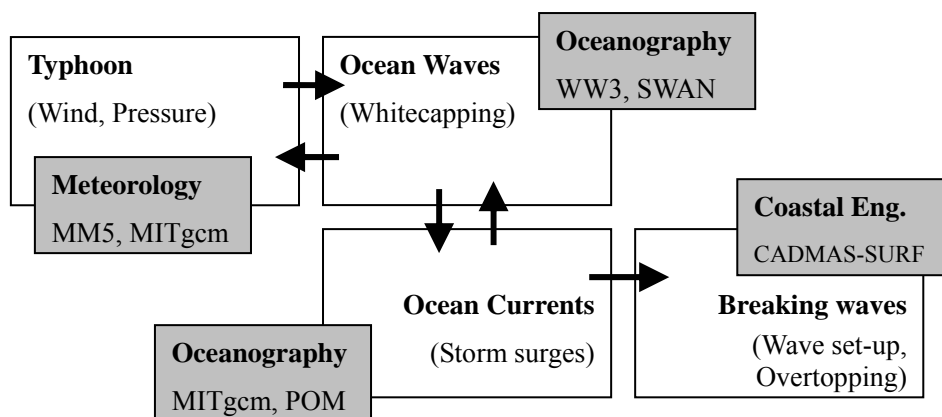
Fig. 2.8 Synoptic diagram of REDES in the case of simulation of coastal disaster caused by storm surge
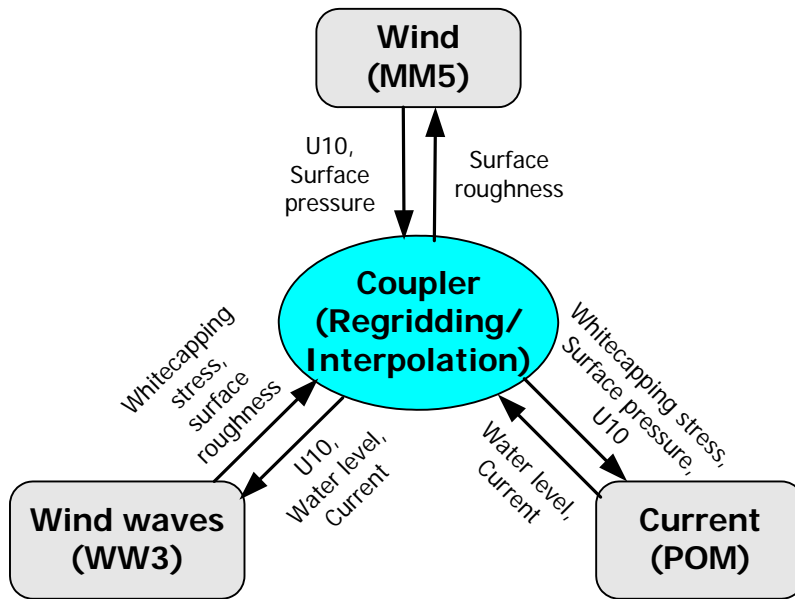
Fig. 2.9 The structure of wind-wave-current model
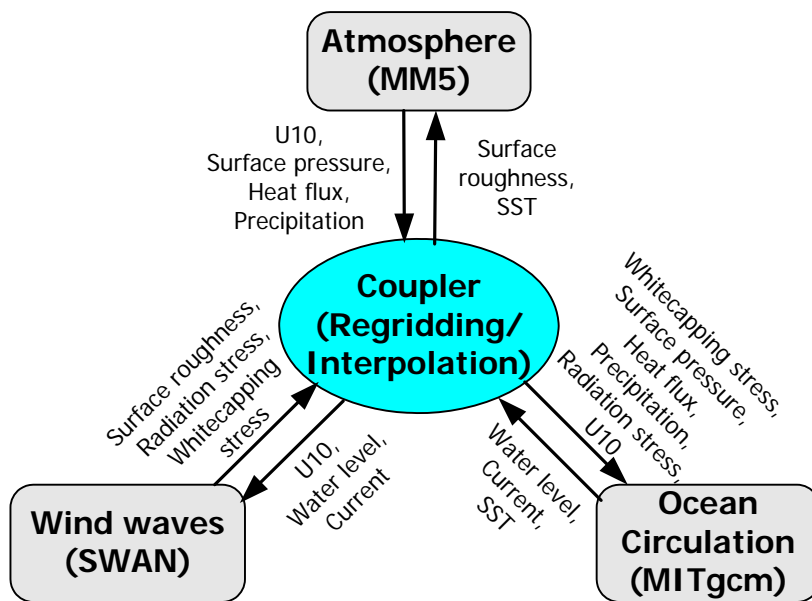
Fig. 2.10 The structure of atmosphere-wave-ocean model

These coupled models are established and used for many studies on a low-cost High Performance Computing (HPC) platform which is a clustered machine of specialized PC with open source Operating System (OS; Linux) (Fig 2.11).

The *objectives* of REDES development are to improve the numerical assessment method to disaster events and environment problems by introducing the coupling effects between different systems through the existing interactions and to enhance our understanding of the physical processes of natural disasters and environmental issues.
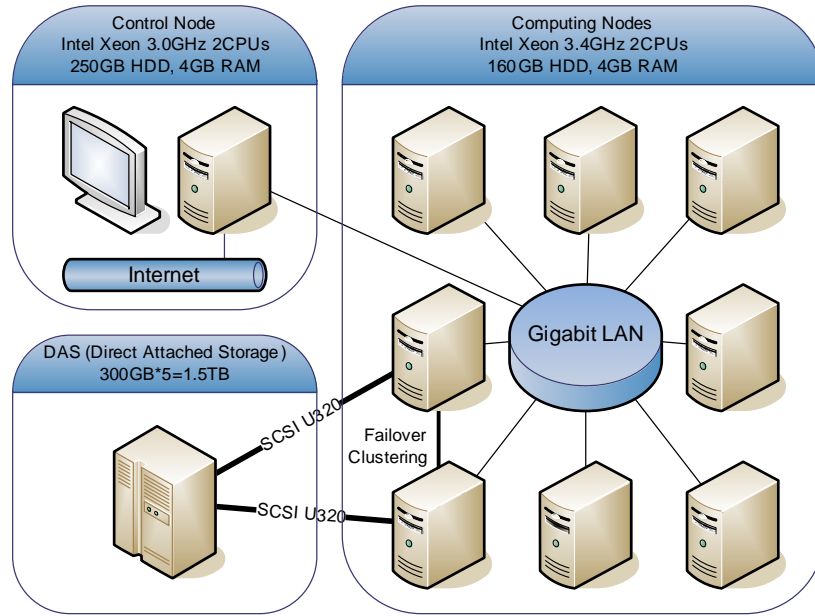
Fig. 2.11 The system structure of low-cost high performance computing Linux cluster platform

2.9 Summary

The Regional Environment and Disaster Prevention Simulator (REDES) and its components that represent meteorological condition, oceanic condition, sea surface condition and coastal and estuarine conditions are described focusing on both governing equations and model concepts.

1) Meteorological part is being modeled by MM5 with appropriate physics and FDDA applied and MITgcm can be also used for the atmospheric circulation,

2) Ocean currents and circulations are described by MITgcm and POM in both barotropic and baroclinic modes,

3) Sea surface waves are modeled by the third-generation wind wave models, SWAN and WW3 doing its role between atmosphere and ocean,

4) Coastal and estuarine conditions such as overtopping, wave set-up and sediment transport can be accounted by CADMAS-SURF and ECOMSED.

The design concept and objectives of REDES are described.

1) Wind(MM5)-wave(WW3)-current(POM) coupled model uses the specially-designed coupler for exchanging data such as wind, pressure, current and water level. This wind-wave-current model has been extensively used for storm surge simulations.

2) The atmosphere (MM5) and ocean (MITgcm) coupled model was developed by using special coupler based on the state-of-the-art coupling library called OASIS3 (Valcke, 2006) for controlling the coupled model, transferring and regridding the data between the component models. The ocean state is simulated in baroclinic condition in this atmosphere and ocean coupled model, while the ocean is treated in barotropic condition in wind-wave-current coupled model.

3) REDES has been developed to improve the numerical assessment method to disaster events and environment problems by introducing the coupling effects between different systems through the existing interactions and to enhance our understanding of the physical processes of natural disasters and environmental issues.

References

Ballard, S. P., B. W. Golding, and R. N. B. Smith, (1991): Mesoscale model experimental forecasts of the Haar of northeast Scotland, *Mon. Wea. Rev.,* **119,** 2107–2123.

Battjes, J.A., and J.P.F.M., Janssen, (1978): Energy loss and set-up due to breaking of random waves, *Proc. 16th int. Conf. Coastal Engineering*, ASCE, 569-587.

Betts, A. K., and M. J. Miller, (1986): A new convective adjustment scheme. Part II: Single column tests using GATE wave, BOMEX, ATEX and Arctic air-mass data sets, *Quart. J. Roy. Meteor. Soc.*, **112**, 693-709.

Betts, A. K., and M. J. Miller, (1993): The Betts-Miller scheme. The representation of cumulus convection in numerical models, K. A. Emanuel and D. J. Raymond, Eds., Amer. Meteor. Soc., 246 pp.

Burke, S.D. and W.T. Thompson, (1989): A vertically nested regional numerical weather predictions model with a second order closure physics, *Mon. Wea. Rev.*, **117**, 2305–2324.

Chalikov, D. V. and M. Y. Belevich, (1993): One-dimensional theory of the wave boundary layer, *Bound. Layer Meteor.*, **63**, 65-96.

Chalikov, D. V., (1995): The parameterization of the wave boundary layer, *J. Phys. Oceanogr.*, **25**, 1333-1349.

Chen, F., and J. Dudhia, (2001): Coupling an advanced land-surface/hydrology model with the Penn State/NCAR MM5 modeling system. Part I: Model implementation and sensitivity, *Mon. Wea. Rev.*, **129**, 569-585.

Chen, F., and J. Dudhia, (2001): Coupling an advanced land-surface/hydrology model with the Penn State/NCAR MM5 modeling system. Part II: Preliminary Model validation, *Mon. Wea. Rev.*, **129**, 587-604.

Cramer. M. S., (2002): Navier-Stokes equations, http://navier-stokes.net

Dudhia, J., (1996): A multi-layer soil temperature model for MM5, *The 6th PSU/NCAR*

Mesoscale Model Users Workshop.

Dudhia, J., D. Grill, K. Manning, W. Wang, C. Bruyere, S. Kelly, K. Lackey, (2005): PSU/NCAR mesoscale modeling system tutorial class notes and user's guide: MM5 modeling system version 3, Mesoscale and microscale meteorology division, National Center for Atmospheric Research.

Fitri, R. (2006): Simulation model for cohesive sediment transport and bottom topography changes in estuary, Ph.D dissertation, Kyoto University, Japan.

Fritsch, J. M., and C. F. Chappell, (1980): Numerical prediction of convectively driven mesoscale pressure systems. Part I: Convective parameterization, *J. Atmos., Sci.*, **37**, 1722-1733.

Grell, G. A., J. Dudhia and D. R. Stauffer, (1995): A description of the fifth-generation Penn State/NCAR mesoscale model (MM5), NCAR Technical Note, NCAR/TN-398+STR, 117 pp.

Hack, J. J., (1993): Parameterization of moist convection in the National Center for Atmospheric Research Community Climate Model (CCM2), *J. Geophys. Res.,* **99,** 20785–20813.

Hasselmann, K., (1962). On the non-linear transfer in a gravity wave spectrum, part 1. General theory, *J. Fluid Mech.*, **12**, 481-500.

Hasselmann, K., (1963a): On the non-linear transfer in a gravity wave spectrum, part 2. Conservation theory, wave-particle correspondence, irreversibility, *J. Fluid Mech.*, **15**, 273-281.

Hasselmann, K., (1963b): On the non-linear transfer in a gravity wave spectrum, part 3. Evaluation of energy flux and sea-swell interactions for a Neumann spectrum, *J. Fluid Mech.*, **15**, 385-398.

Hasselmann, K. et al., (1973): Measurements of wind-wave growth and swell decay during the Joint North Sea Wave Project (JONSWAP), *Dtsch. Hydrogr. Z.A(8)*, 1-94.

Hasselmann, S. and K. Hasselmann, (1985): Computations and parameterizations of the nonlinear energy transfer in a gravity-wave spectrum. Part I: A new method for efficient computations of the exact nonlinear transfer integral, *J. Phys. Oceanogr.*, **15**, 1367-1377.

Hasselmann, S., K. Hasselmann, J. H. Allender and T. P. Barnett, (1985): Computations and parameterizations of the nonlinear energy transfer in a gravity-wave spectrum. Part II: Parameterizations of the nonlinear energy transfer for application in wave models, *J. Phys. Oceanogr.*, **15**, 1378-1391.

Hong, S-Y. and H.-L. Pan, (1996): Nonlocal boundary layer vertical diffusion in a medium-range forecast model, *Mon. Wea. Rev.*, **124**, 2322-2339.

Janjic, Z. I., (1990): The step-mountain coordinate: physical package, *Mon. Wea. Rev.*, **118**, 1429-1443.

Janjic, Z. I., (1994): The step-mountain eta coordinate model: further developments of the convection, viscous sublayer and turbulence closure schemes, *Mon. Wea. Rev.*, **122**, 927-945.

Janssen, P.A.E.M, (1989). Wave induced stress and the drag of air flow over sea waves, *J. Phys. Oceanogr.*, **19**, 745-754.

Janssen, P.A.E.M, (1991): Quasi-linear theory of wind-wave generation applied to wave forecasting, *J. Phys. Oceanogr.*, **21**, 1631-1642.

Kain, J. S., and J. M. Fritsch, (1993): Convective parameterization for mesoscale models: The Kain-Fritsch scheme. The representation of cumulus convection in numerical models, K. A. Emanuel and D. J. Raymond, Eds., Amer. Meteor. Soc., 246 pp.

Kim, K. (2005): Coastal ocean model with consideration of meteorological-oceanographic mesoscale interaction, Ph.D dissertation, Kyoto University, Japan.

Komen, G. J., S. Hasselmann and K. Hasselmann, (1984): On the existence of a fully developed wind-sea spectrum, *J. Phys. Oceanogr.*, **14**, 1271-1285.

Lin, Y. L., R. D. Farley, and H. D. Orville, (1983): Bulk parameterization of the snow field of

the cloud model, *J. Climate Appl. Meteor.*, **22**, 1065-1092.

Madsen, P. A. and O. R. Sørenson, (1993). Bound waves and triad interactions in shallow water, *Ocean Engineering*, **20(4)**, 359-388.

Marshall, J., A. Adcroft, C. Hill, L. Perelman, and C. Heisey, (1997a): A finite-volume, incompressible navier-stokes model for studies of the ocean on parallel computers, *J. Geophys. Res.*, **102(C3)**, 5753-5766.

Marshall, J., C. Hill, L. Perelman, and A. Adcroft, (1997b): Hydrostatic, quasi-hydrostatic, and non-hydrostatic ocean modeling, *J. Geophys. Res.*, **102(C3)**, 5733-5752.

Mellor, G.L., and T. Yamada, (1982): Development of a turbulence closure model for geophysical fluid problems, *Rev. Geophys. Space Phys.*, **20**, 851-875.

Mellor, G.L., (2004): Uses guide for a three-dimensional, primitive equation, numerical ocean model, 56pp.

Minami, M. and N. Notoya, (2003): Numerical simulation of run-up height using the CADMAS-SURF method on the gentle slope-type seawall, *J. Hachinohe National College of Technology*, **38**, 149-155.

Mlawer, E. J., S. J. Taubman, P. D. Brown, M. J. Iacono, and S. A. Clough, (1997): Radiative transfer for inhomogeneous atmospheres: RRTM, a validated correlated-k model for the longwave, *J. Geophys. Res.*, **102**, 16663-16682.

Pleim, J. E., J. S. Chang, (1992): A non-local closure model for vertical mixing in the convective boundary layer, *Atm. Env.*, **26A**, 965-981.

Reisner, J., R. M. Rasmussen, and R. T. Bruintjes, (1998): Explicit forecasting of supercooled liquid water in winter storms using the MM5 mesoscale model, *Quart. J. Roy. Metero. Soc.*, **124 B**, 1071-1107.

Schultz, P. (1995): An Explicit Cloud Physics Parameterization for Operational Numerical Weather Prediction, *Mon. Wea. Rev.*, **123(1)**, 3331–3343.

Shafran, P. C., Seaman, N. L. and Gayno, G. A. (March 2000): Evaluation of Numerical Predictions of Boundary Layer Structure during the Lake Michigan Ozone Study, *J. Applied Meteor.*, **39(3)**, 412–426.

Snyder, R. L., F. W. Dobson, J. A. Elliott and R. B. Long, (1981): Array measurements of atmospheric pressure fluctuations above surface gravity waves, *J. Fluid Mech.*, **102**, 1-59.

Tao, W.-K., J. Simpson, and M. McCumber, (1989): An ice-water saturation adjustment, *Mon. Wea. Rev.*, **117**, 231-235.

Tao, W.-K., and J. Simpson, (1993): The Goddard Cumulus Ensemble Model. Part I: Model Description, *Terrestrial, Atmospheric and Oceanic Sciences,* **4**, 19-54.

Tolman, H. L. and D. V. Chalikov, (1996): Source terms in a third-generation wind-wave model, *J. Phys. Oceanogr.*, **26**, 2497-2518.

Tolman, H. L., (2002): User manual and system documentation of WaveWatch-III version 2.22, TN-No 222, NCEP MMAB, 133pp.

Tracy, B. and D. T. Resio, (1982): Theory and calculation of the nonlinear energy transfer between sea waves in deep water, WES report 11, US Army Corps of Engineers.

Valcke, S. (2006): OASIS3 User Guide (prism_2-5). PRISM Support Initiative Report No 3, 64 pp.

Webb, D. J., (1978): Non-linear transfers between sea waves, *Deep Sea Res.*, **25**, 279-298.

Xiu, A., and J.E. Pleim, (2000): Development of a land surface model. Part I: Application in a mesoscale meteorology model, *Journal of Applied Meteorology*, **40**, 192-209.

Zangl, G., (2002): An improved method for computing horizontal diffusion in a sigma-coordinate model and its application to simulations over mountainous topography, *Mon. Wea. Rev.*, **130**, 1423-1432.

Chapter 3

Applications to Storm Surge and

Extreme High Wave Simulation

REDES has been applied to many related problems from the small scale water circulation in reservoir, overtopping by high waves, extreme wave climate by strong winds, and storm surge by typhoons and hurricane. In this section, the first application of REDES to Hurricane Katrina will be presented mainly concerning the storm surge in the Gulf of Mexico which caused the unprecedented damage in United States. The hurricane generated wind field was also investigated with other wind models for bogussing as well as the mesoscale model-embedded Rankine vortex. The other application of REDES is the simulation of extreme high wave fields induced by Typhoon 7920, TIP, to make clear the generation mechanism of the high waves both in the Pacific Ocean and coastal sea (Suruga Bay).

3.1 Storm surge caused by Hurricane Katrina in the Gulf of Mexico

3.1.1 Introduction

Hurricane Katrina caused one of the most destructive natural disasters ever occurred in the United States that was the one of the most expensive catastrophe losses that the United Sataes has ever experienced. Some of the loss could possibly be evitable if proper actions were taken for the upcoming natural hazards. In this study, only the natural external forces such as wind, wave and storm surge fields caused by Katrina were investigated by numerical simulations.

The bogussing scheme (C.A. Davis and S. Low-Nam, 2001) for tropical storms had been proven to be effective to simulate the storm surge at the coast in barotropic condition of ocean under typhoon (Kim and Yamashita, 2005) and be shown that it can be applied to reproduce even the subtropical meteorological depression in Japan/East Sea in wintertime to

simulate the abnormal high waves along the Japan's coast (Kim et al., 2005). However, the bogussing scheme used for simulations of many typhoons and subtropical depressions is based on several assumptions which are mainly due to a lack of observation data and coarse resolution. In this study, the bogussing scheme in mesoscale model MM5 was discussed and modified with Rankine vortex and other models of the modified Rankine vortex, Sea Lake and Overland Surge from Hurricane (SLOSH) wind model and Holland wind model, which were used to simulate the wind field of Hurricane Katrina and the storm surge by a coupled numerical model.

3.1.2 Hurricane Katrina

Referred to detailed RMS report (2005), Hurricane Katrina was initially identified as a tropical storm in the Bahamas. Tracking across Florida on August 25, 2005 as a category 1 hurricane, it then entered the Gulf of Mexico and underwent a dramatic intensification to a central pressure of 902hPa (category 5) before making landfall on the Gulf Coast in the south of the United States. It continued on as a strong storm through the central United States. Katrina lasted nine days from its inception as a tropical depression on August 23 to its dissipation over Canada on August 31. Katrina was extremely powerful storm. At landfall in Louisiana its central pressure of 920hPa was the third lowest recorded at landfall of any U.S. hurricane, and its winds were the eighth strongest recorded at landfall. The U.S. National Hurricane Center (NHC) advised maximum sustained wind speeds of 140mph (62.6 m/s), although observed winds onland appeared somewhat lower than this. The storm accompanied by Hurricane Katrina drove forward an extreme storm surge reaching over 30 ft (9.144m) in some low-lying places and poured a wall of violent seawater into the vulnerable places.

At the time of first landfall of Hurricane Katrina, water levels were near predictions at stations along eastern Florida. Water levels elevated after Katrina had passed, on 26th August. At the time of the second landfall, Katrina's maximum sustained winds were between 135 ~ 145mph (60.35 ~ 64.82m/s) with higher gusts and the minimum barometric pressures were between 918 ~ 923mb on 29th August. The station at Ocean Spring, MS (Fig. 3.6) recorded the highest storm tide of 13.26ft (4.043m) above Mean Lower Low Water (MLLW). However, the sensor failed transmissions at this point and could not record a maximum elevation. At Pilots Station, SW Pass, LA (Fig. 3.6) had the next highest storm tide with successful sensor transmissions during the Hurricane. The observed water level was 1.880 m above the predicted astronomical tide (NOAA, 2005).

3.1.3 Wind field generation

The bogussing scheme employed in mesoscale model, MM5, is using Rankine vortex for generating the winds from coarse resolution background data. The Rankine vortex wind profile generates wind speed as

$$V = V_{\max} \left(\frac{r}{R_{MW}} \right)^{\alpha} \tag{3.1}$$

where R_{MW} is maximum wind radius and V_{max} is maximum tangential wind. $\alpha = 1$ if $r < R_{MW}$ and $\alpha = -0.7$ if $r \geq R_{MW}$.

There are three commonly used parametric and analytic wind models such as modified Rankine vortex model, SLOSH wind model (Jelesnianski, 1992) and Holland wind model (Holland, 1980). These wind models can be used to generate wind field of hurricanes, tropical cyclones and typhoons showing wind speed of zero at the centre of low pressure and drastic increase to its maximum at the maximum wind radius (R_{MW}) and then decreases generally outerwards.

The modified Rankine vortex wind is based on Rankine vortex with a shape parameter, X, for wind speed distribution in the direction of radius as

$$V = V_{\max} \left(\frac{r}{R_{MW}} \right)^{X} \quad \text{if } r < R_{MW}$$

$$V = V_{\max} \left(\frac{R_{MW}}{r} \right)^{X} \quad \text{if } r \geq R_{MW} \tag{3.2}$$

The shape parameter, X, was determined empirically ranging from 0.4 to 0.6 (Hughes, 1952) and average value of 0.5 (Phadke et al., 2003) can be used to predictive experiments. In this study this average value of X was used.

SLOSH is currently operating storm surge model at National Weather Service, NOAA and its reproduced wind field from parametric wind model proven to be realistic (Houston et at., 1999) is generated by the following equation;

$$V = V_{\max} \frac{2 R_{MW} r}{R_{MW}^{2} + r^{2}} \tag{3.3}$$

as described in the Eqs.(3.1)~(3.3), the maximum wind radius, R_{MW} and maximum wind speed, V_{max} are needed for parametric wind models. However R_{MW} and V_{max} are frequently found to be failed to observe or contain discrepancies between observed and estimated values.

The analytic Holland wind model is based on the exponential distribution of the atmospheric pressure that is the given by

$$\frac{p - p_c}{p_n - p_c} = \exp\left\{-\left(\frac{R_{MW}}{r}\right)^B\right\} \tag{3.4}$$

where p is the pressure at radius r, p_c is central pressure and p_n is the ambient pressure. Therefore the wind profile of gradient wind equation is described below,

$$V = \left[\frac{B(p_n - p_c)}{\rho}\left(\frac{R_{MW}}{r}\right)^B \exp\left\{-\left(\frac{R_{MW}}{r}\right)^B\right\} + \frac{r^2 f^2}{4}\right]^{1/2} - \frac{rf}{2} \tag{3.5}$$

where B is scaling parameter and f is Coriolis factor. The scaling parameter B determines the shape of wind profile in the radius direction and was recently suggested by an empirical relation (Harper and Holland, 1999) as

$$B = 2 - \frac{p_c - 900}{160} \quad \text{for } 1.0 < B < 2.5 \tag{3.6}$$

The maximum wind speed in Holland wind model is derived from Eq.(3.5) with relation to Eq.(3.4) at R_{MW} where Coriolis parameter is relatively small compared to the pressure gradient and centrifugal forces as

$$V_{\max} = C\left(p_n - p_c\right)^{1/2} \tag{3.7}$$

where $C = (B/\rho e)^{1/2}$. As the maximum wind speed is estimated by Eq.(3.7), the R_{MW} and p_c are necessary to produce the wind profile in Holland wind model. The maximum wind speed required for the parametric wind model can be obtained from empirical relations to the central pressure, p_c (Atkinson and Holiday, 1977; Takahashi, 1939; Kraft, 1961; Fujita, 1971)　in most cases when no observed and estimated data are available. However the maximum wind radius (R_{MW}) has large uncertainties and is continuously changing during the lifespan of the storms. It has large influences on the maximum wind speed causing large errors in V_{max} from small differences of R_{MW}. R_{MW} is normally observed directly by aircraft flying through the storms or by the observed pressure distribution on the surface and recently by a new technique using satellite data (Hsu et al., 2000; Hsu and Babin, 2005). The satellite method is using the measurement of the distance between the coldest temperature near the eye of the storms and the warmest temperature in the eye (Hsu and Babin, 2005).

In the bogussing scheme of mesoscale model (MM5), R_{MW} is somewhat pre-determined in a sense that R_{MW} is double or triple size of horizontal resolution. For example, it will be 90km if the horizontal resolution is 45km and 50~60km for 15km resolution. It is shown after calibration experiments that R_{MW} values are relatively large to reproduce the wind field compared to observation data. However in the near real-time simulation of the storms, R_{MW} should be determined for the bogussing scheme in MM5 with difficulties including large

uncertainty. The available information of BestTrack data which might result in overestimation in simulated R_{MW} and underestimation in simulated V_{max} was used for this study.

The reproduced wind fields using Rankine vortex, modified Rankine vortex and SLOSH wind model were compared with direct measurements of Hurricane Katrina by National Hurricane Center/Tropical Prediction Center and Us Air Force Reseves (AFRC) air reconnaissance (RECCO). The air RECCO data taken from flight level of 700hPa or 850hPa depending on the aviating condition should normally be adjusted to surface level data to make comparisons to wind models. Powell and Houston (1996) shows adjustment of flight level winds to the surface winds in two steps. First, flight level winds are changed to mean boundary layer (MBL) winds and then, MBL winds are converted to the surface winds which that result in 1-min averaged maximum wind at 10m above the surface. This conversion is valid only for marine exposure of tropical storms. More recently, Dunion et al. (2003) suggested new methodologies for the adjustment of flight level winds to the surface by analyzing GPS dropsondes data. However, this adjustment of data can be avoided since MM5 is a non-hydrostatic mesoscale atmospheric model adopting sigma coordinate which can be converted to P-coordinate in the post-processing. Therefore the flight level data of 700hPa was directly compared to the counterparts of MM5 winds in this study.

Fig. 3.1 Tracks of Hurricane Katrina (black star with lines), air RECCO.(black filled circle) and cross section for simulation result (red line) and their observed and simulated time respectively. The supplementary vortex messages directly measured for tropical storms before making landfall show their winds profile and the data for Katrina recorded starting at 03:32Z on 29th August was chosen because it shows relatively well the wind profile of the storm in the simulation time scope.
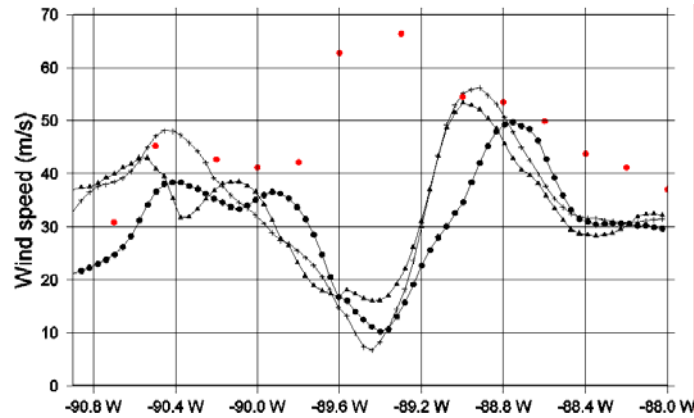
Fig. 3.2 Wind profiles of observed supplementary vortex data (red circle) at 03:32Z 29th and simulated wind profiles by Rankine vortex (black circle), modified Rankine vortex (black triangle) and SLOSH (black cross) wind model at 04:00Z 29th. The simulations were performed using R_{MW} decided from BestTrack data and 27km mesh size together with Four Dimensional Data Assimilation (FDDA).
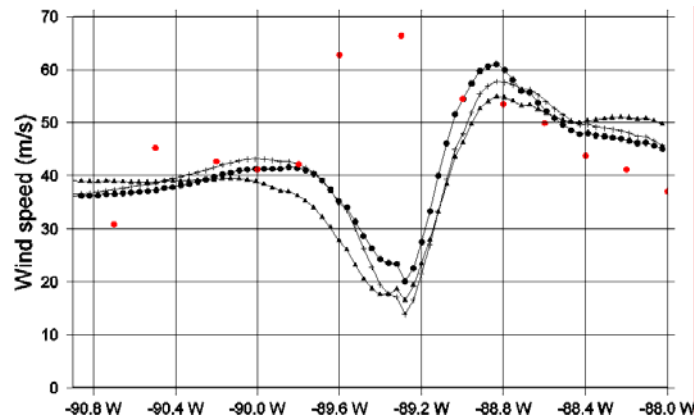
Fig. 3.3 Wind profiles of observed supplementary vortex data (red circle) at 03:32Z 29th and simulated wind profiles by Rankine vortex (black circle), modified Rankine vortex (black triangle) and SLOSH (black cross) wind model at 04:00Z 29th. The simulations were performed using R_{MW} decided from BestTrack data and 9km mesh size together with FDDA.
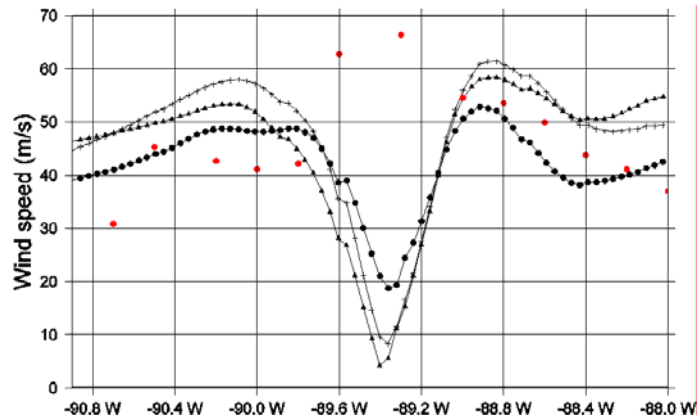
Fig. 3.4 Wind profiles of observed supplementary vortex data (red circle) at 03:32Z 29th and simulated wind profiles by Rankine vortex (black circle), modified Rankine vortex (black triangle) and SLOSH (black cross) wind model at 04:00Z 29th. The simulations were performed using R_{MW} decided from BestTrack data and 9km mesh size without FDDA.
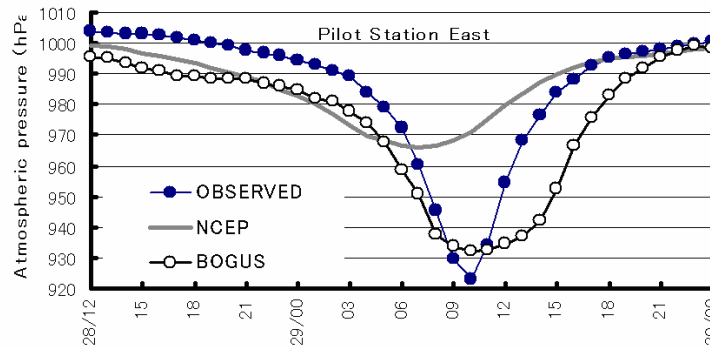
Fig. 3.5 Time variation of atmospheric pressure of observed data, NCEP final analysis data and the MM5 simulation result with bogus scheme applied at Pilot Station East.

Numerical experiments with varying condition of R_{MW} and horizontal resolution had been performed with modified bogussing scheme. Although it is difficult to validate the simulated wind fields with the wind profile data measured by aircraft because they were taken in different time while the hurricane is changing every minute, it is feasible to show their characteristics of wind profiles. Figs. 3.2 through 3.4 shows the simulated wind profiles and observed data by aircraft measurement. Throughout the simulations, underestimation of maximum wind speed and overestimation of wind speed at large radii were found. It can also be seen that V_{max} is too smoothed. When four dimensional data assimilation (FDDA) is applied to the simulation it shows better agreements with observations at radii lager than R_{MW}, but it can not resolve the spatial distribution of wind well near the maximum wind radius R_{MW}. Simulations with high horizontal resolution shows better wind profiles in R_{MW} with wind speed

57

close to zero. The overestimation of wind speed at large radii is possibly due to the pressure gradient near the search radius between background field and newly generated bogus field. The SLOSH wind model generated stronger wind speed than Rankine and modified Rankine vortex model at and outer R_{MW} while modified Rankine vortex model generated weaker wind speed at R_{MW}.

3.1.4 Wave field simulation

The wind wave field induced by Hurricane Katrina was simulated by WW3 and SWAN in this study. The simulations were made with different wind input source term (S_{in}) in WW3, which are the Janssen method and Tolman method as described in chapter 2. Fig. 3.6 shows the offshore wave observation buoys (42007, 42040) with their installed water depth operated by National Data Buoy Centre at NOAA. The simulated significant wave height, wind input source term and whitecapping dissipation term by two models and the observed significant wave heights are plot in Fig. 3.7 (at 42007 buoy) and Fig. 3.8 (at 42040 buoy). The other buoy, 42003 in further south of 42040 recorded the highest wave height ever since its operation for about 30 years. The observed data at 42007 after 08/29/06:00 UTC are not reliable because of observation system's trouble, then these data are marked with void circles. From the simulation results the Janssen method in WW3, the wind input source term is calculated larger than the whitecapping dissipation term that is considered to produce wave heights higher than those by the Tolman method. In deep water (42040 buoy), the results from SWAN is closer to that by Tolman method in WW3 and in shallow water (42007 buoy), the wave heights by SWAN show much decrease than those computed by WW3. This is the reason why SWAN considers the depth-induced breaking dissipation, while WW3 does not consider the effects. It can be said that WW3 may overestimate wave height in the shallow region.
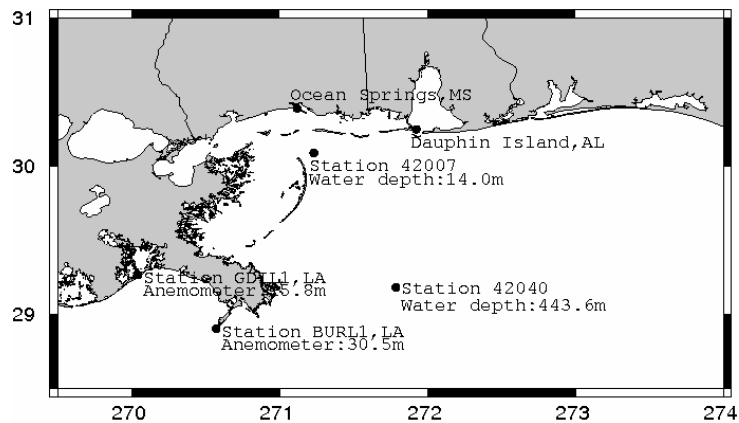
Fig. 3.6 Offshore buoy stations for wave observation off Mississippi delta
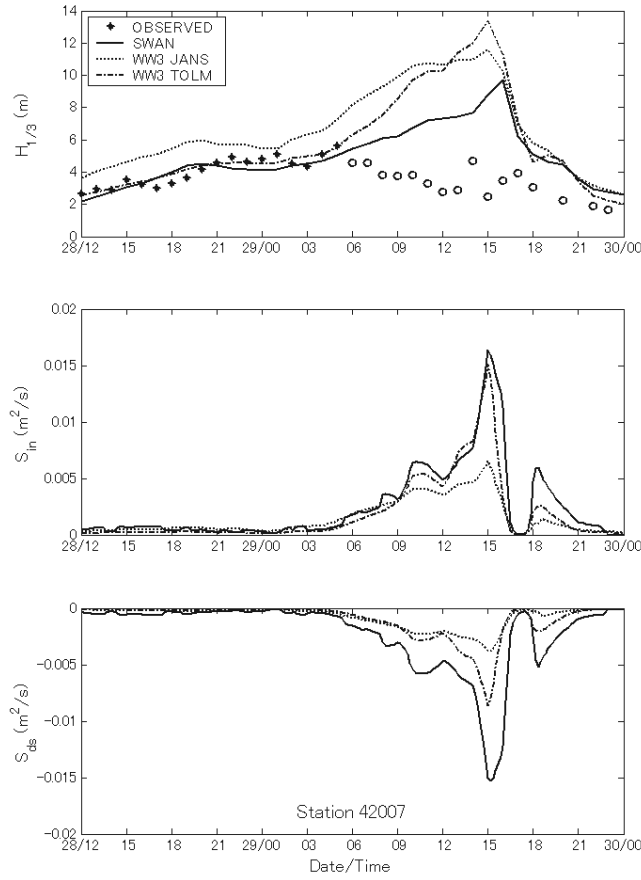
Fig. 3.7 Time variation of observed and calculated significant wave heights and source terms of Sin and Sds in the computations of SWAN and WW3 at Station 42007.

3.1.5 Storm surge simulation

The recent storm surge simulation considering wind-wave-current coupling effects has been possible by means of simultaneous computation of meteorological, oceanic and wind wave models. Coupled numerical computation of storm surge events of Katrina was conducted with considering the additional two stresses. One is the so-called "wave stress" that comes from the momentum transfer for wave development between planetary boundary layer and waves. The other is the so-called "breaking stress" that comes from the momentum transfer from waves to currents through wave breaking (whitecapping) dissipation (Eq. 3.8; Edson et al., 1999; Kim and Yamashita, 2005). "Breaking stress" in the current computation is defined by using the information of whitecap dissipation in the wind wave simulation as,

$$\tau_{br} = \rho g \iint S_{ds}(f,\theta) C(f)^{-1} df d\theta \qquad (3.8)$$

where $S_{ds}(f, \theta)$ is the whitecap energy dissipation rate in wave frequency f and direction θ space computed in the wave model and $C(f)$ is the wave celerity (such as peak frequency velocity).

The numerical computations in this study were conducted by the coupled numerical model that consists of atmosphere (MM5), ocean (POM; Mellor, 2003) and waves (WW3; Tolman and Chalikov, 1996) parts for their interactions through the surface boundary layer. Simulation was conducted for 6 days from 25th to 30th August, 2005, in the two nesting domains (the first domain covers the Gulf of Mexico, the second domain is focusing on the Gulf coast). The coupling computation for storm surge and waves was carried out only in the second domain.

The numerical experiments of storm surge had been performed with reproduced bogus wind fields by Rankine vortex, modified Rankine vortex and SLOSH wind models and their results were compared to observed data at stations on the Gulf coast (Fig. 3.10).
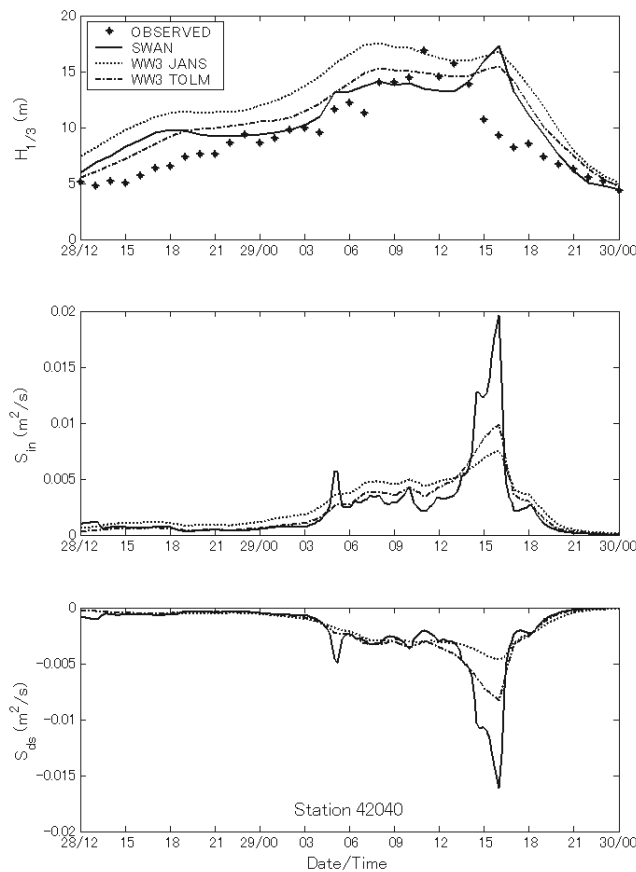
Fig. 3.8 Time variation of observed and calculated significant wave heights and source terms of Sin and Sds in the computations of SWAN and WW3 at Station 42040.
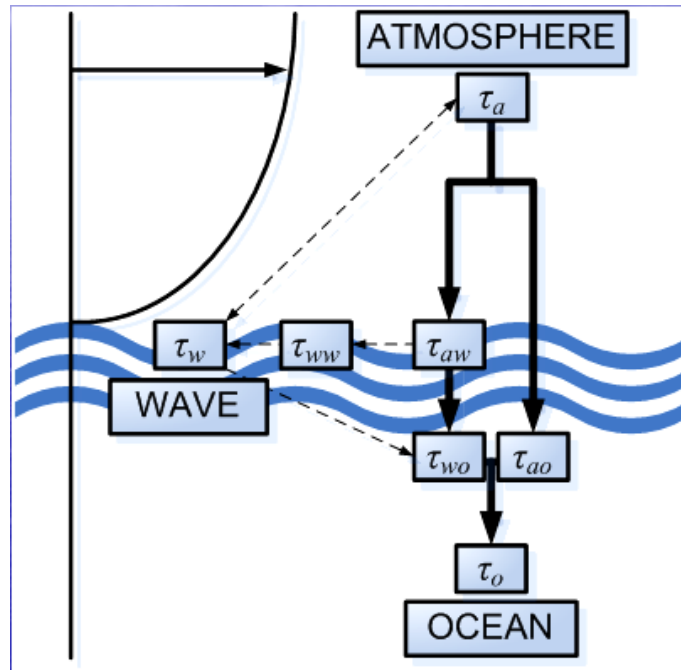
Fig. 3.9 Relation of interaction in the wind-wave-current system (Kim, 2005).

Because the sensors ceased transmissions of water level data, sea water level stations at Waveland, MS (Fig. 3.11) and Biloxi, MS (Fig. 3.12) failed observing water level during the passage of Katrina. The simulated maximum water levels at Waveland and Biloxi are 5.8m at about 12:00 UTC 29th and 6.2m at about 14:00 UTC 29th, respectively. The simulated water level at Dauphin Island, AL (Fig. 3.13) was overestimated with about 0.5m compared to the observed water level at 16:00 UTC 29th. It is probably caused by the overestimation of the reproduced wind field. The station at Ocean Spring, MS (Fig.3.14) shows the highest simulated water level of 5.2m at 16:00 UTC. However observation was also failed in recording the water level.
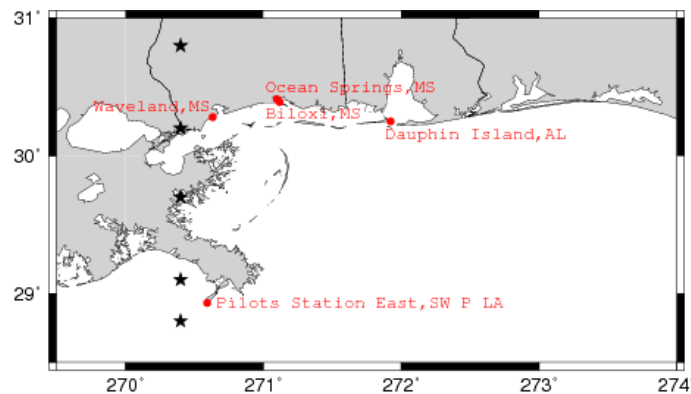
Fig. 3.10 Water level measuring stations along the Gulf coast and 3-hr interval Best Track positions of Hurricane Katrina (black stars)
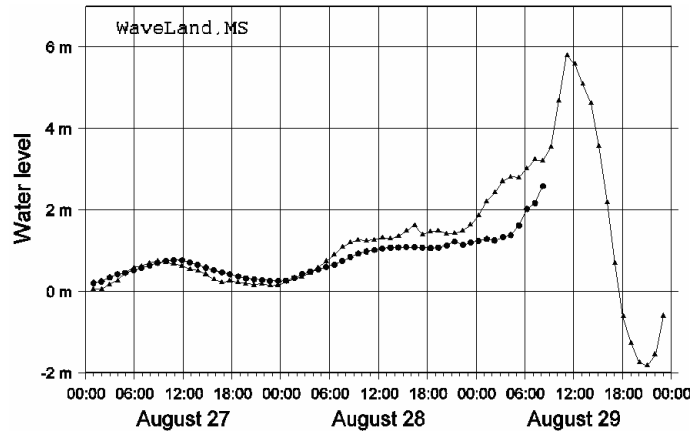
Fig. 3.11 Observed water level (circle) and simulated water level (triangle) at Waveland, MS
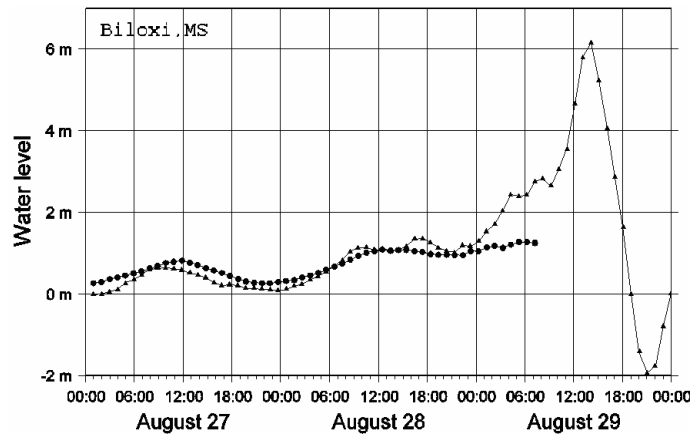
Fig. 3.12 Observed water level (circle) and simulated water level (triangle) at Biloxi, MS
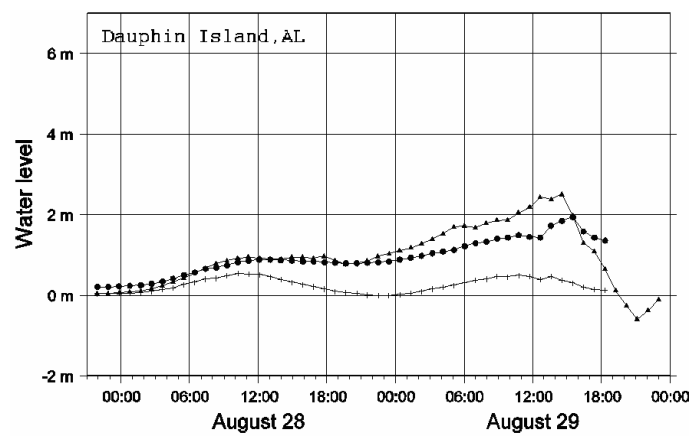
Fig. 3.13 Observed water level (circle), simulated water level (triangle) and predicted astronomical tide level (cross) at Dauphin Island, AL.

62
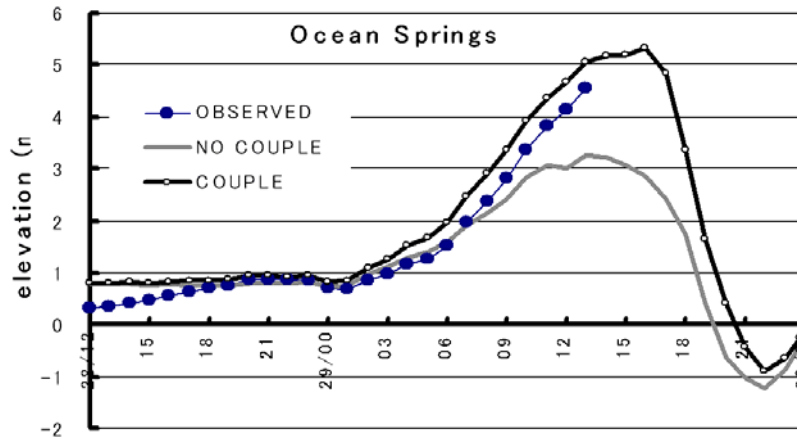
Fig. 3.14 Observed and simulated water level variation in time at Ocean Spring
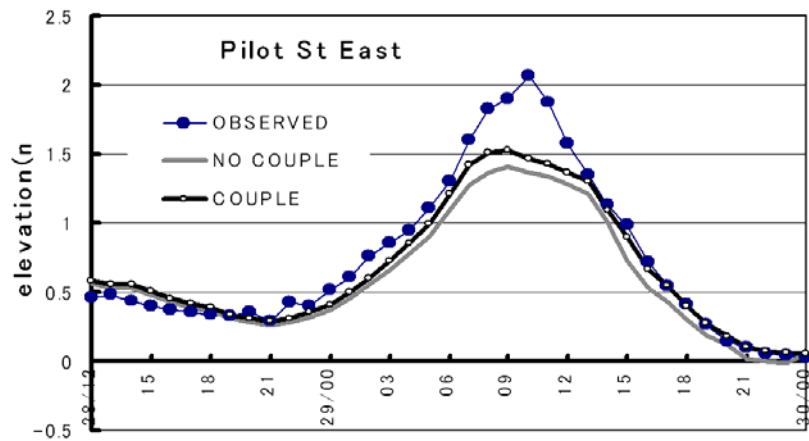
Fig. 3.15 Observed and simulated water level variation in time at Pilot St East.

The predicted astronomical tide and simulated water level are in good agreement at Ocean Spring. The computed sea water level is 5.3m in this study. In Fig. 3.14, the water level result of coupled run which considered the wind wave effects on currents as additional stress from waves to currents by whitecapping dissipation term shows good agreement with the observed water levels with in the ranges of the available record, while the result from the no-coupled run shows much lower than the observed ones. This is mainly caused by the wide continental shelf off Ocean Spring in the Gulf of Mexico. The water level set-up got enhanced by the increased whitecapping and strong anti-clockwise currents in the long and wide shelf region. The invert barometer effect is less than 1m.

At the Pilots Station East, LA (Fig. 3.15), the maximum water level of 2.362m was recorded at 09:30 UTC 29th but the simulated water levels show 1.53m and 1.4m by coupled and no-coupled run at about 7:30 UTC 29th . The differences between the observed and simulated

water levels may partly come from the difference of datum of water level of MLLW (observation) and MSL (simulation). The second reason considered is the incorrect bathymetry used for the study that could not resolve the low lying coastal region of the Pilots Station East. The last reason is wind field simulation in which R_{MW} used shows underestimation in the simulated wind profile as shown in Fig. 3.10. The wind wave effects by coupled run at Pilots Station East were not so significant compared to that at Ocean Spring with shallow water bathymetry.

3.1.6 Summary

Underestimation of reproduced wind field by Rankine vortex was improved by modified bogus scheme with modified Rankine vortex and SLOSH wind model. Although the wind field by modified bogus scheme was improved, it shows the underestimation of V_{max} near R_{MX} and the overestimation of wind speed at large radii. It is overestimated possibly due to the pressure gradient between background data and bogus field. Therefore bogus scheme is necessary to reproduce the wind field and typhoon intensity for the storm surge simulation in barotropic condition. However, special care is needed for the R_{MX} values, grid size of the domain and the baroclinic simulation of ocean when the bogus scheme is applied.

In the wind wave simulations, WW3 tends to overestimate the wave height in shallow region compared to that by SWAN. It is mainly because SWAN considers the effect of depth-induced breaking dissipation among the sink terms while WW3 does not consider it.

One of the additional stresses in the coupling process computation, breaking stress by wave breaking (whitecapping), plays very important role in the storm surge in shallow region. The water level variation in time at Ocean Springs depicts the significance of the breaking stress (τ_{br}) by whitecapping dissipation in the coupling process for storm surge simulation. The computed water level shows good agreement with the observed water level until the failure of recording.

64

3.2 Extreme high waves by Typhoon 7920

Extreme high waves of 10m induced by the super Typhoon 7920, TIP, were observed at the coastal observation station of Hara, Suruga Bay in Japan in 19th Oct., 1979. A wind-wave-ocean coupled model was applied to simulate the extreme waves and its generation mechanism with consideration of the interaction between the storm, tide and waves. In wave and current interaction, the stress caused by whitecapping dissipation is a driving force to generate current, which plays an important role in shallow region, while the tidal currents and water level variation of storm surge are given to the simulation of ocean waves. From the simulation results, it is found that the estimated values by wind wave model were not able to reproduce the extreme high waves and wave conditions around Hara while the other sites around Suruga Bay showed general agreement with the observed values. Discussion on the generation mechanism of such extreme waves is given in the present study.

3.2.1 Introduction

It is well known that extreme waves often occur in areas where waves propagate into a strong opposing current. One of the famous instances is the Agulhas current outside South Africa. The strong Agulhas current going south meets the swell by storms being propagated from the Antarctic Ocean (Dysthe et al., 2005). In this exceptional case, the extreme waves can be somewhat predicted. However, the extreme waves, the Freak waves and Rogue waves, in the open ocean can not be explained by the present spectral wind wave models.

In areas where waves from storms in the open ocean approach shallower waters (e.g. most of Japanese coast, especially along the coast faced to Japan/East Sea and the Pacific Ocean), the waves will be deformed in terms of refraction, diffraction and shoaling. Such deformation of waves, either due to currents or bathymetry, can be estimated and in a certain sense those waves may be predicted. There may be focusing of wave energy in certain shallow areas such that the probability of extreme high waves is much greater than in other areas (e.g. at Hara in Suruga Bay, Japan under the Typhoon 7920 condition).

Recently, works of Battjes and Groenendijk (2000) and Toffoli et al. (2006) focused on large waves in shallow water and showed that height distributions of depth limited waves can differ considerably from the Rayleigh distribution. Chien et al. (2002) discussed the properties of observed *coastal freak waves* and noted that wave grouping and bimodality increase the probability of occurrence of a coastal freak wave. However the generation mechanism of extreme wave in shallow water under typhoon, hurricane and cyclone conditions is still veiled. Callahan et al. (2006) studied such extreme wave of 20m under a tropical cyclone condition

with a concept of fatch enhancement to explain the generation mechanism.

In the present study, efforts were made to explore the generation mechanism of extreme high wave at Hara in Suruga Bay, Japan in Typhoon 7920(TIP) condition with resort to a wind-wave-ocean coupled model. The history of Typhoon TIP will be presented in subsection 3.2.2 and the simulation design and results are followed in 3.2.3. Finally, discussions on the generation of extreme waves will be given together with conclusions.

3.2.2 History of Typhoon 7920

This subsection on the history of Typhoon 7920 is largely based on the past report on the damage in coastal area by the typhoon (Okusa et al., 1979).

T7920 was incepted at around 153E longitude and 7N latitude at the east of Caroline Islands in the Pacific at 4th of Oct. 1979 and it stayed as a tropical depression for 2 days after inception and grew to a tropical storm. After growth in intensity, it became a typhoon at 9th of Oct. and then showed rapid growing to typhoon level 5 based on Saffir-Simpson scale at 12th of Oct. 1979. The central sea surface pressure of T7920 at about 12P.M at 12th of Oct. was 870hPa that was recorded for the strongest and lowest one with the 400km radius of wind gust. Afterwards, T7920 made landfall on Shirahama, Wakayama Prefecture at 09:40JST 19th Oct. and passed through the north of Shizuoka Prefecture (Fig. 3.16). Then it became weak and turned into a tropical storm over Hokkaido on the night of 19th Oct. 1979.
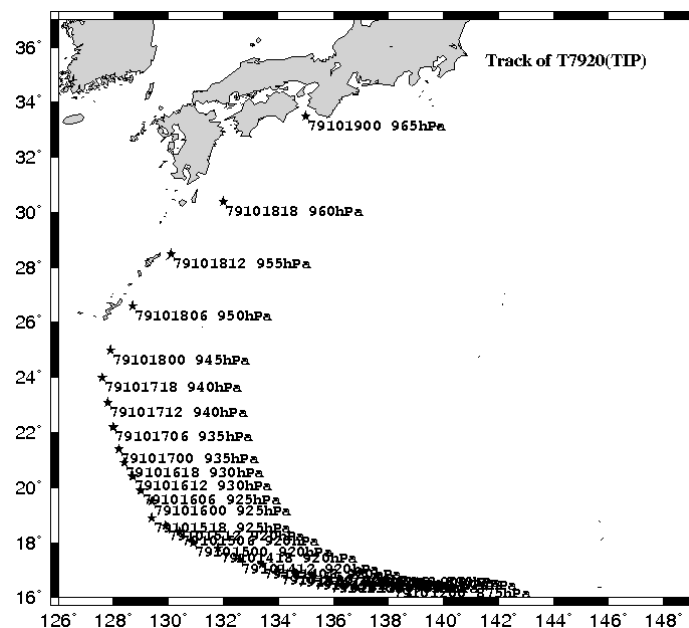
Fig. 3.16 The track of Typhoon 7920 (TIP)

Due to such strong typhoon, huge damages were reported around the Suruga Bay, particularly in the in the northwest of Suruga Bay (Fig. 3.18), Kunou coast and Shimizu harbor, local roads running by the coast were collapsed and the residential and agricultural area were impacted by high waves and overtopping (Fig. 3.17).

Suruga Bay, the study area, is located in the east of Shizuoka prefecture between Omaezaki cap in the west and Izu peninsula in the east, Suruga Bay is the deepest bay in Japan, reaching 2500m at the south entrance of the Bay. Hara with the extreme wave height is located at innermost north of Suruga Bay where the narrow and deep bottom channel ends (Fig. 3.18)
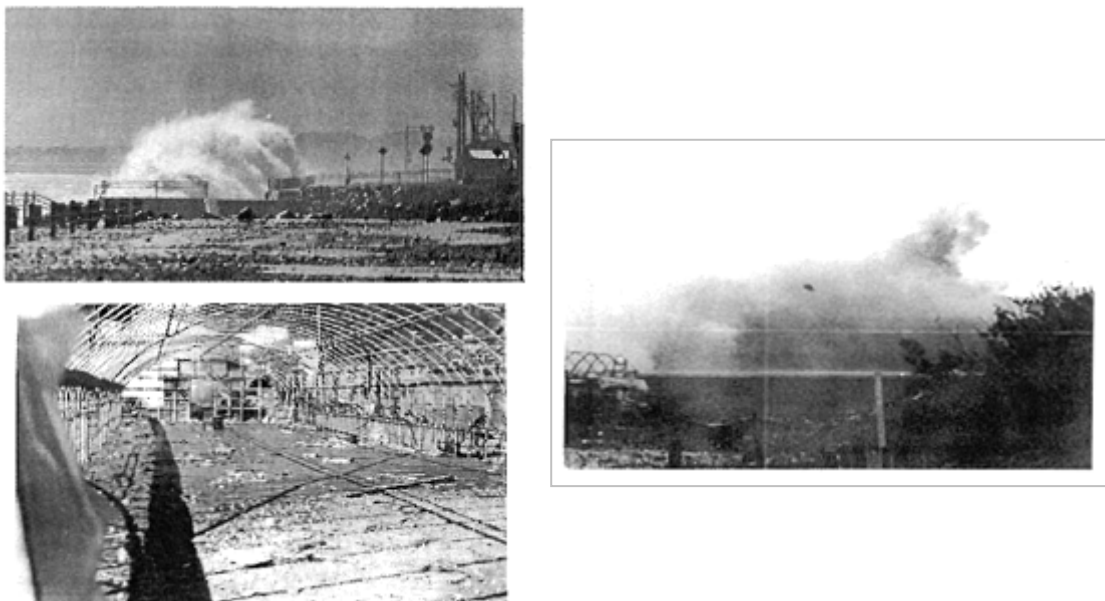
Fig. 3.17 Photos showing the wave overtopping and damaged houses (left) and other wave overtopping at about 14:00JST 19th Oct. 1979 (right) by Typhoon 7920, TIP (Okusa et al., 1979).
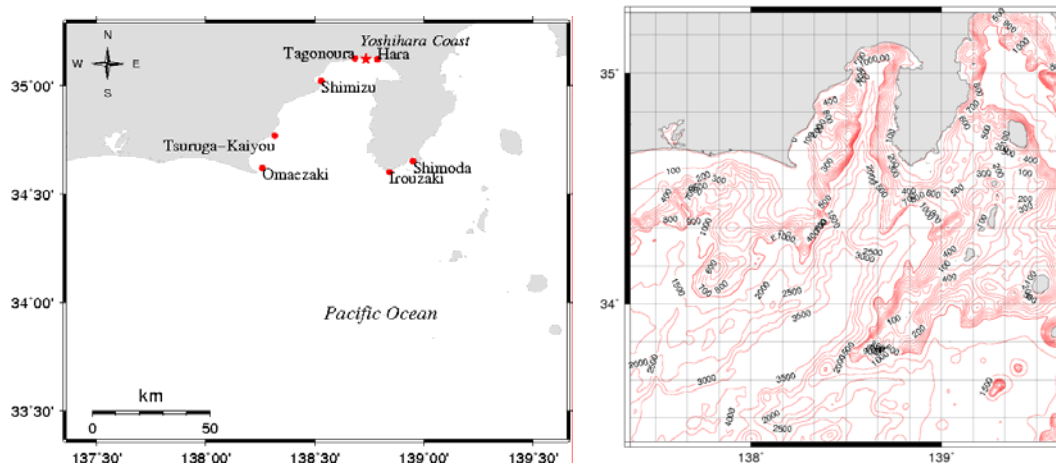
Fig. 3.18 Observation stations for meteorological conditions and wave climate (left) and the bathymetry of Suruga Bay and its vicinity (right).

3.2.3 Simulations of wind, wave and tide

Simulation conditions of MM5, WW3 and POM (including tide)

The simulations of the high waves in Hara, Suruga Bay, by typhoon, 7920, had been performed with the wind-wave-ocean (MM5-WW3-Ocean) coupled model. The wind-wave coupled model, first, was applied to study the typhoon generated wind waves without the interactions with ocean. Next, the wind-wave-ocean coupled model was applied for the reproduction of high waves in Hara in consideration of the interactions with ocean such as water level and currents.

Fig. 3.19 showed the computational domains used for MM5 and WW3. The three domains are one-way nested in both MM5 and WW3. The domains have their grid size of 27, 9 and 3km for the largest domain, the middle and the smallest one, respectively. In the simulation of POM, the only smallest domain was used being coupled with the counterpart of WW3 simulation. In MM5 simulations, four dimensional data assimilation (FDDA) (Grell et al., 1995) was applied to the first domain in wind, temperature and mixing ratio field and the physics parameterizations such as the cumulus scheme, moisture scheme, planetary boundary layer model, and cloud atmospheric radiation scheme were used for the simulations (see Chapter 2 for details of the physics).

The interaction between two models was actually dealt with in one-way from MM5 to WW3 through the wind velocity at 10m above the surface (U_{10}) and the MM5-POM interaction was also treated one-way from MM5 to POM through the surface wind and atmospheric pressure. However, in the WW3-POM interaction for the simulation of tidal currents and storm surge effects on wind waves, the two-way coupling was made through the whitecapping stress

of wind waves (WW3) to surface currents (POM) and the currents velocity by tide and water levels by storm surge (POM) to wind waves (WW3).

The initial and boundary condition of MM5 were provided with ECMWF ERA 40 ($2.5 \times 2.5°$ resolution) global data and the initial condition of POM was given in homogeneous temperature and salinity profiles both horizontally and vertically (barotropic ocean states). Real-time tidal elevations were imposed at the open boundary of POM.

The initial wave frequency increment factor, first frequency, number of frequencies and direction in WW3 were given as 1.1, 0.025, 36, and 24 respectively. The source terms used in WW3 were the wind input and dissipation terms by Tolman and Chalikov (1996), the non-linear wave-wave interaction by DIA method, and the bottom friction by JOHNSWAP formulation. The boundary conditions of the incident wave spectra for the second and third domains were taken from their mother domains in WW3.
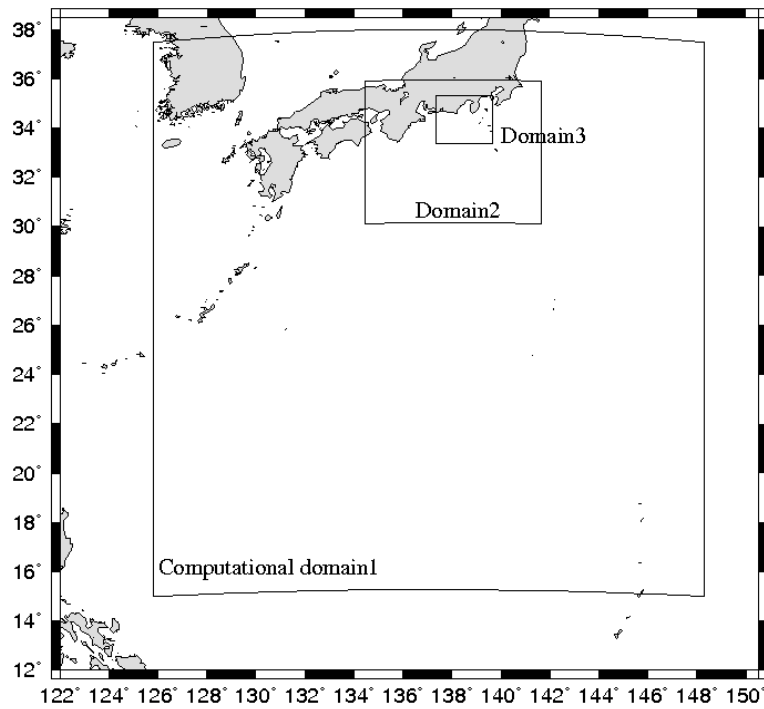
Fig. 3.19 Computational domains for MM5, WW3 and POM (used only in the domain3)

Simulation results

(a) Wind

The simulated wind field at Hara of Typhoon, TIP by MM5 and typhoon model were shown in comparison to the observed values in Fig. 3.20 in meridional (N-S) and zonal (E-W) directions. In zonal direction, the observed wind did not show much increase at the time of typhoon passage, while the observed meridional wind increased rapidly up to 20m/s. The result

from typhoon model in zonal wind, the direction change was clearly captured while the results from MM5 and the observed values were rather uncertain. The zonal wind velocity by typhoon model was overestimated. This result can be partially explained that the typhoon model is not able to describe the topographical effects which are considered in MM5.

In meridional wind, both the typhoon model and MM5 could reproduce the peak wind speed at around 14:00JST 19th Oct. close to the observed value of 20m/s. However, the meridional wind before the peak wind by typhoon model was also overestimated and after the peak wind, it showed sharp change in direction and increase in velocity at 20:00JST 19th Oct. in 1979. The result of MM5, on the other hand, showed very good agreement with the observed values after the peak wind. Before the peak, the meridional wind by MM5 was slightly overestimated for several hours, but still showed general agreement with the observed wind.
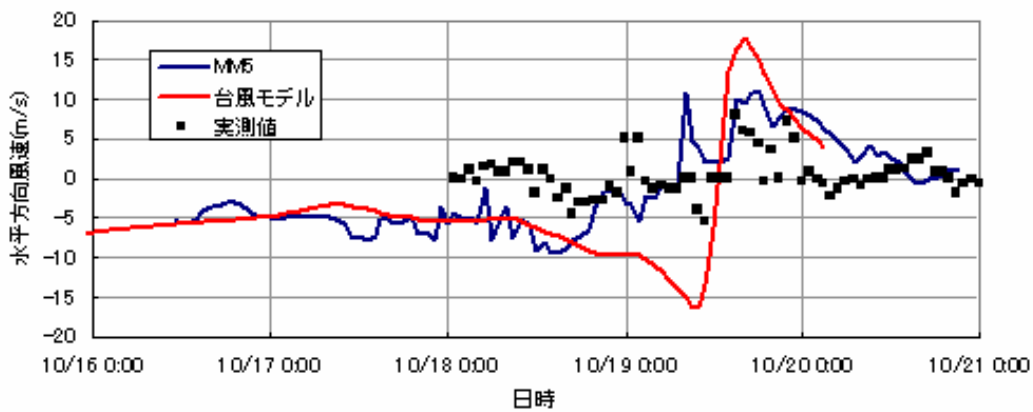
(a) zonal direction
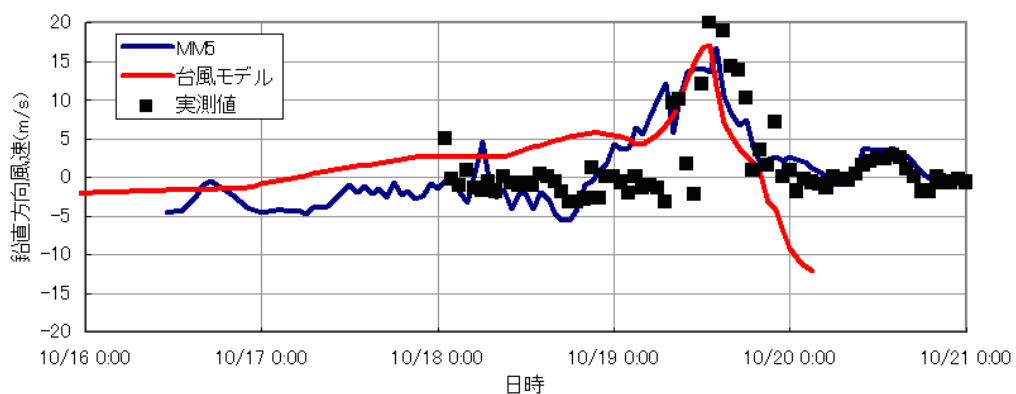
(b) meridional direction

Fig. 3.20 Time-series of (a) zonal and (b) meridional wind velocity from observed data (square) and calculated data by MM5 (blue line) and Typhoon wind model (red line) at Hara.

b) Waves

The observed wave height and period at Hara were presented in Fig. 3.23 together with the simulated wave height and period by WW3. During the numerical simulations of wind waves, first, the observed long period (about 15sec) waves before the sudden drop in wave period at around 06:00Z 19th August were the main concern to reproduce such waves. To simulated such long waves, which is swell generated under the storm condition, the simulation of typhoon had to include the early stage of typhoon in wide domain region (Fig. 3.21(a)). The swell generated in early stage and in slowly moving part of typhoon was the main cause of such long waves observed before the maximum significant wave height.

As Typhoon TIP moved very slowly at about 18N with the minimum central pressure of 870hPa for a couple of days, much time was allowed for surface wind to act on the water surface to generate and grow the typhoon generated wind waves. By using multi-nested simulation (Fig. 3.21), such typhoon generated swell could be reproduced and showed general agreement with the observed values. However, the extreme wave height observed at 14:00Z 19th had 4m difference with the simulated values, which is discussed in next section. In the meantime, the simulated wave height at Irouzaki showed good agreement in significant wave height of about 9m with 2hrs lag in occurrence time.

3.2.4 Discussion on the extreme high waves

With a number of numerical simulations applied to this high wave conditions, the results of simulations were not able to clearly reproduce the wave condition in Hara. Here the generation mechanism of such high waves is discussed mainly based on the observed data at that time.

First, a question arises whether the observed wave heights are correct or not? Fig 3.25 shows the observed maximum and significant wave heights at Shimizu harbor, Tagonoura, Hara and Irozaki. The observation from about 10:00JST to 16:00JST at 19th October at Shimizu harbor and Tagonoura failed with some troubles of measurement that was made with a pressure gauge at about 20m deep. While other point, for instance, Irouzaki shows general agreement between the observed height and simulation result as shown in Fig.3.22. However, the simulated wave height at Hara had appreciable discrepancy compared to the observed one. It is interesting to note that the observed wave heights at Hara (inner bay observation station) and Irozaki (open ocean observation station) are almost identical each other. Therefore, a question that the observation was made accurately and in proper manner, is still one of the possible reasons of above mentioned Hara-Irozaki paradox.

(1) Possibility of High Waves at Hara Station

To investigate the question and find the answer except wave gauge problems, additional simulations were conducted with an assumed typhoon which takes the track passing through just left of Suruga Bay where the radius of maximum wind just locates in the Suruga Bay during the passage of typhoon. The track of this imaginary typhoon was set to be the track shown in Fig. 3.26 that was shifted to right from the Typhoon 5915 (IseWan Typhoon).

(a) Domain 1
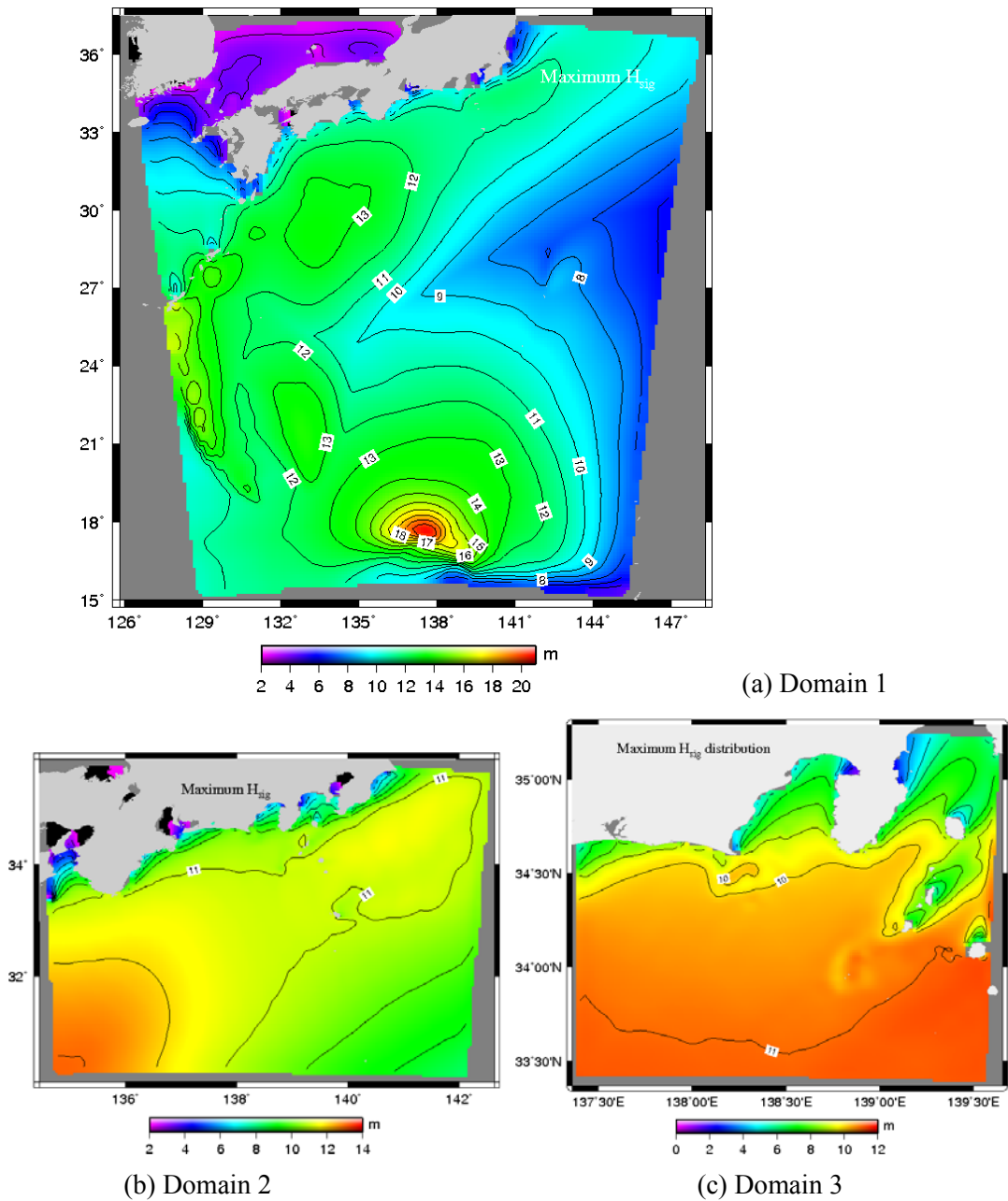
(b) Domain 2

(c) Domain 3

Fig. 3.21 Maximum significant wave height distribution in every domains.
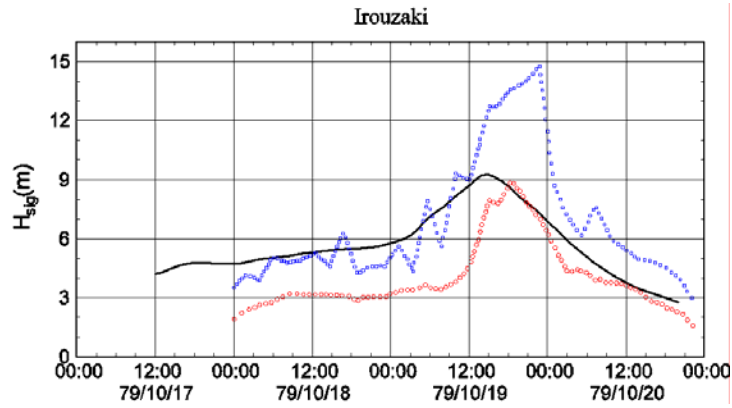
Fig. 3.22 Time-series of wave heights from the observed (significant wave height : red and maximum wave height : blue circles) and simulation (plain line) at Irouzaki
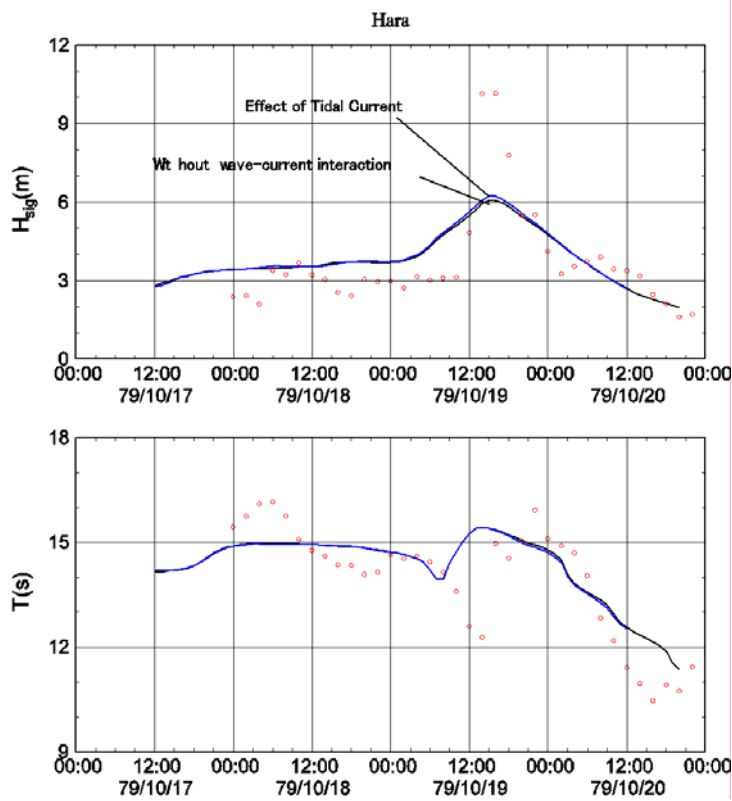
Fig. 3.23 Time-series of wave heights and periods from the observed (red circles) and simulation (plain line) at Hara. Black line indicates the simulated wave height and period without the tidal currents and storm surge effects while the blue line indicates the results with consideration of tidal currents and storm surge effects.
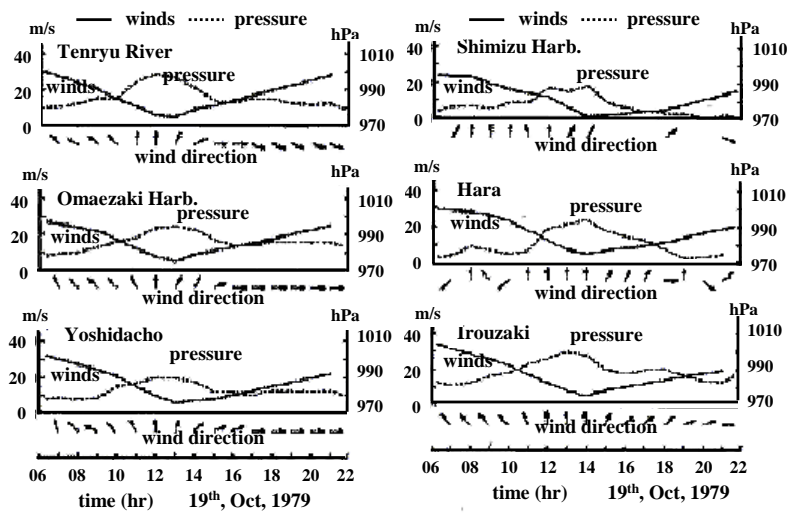
Fig. 3.24 Time-series of the observed wind, wind direction and atmospheric pressure at
Tenryugawaguchi, Shimizu, Omaezaki, Hara, Yoshidamachi and Irouzaki (Okusa et al., 1979).
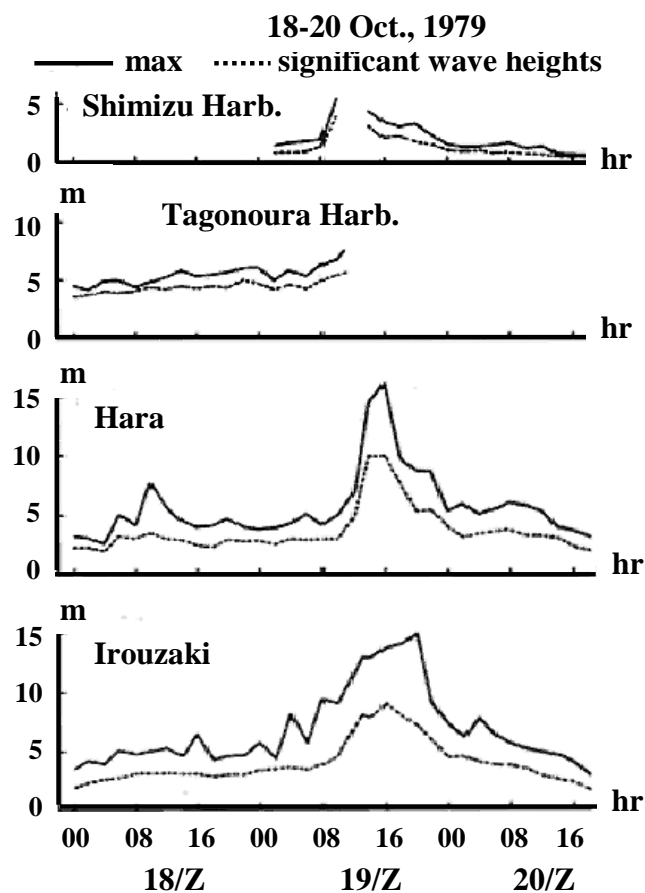
Fig. 3.25 Time-series of the observed maximum wave heights (plain line) and significant wave
height (dotted line) at Shimizu, Tagonoura, Hara and Irouzaki (Okusa et al., 1979).

74
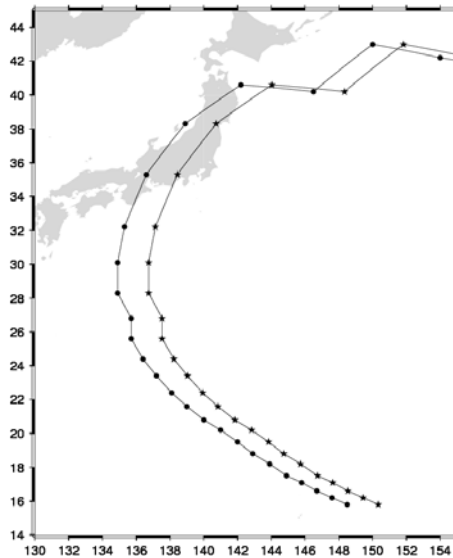
Fig. 3.26 The track of Typhoon 5915 (IseWan Typhoon). Original track (circles) and shifted track (stars) used for the imaginary typhoon experiment that passes through just in the left of Suruga Bay.

The results from the imaginary typhoon case depicts that the wave height at Hara was reproduced up to almost 10m high that was equivalent to the observed value. Moreover, the wave height production was quite sensitive to the track in this case, because the typhoon could bring the wind waves directly towards the inner bay up to Hara station without any interference with surrounding boundary during the wave propagation. The sensitive relations between the wind field and topography have to be discussed carefully in this simulation. However, as mentioned before, typhoon bogussing which was employed in this study has still problem of smoothed maximum wind near the radius of maximum winds. This shortcoming of the typhoon model used in this study may have a possibility of the reason why the model can not reproduce of high waves at Hara.

(2) Wave-Current Interaction

The second possibility is the wave and current interaction. It was investigated since the effects of current on the wave are significant under storm conditions. Therefore, the effects of tide and storm surge (Tolman, 1991) by Typhoon 7920, TIP were studied by the wind-wave-current (MM5-WW3-POM) coupled model (see Chapter 2 for the details of the coupled model and their interaction).

Fig 3.27 shows the water level variation at Tagonoura observed by tidal gauge. It can be seen that the observed high waves at Hara station (fluctuations around 16:00 Oct. 19th) were occurred at the changing phase of tidal current from flood to ebb that was changes from 2.4m to

2.7m in tide.

The simulation results by the coupled model with consideration of the currents and storm surge effects on waves have shown in Fig 3.23. During the approach of typhoon and after the landfall onto main island of Japan, the influences of currents and storm surge were not significant while the effect on wave at the time of peak wave height was estimated about 30cm increase in wave height and about 0.3sec decrease in wave period. This result means that the wave propagating into the Hara located in almost innermost part of Suruga Bay encountered the ebb tidal fronts which induced such increase in wave height and decrease in wave period. However the tidal currents and storm surge effects on wind waves are not sufficient to explain the high waves at Hara.
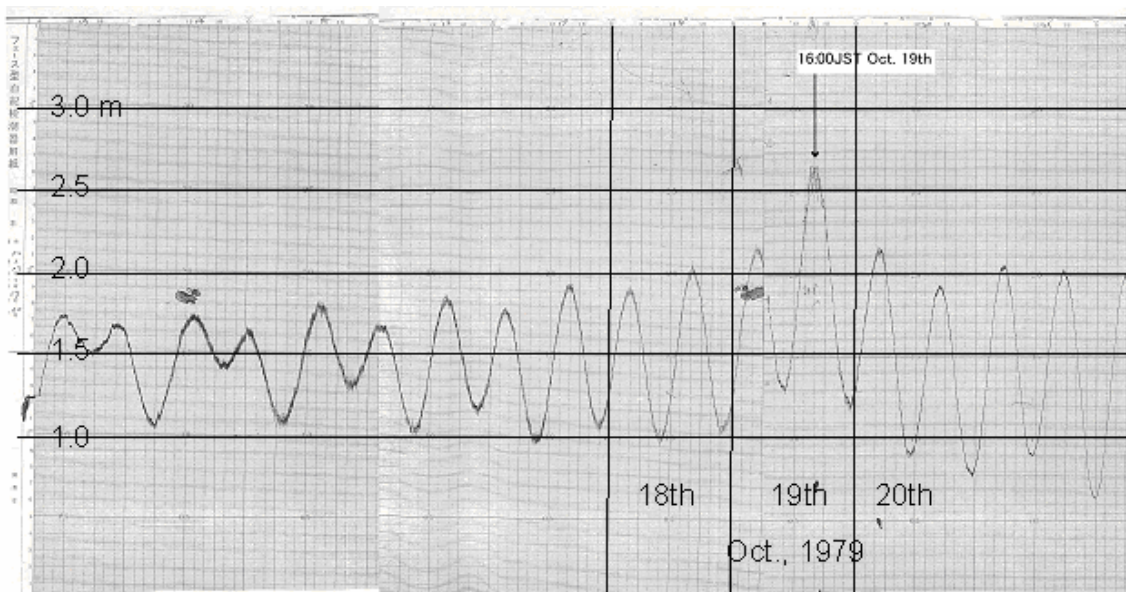
Fig. 3.27 Time-series of observed water level variation at Tagonoura.

(3) Seiche

The third possibility is the effect of resonance of seiche in Suruga Bay. In general, the effects of resonance amplifications are related to geographical conditions of coastal structure and region such as harbor, bay, channel, etc and became significant when the long period incident wave coincides with the natural frequency of the harbor, bay, etc. The resonance under the typhoon condition is also related to the movement of typhoon. If the typhoon passes over the interested region with certain translational speed which coincides with the natural frequency, the resonance amplification of water levels due to the inverted barometer effect as well as the typhoon generated swell will take place and give rise to significant consequences. In such cases, the storm surge in the coastal region will be appeared far higher than the predicted level.

76

It has investigated by Name (author of Fig.3.28) by using observed tidal variation and seiche level changes at Hara as shown in Fig 3.28 in which the tidal anomaly at Omaezaki, Shimizu and Uchiura and seiche levels at same locations. The seiches at Omaezaki and Naiura were over 30cm while the value at Shimizu was about 20cm and thus, the value at Hara can be estimated with about 20cm. Therefore, the high waves at Hara can not be explained by the resonance effects, either.
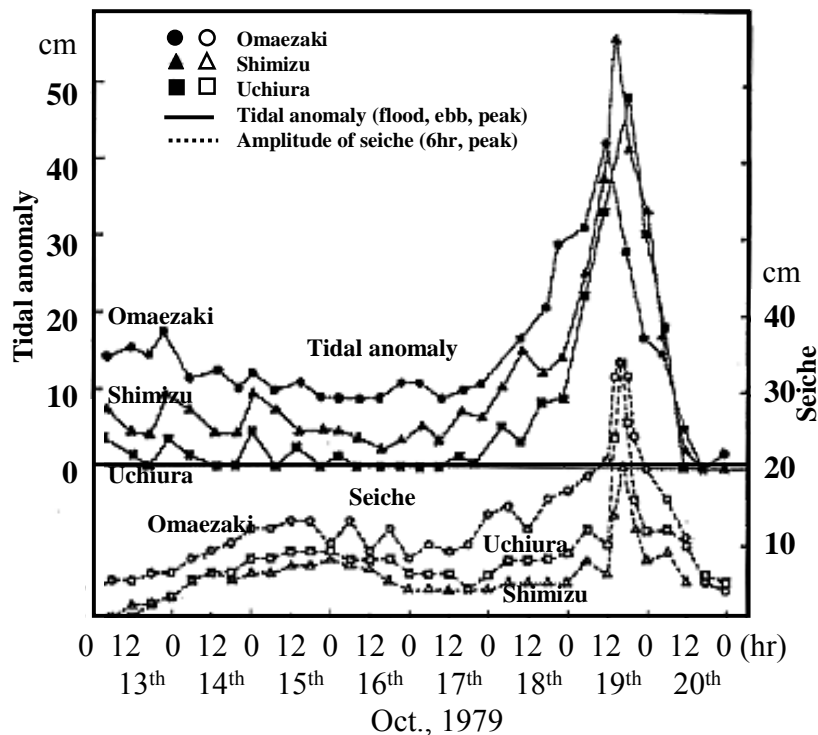
Fig. 3.28 Time-series of observed tidal variances (plain lines) at Omaezaki (circles), Shimizu (triangle) and Uchiura (square) and resonance levels every 6hrs (dotted lines) (Okusa et al., 1979).

Finally, the extreme high waves could be the complicated phenomena that result from all of the possibilities above. It reveals that our understanding of such extreme waves and wind-wave-ocean coupled system is very limited to be explored.

3.2.5 Summary

Typhoon TIP which is the strongest typhoon that human have ever recorded, caused huge damages in the coastal region in Suruga Bay by accompanied storm surge, high waves, wave overtopping. The extreme high waves observed at Hara (inner station in the Suruga Bay)

that was caused by Typhoon 7920, TIP were discussed by means of the simulation results with wind-wave-ocean (MM5-WW3-POM) coupled model. The results of numerical simulation showed that the estimated wave climate around Suruga Bay depicted general agreement with the observed values except at Hara.

Some possibilities to explain the high waves at Hara are discussed in this chapter and listed below.

1) First possibility: Numerical experiment for imaginary IseWan Typhoon which takes the track passing through just left of Suruga Bay where the radius of maximum wind just locates in the bay. The results from the imaginary typhoon case showed that the wave height at Hara was reproduced up to almost 10m that was equivalent to the observed value. It was also made clear that the wave height production was quite sensitive to the track in this case, because the typhoon could bring the wind waves directly towards the inner bay up to Hara station without any interference with surrounding boundary during the wave propagation. However, typhoon bogussing which was employed in this study has still problem of smoothed maximum wind near the radius of maximum winds. This shortcoming of the typhoon model used in this study may have a possibility of the reason why the model can not reproduce of high wave at Hara.

2) Second possibility: The tidal currents and storm surge were considered in wind wave model simulation for the wave-current interaction. In the ebb currents condition, the wave encountered the tidal fronts resulting in the increase of wave height and decrease of wave period. However the computed currents and wind waves interaction was not sufficient to explain the high waves at Hara.

3) Third possibility: The resonance of seiche in the Suruga Bay was investigated based on the observed tidal variance and resonance wave levels. The resonance amplification of wave levels was about 20cm at Hara.

It would be finally concluded that the high waves observed at Hara may actually occurred in the Suruga Bay. It may be reproduced by the simulator if the shortcoming of bogussing typhoon model (smoothed maximum wind near the radius of maximum winds) is made clear.

References

Atkinson, G. D., and C.R. Holliday, (1977): Tropical cyclone minimum sea level pressure/maximum sustained wind relationship for the Western North Pacific, *Mon. Wea. Rev.*, **105(4)**, 421-427.

Battjes, J.A. and H. W. Groenendijk, (2000): Wave height distributions on shallow foreshores, *Coastal Engineering*, **40**, 161-182.

Callaghan, D. P., J. Callaghan, P. Nielsen, and T. Baldock, (2006): Generation of extreme wave conditions from an accelerating tropical cyclone, *Proc. 30th int. Conf. Coastal Engineering*, San Diego, USA, 752-760.

Chien, H., C. Kao, and L.Z.H. Chuang, (2002): On the characteristics of observed coastal freak waves, *Coastal Engineering Journal*, **44(4)**, 301-319.

Davis, C.A.and S. Low-Nam, (2001): The NCAR-AFWA Tropical Cyclone Bogussing Scheme, Air Force Weather Agency report, NCAR, Boulder, Colorado.

Dunion, J.P., C.W. Landsea, S.H. Houston and M.D. Powell, (2003): A Reanalysis of the Surface Winds for Hurricane Donna of 1960, *Mon. Wea. Rev.*, **131**, 1992-2011.

Dysthe, K. B., H. E. Krogstad, H. Socquet-Juglard, and K. Trulsen, (2005): Freak waves, rogue waves, extreme waves and ocean wave climate, http://www.math.uio.no/~karstent /waves/index_en.html

Edson, J., T. Paluszkiewicz, S. Sandgathe, L. Vincent, L. Goodman, T. Curtin, J. Hollister, and M. Colton, (1999): Coupled Marine Boundary Layers and Air-sea interactions initiative: Combining process studies, simulations, and numerical models, 18-46.

Fujita, T.T. (1971): Proposed characterization of tornadoes and hurricanes by area and intensity, *SMRP Internal Research Paper*, **91**.

Harper, B.A. and G.J. Holland, (1999): An updated parametric model of the tropical cyclone, *Proc. the 23rd conference of Hurricane and Tropical Meteorology*, Dallas, Texas, 893-896.

Holland, G.J., (1980): An analytical model of the wind and pressure profiles in Hurricanes, *Mon. Wea. Rev.*, **108**, 1212-1218

Houston, S.H., W.A. Shaffer, M.D. Powell, and J. Chen, (1999): Comparisons of HRD and SLOSH surface wind fields in Hurricanes: Implications for storm surge modeling, *Weather and Forecasting*, **14(5)**, 671-686.

Hsu, S.A., M.F. Martin, Jr., and B.W. Blanchard, (2000): An evaluation of the USACE's deepwater wave prediction techniques under hurricane conditions during Georges in 1998, *J. Coast. Res.*, **16**, 823-829.

Hsu, S.A., (2005): Estimating the radius of maximum winds via satellite during Hurricane Lili (2002) over the Gulf of Mexico,

Hughes, L.A., (1952): On the low level wind structure of tropical cyclones, *J. Meteor.*, **9**, 422-428.

Jelesnianski, C.P., J. Chen, and W.A. Shaffer, (1992): SLOSH:Sea, lake and overland surges from hurricanes. NOAA Tech. Report NWS 48, 71pp

Kim, K. (2005): Coastal ocean model with consideration of meteorological-oceanographic mesoscale interaction, Ph.D dissertation, Kyoto University, Japan.

Kim, K.O., H.S. Lee, and T. Yamashita, (2005): Winter Huge Wave Simulation in Japan Sea by MM5 and WW3 Coupled Model Using Depression Bogussing, *Annual J. Coastal Eng.*, JSCE, **52(2)**, 176-180. (in Japanese).

Kim, K., T. Yamashita, (2005): Reanalysis of Storm Surges Caused by Cyclone in 1991 in Bay of Bengal: Effects of Whitecap Dissipation in Wave-Surge Coupled Model, *Annual Journal of Coastal Engineering*, JSCE, **52**, 211-215. (in Japanese)

Kraft, R.H., (1961): The hurricane's central pressure and highest wind, *Mar. Wea. Log*, **5**, 157.

Mellor, G.L., (2003): Users guide for a three-dimensional, primitive equation, numerical ocean model, 53pp., *Prog. in Atmos. And Ocean. Sci*, Princeton University.

NOAA, 2005. Preliminary Report, (2005): Hurricane Katrina Storm Tide Summary, National Ocean Service, NOAA, Silver Spring, MD.

Okusa, S., K. Hishita, M. Hoshino, A. Saito, O. Toyoshima, S. Kosuke, M. Kemuriyama, A. Hosoi, A. Ishida., (1979): Coastal disaster in Kunou Coast, Shizuoka, 45-85. (in Japanese)

Phadke, A.C., C.D. Martino, K.F. Cheung and S.H. Houston, (2003): Modeling of tropical cyclone winds and waves for emergency management, *Ocean Eng.*, **30**, 553~578.

Powell, M.D., S.H. Houston, and T.A. Reinhold, (1996): Hurricane Andrew's landfall in South Florida. Part I: Standardizing measurements for documentation of surface wind fields, *Weather and Forecasting*, **11(3)**, 304-328.

RMS report. (2005): Hurricane Katrina : Profile of a super cat, Lessons and Implications for Catastrophe Risk Management, Risk Management Solutions, INC. CA, USA.

Takahashi, K. (1939): Distribution of pressure and wind in a typhoon, *J. Meteoro. Soc. Japan*, Ser. 2, **17**, 417-421.

Toffoli, A., M. Onorato, and J. Monbaliu, (2006): Wave statistics in unimodal and bimodal seas from a second-order model, *European Journal of Mechanics - B/Fluids,* **25(5),** 649-661.

Tolman, H. L., (1991): Effect of tide and Storm surge on North Sea wind waves, *J. Phys. Oceanogr.*, **21**, 766-781.

Tolman, H. L. and D. V. Chalikov, (1996): Source terms in a third-generation wind-wave model, *J.Phys. Oceanogr.*, **26**, 2497~2518.

Chapter 4

Numerical Experiment of Typhoon-Ocean Interaction

In this chapter, two types of numerical experiments on typhoon-ocean interaction were conducted in which non-hydrostatic 3-D ocean model, MITgcm was employed. One is an one-way experiment from typhoon to ocean circulation assuming an idealized typhoon model of Rankin vortex and ocean of uniform depth. The other is a typhoon-ocean interaction experiment in which full coupling computation between the atmosphere (MM5) and ocean (MITgcm) under the condition of real Typhoon 0310 (ETAU) was considered.

In the typhoon-ocean interaction experiment, simulation results depicted good accordance with previous study (Bender et al., 1993) and sea surface temperature (SST) measured by satellite TMI (TRMM Microwave Imager) radiometer. The physical processes of negative feedback, e.g. the typhoon caused SST cooling consequential decreases typhoon intensity, were clearly revealed in the experiment. It was also made clear that the Kuroshio Warm Current (KWC) provides large amount of latent heat to the typhoon to maintain its intensity until landfall. However, the result from coupled simulation rather underestimated the typhoon intensity after crossing KWC because of larger decrease in SST than the observation.

4.1 Introduction

Typhoon-ocean interaction is quite important in the forecast of typhoon in its track and due to advanced computing technologies, improved dynamic models and satellite observations, the forecast of typhoon track have been gradually improved. However, due to our limited understanding of the air-sea interaction the forecast of typhoon intensity variation is a difficult task to be explored.

It has been well studied that there is a positive and negative feedbacks mechanism in typhoon-ocean interaction. As the generation of typhoon is related to the sea surface temperature (SST) higher than 26℃ (Wendland, 1977), typhoons are growing and become intensified due to the increased evaporation rate by strong surface wind stress. The increased

moisture supply results in the enhancement of latent heat flux that drives the circulation of typhoon. This is the positive feedback in the inception and development stage of typhoons. As the typhoon gets stronger, the turbulent mixed layer gets developed and deepened by the strong wind stress, resulting in the decrease of SST. The SST reduction is due to the current velocity shear production that brings the cool thermocline water to turbulent mixed layer. Consequently, the reduction of SST leads to the decrease of typhoon intensity. This is the negative feedback in typhoon-ocean interaction. Thus SST variation is very important in the intensity change of typhoon and have been well studied both theoretically (Emanuel, 1986) and numerically (Chang, 1979; Tuleya and Kurihara, 1982; Bender et al., 1993). Recently the observation by satellites confirm the SST reduction as much as 5-6℃ in the cold wake of slowly moving typhoons (Nelson, 1996; Monaldo et al., 1997; Wentz et al., 2000).

The positive and negative feedbacks in typhoon-ocean interaction have been studied by a number of numerical modeling studies in order to understand the interaction mechanisms and to estimate the various typhoon and ocean responses. In early stage of numerical simulation studies, mostly the typhoon response to the SST variation was investigated in terms of typhoon intensity changes. Chang (1979) used the rather coarse resolution (60km) axisymmetric multilayer numerical model to estimate the tropical cyclone response to local, instantaneous changes of SST showing that the sensitivity of tropical cyclone to instantaneous SST change within the inner radius of 300km in the cyclone. In the work of Chang and Anthes (1979), an earlier coupled model, an axisymmetric hurricane model and a two-layer baroclinic axisymmetric ocean model, was used to study the mutual response of tropical cyclone and ocean. In their study, the coupled model was integrated for 24hrs and the result depicts that the SST reduction did not induce the considerable change in hurricane intensity for a short period of time (24hrs).

Bender et al. (1993) performed numerical experiments on idealized tropical cyclone-ocean interaction utilizing the high-resolution NOAA Geophysical Fluid Dynamics Laboratory (GFDL) tropical cyclone model coupled with primitive equation multi-layer stratified ocean model. In the idealized numerical experiments, the initial state of ocean was assumed homogeneous and quiescent and results indicated that the sea surface cooling caused by the tropical cyclone resulted in a significant effect on the maximum storm intensity due to the reduction of total heat flux directed into tropical cyclone above the region of the decreased SST. Recently Bender and Ginis (2000) applied a coupled model, which consists of the NOAA GFDL hurricane model and a high-resolution (1/6°) version of Princeton Ocean Model (POM) for hurricane and ocean states respectively to four real hurricanes. The results from the simulations confirmed the positive and negative feedbacks in real-case hurricanes emphasizing the importance of an accurate initial SST analysis as well as the coupling with the ocean for

accurate prediction of hurricane intensity.

Hodur (1997) applied a coupled ocean-atmosphere mesoscale prediction model to idealized tropical cyclone condition which the initial temperature and salinity condition of ocean state was obtained from the generalized digital environment model (Teague et al., 1990). The simulation results also depict the negative feedback and SST cooling up to 8℃ over the reported value (5-6℃) within the radius of maximum winds and thus much decrease of cyclone intensity.

More recently, Chan et al. (2001) performed numerical experiments with various SST conditions in ocean mixed layer utilizing a three-dimensional atmospheric and a simple two-layer ocean coupled model. In the results of their simulations, the sensitivities of the tropical cyclone intensity to the ocean mixed layer depth and the vertical temperature profile in ocean were shown as well as the negative feedback due to decreased SST.

In most of the numerical simulation studies, the typhoon-ocean interaction was investigated with regard to the intensity and track changes of typhoons. Although the substantial SST reduction is well agreed with observed data and previous numerical studies, the ocean response to typhoon that deepens the ocean mixed layer and causes the SST reduction by bringing up the cool thermocline water to mixed layer is not well studied by a coupled model in real-case typhoon.

The objectives of this study is to investigate the dynamic ocean response to typhoon as well as that of typhoon in terms of ocean mixed layer, mixed layer currents and temperature profiles in the wake of typhoon in addition to SST changes by a coupled three-dimensional atmosphere and ocean model. The descriptions of the atmosphere and ocean models are presented in section 2. The model configurations for simulations including the initial conditions are also described in this section. One simulation of an idealized typhoon and a real-case application to Typhoon 0310 named ETAU are described in section 3 and the conclusion and discussion are given in section 4.

4.2 Model description and configuration

4.2.1 Atmosphere model

The atmosphere model in a coupled typhoon-ocean simulation model adopted an three- dimensional nonhydrostatic meso-scale model, MM5, developed at Pennsylvania State University (PSU)-National Center for Atmospheric Research (NCAR). The details of MM5 are referred to Grell et al., (1995). This model is based on nonhydrostatic, compressible form of governing equations in spherical and sigma coordinates with physical processes such as precipitation physics, planetary boundary layer (PBL) processes and atmospheric radiation

processes incorporated by a number of physics parameterizations.

The simulations were performed on three nested domains with the first domain of 27km grid size and subdomains of 9 and 3 km grid size with 23 vertical levels. These domains were nested in one-way with their topographies taken from 5, 2 min and 30 sec resolution global terrain and landuse data. In the model run, four dimensional data assimilation (Grell et al., 1995) was applied to the first and second domains in wind, temperature and mixing ratio field. The physics in the model run such as graupel (reisner 2) moist scheme to all domains, Grell cumulus scheme (Grell 1993) to the first and second domains, MRF planetary boundary layer (Hong and Pan, 1996) to the bigger two domains and high-resolution Blackadar planetary boundary layer (Zhang and Anthes, 1982) to the smallest domain and cloud atmospheric radiation scheme to all domains were applied in the simulation. The initial model field and lateral and surface boundary condition every 6 hrs were imposed from global final analysis (1x1 deg resolution) data provided by National Centers for Environmental Prediction.

4.2.2 Ocean model

As emphasized by Bender and Ginis (2000), the realistic modeling of ocean response need the highly accurate representation of ocean mixed layer in the upper ocean and stratified region below since the ocean response to typhoon is very sensitive to the ocean mixed layer processes. Therefore, the ocean model used in the present study adopted a recently developed ocean general circulation model, MITgcm (Marshall et al., 1997a, 1997b), from Massachusetts Institute of Technology. This model is a nonhydrostatic three-dimensional model based on the incompressible Navier-Stokes equations with Boussinesq approximation formulated in finite volume method. MITgcm can be applied to study from small scale phenomena like local convection in the ocean to large scale processes such as global thermohaline circulation due to the nonhydrostatic capability with full three-dimensional Coriolis effects retained. It also includes many numerical schemes for the advection and diffusion of momentum and tracers. Bottom topography in the ocean and solid boundary abut on coastline are represented by shaved cells (partial steps) with finite volume method formulation (Adcroft et al., 1997) in z coordinate avoiding the horizontal pressure gradient errors over the steep topography in sigma coordinate ocean model. The important vertical mixing processes in ocean mixed layer in typhoon-ocean interaction can be calculated by several alternatives to the second-order turbulent closure model (Mellor and Yamada, 1982). The alternatives are non-local K-profile parameterization (Large et al., 1994), ocean penetrative plume scheme (Paluszkiewicz and Romea, 1997), vertical mixing parameterization by Pacanowski and Philander (1981), and simple eddy kinetic energy model for oceanic vertical mixing by Gaspar et al., (1990).

4.2.3 Experimental set-up

4.2.3.1 One-way experiment

The numerical experiment of idealized typhoon-ocean interaction was conducted to configure the ocean model, thus note that the results from this experiment are similar with the previous studies.

In this experiment, the meteorological forcing by typhoon to ocean were the momentum flux by wind stress and the atmospheric pressure on the sea surface. The wind stress was set to $2.5N/m^2$ equivalent to about 30m/s in wind speed at the radius of maximum wind by Rankine vortex and the atmospheric pressure was given in logarithmic distribution with the minimum pressure of 950hPa for the typhoon center (Fig. 4.2). The initial position of the idealized typhoon was located at 27.5N in latitude and 135.0E in longitude moving to 32.5N in latitude at same longitude with the translation velocity of 10m/s. The ocean response in this experiment was simulated by MITgcm with uniform water depth. To describe the ocean response to typhoon accurately the ocean domain adopted 0.1 ° high horizontal resolution and the vertical levels were divided into 50 levels with constant resolution of 10m to ensure the accurate representation of SST reduction by the vertical mixing process in ocean mixed layer. The initial temperature profile was given by Japan Coastal and Ocean Prediction Experiment (JCOPE) system high-resolution regional model (Miyazawa, 2004), which is based on POM, at the offshore point of Kyi-peninsula, Japan in the archive of the time 7th Aug. 2003 (Fig. 4.1) with horizontal homogeneity. The salinity of initial state was set to 35psu and then kept constant during the simulation and the current field was not considered.
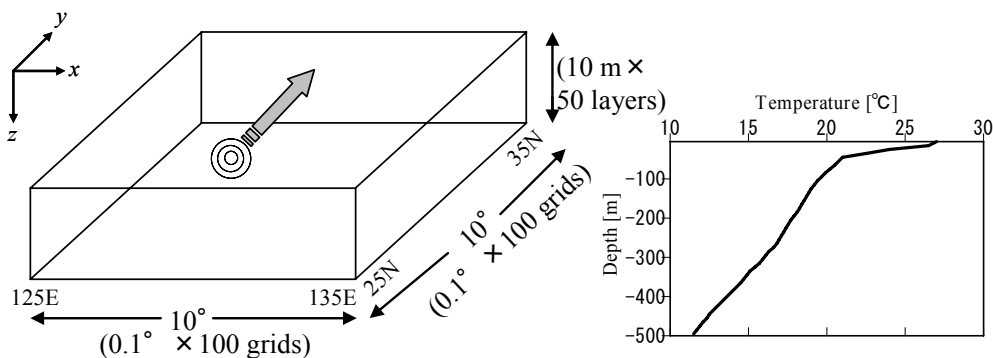
Fig. 4.1 The idealized computation domain of ocean model and initial vertical temperature profile
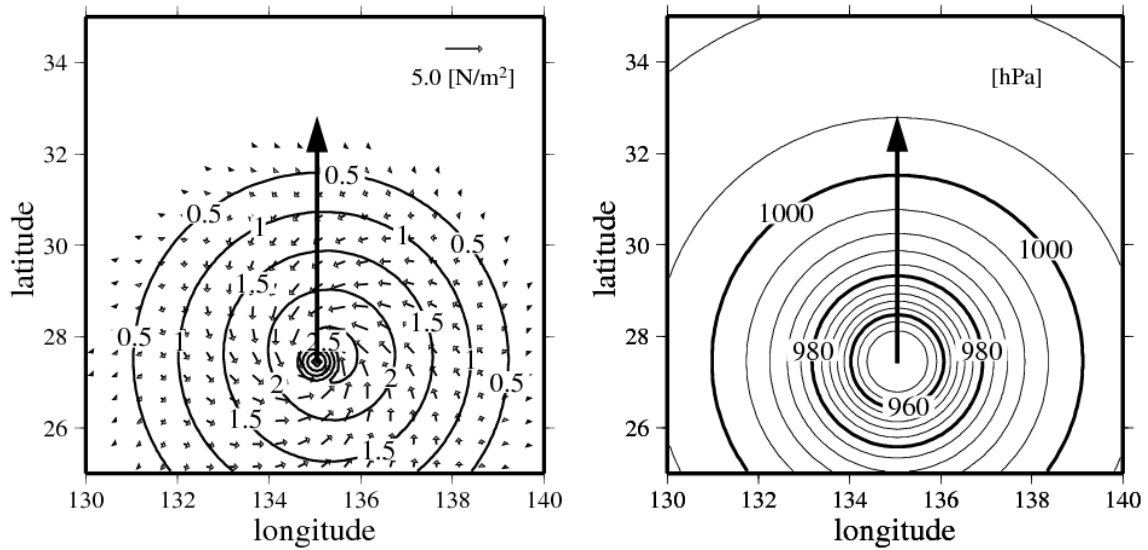
Fig. 4.2 Initial distributions of wind stress and atmospheric pressure

4.2.3.2 Atmosphere-Ocean interaction experiment (Typhoon 0310)

The coupled model for the typhoon-ocean interaction simulation was applied to the real typhoon 0310 (ETAU). Typhoon ETAU was incepted in the middle of north Pacific far east of Philippine islands in 3rd Aug. 2003 and got grown into category 1 in Saffir-Simpson scale at about 18:00 UTC 4th Aug. in 2003. Then Typhoon ETAU became intensified up to category 3 in 7th Aug. and made landfall at Cape Muroto, Kochi prefecture on the night of 8th August. After the landfall, Typhoon ETAU went through Japan islands to north for 3 days causing total 111 casualties and huge damage (Yumoto, 2006). The simulations were performed for 90hrs from 00:00 UTC 5th Aug. to 18:00 UTC 8th Aug. in 2003 until the typhoon made landfall for typhoon-ocean interaction. In this application, three simulations were performed; 1) the MM5 simulation was carried out alone without coupling to ocean, 2) MITgcm run was conducted alone without coupling to atmosphere and 3) the coupling run between MM5 and MITgcm was carried out through the typhoon-ocean interaction. In the MM5-alone case, the initial value of SST used in MITgcm was kept constant in the surface boundary condition during the period of simulation. In the MITgcm run without coupling, the ocean state was described by the density gradient in initial condition and boundary flow at open boundaries without the external forcing through the surface. In the coupling simulation, MITgcm obtained the surface heat flux, momentum flux by wind and sea surface pressure from MM5 integration while MM5 got the SST value from MITgcm integration for multiple common time steps.

The initial and background data for MM5 used in all simulations was provided by NCEP final analysis data (1×1 deg). The bogus scheme (Davis and Low-Nam, 2001) employed

for the improvement of tropical cyclone modeling in MM5 was proven to be effective (Kim and Yamashita, 2005) and applied in all experiments because the coarse resolution initial data can not resolve the real typhoons well.

The bottom topography of ocean model was taken from Global Bathymetric Chart of the Oceans (GEBCO) 1-min gridded global bathymetry covering the same region with the largest domain of atmosphere model from 125E to 144E and from 15N to 36N in the northwestern Pacific Ocean (Fig. 4.5). The domain of ocean model, however, had $1/6°$ horizontal resolution and thus the interpolation was used during the data exchanges for the typhoon-ocean interaction. Since the high resolution in the vertical level is required for the accurate ocean mixed layer processes, the 26 vertical layers were constructed taking into account the numerical stability by limiting the value of $dz(k+1)/dz(k)$ less than 1.4. The vertical mixing processes in ocean model was calculated by the non-local K-profile parameterization scheme and the background horizontal eddy viscosity and vertical eddy diffusivity were set to $10^{-2}m^2/s$ and $10^{-3}m^2/s$, respectively, as known, in general, the vertical eddy diffusivity is much smaller than the horizontal eddy viscosity. The boundary conditions of no-slip bottom (u=0 where u is velocity parallel to bottom) and free surface ($w = \partial\eta/\partial t$ where η is free surface height) were applied in ocean model.

4.2.3.3 Initial and boundary conditions of ocean model

The initial state of ocean is very important in real-case typhoon-ocean interaction that the ocean response to typhoon highly relies on the initial temperature, salinity profiles and current field. There are two ways of obtaining the realistic initial ocean state; 1) from the global ocean general circulation model if available and 2) from necessary spinup of the ocean circulation using available climatological ocean data together with high-resolution SST data.

The JCOPE had been started the ocean weather forecast since Dec. 2001 and recently has achieved the near operational forecasting for the northwestern Pacific with high-resolution ($1/12°$ deg and 45 vertical levels) ocean model being nested in the relatively low-resolution ($1/4°$ deg and 21 vertical levels) utilizing the almost all available data for data assimilation obtained from the satellites, Argo floats and ships. Therefore, in the present simulation of Typhoon ETAU, the near operational forecasting data from the high resolution JCOPE regional ocean model was incorporated for the initial condition of ocean states. The initial temperature, salinity profiles and currents field were interpolated onto the ocean model grid for the 3rd Aug. 2003 and two days spinup had been performed until the start time of coupling process, 00:00 UTC 5th Aug. in 2003. The boundary flows at open boundaries were also taken from the JCOPE model data.

4.3 Model results

4.3.1 One-way experiment of ocean circulation

From this idealized case experiment, the results of the ocean response to typhoon were confirmed with those of previous studies. As the typhoon moved straightforward to north with 10m/s translational speed, the maximum SST reduction after 48hrs from the initial condition was estimated about 4.3℃ at right hand side of typhoon movement in the cold wake (Fig. 4.3(a)) and the currents field in ocean mixed layer is shown in Fig. 4.3(b). The mixed layer currents in the front of typhoon showed the counter-clockwise circulation in nearly symmetric pattern as the wind stress rotated in same direction by typhoon. However, the mixed layer currents in the wake of typhoon depicted strong asymmetric patterns. Following Chang and Anthes (1979) results of numerical simulation, this asymmetric pattern was attributed by the accelerated clockwise inertial flow due to the rotating wind stress in the right side of typhoon wake while the inertial flow got decelerated on the left side. The asymmetry of currents in this idealized experiment was placed slightly left of typhoon track compared to the previous study (Bender at el., 1993) implying the importance of initial currents field since this idealized experiment was forced from zero state of currents. The strong easterly or northeasterly flow such as Kuroshio currents in northwestern Pacific would make significant influence in mixed layer currents in case of typhoon.

The deepening of ocean mixed layer was shown in Fig. 4.3(c) and was a result from the ocean mixed layer currents that induced the local upwelling in the wake of typhoon and the local downwelling in the front and underneath of typhoon by the current velocity shear between the ocean mixed layer and thermocline. The instability due to the velocity shear induced the turbulent mixing bringing the cool water in stratified region below. The result estimated the maximum value of the mixed layer depth deepening about 60m in the right wake, which is due to the right bias of mixed layer currents. Fig. 4.3(d) were the anomaly of temperature profile (contours) estimated in the same way of SST reduction (Fig. 4.3(a)) and the vertical velocity (shaded) after 48hrs of model integration at the cross section at 135.5E. The temperature reduction in the uppermost levels (0-30m in water depth) and the temperature increase underneath of the upper levels (35-70m) were revealed and the upwelling and downwelling processes by the mixed layer currents were confirmed.

In addition to the idealized typhoon, two additional experiments were performed; 1) A slowly moving typhoon with the translational velocity of 2.5m/s was considered having the other experiment conditions exactly same with faster (10m/s) moving typhoon case and 2) Simplified surface heat flux was given over the slowly moving typhoon case, thus the other

experiment conditions were also exactly same. The typhoon was divided into three parts as the typhoon center part (typhoon eye), intermediate part (cloud covered area) and outer part (ambient area). Then the surface heat budget was given synoptically that the downward shortwave radiation for each part was assumed to be 800, -150 and 800 W/m^2, respectively and the sum of sensible and latent heat fluxes and long wave radiation of each part was assumed to be 300, -300 and 500 W/m^2, respectively.

From the slowly moving typhoon case (Fig. 4.4(a)), the maximum SST reduction was estimated about 5.5℃ showing good agreement with previous study (Bender et al., 1993) and the depth of the ocean mixed layer reached about 90m by the strengthened turbulent mixing. In Fig. 4.4(b), after the consideration of surface heat flux, the SST got further decreased about 0.5℃ and totally 6℃ depicting that the turbulent mixing process by the mixed layer currents was much dominant in the reduction SST.
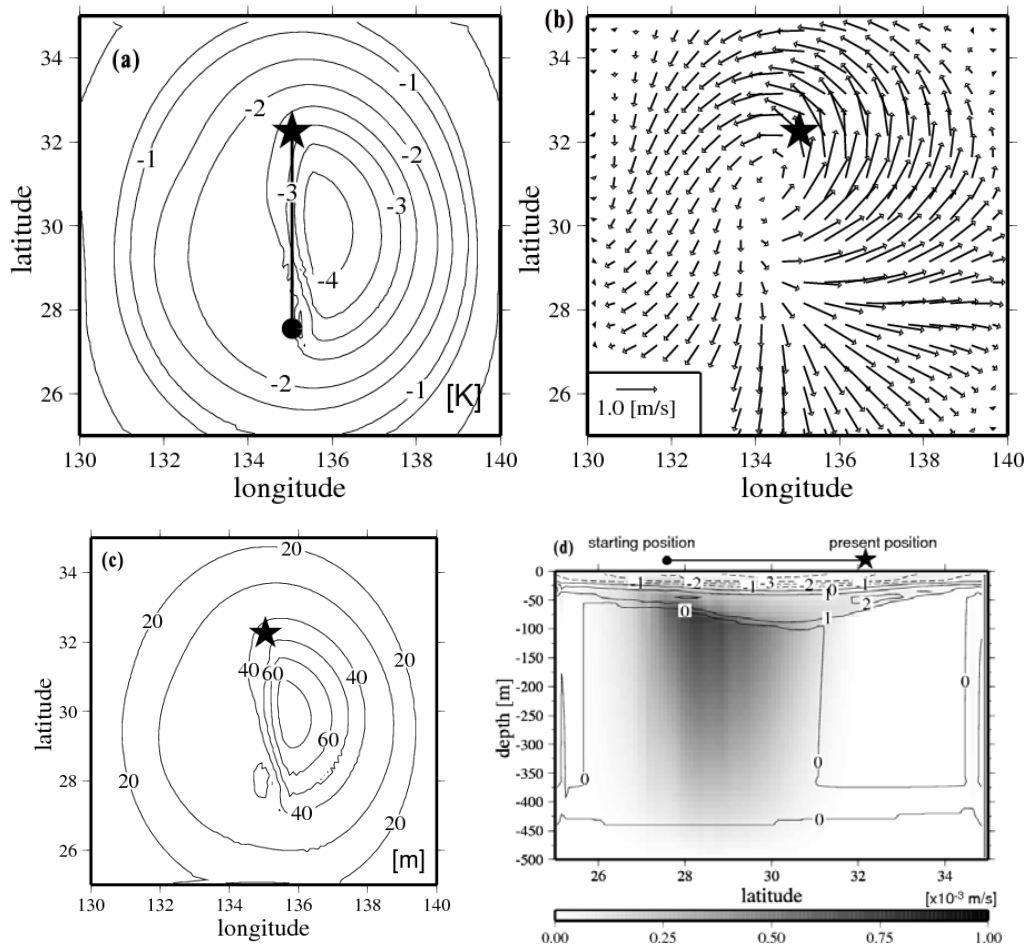
Fig. 4.3 The results of ocean responses after 48hrs model integration: (a) the SST reduction, (b) the ocean mixed layer currents, (c) the ocean mixed layer depth and (d) the temperature profile anomaly (contours) and vertical current velocity (shaded)
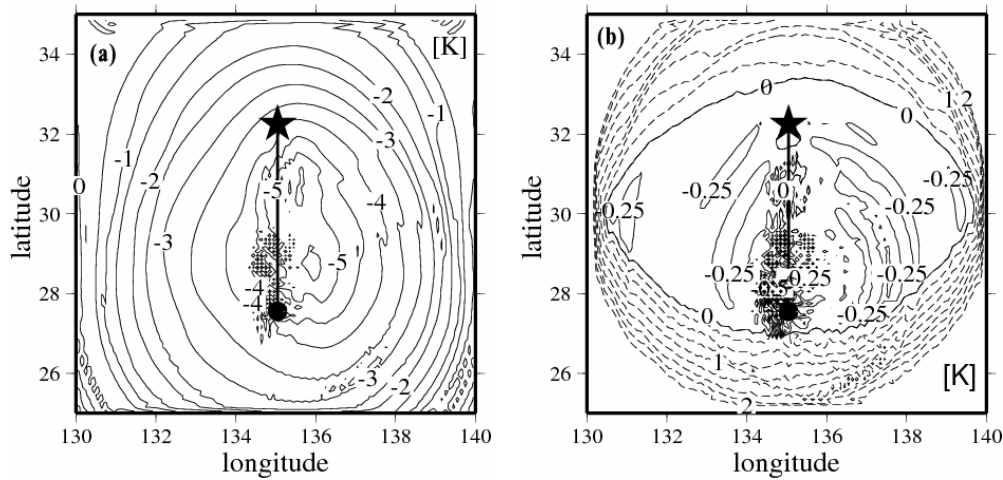
Fig. 4.4 (a) SST reduction in case of slowly moving typhoon and (b) SST reduction in case of surface heat flux forcing compared to the SST of slowly moving typhoon case.

4.3.2 Atmosphere-Ocean interaction for the case of Typhoon 0310 (ETAU)

This section presents the results of typhoon-ocean interaction for Typhoon 0310, ETAU by means of a coupled model. The ocean response to the typhoon and the typhoon response to SST variation are described. Validations of the model in terms of SST cooling in ocean response were made with satellite images of 3-days mean SST with 1/4º resolution from Tropical Rainfall Measuring Mission (TRMM) Microwave Imager (TMI) radiometer and other related previous studies. The influence of Kuroshio Warm Currents (KWC) is given with respect to sea level pressure changes.

4.3.2.1 Ocean response in typhoon-ocean interaction

The ocean responses were studied by investigating the results of MM5-alone (uncoupled) and MITgcm-MM5 coupling run (coupled). The key issue in the ocean response to typhoon is the cooling of SST and the process of SST cooling by the currents in ocean mixed layer.

The ocean mixed layer currents from the coupled run are demonstrated in Fig. 4.6 at 12hrs, 36hrs, 60hrs and 84hrs integration time of simulation. As first identified by Chang and Anthes (1978) and numerically studied by Bender et al. (1993), the asymmetry that results from the acceleration effect on the inertially rotating flow in the right wake of typhoon and the deceleration in the left wake was clearly revealed at 36hrs, 60hrs and 84hrs in coupled run. However, the cyclonic rotational flow in front of typhoon and the decelerated inertially rotating flow in the left wake of typhoon as in idealized experiment (Fig. 4.3(b)) were not clearly

depicted due to the ambient flow.
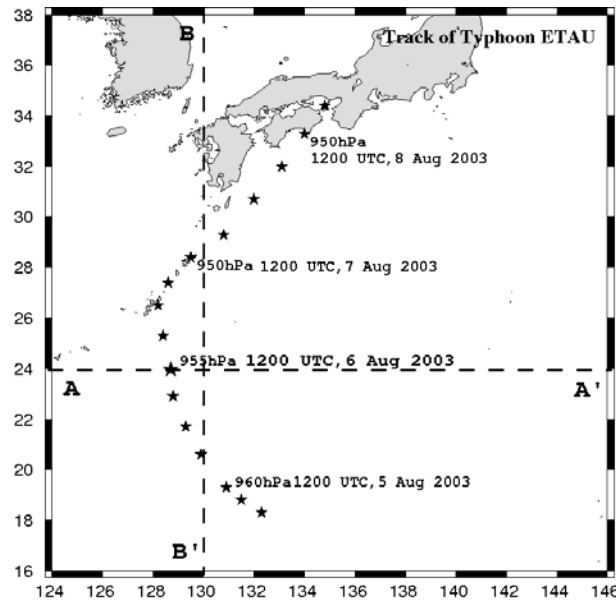
Fig. 4.5 The track of Typhoon 0310 and the computational domain. The information of central pressure and the time of its position are shown every 24 hrs from 12:00 UTC 5th Aug. in 2003.

The divergence of mixed layer currents is important that it causes the vertical motion resulted from the upwelling and downwelling after the passage of typhoon. It is interesting to note that the asymmetric divergent patterns of mixed layer currents were maintained well after the passage of typhoon (Fig. 4.6(c) and (d)) such that they induce the consequential continuous SST cooling behind the typhoon. The prolonged mixed layer currents velocities are larger than those of rather instantaneous mixed currents and both are averagely over 1.5m/s. The mixed layer currents within a day later after the passage of typhoon change their direction from the northeastward to southeastward. Those mixed layer patterns are well agreed with previous numerical study by Bender et al. (1993).

The thermocline layer currents in Fig. 4.7 show quite different characteristics from the mixed layer currents since their generation mechanisms are different. The thermocline layer currents are results of pressure gradients by the mixed layer currents induced vertical motions, whereas the mixed layer currents are the substantial response to surface wind stress. The thermocline layer currents by coupled run were found noticeable in 60hrs and 84hrs by enhanced gradient currents due to prolonged mixed layer current that might enhance the vertical motion but the currents patterns are rather different from the previous numerical studies. It is mainly due to the initial condition of ocean model that the ocean state in the present study was initialized with realistic initial temperature and salinity profiles and velocity field while in

92

previous idealized experiments, the initial currents were given in quiescent or simple easterly flow conditions (Bender et al., 1993; Chan et al., 2001). Due to the different patterns and dynamics of the mixed layer and thermocline currents, the shear instability from the velocity shear is predominant in the base of mixed layer in the wake, which is the primary cause of SST cooling.
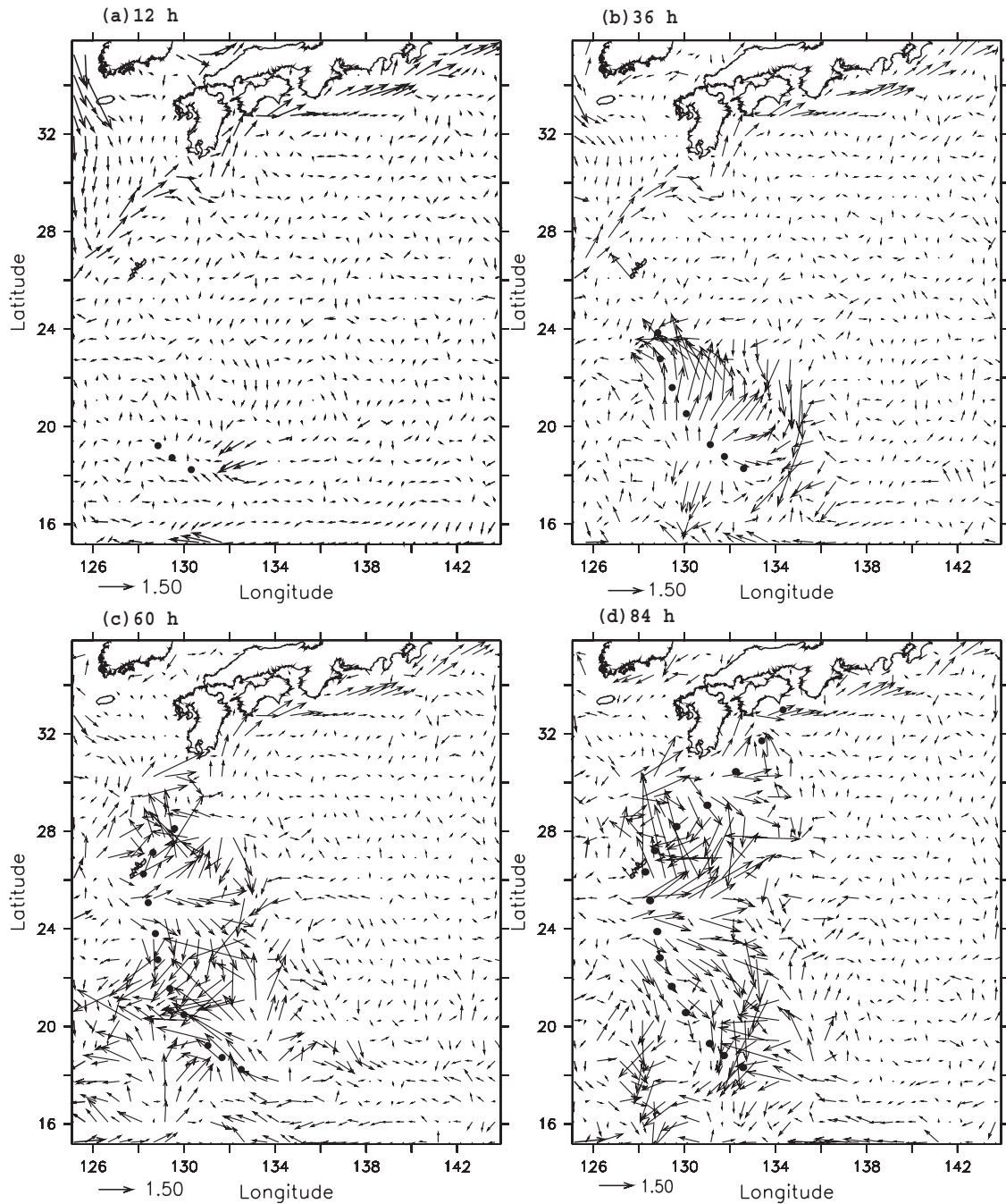
Fig. 4.6 The currents velocities in ocean mixed layer at (a) 12 hrs, (b) 36 hrs, (c) 60 hrs and (d) 84 hrs integration in coupled run. The black circles indicate the typhoon centers from the initial to current position every 6 hrs.
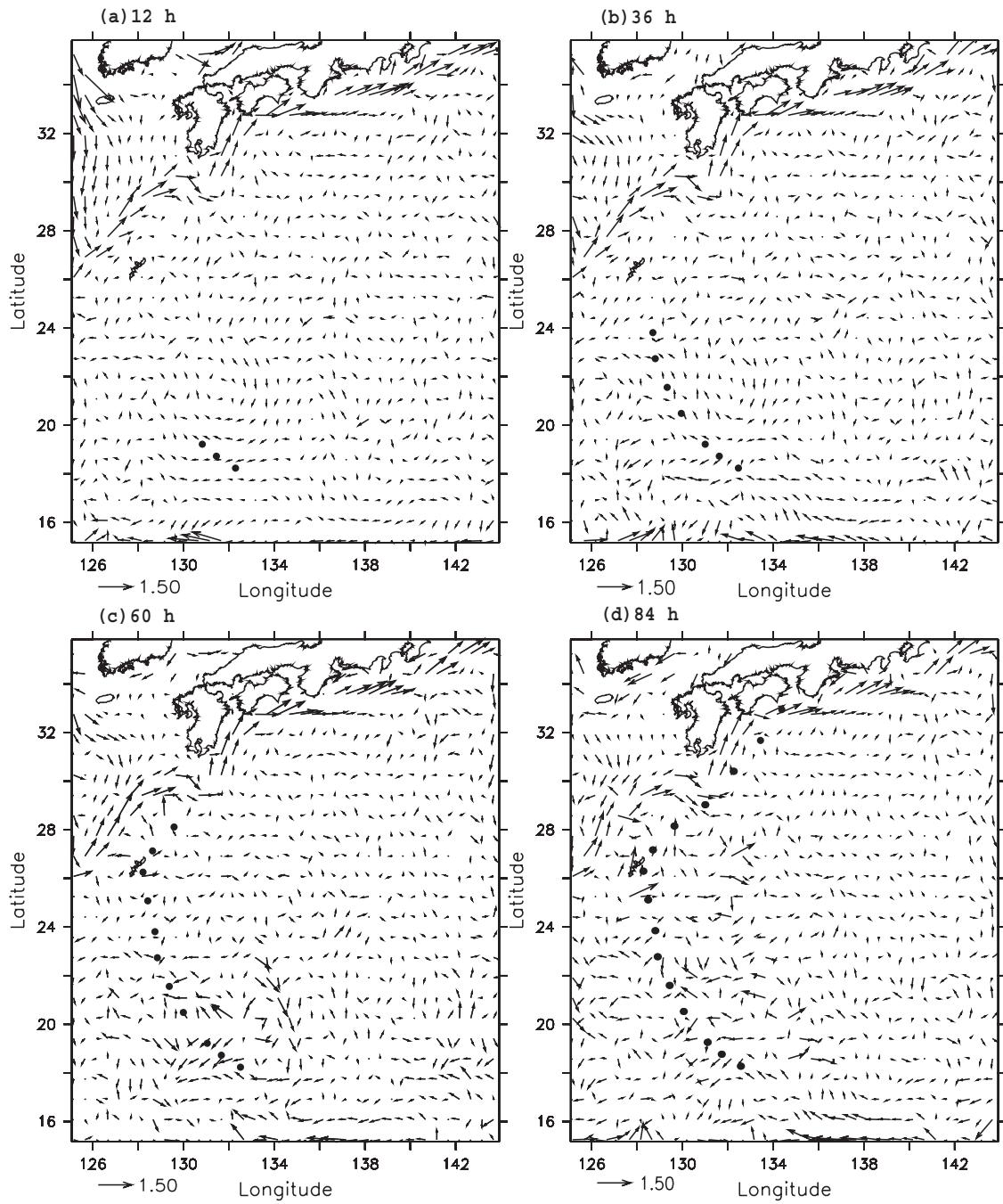
Fig. 4.7 The currents velocities in thermocline layer. Other notations as same as in Fig. 4.6.
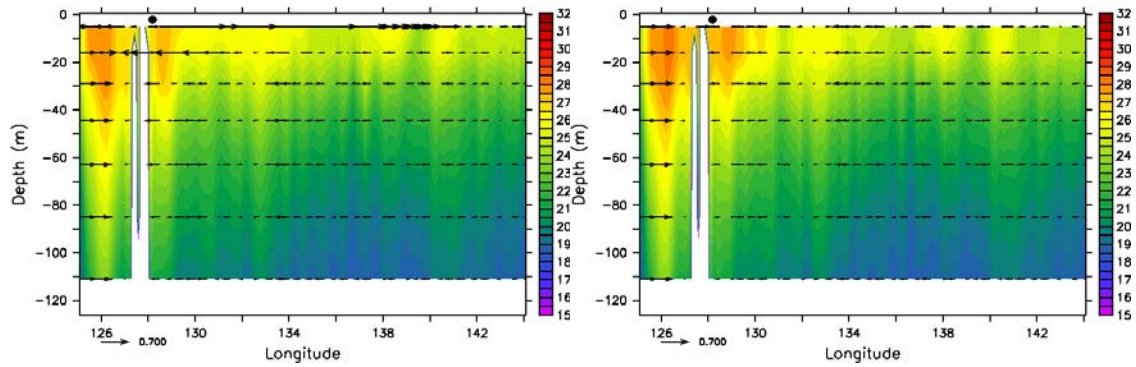
(a) A-A'
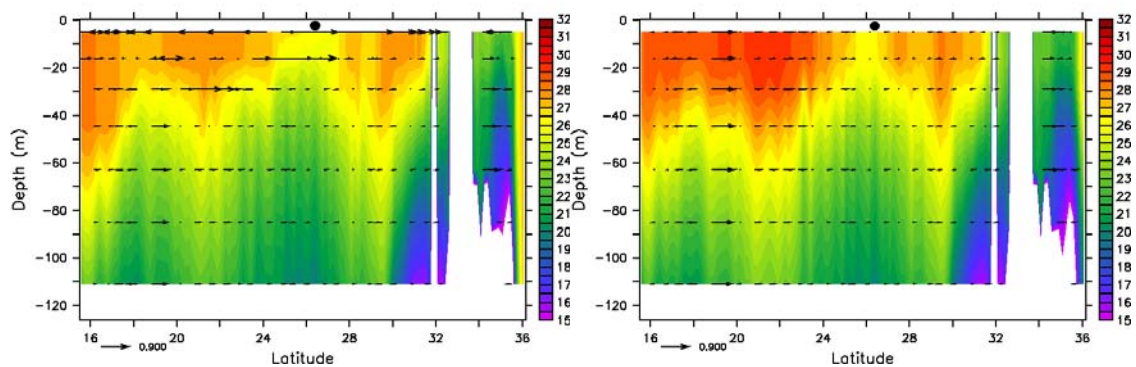
(b)B-B'

Fig. 4.8 Vertical temperature profiles and currents vectors at 48hrs from coupled (left) and uncoupled (right) run at cross section A-A' and B-B' (see Fig. 4.5). The black dots on the surface indicate the current position of typhoon.

In Fig. 4.8, the vertical temperature profiles and currents at A-A' and B-B' cross sections at 48hrs are presented from coupled and uncoupled runs. The velocity shear by currents is clearly shown and the temperature reduction in vertical profile is also found. In the meridional section, the temperature profile decreased in wide region from the underneath of typhoon center to the wake and the considerable decrease of temperature profile due to strong turbulent mixing processes at 48hrs was found at about 22N where the velocity shear was prevailing and strong. The substantial SST cooling by the mentioned turbulent mixing process is shown in Fig. 4.9 and Fig. 4.10. The maximum SST reduction in coupled run at 84 hrs (Fig. 4.9) was about 5 - 6℃ which shows good agreement with the TMI observed SST reduction (Fig. 4.11(d)). The sharp decreases of SST in coupled run were found in the off-east of Okinawa and initial position of typhoon and far-east of Okinawa at around 134E and 27N. The temperature decreases in the east of Okinawa with 5.25℃ and initial position of typhoon with 5℃ are well agreed with the TMI values of about 5℃ and 4.75℃ respectively, while the other point is somewhat overestimated than the observed TMI value. This can be possibly explained by the fact that in the far east of

Okinawa, the horizontal gradient of SST in the initial condition was 3 - 4℃ lager than that of observed TMI values, and thus the large SST reduction was estimated in relatively weak wind stress condition due to the intrusion of cool water in horizontal as well as from the below of mixed layer by velocity shear. In addition, the large horizontal gradient of SST below the KWC was not found in any of the TMI observed images (Figs. 4.10(a) and 4.11(a)). The right biased distribution of SST anomalies with regard to the typhoon movement is related to the mixed layer current patterns in the right wake of typhoon implying again that the cool thermocline water brought by turbulent mixing processes due to the velocity shear is the primary cause of SST reduction. Thus the asymmetry in SST distribution depends on the translational velocity of typhoon and the horizontal wind distribution which determine the ocean's exposure time to wind stress. Therefore the horizontal wind distribution from the coupled run might have differences with real wind field since the movement of typhoon was rather well simulated. It is also interesting to note that the SST reduction in the south of Jechu island, Korea, in the west of Okinawa, Japan, and in the southwest corner boundary in TMI observed values are also clearly depicted in Fig. 4.9.
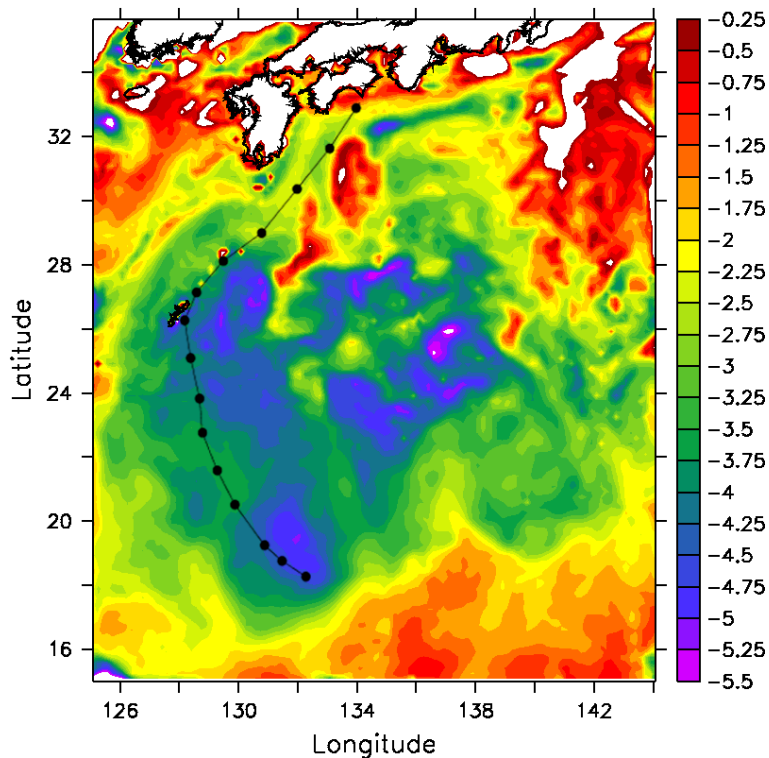
Fig. 4.9 The distribution of SST anomaly at 84hrs in coupled run
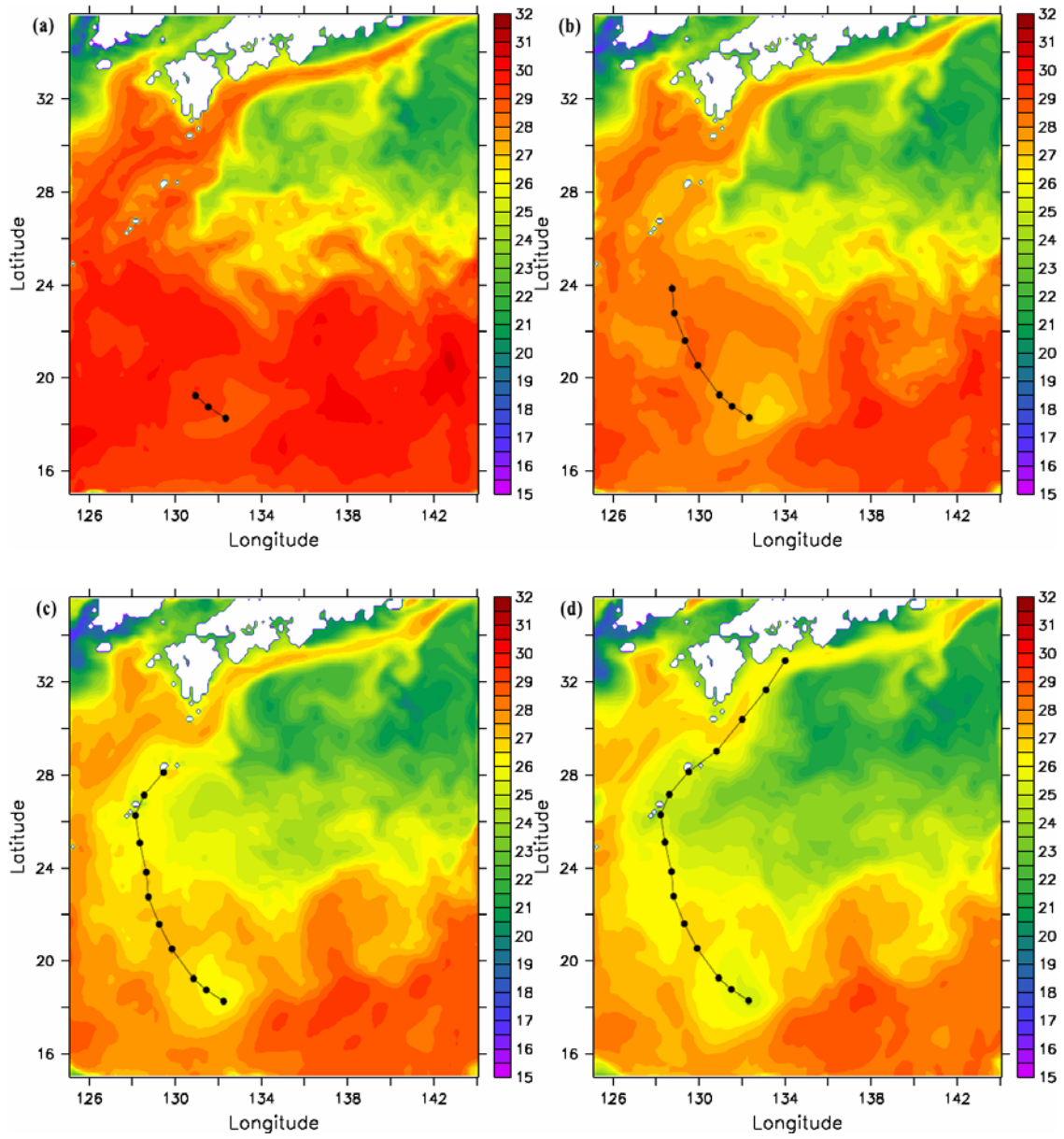
Fig. 4.10 The SST distributions as in Fig. 4.6
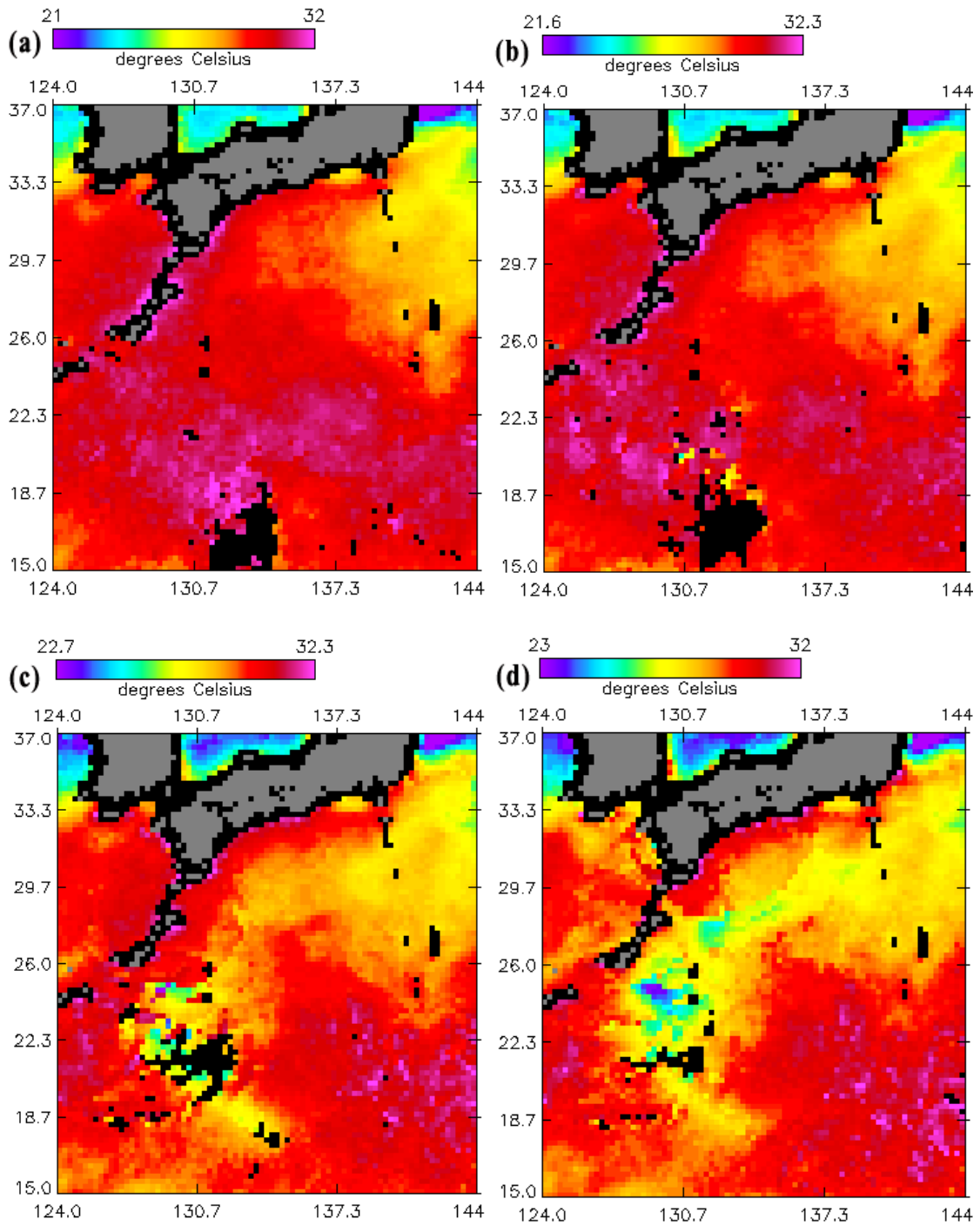
Fig. 4.11 The 3-days mean TMI SST distributions in relative color scale at (a) 5th Aug., (b) 6th Aug., (c) 7th Aug. and (d) 8th Aug. in 2003.

4.3.2.2 Typhoon response in typhoon-ocean interaction

The influence of SST variation on the heat flux, typhoon intensity with respect to the precipitation and equivalent potential temperature by coupling the ocean are presented here comparing the results between the coupled and uncoupled (MM5-alone) run. The uncoupled run was initialized with the same SST distribution that was used for the initial condition of coupled run. However, the initial SST distribution remained constant during the 90hrs simulation in the uncoupled run.

The typhoon response to SST variation was very sensitive and clearly captured in heat flux quantity. The maximum decrease of sensible heat flux was found in the cold wake of typhoon and in the most of region sensible heat flux decreased less than $30W/m^2$. In the meantime, the change of latent heat flux was more sensitive to SST reduction showing the decrease of about $250-300W/m^2$ in the cold wake since the evaporated moisture and consequential latent heat flux got reduced due to SST cooling. The decrease of net heat flux which is the sum of sensible and latent heat flux is clearly seen in the anomaly of net heat flux (Fig. 4.13). As rather expected, the distribution of net heat flux well coincides with the distribution of SST anomaly (Fig. 4.9) showing the maximum reduction of about $350-400W/m^2$ mainly due to the decrease of latent heat flux.
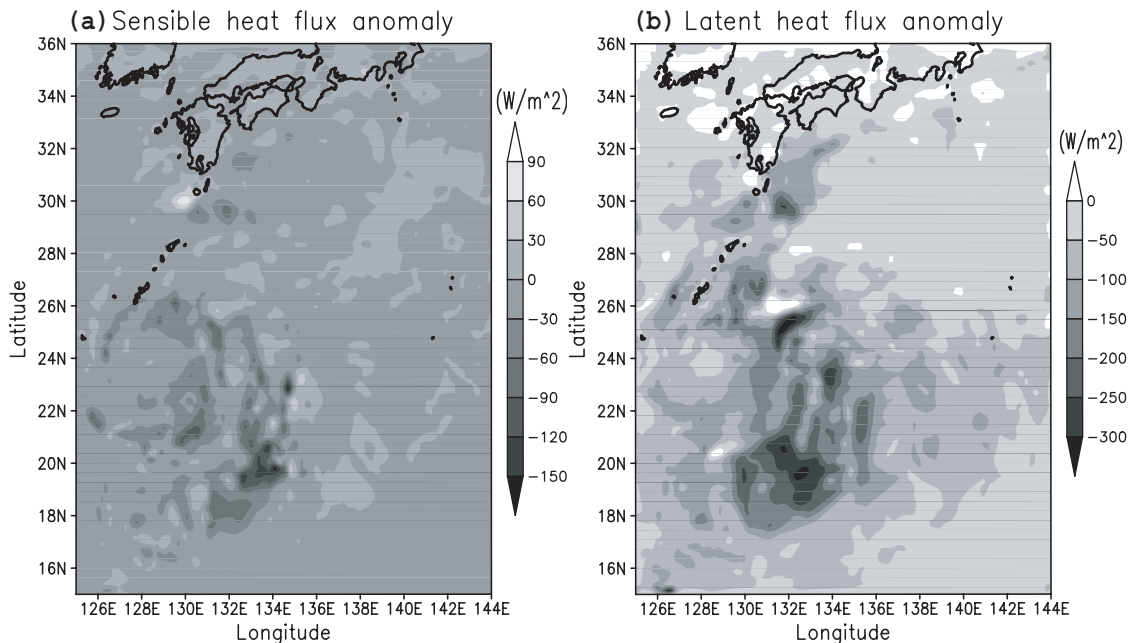
Fig. 4.12 The distribution of (a) sensible heat flux anomaly and (b) latent heat flux anomaly at 36hrs between coupled and uncoupled run (positive values indicate upward direction)
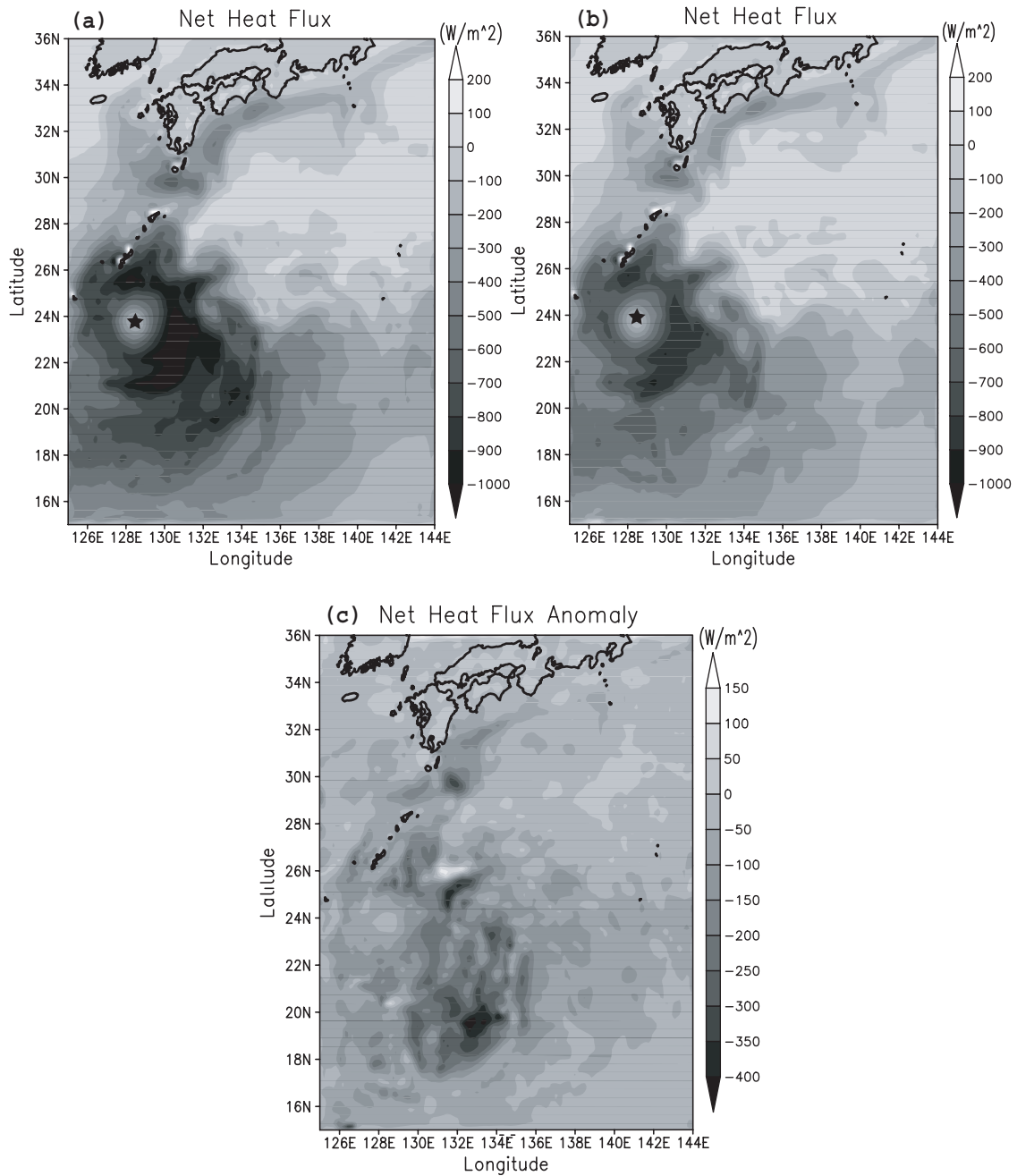
Fig. 4.13 The distribution of net heat flux (sum of sensible and latent heat flux) at 36hrs from (a) uncoupled and (b) coupled run and (c) the anomaly of net heat flux

The changes of net heat flux causes the ensuing changes in other features of typhoon simulation and one of them is the total accumulated precipitation. In Fig. 4.14, total accumulated precipitations integrated for 90hrs from uncoupled and coupled run and its anomaly are presented. The large portions of decrease in coupled run were found in the right wake of typhoon reaching about 5% (300mm) of uncouple values. It should be noted that the

reduction of total precipitation in coupled run after the typhoon moved onto KWC was significant compared to that before approaching to KWC. Its distribution in the right of typhoon track that is the far south of Shikoku, Japan, is quite broad expanding over a couple of 100km compared to the narrow band-shape distribution in the beginning of simulation.
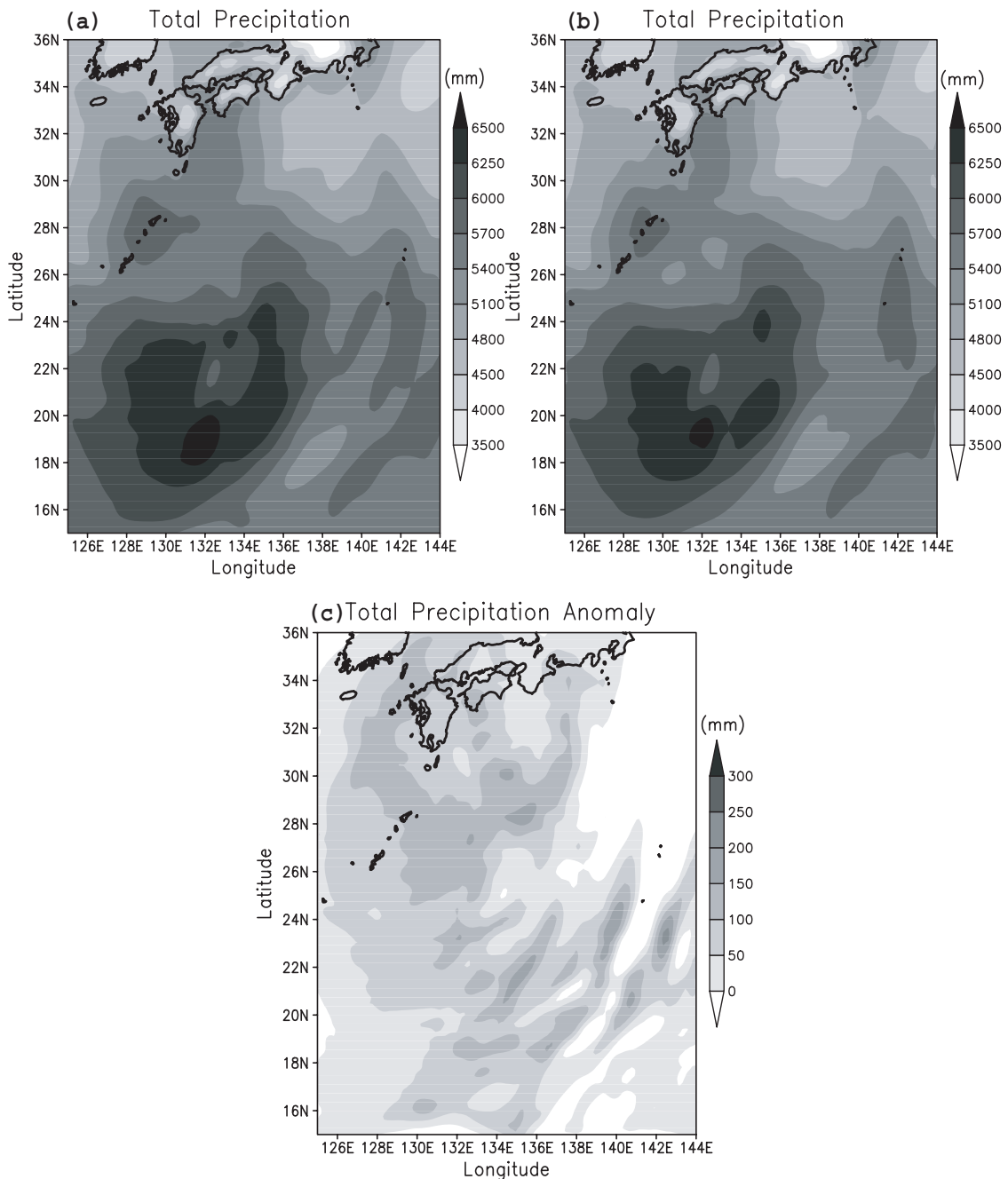
Fig. 4.14 The distribution of total precipitation (total accumulated value from the 90hrs integration) from (a) uncoupled and (b) coupled run and (c) the anomaly of total precipitation
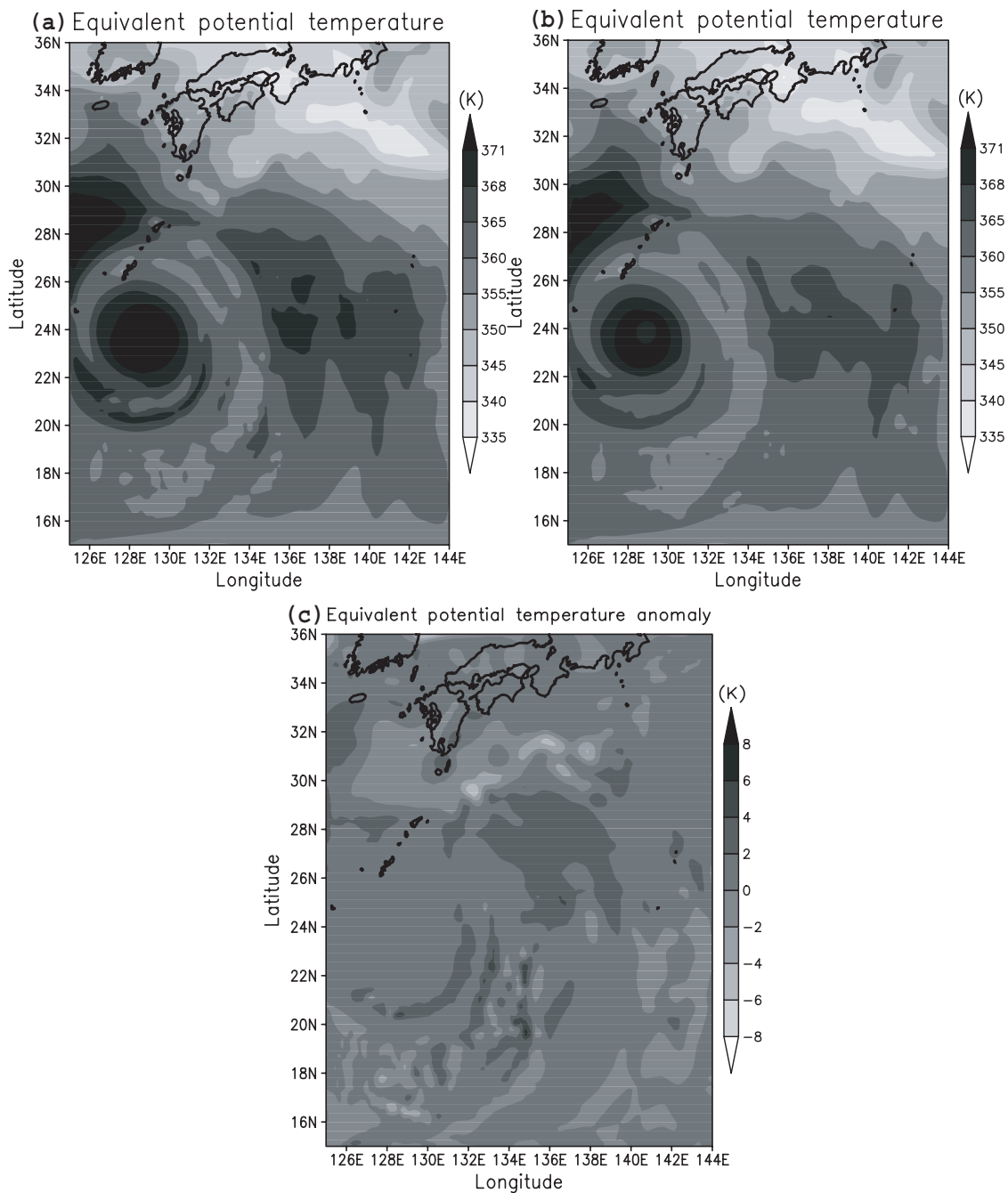
Fig. 4.15 The distribution of equivalent potential temperature at 36hrs from (a) uncoupled and
(b) coupled run and (c) the anomaly of equivalent potential temperature

In addition to the changes in total precipitation, the horizontal structure of equivalent potential temperature (EPT) influenced by the reduction of net heat flux is shown in Fig. 4.15. The EPT which indicates the instability of the air at a given meteorological conditions, depicts the value in lower boundary layer and the maximum decrease of 6°-7° in narrow band shape. Large decrease (2°-4°) in the northeast quadrant of typhoon was found while in the south and

west region of typhoon, the EPT decrease was relatively small.

4.3.2.3 Effects of Kuroshio Warm Current (KWC) on typhoon intensity

In general, the typhoon intensity got decreased due to the negative feedback of the ocean and the typhoon became weak turning into low-level in Hurricane category or tropical storms when it made landfall. Such phenomenon was studied and shown by a series of idealized numerical experiments (Chan et al., 2001). However, the KWC, the high horizontal gradient of SST, has a significant effect that keeps or even enhances the typhoon intensity when the typhoon passes over KWC. The Fig. 4.16 shows the observed minimum sea level pressures of Typhoon ETAU with the simulation result of coupled run. As Typhoon ETAU approached to Okinawa islands, Japan, it became intensified due to the positive feedback and the minimum sea level pressure of 945hPa was appeared at 06:00 UTC 7th Aug. 2003. Then shortly after the minimum surface pressure point, it moved onto KWC at about 12:00 UTC 7th August (see Figs. 4.6 and 4.10). As the maximum SST reduction was found in the right wake of typhoon after the minimum surface pressure occurred (Figs. 4.9 and 4.11), the typhoon, in general, would have weakened because of the negative feedback from ocean to typhoon. However, the Typhoon ETAU remained constant in its intensity in terms of sea level pressure (Fig. 4.16) and maximum wind speed (not presented here), due to the enhanced evaporation and consequential increment of latent heat flux by KWC. Therefore, Typhoon ETAU retained its intensity until it made landfall on the night of 8th Aug. 2003. The TMI SST distribution at 8th August (Fig. 4.11(d)) revealed that the KWC did not show significant decrease in surface temperature while the SST distribution at 84hrs by coupled run (Fig. 4.10(d)) had considerable reduction in KWC surface temperature. This temperature difference of 2-3℃ between them can partially explain the sharp increment of minimum surface pressure in coupled run result after 64hrs integration.
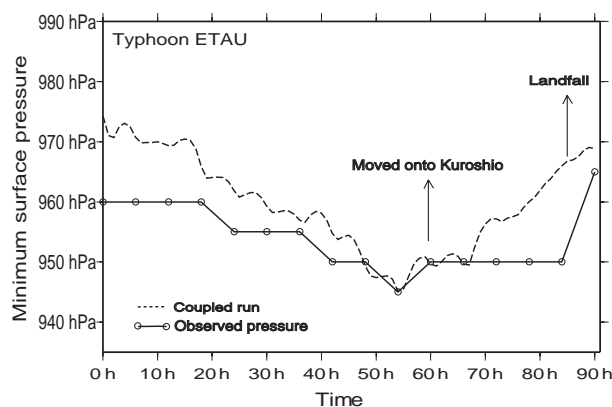
Fig. 4.16 Time series of minimum sea level pressure from the coupled run (dashed line) and observed values (plain line with blank circles that indicate every 6 hrs).

4.4 Conclusions and discussions

A 3D non-hydrostatic ocean model, MITgcm, was employed in this study to investigate the ocean response to the moving typhoon. Two types of numerical experiments were conducted. One is the one-way experiment for ocean circulation in which an idealized Rankin vertex typhoon model was used. The other is atmosphere-ocean interaction experiment in which the atmosphere (MM5) and ocean (MITgcm) coupled model was established to investigate the mechanism of typhoon-ocean interaction in the real ocean including KWC.

From the one-way ocean circulation experiment by idealized typhoon, two followings are confirmed with previous numerical studies.

1) Slow and fast moving typhoon cases: Typhoon moving speeds of 2.5m/s and 10m/s were assumed and no surface heat flux budget was considered. From the slowly moving typhoon case (Fig 4.4(a)), the maximum SST reduction was estimated about 5.5℃ showing good agreement with previous study (Bender et al., 1993) and the depth of the ocean mixed layer reached about 90m by turbulent mixing.

2) Consideration of surface heat flux in slowly moving typhoon case: The typhoon was divided into three parts as the typhoon center (eye area), intermediate part (cloud covered area) and outer part (ambient area). Downward shortwave radiation each part was assumed to be 800, -150 and 800 W/m^2, respectively. Then the sum of sensible and latent heat fluxes and long wave radiation of each part was assumed to be 300, -300 and 500 W/m^2, respectively. The simulated SST reduction was enhanced a bit to be about 6℃. This result indicates that the turbulent mixing effects are dominant in the mechanism of SST reduction by typhoon.

Two-way typhoon-ocean interaction experiments were performed by the atmosphere (MM5)-ocean (MITgcm) coupled model for the real Typhoon 0310 (ETAU) from 00:00 UTC 5th Aug. to 18:00 UTC 8th Aug., 2003. The following three cases were conducted as; 1) the atmosphere-alone (uncoupled) run, 2) the ocean-alone (uncoupled) run and 3) last, the atmosphere-ocean (coupled) run. The important initial condition for ocean state was given from a regional high-resolution (1/12$^°$ deg and 45 vertical levels) ocean reanalysis data by JCOPE for the day of the 3rd Aug. 2003 and two-days spin-up had been performed until the start of coupled run.

1) The ocean responses to Typhoon ETAU in the coupled run were presented in terms of the currents in ocean mixed layer, SST cooling and changes of vertical temperature profile. The asymmetric divergent currents in ocean mixed layer that result from the wind stress acting on the inertially rotating flow were clearly revealed. However, the cyclonic rotational flow in front of typhoon and the decelerated inertially rotating flow in the left wake of typhoon as in idealized

experiments were not clearly depicted due to the ambient flow. Interestingly, the asymmetric divergent patterns of mixed layer currents were maintained well after the passage of typhoon, which were generally over 1.5m/s and induced the consequential continuous SST cooling behind the typhoon. The mixed layer currents about one day after the passage of typhoon changed their direction from the northeastward to southeastward. Unlike the one-way ocean circulation experiments, the ambient flow in the real ocean played an important role that limits the spatial scale of divergent mixed layer currents less than about 300km in its radius.

2) In the vertical temperature profile changes, the SST cooling due to the cool thermocline water brought by the velocity shear between ocean mixed layer currents and thermocline currents was shown. Large SST reductions were simulated in the east of Okinawa with 5.25℃ and in the east of initial position of typhoon with 5℃ and these values were validated with satellite (TRMM Microwave Imager radiometer) observed SST values of about 5℃ and 4.75℃, respectively.

3) In typhoon response in the coupled run, the net heat flux (sensible plus latent) was reduced about 350-400W/m^2 in the cold wake of typhoon and its distribution well coincided with the distribution of SST anomaly mainly due to the decrease of latent heat flux. Accompanied by the decrease of net heat flux, the total precipitation and the equivalent potential temperature were reduced with 5% (about 300mm) and 6°-7° in maximum locations, respectively.

4) The influence of KWC which produces large horizontal SST gradient was evaluated with respect to typhoon intensity when Typhoon 0310 moved onto KWC. After typhoon moved on KWC until it made landfall, it was found that the typhoon maintained its intensity for about one day due to the constant heat supply from KWC. In the coupled run, however, the influence of KWC just before the landfall was not able to be captured due to the lager decrease of SST (2-3℃) than the observed value. It is partially explained that the horizontal mixing processes might also important in SST cooling in high horizontal SST gradient condition of ocean. The boundary condition with 2-days temporal resolution of JCOPE data is not sufficient to supply the persistent heat budget from KWC.

Initial condition is very significant for ocean computation. JCOPE data used for the initial ocean states in the present study rather underestimated in SST in wide region below the KWC such that resulted in significant changes in typhoon intensity. Although surface waves may play crucial roles in air-sea interaction such as heat flux exchanges, SST changes, momentum flux transfer, etc, the surface wave is not taken into account in this coupling model. It will be strongly recommended that surface wave effects on typhoon-ocean interaction should be investigated in the future study.

References

Adcroft, A., C. Hill, and J. Marshall, (1997): Representation of topography by shaved cells in a height coordinate ocean model. *Mon. Wea. Rev.*, **125(9)**, 2293-2315.

Bender, M. A., I. Ginis, and Y. Kurihara, (1993): Numerical simulations of tropical cyclone-ocean interaction with a high-resolution coupled model. *J. Geophys. Res.*, **98(D12)**, 23245-23263.

Bender, M. A. and I. Ginis, (2000): Real-case simulations of Hurricane-Ocean interaction using a high-resolution coupled model: Effects on hurricane intensity. *Mon. Wea. Rev.*, **128(4)**, 917-946.

Chan, J. C. L., Y. Duan and L. K. Shay, (2001): Tropical Cyclone Intensity Change from a Simple Ocean–Atmosphere Coupled Model. *J. Atmos. Sci.*, **58(2),** 154-172.

Chang, S. W., (1979): The response of an axisymmetric model tropical cyclone to local variations of sea surface temperature. *Mon. Wea. Rev.*, **107(6)**, 662-666.

Chang, S. W. and R. A. Anthes, (1979): The mutual response of the tropical cyclone and the ocean. *J. Phys. Oceanogr.*, **9(1)**, 128-135.

Davis, C. A. and S. Low-Nam, (2001): The NCAR-AFWA Tropical Cyclone Bogussing Scheme. Air Force Weather Agency report, NCAR, Boulder, Colorado

Emanuel, K. A., (1986): An air-sea interaction theory for tropical cyclones. Part I : Steady-state maintenance. *J. Atmos. Sci.*, **43(6)**, 585-604.

Gaspar, P., Y. Grégoris, and J.-M. Lefevre, (1990): A simple eddy kinetic energy model for simulations of the oceanic vertical mixing: Tests at Station Papa and long-term upper ocean study site. *J. Geophys. Res.*, **95(C9)**, 16179-16193.

Grell, G. A., (1993): Prognostic evaluation of assumptions used by cumulus parameterizations. *Mon. Wea. Rev.*, **121(3)**, 764-787.

Grell, G. A., J. Dudhia, and D. R. Stauffer, (1995): A description of the fifth-generation Penn

State/NCAR mesoscale model (MM5). NCAR Technical Note, NCAR/TN-398 + STR.

Hodur, R. M., (1997): The Naval Research Laboratory's coupled ocean/atmosphere mesoscale prediction system (COAMPS). *Mon. Wea. Rev.*, **125(7)**, 1414-1430.

Hong, S-Y. and H.-L. Pan, (1996): Nonlocal boundary layer vertical diffusion in a medium-range forecast model. *Mon. Wea. Rev.*, **124(10)**, 2322-2339

Kim, K.O., H.S. Lee, and T. Yamashita, (2005): Winter Huge Wave Simulation in Japan Sea by MM5 and WW3 Coupled Model Using Depression Bogussing. *Annual J. Coastal Eng.*, JACE, **52(2)**, 176-180 (in Japanese).

Large, W., J. McWilliams, and S. Doney, (1994): Oceanic vertical mixing: A review and a model with nonlocal boundary layer parameterization. *Rev. Geophys.*, **32(4)**, 363-404.

Marshall, J., C. Hill, L. Perelman, and A. Adcroft, (1997a): Hydrostatic, quasi-hydrostatic, and nonhydrostatic ocean modeling. *J. Geophys. Res.*, **102(C3)**, 5733-5752.

Marshall, J., A. Adcroft, C. Hill, L. Perelman, and C. Heisey, (1997b): A finite-volume, incompressible Navier Stokes model for studies of the ocean on parallel computers. *J. Geophys. Res.*, **102(C3)**, 5753-5766.

Mellor, G. L. and T. Yamada, (1982): Development of a turbulence closure models for geophysical fluid problems. *Rev. Geophys. Space Phys.*, **20**, 851-875.

Miyazawa, Y, (2004): The JCOPE ocean forecast system. *Frontier Newsletter*, **24**, 2-3.

Monaldo, F. M., T. D. Sikora, S. M. Babin, and R. E. Sterner, (1997): Satellite imagery of sea surface temperature cooling in the wake of hurricane Edouard (1996). *Mon. Wea. Rev.*, **125(10)**, 2716-2721.

Nelson, N. B., (1996): The wake of hurricane Felix. *Int. J. Remote Sens.*, **17**, 2893-2895.

Paluszkiewicz, T. and R. D. Romea, (1997): A one-dimensional model for the parameterization of deep convection in the ocean. *Dyn. Atmos. Oceans*, **26**, 95-130.

Philander, S. G. H., and R. C. Pacanowski, (1981): Response of equatorial oceans to periodic forcing. *J. Geophys. Res.,* **86(C3)**, 1903-1916.

Teague, W. J., M. J. Carron, and P. J. Hogan, (1990): A comparison between the generalized digital environmental model and Levitus climatologies. *J. Geophys. Res.*, **95(C5)**, 7167-7183.

Tuleya, R. E. and Y. Kurihara, (1982): A note on the sea surface temperature sensitivity of a numerical model of tropical cyclone genesis. *Mon. Wea. Rev.*, **110(12)**, 2063-2069.

Wendland, W. M., (1977): Tropical storm frequencies related to sea surface temperatures. *J. Appl. Meteor.*, **16**, 477-481.

Wentz, F. J., C. Gentemann**,** D. Smith, and D. Chelton, (2000): Satellite measurements of sea surface temperature through clouds. *Science*, **288(5467)**, 847-850.

Yumoto, M., (2006): Typhoon 0310 ETAU and the damage. National Research Institute for Earth Science and Disaster Prevention report, **39**, 7-16 (in Japanese).

Zhang, D. and Anthes, R. A., (1982): A High-Resolution Model of the Planetary Boundary Layer—Sensitivity Tests and Comparisons with SESAME-79 Data. *J. Appl. Meteor.*, **21(11)**, 1594–1609.

Chapter 5

Application to Dam Lake Hydrodynamics

In this study, 3D non-hydrostatic circulation model (MITgcm) has been applied to study the thermal structure, its evolution and water circulation in Yachiyo Lake, Hiroshima, Japan. The simulations were conducted for one month in July 2006 coupling with the meteorological simulation by MM5. Exchanging variables in the coupling system are the wind stress, atmospheric pressure at surface and heat flux transfer through the lake surface. Vertical mixing in the lake was calculated by the non-local K-profile parameterization method. The one month integration of numerical simulation revealed that the thermal structure in the lake and its evolution both in space and time shows very good agreements with the observation. The internal gravity waves which are crucial for the mixing in the stratified lake in summertime are depicted by the vertical fluctuation of isotherms. Non-dimensional gradient Richardson number indicates that the Yachiyo Lake forms strong thermal stratification in summer.

5.1 Introduction

The dynamics of surface mixed-layer and circulation in lakes are well documented in many previous studies by means of field measurements and numerical experiments. The study of vertical mixing by turbulence in mixed-layer and circulation by meteorological conditions are numerically studied by one-dimensional mixed-layer models and three-dimensional circulation models from shallow and small to deep and large scale of lakes at various locations in latitude with different boundary conditions at the bottom and surface of lakes. In the one-dimensional models, the simulations are performed based on assumption that the vertical scale of the heat and momentum is locally much greater than the horizontal scale (Herb and Stefan, 2005; Spigel et al., 1986) regarding the modeling results as a horizontally averaged vertical structure of a study lake (Kantha and Freeth, 1996). Spigel et al. (1986) applied their one-dimensional mixed-layer model to study on diurnal mixed-layer changes with observed meteorological input. With limitations of model which are one-dimensional and mixed-layer model excluding the hypolimnion circulation below the thermocline in vertical thermal stratification, the results

shows good agreements with the observed diurnal mixed-layer data. In the study of shallow lake with macrophytes (vascular plants) bed boundary condition, Herb and Stefan (2005) applied one-dimensional model with a first-order turbulence closure model to Otter Lake, the United States, to simulate the vertical mixing in the mixed-layer and the effects of macrophytes on the vertical mixing and thermal stratification. With the observed meteorological forcing, the model showed reasonable results under weak wind condition and effects of macrophytes of which they enhance the thermal stratification in daytime and reduce the thickness of mixed-layer and wind mixing. In the study of the 1986 disaster in Lake Nyos, Cameroon in West Africa which killed approximately 1700 persons and huge livestock, Kantha and Freeth (1996) applied one-dimensional model based on Reynolds averaged governing equations with the second-order closure of turbulence (Kantha and Clayson, 1994) to study the cause of disaster and estimate the possibility of prediction of such a disaster in the future. It is thought to be the gas released out of the CO_2-rich water from the lake that triggered the catastrophic disaster. From the numerical simulations, it is found that the most feasible trigger of the disaster is an anomalous surface event such as a storm with the accompanied surface cooling which consequently results in mixed-layer deepening and then, convective plumes bringing the CO_2-rich bottom water to the surface. Due to the absence of observation for meteorological conditions such as wind stress, downward radiation and heat flux, reasonable approximations were made to get the seasonal structure and evolution of lake more realistic.

A three-dimensional numerical model based on non-hydrostatic Boussinesq equations was applied by Walker and Watts (1995) to investigate the deep convection in temperate lakes. The vertical mixing by the convective plumes that is believed to be triggered by external forcing such as storm surge and internal waves was studied numerically. However the model is not externally forced by the storm surge events or internal wave motions but derived by statically unstable temperature profile initial condition.

Williams (2001) applied a high-resolution three-dimensional model based on hydrostatic primitive equations in sigma coordinates to study the circulation and vertical mixing of antarctic subglacial Lake Vostok. In the lack of topographic data of lake, the numerical model was performed with constant and simple representation of water depth deduced from the volume estimate. In this study, the heat flux between the ice sheet and water surface of lake and geothermal heat flux at the lake bottom were imposed as the surface and bottom boundary conditions, respectively.

In studies of Lake Kinneret in Israel, the effects of the spatial and temporal variation in meteorological forcing such as wind and heat flux on basin-scale internal wave and mean currents was shown by Laval et al. (2003) with 3D hydrostatic model and Antenucci et al.(2000) showed the effects of daily sea breeze on the basin-scale internal Kelvin and Poincare wave. Pan

et al. (2002) also studied the summertime circulation and thermal structure of the Lake Kinneret with 3D hydrostatic lake model being derived by the calculated wind stress and heat flux with non-hydrostatic atmospheric model. In their study, they found the wind forcing dominates the lake circulation, surface currents and thermocline displacement assuming the constant long wave radiation off the lake surface and used simple bulk formulae for the short-wave radiation, which is differ from our present study.

The objective of this study is to investigate the circulation and vertical mixing of Yachiyo Lake in response to the meteorological input with a non-hydrostatic three-dimensional model and establish the lake modeling system for further accurate simulation with observed external forcing and boundary condition. We also experienced the lack of observed data for meteorological conditions of Yachiyo Lake in the study period of one month, July 2006. However instead of making approximation from the nearest available observation station (Kantha and Freeth, 2006), the meteorological conditions used were provided by simulating with non-hydrostatic atmospheric meso-scale model (Dudhia, 1993; Grell et al., 1995). This one-way coupling of two models would be extended to two-way coupling system for the study of regional climate exploring the recent high performance computing benefits.
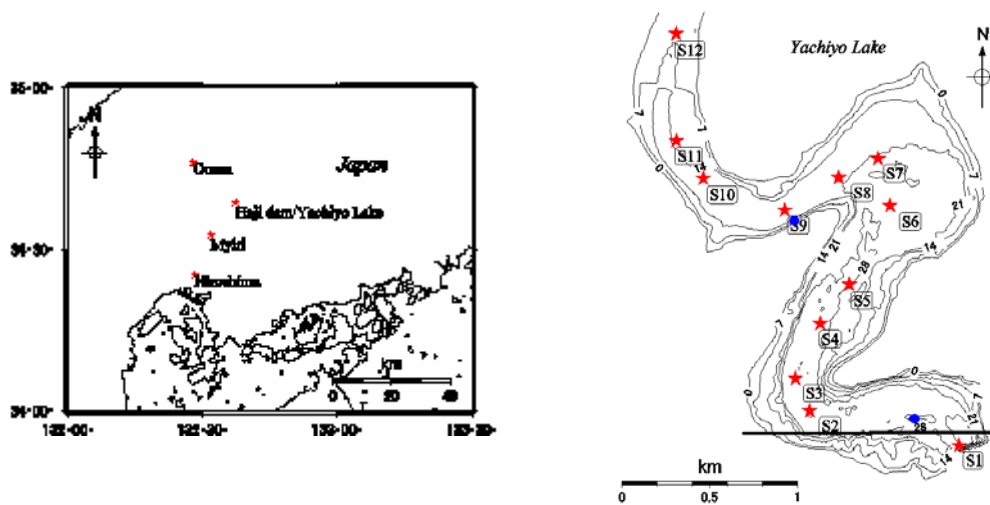
Fig. 5.1 The Haji dam and Yachiyo Lake (left) and the bathymetry of Yachiyo Lake (right). The nearest meteorological observation stations of Japan Meteorological Agency, Ooasa and Myiri (left). The lake observation points in Oct. 2005 are shown with stars and the lake monitoring stations are with circles in the right figure.

5.2 Study site : Yachiyo Lake and Haji Dam

Haji dam and the dam-made Yahciyo Lake are located at 132˚37´14.55˝E in longitude

and 34°38´37.23″N in latitude in the center of Hiroshima Prefecture, Japan. It was completed of its construction in March, 1974 and started to operate as a multi-purpose dam conducting flood control, water utilization and generation of electricity since then. It is the very important source of drinking water for Hiroshima city about 25km southwest of Haji dam. The statistics and location of Haji dam and Yachiyo Lake are shown in Table 5.1 and Fig. 5.1, respectively. The Yachiyo Lake is formed in a meandering valley between two neighboring mountains.

Since the Haji dam was completed, it was foreseeable that the water quality problem and its countermeasure would be the main concerns as experienced in many precedents. Yachiyo Lake recently suffers from the severe eutrophication induced by inflowing redandunt chemical nutrients, nitrogen and phosphorous, loading from its watershed. Consequently the prolonged algae bloom over the water near the dam wall and edge of water body close to side-land is found. Some researches have been undergoing to analyze the pollutant sources and build the countermeasures to them in the watershed in which the Yachiyo Lake is involved.

Table 5.1 Haji dam statistics

Dam statistics			
Dam height	50.0 m	Yachiyo Lake area	2.80 km^2
Dam top length	300.0 m	Purpose of the Dam	Flood control, water utilization and generation of electricity.
Dam volume	210,000 m^3	Electric enterprise	The Chugoku Electric Power Co. Ltd.
Entire lake capacity	47,300,000 m^3	Power plant name (Approval output)	Kabe power plant (38,000kW)
Effective storage	41,100,000 m^3	Starting/completion construction year	1966 /1974 year
Watershed area	307.5 km^2		
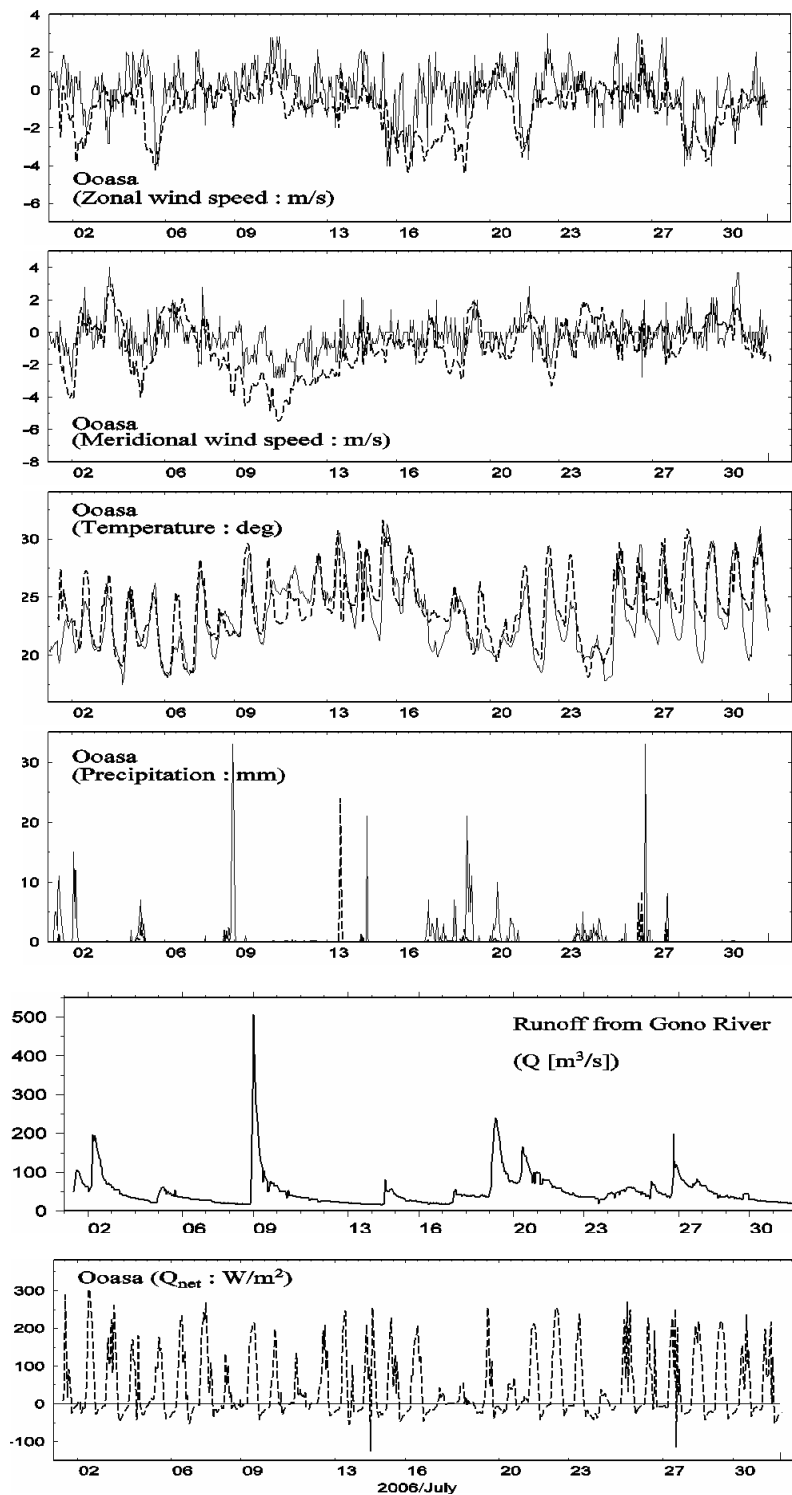
Fig. 5.2 Meteorological conditions used for this study. The observed (plain line) and calculated (dotted line) data of zonal and meridional wind speed at 10m above the surface, the temperature at 2m above the surface, the precipitation and the net heat flux at Ooasa station. Heat flux is not observed.

5.2.1 Observations

There are five monitoring stations being operated by the dam administration office. Among them, two stations (blue circle points in Fig. 5.1) are located within the Yachiyo Lake and model domain, two are in the upstream river, Gono Gawa, and the last one is just beside dam wall. The two stations inside lake provide hourly monitoring data including the temperature profile, conductivity, concentration of chemical nutrients, dissolved oxygen, biological oxygen demand, and so on. There also have been irregular observations mainly in the upstream rivers within the Haji Dam watershed and rarely in the lake. The twelve star points in Fig. 5.1 show the irregular observations conducted in 10 Nov. 2005. The bathymetry of the lake was firstly measured in Oct. 2006 and there is no previous research on the dynamics of the lake by numerical experiments. In the middle of the lake between the St.1 and St.3, eight aeration instruments were established and being activated mainly in summertime. In this study, the influence of the aeration instruments is not taken into account showing that the effect of these instruments on thermal structure and dynamics of the lake can be inversely evaluated from the simulation results. During the study period of one month, July 2006, the observation data at the fixed station near St.9 had failed observing in the intermittent short periods from 04:00 JST to 19:00 JST 4 July, from 11:00 JST to 19:00 JST 18 July, and from 11:00 JST to 12:00 JST 25 July.

5.3 Meteorological data

Although the sound and accurate meteorological data from observation is most recommended, it is rare to have such observed data for the study site and the Yachiyo Lake is not the exception. In this study the important meteorological forcing that derives the thermal structure and its evolution of the lake was reproduced by non-hydrostatic atmospheric meso-scale model, MM5, instead of making approximations from nearby stations. The simulation of meso-scale model was carried out for one month from 09:00 UTC 1 to 18:00 UTC 31 July 2006 with frequent rainy conditions within the period as shown in Fig. 5.2.

The simulation was performed on four domains with the first domain of 27km grid size and subdomains of 9, 3, and 1 km grid size. These domains were set on one-way nesting with their topographies taken from 5, 2 min and 30 sec resolution global terrain and landuse data. In the model run, four dimensional data assimilation (Grell et al., 1995) was applied to the first and second domains in wind, temperature and mixing ratio field. The physics in the model run such as graupel (reisner 2) moist scheme to all domains, Grell cumulus scheme (Grell 1993)

to the first and second domains, MRF planetary boundary layer (Hong and Pan, 1996) to the bigger two domains and high-resolution Blackadar planetary boundary layer (Zhang and Anthes, 1982) to the smaller two domains and cloud atmospheric radiation scheme to all domains were applied in the run. The initial model field and lateral and surface boundary condition every 6 hrs were imposed from global final analysis (1x1 deg resolution) data provided by National Centers for Environmental Prediction.

The wind speed at 10m above the surface, surface atmospheric pressure, radiation and heat flux from the MM5 run were considered as meteorological conditions for modeling of Yachiyo Lake. The observed data at nearby station, Ooasa (Fig. 5.1), operated by Japan Meteorological Agency (JMA) was used for the validation of meteorological data by MM5 run. As shown in Fig. 5.2 the overall wind conditions are weak and calm over the simulation period and the calculated zonal and meridional wind shows general accordance with the observation in pattern and magnitude. However there are some overestimations found around 10 July in calculated meridional wind. The calculated precipitations by the atmospheric modeling reproduce the rainfall events well but the quantitative amount of rainfall has rather big difference and need to be improved. In this study, the freshwater fluxes that influence the salinity and surface water level, which are the evaporation off the surface and the precipitation are not considered for the external input. The momentum flux which is the wind stress from wind 10m high was calculated from the bulk formulae by Large and Pond (1981). The net heat flux transfer at the lake surface was calculated by

$$Q_{net} = Q_{swd} - (Q_{lhf} + Q_{shf} + Q_r) \qquad (5.1)$$

where Q_{swd} is downward shor-wave solar radiation, Q_{lhf} is evaporative latent heat flux, Q_{shf} is sensible heat flux and Q_r is back radiation from surface.

5.4 Computational method

5.4.1 Water circulation model

MITgcm (Marshall et al., 1997a, 1997b) used for three-dimensional modeling of lake integrates the incompressible Navier-Stokes equations with Boussinesq approximation that the density perturbation, ρ', is much small as compared to the reference value, ρ_r. The equations in a rotating system (Legg and Adcroft, 2003) solved in MITgcm are re-written here following the section (2.5.2);

$$\frac{\partial \mathbf{u}}{\partial t} + \mathbf{u} \cdot \nabla \mathbf{u} + f\hat{\mathbf{k}} \times \mathbf{u} = -\frac{1}{\rho_r}\nabla p + b\hat{\mathbf{k}} + v_h\left(\frac{\partial^2}{\partial x^2} + \frac{\partial^2}{\partial y^2}\right)\mathbf{u} + v_v\frac{\partial^2}{\partial z^2}\mathbf{u} \tag{5.2}$$

$$\nabla \cdot \mathbf{u} = 0 \tag{5.3}$$

$$\frac{\partial b}{\partial t} + \mathbf{u} \cdot \nabla \mathbf{u} = \kappa \nabla^2 b \tag{5.4}$$

$$\rho = \rho(T, S) \tag{5.5}$$

where $\mathbf{u} = (u, v, w)$ is the velocity vector in zonal, meridional and vertical directions, f is Coriolis parameter, p is the pressure, b is the buoyancy ($-g\left(\delta\rho/\rho_r\right)$), T and S are the water temperature and salinity, v_h and v_v are the horizontal and vertical viscosity coefficients and κ is diffusivity coefficient of tracer. Here $\times$ is cross product of vector, ∇ and $\nabla \cdot$ are the gradient and divergence operators, and $\hat{\mathbf{k}}$ is the unit vector in vertical direction. The linear equation of state was used assuming the density only depends on the temperature with homogeneous salinity;

$$\rho = \rho_r(1 - \alpha(T - T_r) + \beta(S - S_r)) \tag{5.6}$$

where α (=2.4E-4) is the thermal expansion coefficient and β (=0) is the haline contraction coefficient of temperature and salinity. T_r and S_r are the reference temperature and salinity.

5.4.2 Configuration of water circulation computation

Representation of topography in the model is achieved by shaved cells (partial steps) with finite volume method formulation (Adcroft et al., 1997). The grid cells that abut on the solid boundary such as topographic bottom and coastline are "shaved" to fit the boundary.

Following Marshall et al., (1997), the hydrostatic approximation in the modeling of the atmosphere and ocean is valid for large (Global/basin) scale phenomenon in which the vertical scale of motion is negligible. However, in the small scale phenomenon of an order less than 1km such as the wind stirring and turbulent mixing in surface mixed-layer the vertical scale of motion is no longer negligible as compared to the horizontal scale. The criterion they introduced for the validation of hydrostatic approximation in terms of the aspect ratio ($\gamma = h/L$) of horizontal (L) and vertical (h) scales and the Richardson number ($Ri = N^2h^2/U^2$) is given by

$$\frac{\gamma^2}{R_i} = \frac{U^2}{L^2 N^2} \ll 1 \qquad (5.7)$$

where $N^2 = -(g/\rho_r)(\partial\rho/\partial z)$ is the buoyancy frequency, U is the horizontal velocity scale and g is the acceleration due to gravity.

In the Yachiyo Lake, the criterion is varying mostly under the regime of hydrostatic approximation but at some critical locations, i.e, around St.9 (Fig. 5.1) with relatively strong horizontal velocity scale, it is an order of 0.1. Therefore the non-hydrostatic capability in the model run is not negligible and retained for the study. The Yachiyo Lake is a midsize lake that the simulation domain is covered by 114 and 110 meshes with 20m and 22m in grid interval in zonal and meridional directions. The bathymetry of Yachiyo Lake was measured in 25 Oct., 2006 showing the maximum water depth near the dam wall is deeper than 20m and the minimum is less than 1m at the downstream of inflowing river. The water depth was divided into 10 layers with the top layer of 0.5m down to the bottom layer of 3.0m interval. Since we just have the measured vertical profile of temperature at two fixed monitoring stations in the lake, the initial temperature profile is taken from the mean value of the two stations assuming the horizontally homogeneity. The surface thermal relaxation with mean value of the two stations was used as well as the surface heat flux transfer to consider the meteorological condition of rainy days. The salinity in the model run was set to zero. So the density of lake water is only a function of temperature.

The vertical and horizontal turbulence scales and intensities in lake flows are known to be very different from each other by measurements (Walker and Watts, 1995) and the turbulent Prantle number, the ratio of momentum viscosity to thermal diffusivity, is varying from 0.7 to 4 (Henderson-Sellers, 1976). The small scale processes of turbulence that can not be simulated explicitly in this study is calculated by the non-local K-profile parameterization scheme (Large et al., 1994) and the background horizontal eddy viscosity and vertical eddy diffusivity are set to $10^{-2} m^2/s$ and $10^{-3} m^2/s$, respectively as known, in general, the vertical eddy diffusivity is much smaller than the horizontal eddy viscosity while considering the numerical stability of model run in this study.

The boundary conditions of no-slip bottom (u=0 where u is velocity parallel to bottom) and free surface ($w = \partial\eta/\partial t$ where η is free surface height) were applied in the simulation.

5.5 Model results

5.5.1 Wind-driven currents

The wind in the modeling period is generally weak with strong directionality without showing distinct daily patterns. From the meteorological forcing results by atmospheric model, the relatively strong zonal and meridional winds are shown in 5 July, 2006 and the calculated air temperature on the same day shows very good agreements with the observed values. The daily transient surface currents on 5 July, 2006 with these forcing are shown in Fig. 5.3. Due to the southward wind at 00:00 JST the transient surface current shows the southward currents being strong at narrow point near St. 3 and 4. The currents keep their directions to southward being gradually reduced in their magnitude as the wind velocity is reduced throughout the day. In the transient current at 12:00 JST, the currents show variable directions mainly to southward below St.5 and northward around St.6 and St. 7 and there is a small clockwise circulation near St.6. Fig. 5.4 shows the currents field by the arrows and the temperature profile by the shaded contours together at zonal cross-section shown in Fig. 5.1. As noticeable in Fig. 5.4 there are velocity shear between the thin surface layer and the mid-layer currents and the surface currents are well agreed with and sensitive to the transient surface currents (Fig. 5.3). Due to the spatially varying surface heat flux, local heating and cooling in the zonal cross-section of the lake are found particularly at 08:00 JST. In the early morning until 08:00 JST 11 July the night cooling results in deepening of the surface mixed-layer down to 4 ~ 5m below the surface and the local convection in the surface mixed-layer is depicted by the strong downward currents velocity. In the daytime until the late-afternoon the southwesterly wind takes the warm surface water to the west and therefore the cool denser water below is upwelling to the surface in the east of the southern part of lake. In the evening the currents inverse the directions when the cool denser water in the east is sinking down as the warm surface water in the west moves to eastward. In Fig. 5.4 it is also found that the currents vertically fluctuate both spatially and temporally. Due to the presence of the small seal in the center of the zonal cross-section the increase of currents fluctuation is also found and its magnitude exceeds the one in the mid-layer.

Fig. 5.5 shows the mean currents at lake surface and at mid-layer (6.25m below the surface) and the depth-averaged mean current from the one month integration of model. The mean current at the surface shows the southwestward direction with the order of 0.01m/s.

It is interesting to note that there are two small gyres found in the mean currents at mid-layer; one is in the east side of point St. 6 in relative shallow region and the other is between the stations, St.1 and St.2. in deep southern part of the lake. The gyre near St. 6 shows clear counterclockwise circulation while the other near St.1 shows the clockwise circulation. Even it is variable in direction and magnitude of currents, the two gyres at the same location in the lake are found in the depth-averaged mean currents (Fig. 5.5). To investigate further the gyres and their mechanism, three numerical experiments that employ similar scenarios with Pan

et al., (2002) were carried out; The first experiment was performed with uniform temperature profile ignoring the Coriolis effect to examine the thermal stratification and earth's rotation, the second one was conducted with flat bathymetry to test the effect of topography, and the third one was set up without the surface heat flux transfer to study the buoyancy effect on currents.
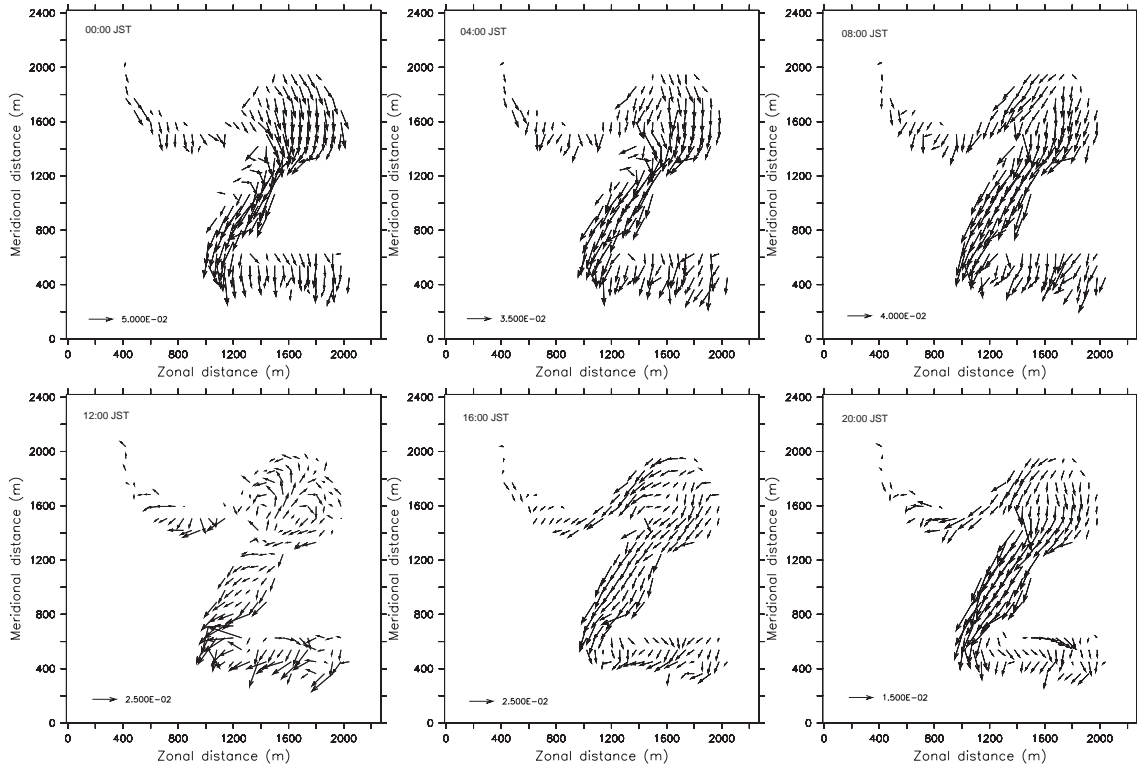
Fig. 5.3 Calculated wind-induced lake surface currents (0.25m below the surface) at different time of a day (0:00, 4:00, 8:00, 12:00, 16:00 and 20:00 JST), 11 July, 2006. (unit : m/s)
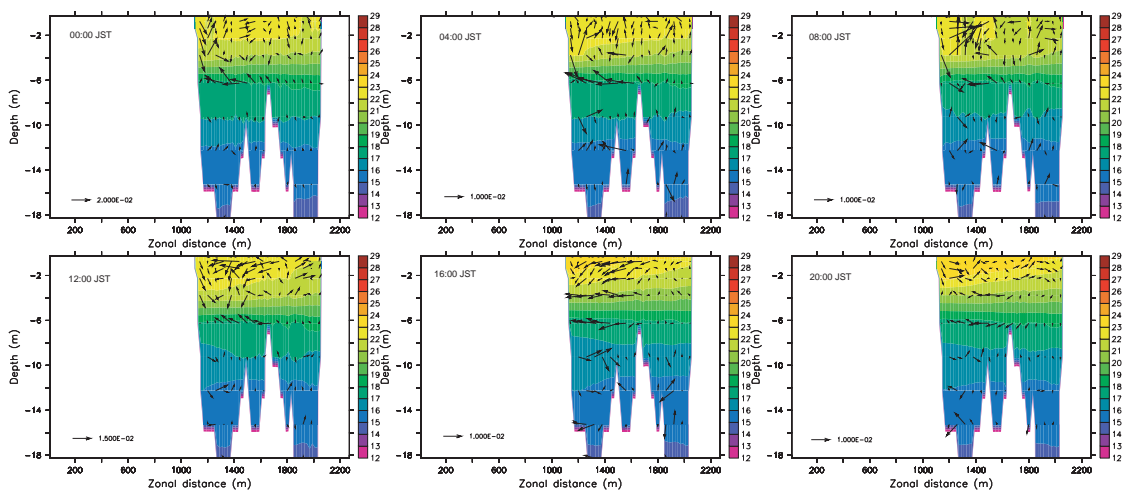
Fig. 5.4 Calculated currents in arrows and thermal profiles in shaded contours at zonal cross-section as in Fig. 5.3. (unit : m/s). The zonal cross-section is shown in Fig. 5.1.
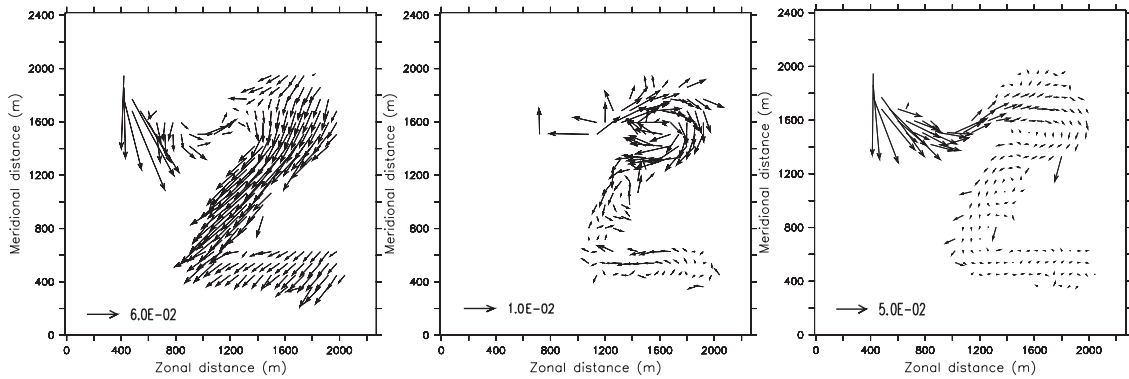
Fig. 5.5 Calculated monthly mean currents in July on the lake surface (left), in the mid-layer of 6.25m below the surface (middle), and depth-averaged current (right). (unit : m/s)
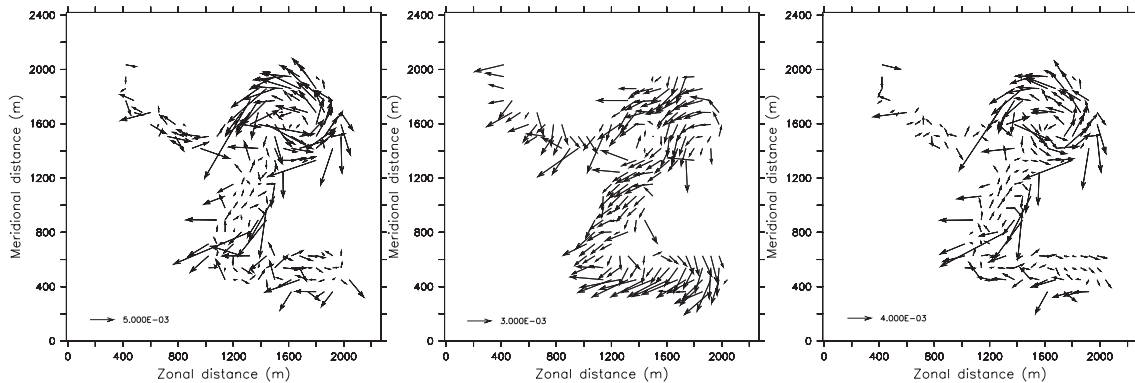
Fig. 5.6 Calculated depth-averaged monthly mean currents in July from numerical experiments with uniform temperature profile ignoring the Coriolis effect (left), with flat bathymetry (middle), and without thermal forcing (right) (unit : m/s)

In all experiments, the same spatially and temporally varying wind field was forced to derive the currents of the lake. Fig. 5.6 shows the simulation results of depth-averaged monthly mean currents from the three experiments. From the first and third experiments, the two gyres near St.6 and between St1. and St.2 are found, even though they slightly differ from the reference case (Fig. 5.5). Therefore the Coriolis effect by earth's rotation in this small lake is not significant and the buoyancy induced by surface heat flux is not responsible for the two gyres of the lake. However, the depth-averaged mean current from the second experiment shows different result from the others, which depicts relatively constant currents field in southward direction without the two gyres in the lake. Therefore, the topography of the lake plays a very important role in the currents of the lake and formation of two gyres.
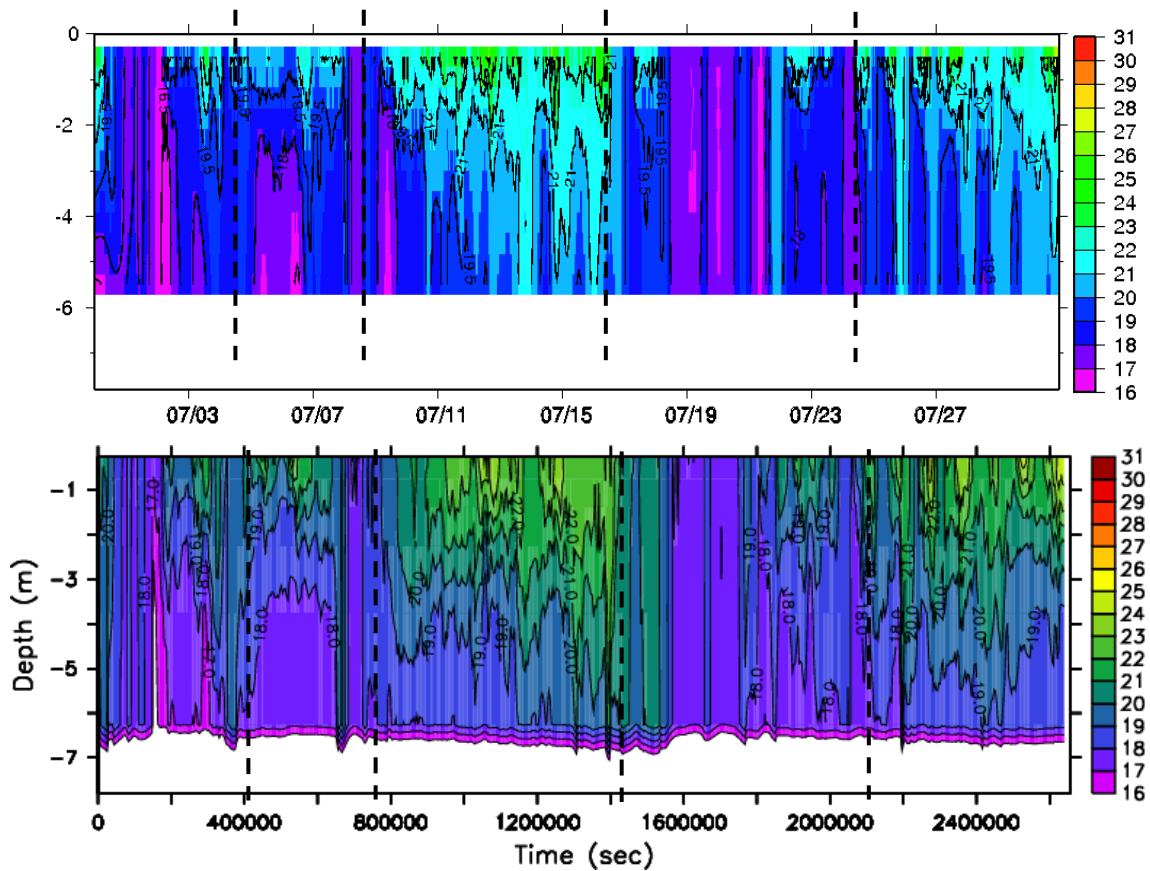
Fig. 5.7 Time-series of temperature profiles. Upper is observation at St.9. Lower is computation. The location of observation points are shown in Fig. 5.1.

5.5.2 Temperature profile and stratification

The temporal evolution of the vertical temperature profiles from the observation at fixed point near St.9 and calculation are shown in Fig. 5.7. During the one month period of simulation, July 2006, the net heat flux transfer at the lake surface is balanced between the downward short-wave solar radiation, the evaporative latent heat flux, the sensible heat flux and the long-wave radiation off the surface. The net heat flux gets increased and absorbed through the surface, which results in the gradual increase of temperature profile of entire lake during the period. In Fig. 5.7 the daily warming and cooling at daytime and nighttime are clearly shown and the thick dashed lines depict the same phases in time. From this evolution of temperature profile, two things are noticeable that the during the rainy days the surface cooling is simulated well particularly from 17th to 21st July and the diurnal cycle of surface warming and cooling at the end of period from 27th July. Since the meteorological forcing is given by non-hydrostatic atmospheric modeling, the surface heat flux in rainy conditions includes many uncertainties as depicted in Fig. 5.2. The surface thermal relaxation together with the surface heat flux transfer

in this modeling shows good results in the evolution of temperature profile considering the rainy conditions.

In Fig. 5.8 the recorded temperature profiles and the calculated values at different times in 08 July, 2006 are shown. In the morning the temperature increase in the thin surface layer is found in both the observed and calculated data while the temperature profile shows a disparity in their vertical gradients and in the afternoon the calculated temperature profiles show good agreements with the observation. The calculated temperature profile in the nighttime shows a difference about 2deg below the thin surface layer at 22:00 JST from the observed value while they are coincided below this disparity. The temperature profiles at points St1, St2, St6, and St9 are also shown in Fig. 5.9. The contours in Fig. 5.9 are labeled every 1.0 degree.
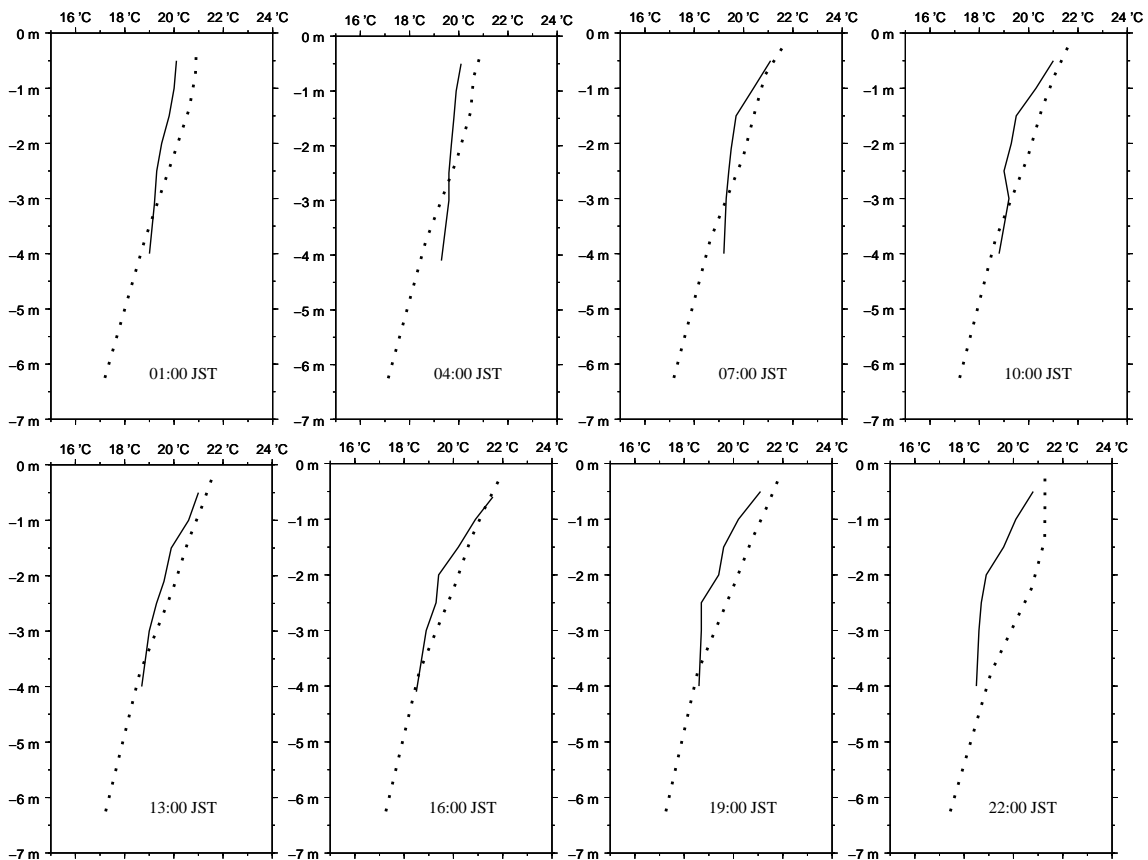
Fig. 5.8 Profiles of temperature from observation (solid) at fixed station near St.9 and calculation (dots) at St.9 at different times of a day, 08 July 2006.

In response to the meteorological forcing, the daily variation of the lake surface temperature is clearly identified. At the changing phase of meteorological conditions from the rainy or cloudy day to the sunny days, the thermal fronts are formed in the surface mixed-layer implying the potential mixing in the formation of the thermal fronts. From the time-depth plots

of temperature, there are several perturbations in strong thermal stratification during the simulation period and after 5 days of simulation start, a strong thermal perturbation is found in all points. This thermal perturbation is mostly due to the relatively strong wind stress because the strong zonal and meridional wind stresses in the morning of 6 July 2006 (Fig. 5.2) is the evidences. This effect of strong wind induces the deepening of surface-mixed layer. The buoyancy anomalies ($\rho' = \rho - \rho_r$ where ρ_r is 999.8kg/m^3) from the model run at the same points as in Fig. 5.9 are shown in Fig. 5.10. From the Fig. 5.10 it is found that as the density only depends on the temperature in this study, the sharp buoyancy anomalies shows the large temperature changes as compared to the ambient flow. Therefore as the buoyancy anomaly of the lake gets larger in the sequences of simulation, the vertical temperature gradients get increased and the surface mixed-layer is getting shallow. In rainy days with weak wind conditions as shown in Fig. 5.2 between 17 and 21 July, the surface cooling and the consequential convection are reproduced well as found in the observation (Fig. 5.7). This process is well agreed with the deep convection in a stormy event in the ocean (Bender et al., 1993).

5.5.3 Internal waves

Due to the strong stratification during the simulation period, the surface mixed-layer is very thin and the mixing below the surface mixed-layer is intermittent and weak by internal gravity waves and boundary mixing around the thermocline. Therefore the internal waves play a very important role in the mixing of stratified Yachiyo Lake.

Fig. 5.12 shows the calculated surface wind stress, the isotherm displacements and buoyancy frequency at St.1. The isotherms of 23˚C, 21˚C, 19˚C, and 17˚C were formed near surface and 8m deep in the beginning of the modeling which are the initial mean value of two fixed stations in the lake and became deeper as the entire lake got warm due to the net heat flux transfer. The vertical separation of isotherms between 21˚C and 19˚C from 10 to 18, July shows small increase while that between 19˚C and 17˚C is almost uniform with about 3m. This vertical separation can be used for study of the basin-scale internal waves (Laval et al., 2003) as it is influenced by the internal waves. However the evidence of basin-scale Kelvin waves and Poincaré waves are not found from this study as the vertical separations of isotherms are almost uniform. It seems that it is mainly due to the small size meandering shape of Yachiyo Lake which the Corilois effect is not significant and there is no periodical and persistent wind that could induce the surface set-up and the consequential cyclic motion.

As seen in Fig. 5.12 the large displacements of isotherms coincide well with the relatively strong surface wind stresses and the largest vertical displacement is found to be about

2m in 5 July, 2006. The buoyancy frequencies in Fig. 5.12 are contoured with 0.002 s^{-1} interval ranging from 0.002 s^{-1} to 0.016 s^{-1} in free internal gravity wave and nonlinear internal wave band which is larger than Corilois parameter, f, with an order of 10 and 10^2 (Saggio and Imberger, 1998). Due to the strong stratification in simulation period, the high buoyancy frequencies in nonlinear internal wave band are found within the 2m below the surface in daytime.
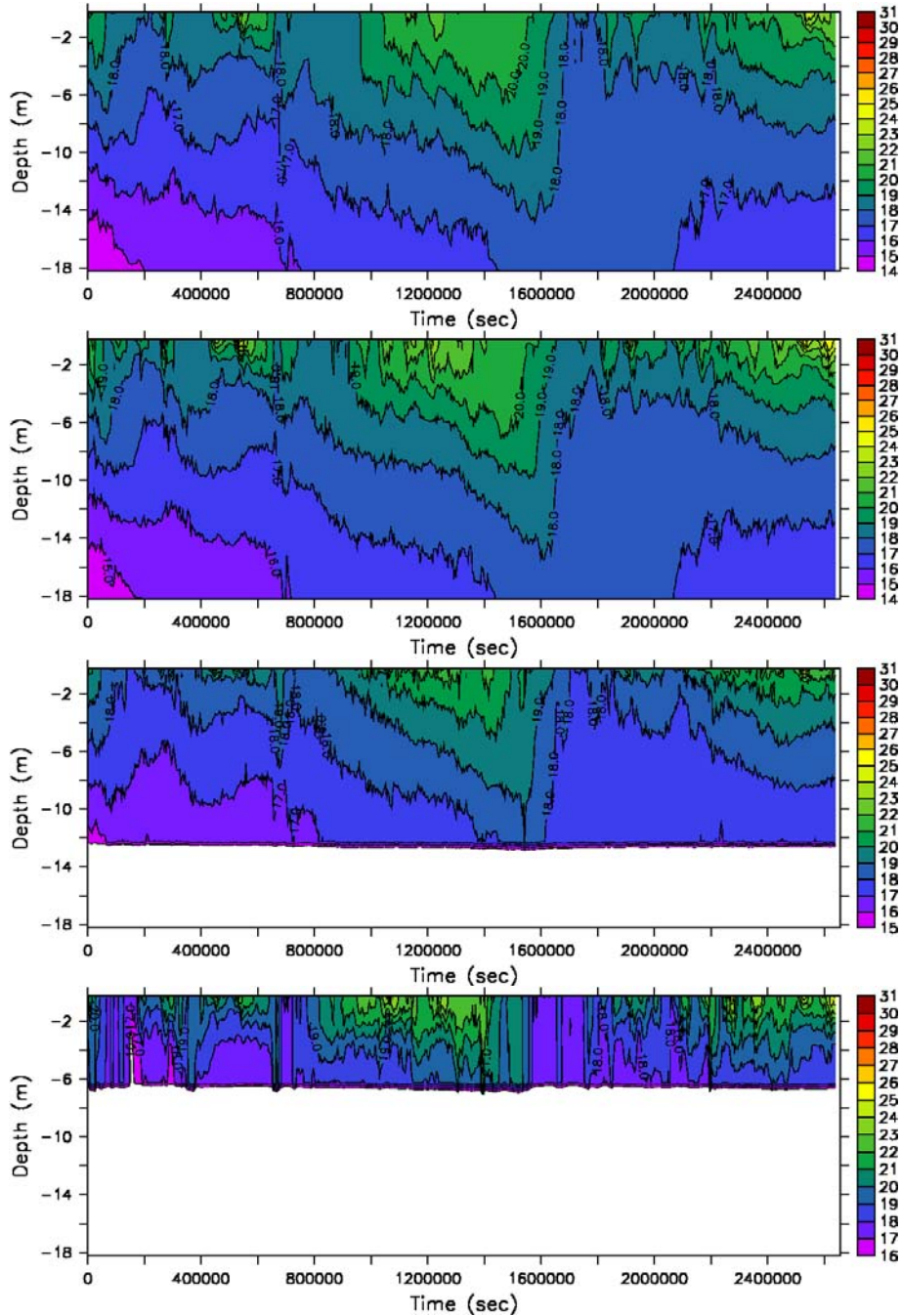
Fig. 5.9 Time-series of temperature profiles at points, St.1 (upper left), St.2 (upper right), St.6 (lower left), and St.9 (lower right).
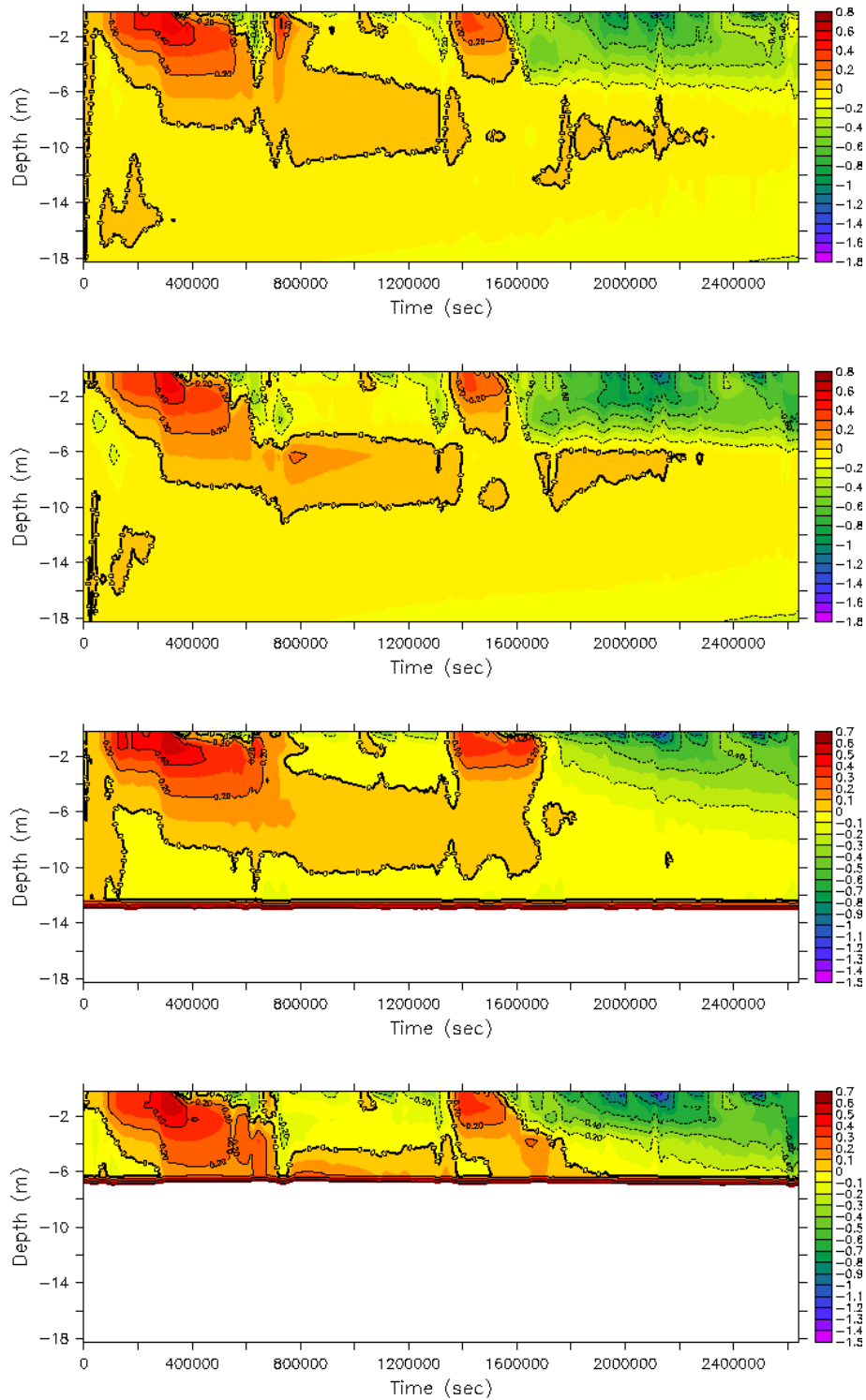
Fig. 5.10 Time-series of calculated density anomaly profiles. Points are same as Fig. 5.9.

125
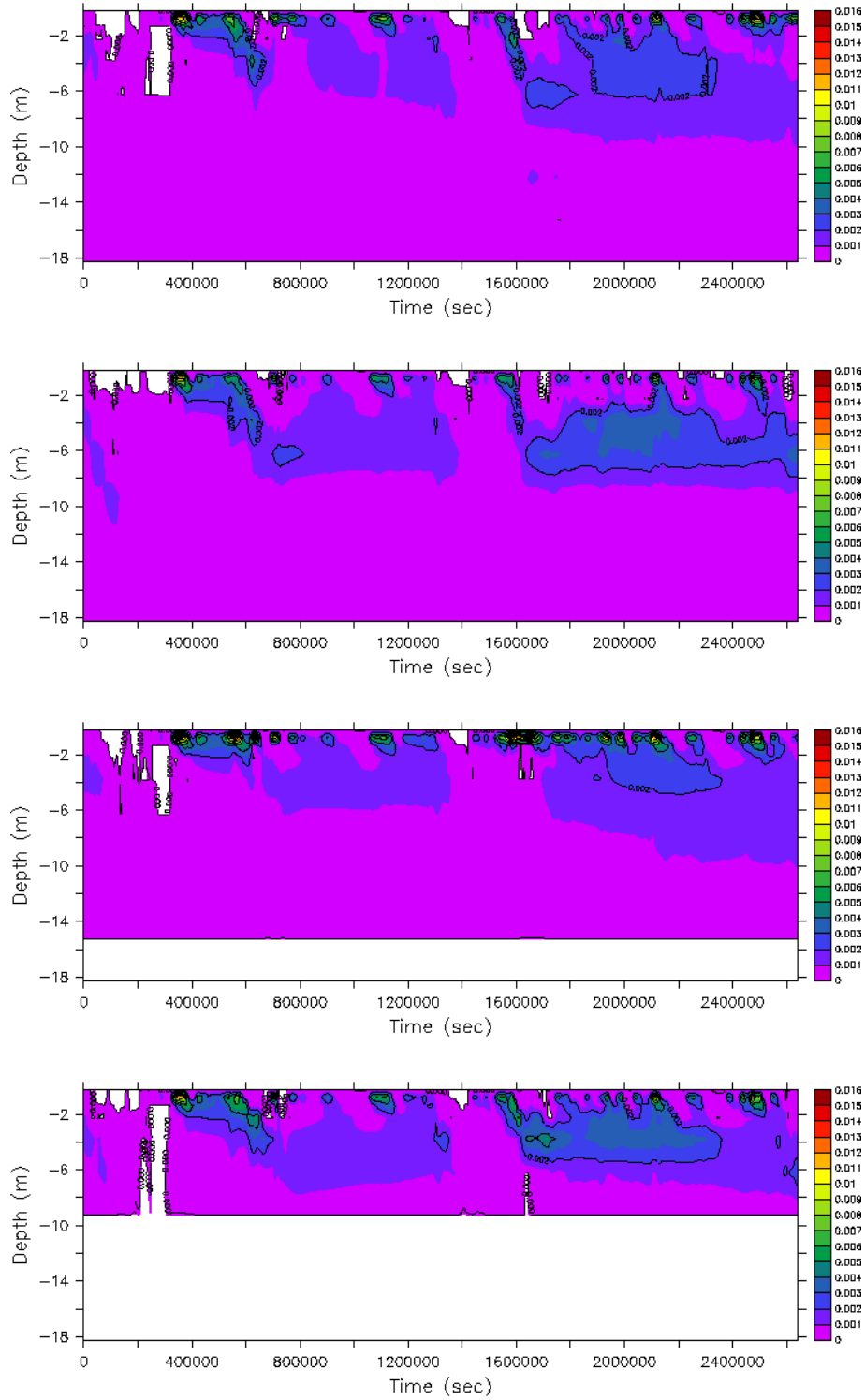
Fig. 5.11 Time-series of calculated buoyancy frequency profiles. Points are same as Fig. 5.9.
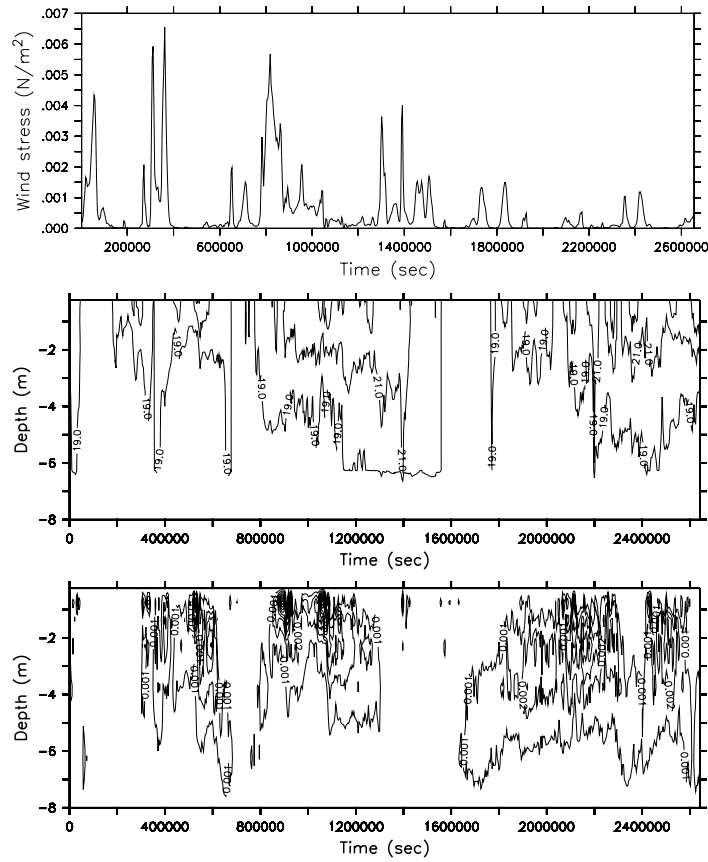
Fig. 5.12 Calculated surface mean wind stress (top), isotherms of 22˚C, 20˚C and 18˚C at St.1 (middle) and buoyancy frequency at St.1 (bottom). The contours in buoyancy frequency are labeled every 0.002s^{-1} from 0.002 s^{-1} to 0.016 s^{-1}.

5.5.4 Static stability: potential mixing

The static stability of a stratified flow can be represented in terms of gradient Richardson number and it is possible to predict the potential mixing by the velocity shear from this non-dimensional number as given by

$$R_i = -\frac{N^2}{(du/dz)^2}$$

(5.8)

Following the linear stability theory, the critical value of non-dimensional number, R_{ic}, is 0.25 and a flow with R_i larger than R_{ic} is stable. As shown in Fig. 5.11 and Fig. 5.12 the buoyancy frequency of Yachiyo Lake during the study period is high overall from 0.002 s^{-1} to 0.016 s^{-1}

while denominator, the square of vertical velocity gradient, is small ranging from 0 s^{-1} to 0.0018 s^{-1}. In the most of simulation period below the thin surface layer, the denominator is found very small less than $0.2*10^{-4}$. Therefore the R_i of Yachiyo Lake shows much larger that the critical value, R_{ic}, and it is quite stable due to the strong stratification.

5.5.5 Inflows from the river discharge

The influence of the runoff from the Haji Dam watershed was also investigated by the other numerical experiments with the open boundary condition (OBC) being imposed in the north of model domain. The observed runoff data of Haji Dam watershed were considered as fresh water flux and inflowing water velocity and temperature. The inflowing water temperature from the upstream river was assumed that it is not much different from the temperature of the northern part of lake. Therefore the observed water temperature at St.9 was used for the OBC of inflowing water temperature. The inflowing water velocity was considered as area-averaged values only in meridional direction due to the topographical condition of the lake.

In the simulations of the Yachiyo Lake with the OBCs, unlike the ones without OBCs, the numerical stability in horizontal velocity fields, U and V, became the one of main concerns due to the quite strong incoming water velocity. The incoming water velocity at open boundary is larger than any values simulated from the rest start without OBCs.

The sub-gird scale process in this experiment with OBCs in northern boundary is calculated by nonlinear viscosities (Smagorinsky, 1963) instead of the non-local K-profile parameterization. The variable viscosity depends on the resolved motions by the grid-scale of this study while ensuring the numerical stability within the Courant-Freidrichs-Lewy constraint.

5.6 Conclusions

The wind induced currents, thermal structure and its evolution, and the internal waves in Yachiyo Lake were investigated by REDES of 3D non-hydrostatic model system of meteorological (MM5) and oceanic (MITgcm) circulation models.

Due to the relatively calm wind condition during the simulation period in summer, the wind stress plays a dominant role in lake circulations. Two gyres were found in the mid-layer currents and depth-averaged monthly mean currents. The effect of topography of Yachiyo Lake is very crucial in the formation of those gyres that was proved by extra three experiments considering the effects of earth's rotation, thermal stratification, buoyancy, and topography.

The thermal structure of Yachiyo Lake and its evolution simulated with the meteorological forcing of the surface heat flux transfer showed good agreements with observed

values. The diurnal cycle of heating and cooling in clear days and the local convection in rainy days in response to the surface cooling were clearly identified. The importance mixing in the stratified lake is caused by the velocity shear between the thin surface layer and mid-layer and the internal waves. The internal gravity waves below the thin surface layer are sometimes depicted in large displacement of isotherms up to 2m in the lake in the direct response to the wind stress. The basin-scale internal waves due to the Coriolis effect and lake surface level set-up are not found and their effect are not significant in the Yachiyo Lake. As identified by non-dimensional gradient Richardson number, the Yachiyo Lake is under control of strong stratification in summer.

The numerical experiments in this study had been performed in one-way coupling of two non-hydrostatic circulation models from atmosphere to lake and the feedbacks from lake to atmosphere such as evaporation off the surface. Surface temperature and the surface gravity waves were not accounted in the simulation. Two-way full coupling system is still under development that will extend the study of regional climate in the future.

References

Adcroft, A., C. Hill, and J. Marshall, (1997): Representation of topography by shaved cells in a height coordinate ocean model, *Mon. Wea. Rev.*, **124**, 2293-2315.

Antenucci, J. P., J. Imberger, and A. Saggio, (2000): Seasonal evolution of the basin-scale internal wave field in a large stratified lake, *Limnol. Oceanogr.*, **45(7)**, 1621-1638.

Bender, M. A., I. Ginis, and Y. Kurihara, (1993): Numerical simulations of tropical cyclone-ocean interaction with a high-resolution coupled model, *J. Phys. Oceanogr.*, **98**, 23245-23263.

Dudhia, J., (1993): A nonhydrostatic version of the Penn State-NCAR mesoscale model; Validation test and simulation of an atlantic cyclone and cold front, *Mon. Wea. Rev.*, **121**, 1493-1513.

Grell, G. A. (1993): Prognostic evaluation of assumptions used by cumulus parameterizations, *Mon. Wea. Rev.*, **121**, 764-787.

Grell, G. A., J. Dudhia, and D. R. Stauffer, (1995): A description of the fifth-generation Pen State/NCAR mesoscale model (MM5), Tech. Note TN-398 + STR, National Center for Atmospheric Research, Boulder, CO.

Hendeson-Sellers, B., (1976): Role of eddy diffusivity in thermocline formation, *J. Env. Eng. Div.*, 517-531.

Herb, W. R. and H. G. Stefan, (2005): Dynamics of vertical mixing in a shallow lake with submersed macrophytes, *Water Resource Res.*, **41**, W02023.

Hong, S. -Y., and H.-L. Pan, (1996): Nonlocal boundary layer vertical diffusion in a Medium-Range Forcast model, *Mon. Wea. Rev.*, **124**, 2322-2339.

Kantha, L. H., and C. A. Clayson, (1994): An improved mixed layer model for geophysical applications, *J. Geophys. Res.*, **99**, 25235-25266.

Kantha. L. H., and S. J. Freeth, (1996): A numerical simulation of the evolution of temperature

and CO2 stratification in Lake Nyos since the 1986 disaster, *J. Geophys. Res.*, **101**, 8187-8203.

Kantha. L. H., and S. J. Freeth, (2000): Small scale processes in geophysical fluid flow, C8, Lakes and Reservoirs, V67, *International Geophysics Series*, Academic Press, USA.

Large, W. G., and S. Pond, (1981): Open Ocean momentum flux measurements in moderate to strong winds, *J. Phys. Oceanogr.*, **11**, 324-336.

Large, W., J. McWilliams, and S. Doney, (1994): Oceanic vertical mixing: A review and a model with nonlocal boundary layer parameterization, *Rev. Geophys.*, *32*, 363-403.

Laval, B., J. Imberger, B. R. Hodges, and R. Stocker, (2003): Modeling circulation in lakes: Spatial and temporal variations, *Limnol. Oceanogr.*, **48(3)**, 983-994.

Legg, S., and A. Adcroft, (2003): Internal wave breaking at concave and convex continental slopes, *J. Phys. Oceanogr.*, **33**, 2224-2246.

Marshall, J., C. Hill, L. Perelman, and A. Adcroft, (1997a): Hydrostatic, quasi-hydrostatic, and non-hydrostatic ocean modeling, *J. Geophys. Res.*, **102**, 5733-5752.

Marshall, J., A. Adcroft, C. Hill, L. Perelman, and C. Heisey, (1997b): A finite-volume, incompressible Navier Stokes model for studies of the ocean on parallel computers, *J. Geophys. Res.*, **102**, 5753-5766.

Pan, H., R. Avissar, and D. B. Haidvogel, (2002): Summer circulation and temperature structure of Lake Kinneret, *J. Phys. Oceanogr.*, **32**, 295-313.

Saggio, A. and J. Imberger, (1998): Internal wave weather in a stratified lake, *Limnol. Oceanogr.*, **43(8)**, 1780-1795.

Smagorinsky, J., (1963): General circulation experiments with the primitive equations, i. the basic experiment, *Mon. Wea. Rev.*, **91**, 99-164.

Spigel, R. H., J. Imberger, and K. N. Rayner, (1986): Modeling the diurnal mixed layer, *Limnol. Oceanogr.*, **31(3)**, 533-556.

Spigel, R. H. and J. Imberger, (1980): The classification of mixed-layer dynamics in lakes of small to medium size, *J. Phys. Oceanogr.*, **10**, 1104-1118.

Walker, S. J. and R. G. Watts, (1995): A three-dimensional numerical model of deep ventilation in temperate lakes, *J. Geophys. Res.*, **100**, 22711-22731.

Williams, M. J. M., (2001): Application of a three-dimensional numerical model to Lake Vostok: An antarctic subglacial lake, *Geophys. Res. Letters.*, **28(3)**, 531-534.

Zhang, D.-L., and R. A. Anthes, (1982): A high-resolution model of planetary boundary layer-Sensitivity tests and comparisons with SESAME-79 data, *J. Appl. Meteor.*, **21**, 1594-1609.

Chapter 6

Applications to Coastal Problems

6.1 Introduction

It is a well-known fact that the reanalysis and accurate numerical simulation of wave climate, coastal currents induced by wind and storm surge simulation require apparently the realistic wind field with consideration of effects of complex land topography. The inland seas and a number of bays in Japan are in the category that needs the accurate wind field for such studies. The reproduction and reanalysis of the wind field, however, had been conducted simply by making spline interpolation of the observed data or by modeling with simple gradient wind typhoon model or by a planetary boundary layer model. Their results showed a deficit in their data qualities. Recently mesoscale meteorological model has been used for hindcast and forecast of atmosphere conditions taking into account of the complex terrain and the reproduction of wind field has been improved in its accuracy.

In this study, the mesoscale meteorological model, MM5, was used for the reanalysis of the 47 past storm and severe weather conditions including 42 typhoons focusing on West Kyushu, Japan since 1959. The results of reanalysis had been utilized for a database construction and studies of wind field characteristics in semi-closed Omura Bay. The reanalysis results were also used to study the characteristics of wind-induced currents in Ariake Sea which is very important in material transport under storm events.

6.2 Reanalysis of past major storms in West Kyushu

For the accurate simulation of wave climate, coastal circulation and currents and storm surge, reliable estimation of wind fields is required, that can be reproduced by using reliable observed data and/or numerical models. Interpolation of the observed winds is, however, applicable only to a relatively uniform topographic region such as plains. Its application to complex topographic region such as mountainous area and inland seas with a number of islands

may cause some problem. In particular, for the long-term simulation or disaster simulation under the severe weather conditions, using observed data is much problematic.

There are many numerical models such as simple gradient wind typhoon model, nonhydrostatic mesoscale model and regional atmospheric model including cumulus physics and in practice, the long-term analysis of meteorological conditions has been generally performed with any gradient wind model, an atmospheric PBL model, a MASCON (Mass Conservation) model or a combined model of three elements. However, those numerical models are limited to apply to complex topographical region that significantly affects on the meteorological processes. In the present study, such complex topographical conditions are taken into account for the simulation of coastal wind distribution by using mesoscale meteorological model, MM5 (see Chapter 2). The past severe meteorological events for about 50 years in West Kyushu in Japan encompassing the Omura bay and Ariake Sea had been reanalyzed by MM5 of REDES.

Model configuration

The initial and surface/lateral boundary conditions were imposed by ECMWF ERA 40 and NCEP reanalysis (both are 2.5°×2.5° spatial resolution) in this study. The nested computational three domains were set up with 27, 9 and 3km grid intervals and the effective bogussing scheme for typhoon simulation was applied in the first domain. Fig. 6.1 shows the computational domains and the Omura Bay in Nagasaki.
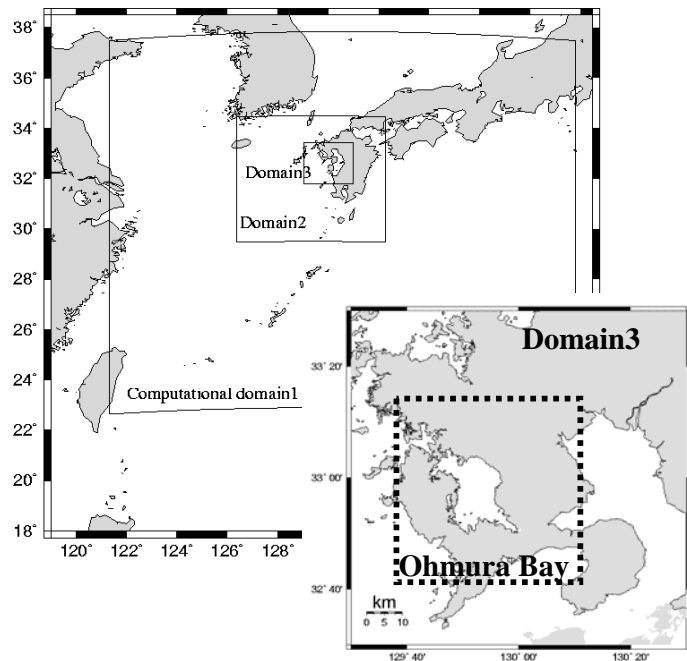
Fig. 6.1 Computational domains of MM5 in Omura Bay, Nagasaki, Japan.

134

Reanalysis of the severe meteorological events

The first selection condition of the past severe meteorological events was based on the list of annual maximum wind field. The storm cases mostly including the typhoons were selected from the list. The second selection condition among the results of the first selection was based on the annual maximum wind field in each wind direction together with available weather chart. The last selection condition was made for the severe meteorological events, by considering the related disasters that caused damages and casualties in interested area from the second selections. Based on the last selection of severe meteorological events, the storms which made the maximum wind field in Omura, West Kyushu, occurred almost in July to October by typhoons. The moving tracks of the typhoons with the maximum wind field had the northward traces from the East China Sea through the west side of Omura Bay. The typical instances of such storms were the typhoons, 9918, 9119 and 8712.

Table 6.1 shows the list of storms with the averaged wind speed over 15m/s at the observation stations of both Omura (Nagasaki airport) and Sasebo and with the averaged wind speed over 10m/s at either station of Nagasaki or Sasebo from the final selections. The remarks by LF and atmospheric LP denote the low pressure system accompanied with fronts and atmospheric low-pressure system by Siberian high in wintertime.

6.2.1 Regional inventory of storm events in West Kyushu

Inventory of reanalysis results of the storms listed in Table 6.1 was made with 2D and 3D meteorological elements shown in Table 6.2. The data from the computational domains with 27, 9 and 3km are all available with 15 min temporal resolution over the simulation periods. These data are available upon a request with a read-in Fortran code. The four station points shown in Fig. 6.2 are available with additional time-series data of wind field.

Table 6.1 List of reanalyzed storms

No.	Simulation period	Observed Max. wind speed(m/s) Nagasaki and Sasebo (WD)	Remarks
1	2004.08.17 ~ 2004.08.19	10. 5 (SSW), 17.4 (S)	T0415
2	2004.08.27 ~ 2004.08.30	11.8(WNW), 20.5(NNW)	T0416
3	2004.09.04 ~ 2004.09.07	23.3(SW), 23.7(W)	T0418
4	2004.09.25 ~ 2004.09.30	14.1(N), 17.6(N)	T0421
5	2004.10.18 ~ 2004.10.21	13.6 (NNE), 22.8 (NNE)	T0423
6	2003.06.18 ~ 2003.06.19	9(SW), 17(S)	T0306
7	2003.08.07 ~ 2003.08.08	9.2(N), 14.4(NNE)	T0310
8	2003.09.10 ~ 2003.09.13	10.5(SSW), 17.2(SSE)	T0314
9	2002.08.29 ~ 2002.09.01	5(NNE), 17(SE)	T0215
10	2001.06.18 ~ 2001.06.25	Omura 20(SW)	LF
11	1999.04.09 ~ 1999.04.11		LF
12	1999.06.24 ~ 1999.06.29	Omura 19(SSW)	LF
13	1999.09.21 ~ 1999.09.25	15.1(N), 11.6(W)	T9918
14	1998.09.28 ~ 1998.09.30	Omura 15(SSE)	T9809
15	1998.10.15 ~ 1998.10.18	8.8(N), 10.4(ENE)	T9810
16	1997.07.31 ~ 1997.08.09	Omura 15(SSW)	T9711
17	1997.09.13 ~ 1997.09.17	12.1(NNE), 11.6(ENE)	T9719
18	1997.11.24 ~ 1997.11.26	Omura 22.0(SSE)	Atmospheric LP
19	1996.06.17 ~ 1996.06.18	Omura 18(SW)	Atmospheric LP
20	1996.08.11 ~ 1996.08.15	15(WNW), 11.1(NNW)	T9612
21	1994.08.13 ~ 1994.08.14	5(NE), 11.0(E)	T9414
22	1993.09.01 ~ 1993.09.05	13.4(NNE), 11.0(N)	T9313
23	1992.08.06 ~ 1992.08.09	13.9(N), 12.1(NNW)	T9210
24	1991.07.28 ~ 1991.07.29	12(SSW), 8(SE)	T9109
25	1991.09.13 ~ 1991.09.14	15(W), 13(N)	T9117
26	1991.09.25 ~ 1991.09.28	25.6(N), 17.6(ENE)	T9119
27	1990.09.11 ~ 1990.09.20	11.8(N), 10.8(NNE)	T9019
28	1989.07.24 ~ 1989.07.29	7.3(NE), 15.8(E)	T8911
29	1987.08.26 ~ 1987.08.30	12(SSW), 12(E)	T8712
30	1985.08.30 ~ 1985.08.31	16(W), 12(W)	T8513
31	1982.08.26 ~ 1982.08.27	13(WNW), 11(W)	T8213
32	1982.09.23 ~ 1982.09.25	7.0(WNW), 11(NE)	T8219
33	1981.07.30 ~ 1981.07.31	9(NNE), 10(NNE)	T8110

34	1979.10.18 ~ 1979.10.19	10.1(N), 12.1(NE)	T7920
35	1976.09.11 ~ 1976.09.13	12.8(WNW), 13.2(NE)	T7617
36	1971.08.29 ~ 1971.08.30	9(N), 13(NE)	T7123
37	1970.08.13 ~ 1970.08.15	17(W), 14(ENE)	T7009
38	1968.07.28 ~ 1968.07.30	12(SW), 11(W)	T6804
39	1968.09.24 ~ 1968.09.27	16.3(NNE), 23.2(NE)	T6816
40	1966.09.23 ~ 1966.09.25	14.3(NNE), 21.7(NNE)	T6626
41	1965.09.10 ~ 1965.09.18	13.7(NNE), 13(N)	T6524
42	1964.08.23 ~ 1964.08.24	14(NNE), 13(NNE)	T6415
43	1964.09.24 ~ 1964.09.25	11(NNE), 11(NNW)	T6424
44	1963.08.09 ~ 1963.08.10	11(WSW), 13(NNE)	T6309
45	1961.09.15 ~ 1961.09.17	14.5(NNW), 15.7(N)	T6118
46	1959.07.15 ~ 1959.07.18	19.1(SW), 19(S)	T5905
47	1959.09.26 ~ 1959.09.27	15.2(NNE), 19.6(NNE)	T5915

Fig. 6.2 Four stations of wind observation in Omura Bay

Table 6.2 Available meteorological elements from the database constructed by the reanalyzed data (15 min temporal resolution)

	3D DATA (23 sigma levels)	2D DATA
1	wind velocity – U, V (m/s)	ground temperature (K) 2m above the ground surface
2	vertical velocity – W (m/s)	accumulated convective precipitation (cm)
3	temperature (C)	accumulated non-convective precipitation (cm)
4	water vapor mixing ratio (kg/kg)	surface sensible heat flux (W/m2)
5	cloud water mixing ratio (kg/kg)	surface latent heat flux (W/m2)
6	rain water mixing ratio (kg/kg)	friction velocity (m/s)
7	geopotential height (m)	sea level pressure (Pa)
8	pressure (Pa)	10m surface wind (m/s) → U10, V10
9	vorticity - vertical component (1/s)	
10	potential vorticity (1/s)	
11	divergence – horizontal component (1/s)	

Table 6.3 Locations of the four stations of wind observation

Station	location
Nagasaki Airport	32:55:00 N, 129:54:08 E
Sasebo	33:09:05 N, 129:43:06 E
Station 1	33:00:00 N, 129:52:00 E
Station 2	32:55:00 N, 129:52:00 E

6.2.2 Results of reanalyzed storms

From the results of reanalyzed storms, the typhoons, 0416 and 0418 were presented here for comparison to observed data. The conventional wind direction (North is zero degree and increase in clockwise direction), wind speed (m/s) and hourly precipitations at Nagasaki, Sasebo and Omura (Nagasaki airport) were shown in Fig. 6.3. The solid circles indicate observed wind speed, wind direction and the bars indicate the observed precipitation and the solid lines with circles are the simulation results by MM5.

The simulated wind direction and wind speed at Omura (Nagasaki airport) and Sasebo showed good accordance with observed data. The variation of wind direction of the Typhoon, 0416 was reproduced accurately through the passage of typhoon. The simulated peak wind speed of typhoon 0416 showed good agreement with the observed one as well. However the

results of peak wind speed of typhoon 0418 at the beginning of simulation (east wind) showed some discrepancy with the observation, although the phase of occurrence time was coincided well. In particular, the wind mainly in NNE direction at Nagasaki had unignorable differences both in wind direction and speed and the observed wind direction was biased toward north.

Based on the all reanalyzed results, the discrepancies in wind direction were found in rather constant manner that seemed to be from the local topographical characteristics of observed points which could not be considered by the present MM5 scale/resolution. The differences of hourly precipitations in some storm results were mainly due to the inappropriate surface boundary condition in MM5 which contains the sea surface temperature (SST) information. The typhoon is known to be sensitive to SST that it is the main factor of typhoon generation, growth and dissipation. This is called positive and negative ocean feedbacks to the typhoon, that was described in Chapter 4. Therefore, the precipitation produced by embedded MM5 physics should be improved by appropriate and accurate surface boundary conditions with high-resolution realistic SST data in space and time (Yamaguchi et al., 2005).

6.2.2.1 The characteristics of wind field in Omura Bay

From the observations
The Omura Bay as shown in Fig. 6.2 is a semi-closed bay in West Kyushu surrounded by mountains and topographical obstacles such that their effects on wind field are appreciable. To investigate the topographical influences on wind field, statistical analysis of the observed wind field at four stations of Nagasaki airport, Sasebo, Nagasaki and Oseto were conducted to get the following results below.
1) The topographical influence at Nagasaki airport is not so significant. Strong winds in NNW-N and SE-SSE directions are dominant due to the surrounding mountainous topography. Its frequency of occurrence is higher than the other points. This is probably due to the location of Nagasaki airport constructed inside the bay where wind attenuation is smaller than in the land.
2) The strong wind direction at Oseto is almost in north, because the west and east winds are screened by the topographical obstacles of Matsuyama and Nagauradake, respectively.
3) Wind direction at Nagasaki is predominant in SW due to the topographical screening on the east side.
4) Wind speed at Sasebo is lower than that at Nagasaki airport, but the wind direction is similar to Nagasaki airport. The topographical influence in Sasebo seem to be not significant compared to those at Oseto and Nagasaki.
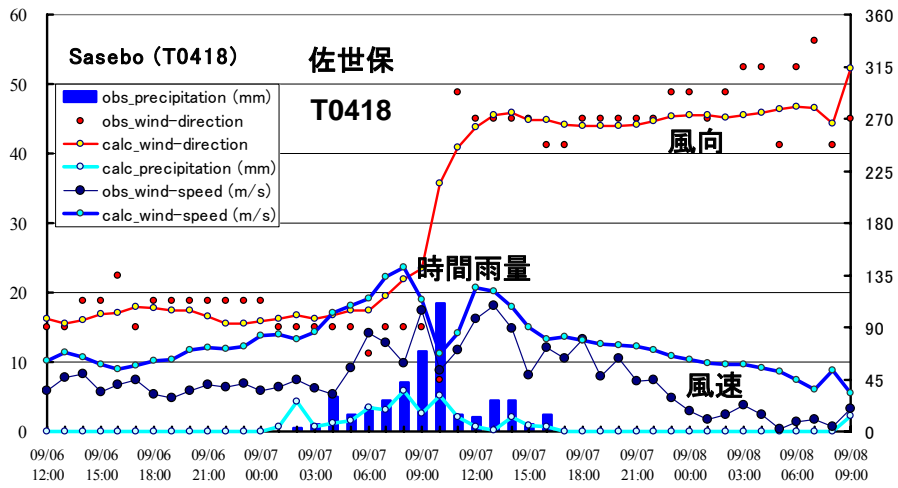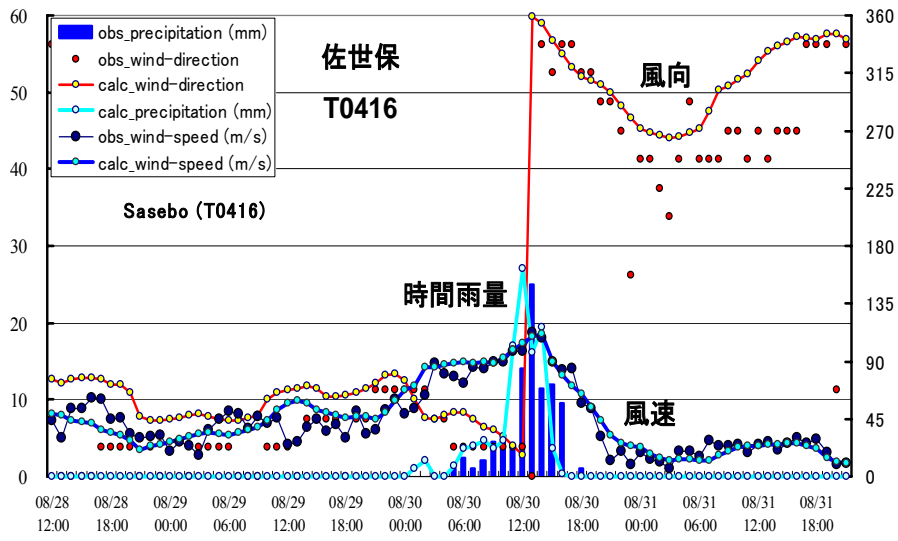
(a)　At Sasebo

Fig. 6.3　The comparison of the wind speed, wind direction and hourly precipitation from the simulated and observed data in case of typhoons, 0416 and 0418.
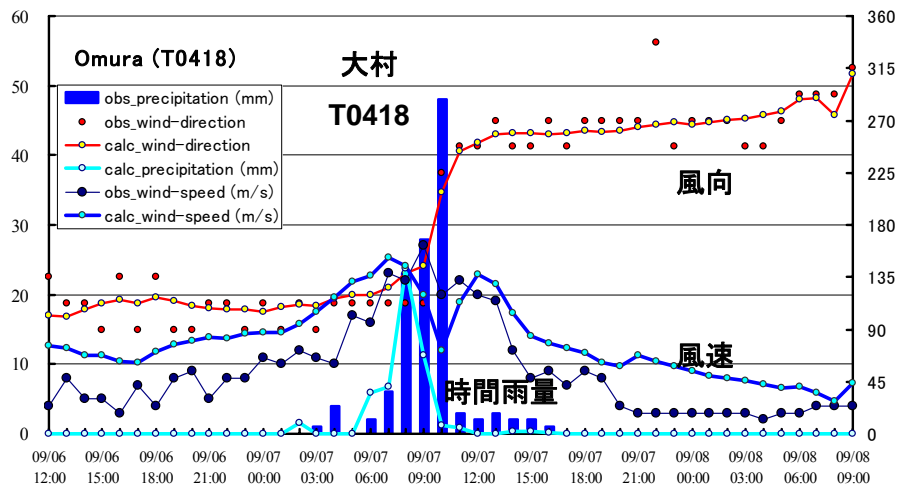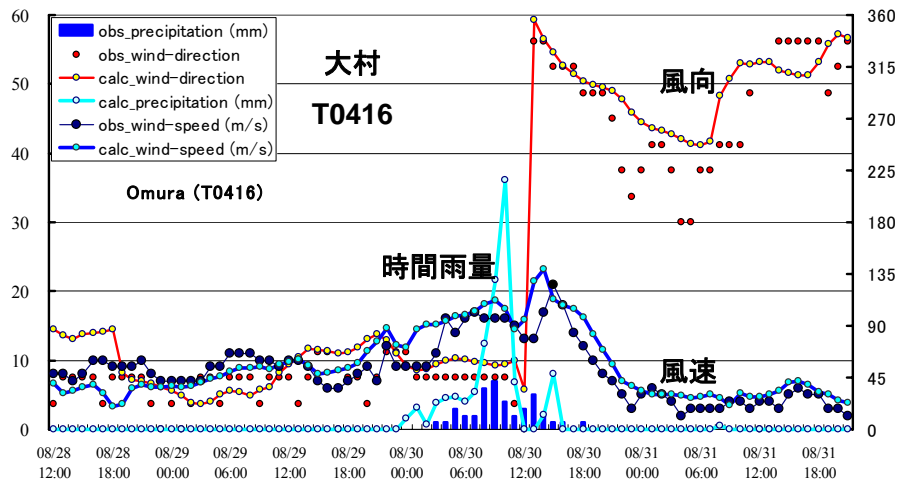
(b) At Omura bay (Nagasaki airport)

Fig. 6.3 Continued
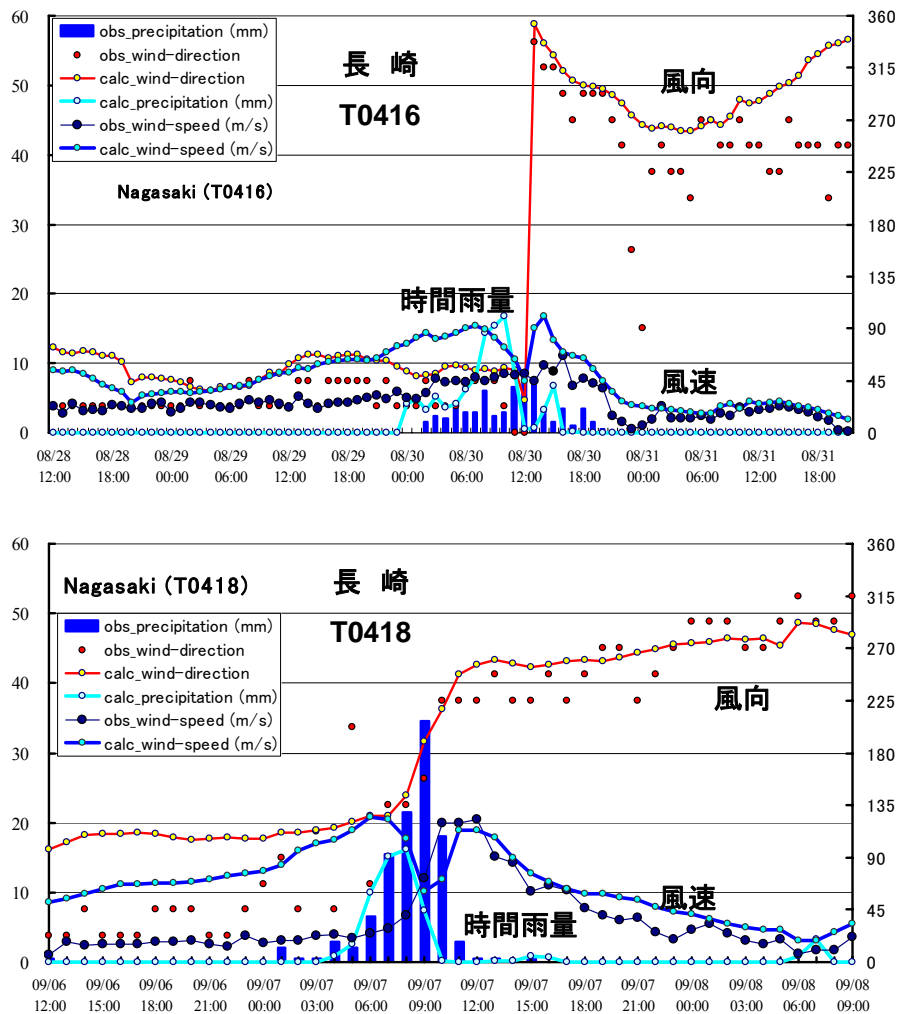
(c) At Nagasaki

Fig. 6.3   Continued

From the reanalysis

From the reanalyzed results by MM5, the cases of averaged wind speed over 15m/s in Omura Bay by typhoon and seasonal winds (mainly due to winter monsoon) were selected. The occurrence of the maximum wind for the simulation period was investigated and three of results were presented in Fig. 6.4, that showed the following characteristics.

1) Wind speed over the bay in any directions is estimated larger than that in vicinity area, because the topographical effects are significant in the vicinity of the bay.

2) Wind in southeast and northwest directions are generally estimated high in the bay that is due to the less effects of surrounding topography.

3) Northeasterly wind, the maximum wind is calculated at east of St.1, through east part of the bay whereas the maximum wind is simulated in St.2 through Nagasaki airport area in easterly

wind.

4) Wind field in south and west direction shows rather constant distribution and the maximum value of wind speed is less than 20m/s. But the general wind in south direction is somewhat estimated higher.

5) Maximum wind in north or northwest direction is estimated in southeast part (Nagasaki airport) of the bay while that in southeast direction is calculated in northwest area of the bay at St.1.

Extreme wind analysis from the reanalysis data

To evaluate the extreme wind in 30 years return period at two points, St.1 and Nagasaki airport, the extreme statistical analysis of wind had been performed with the annual maximum winds of the reanalysis database. The results of probable wind in 30 years return period in every direction were evaluated and presented in Fig. 6.5.

1) In the comparison of probable wind field in 30 years return period at Nagasaki airport and St.1, the probable wind in north through northwest direction, west-southwest through southwest direction and east direction at Nagasaki airport shows higher values than that at St.1

2) In south-southwest through east-southeast direction and northeast direction, the probable wind field at St.1 is higher than those at Nagasaki airport.
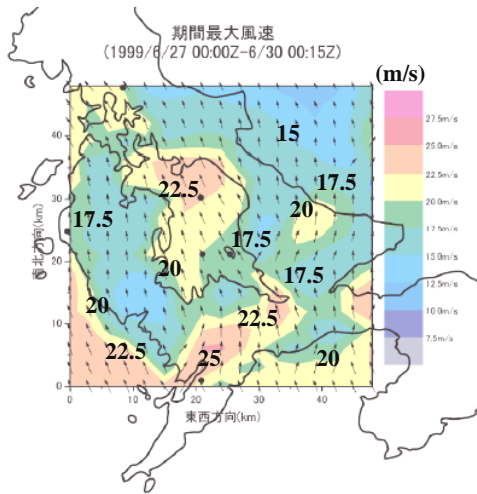
(a) Wind field in case of atmospheric low-pressure with fronts
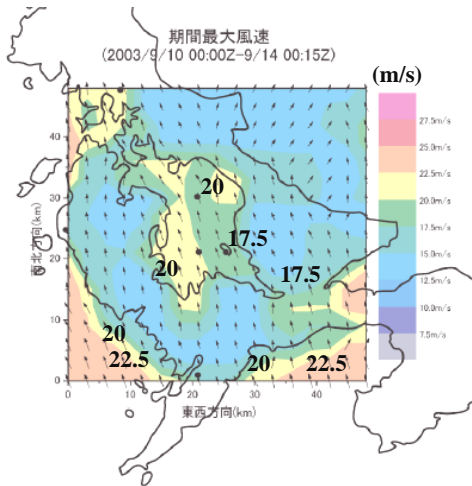
(b) Wind field in case of Typhoon 0314
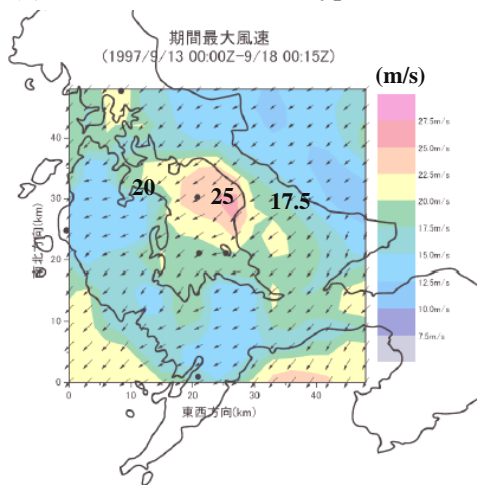
(c) Wind field in case of Typhoon 9719

Fig. 6.4   The maximum wind speed and direction during the simulation period in Omura Bay
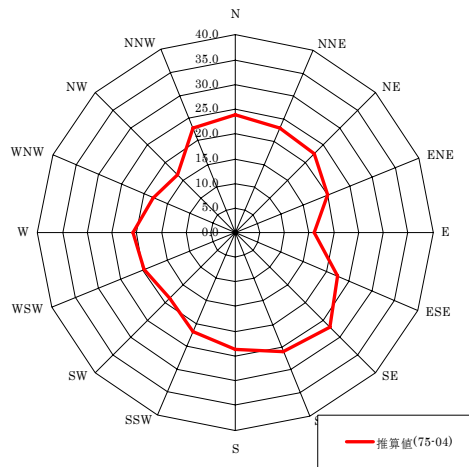
30年確率風速の比較

(a)   St.1
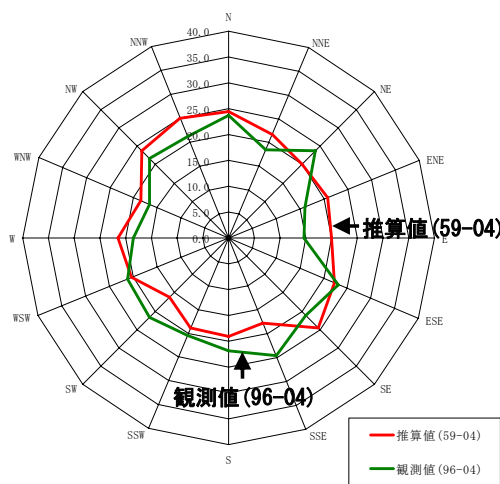
30年確率風速の比較

(b) Nagasaki airport

Fig. 6.5 Probable wind in 30 years return period at St.1 and Nagasaki airport estimated by
extreme statistic analysis of reanalysis database

6.2.3 Wind-induced residual currents in Ariake Sea

Since there have been significant changes in water circulation and consequent environmental and economical problems in fishery after the construction of Isahaya dyke in Ariake Sea, a number of related studies have been carried out in various kind of aspects to investigate such changes and problems (Arakai et al., 2001; Hiramatsu et al., 2005; Ohtsuka

2005). Although the tide and tidal currents system in Ariake Sea well studied with regards to the Isahaya dike construction (Kim, 2005), the wind-induced residual currents in Ariake sea has not studied well. The wind-induced currents as well as the tidal currents are very important forcing that determines the transport of sediments and tracers in water body. Even in the severe storm conditions, the wind-induced currents will directly derive the consequential results in material transports. Therefore the reanalyzsis data of the past major storm conditions would be very helpful to study and understand the long-term water circulation under the storm conditions in the Ariake Sea. Reanalysis data can be used for further study on long-term material transports caused by wind-driven currents.

Additional numerical simulations in addition to the reanalysis of wind field by MM5 (see Table 6.1) were performed to study the water circulation induced by winds. The primitive equation ocean model, POM, was used for this study with a tide simulation code incorporated in. The computational domain was same as the smallest domain of 3km grid size in MM5 computation as shown in Fig. 6.6(b). Eleven vertical sigma levels were used to resolve the water depth. The simulation periods of water circulation of each storm events were identical to those of MM5 simulations. Typhoon tracks selected for storm events in this study was shown in Fig. 6.6(a). The reanalyzed wind and atmospheric pressure were used for the meteorological forcing that derived the circulation in Ariake Sea. The temperature and salinity of Ariake Sea were assumed to be constant in vertical and horizontal directions. Thus homogeneous barotropic simulations were conducted. The real-time based water level variations by tide were imposed at the open boundary with free surface boundary conditions.

Model results

First, the results of tidal circulation were represented in terms of tidal residual currents and validated with the previous studies (Figs. 6.7 and 6.8). The incorporated tide model computed the major 8 diurnal and semi-diurnal constituents (M_2, S_2, K_1, O_1, N_2, K_2, P_1, and Q_1) separately and then they were composed for real-time simulation for the simulation periods. Four computational trials of the tidal residual currents were conducted, which are persistent currents induced by tide and very important for the long-term transport of sediment, tracers and any materials. The reanalyzed depth-averaged tidal residual current velocities shown in Fig. 6.9 depict good agreements with the observation and previous numerical study even though there exist some differences in the magnitude. The relatively large clockwise circulation in the northeast inner area of the bay (Fig. 6.8) was clearly reproduced in the simulation.

Tracks of reanalyzed typhoons
Data : Best Track data of 47 Typhoons
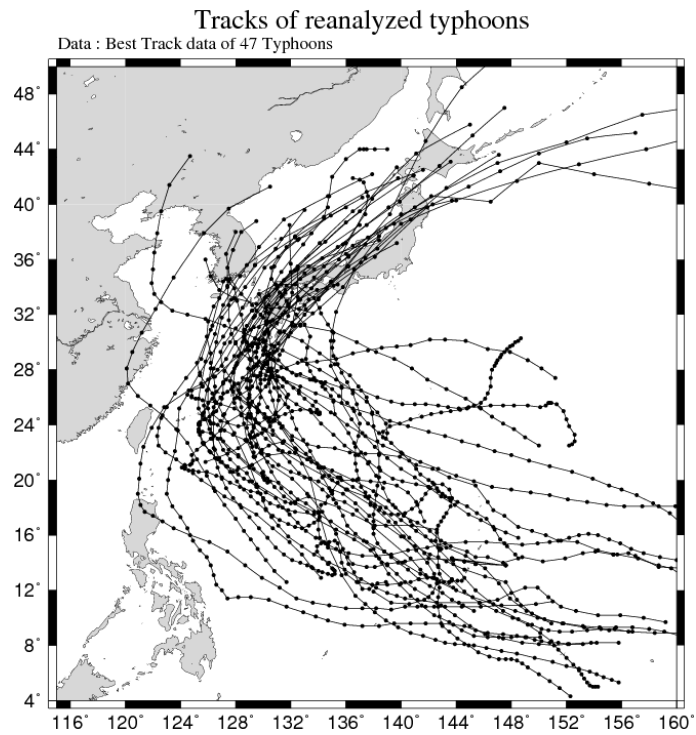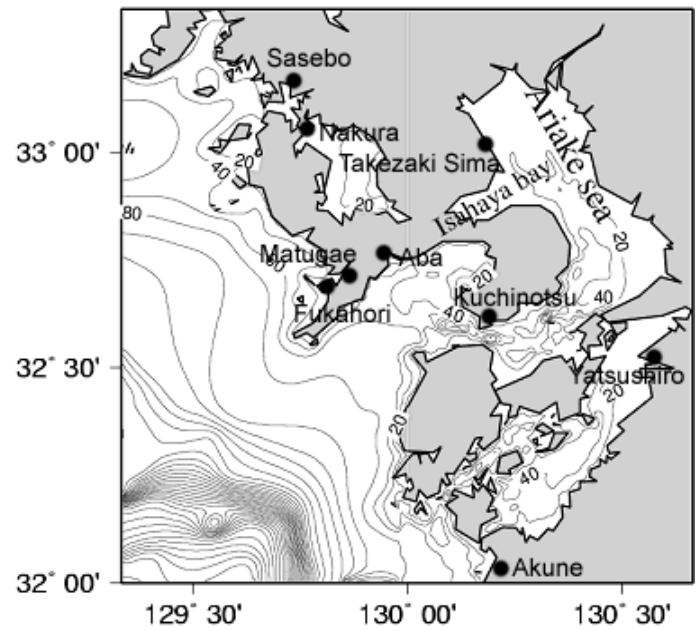
(a) Typhoon tracks

(b) Ariake sea

Fig. 6.6 The tracks of typhoons reanalyzed by MM5 and employed as same events for water circulation by POM (a). Computational domain 3 of Ariake Sea and Isahaya Bay with water depth contours. ● indicates tidal stations (b) (Kim, 2005).
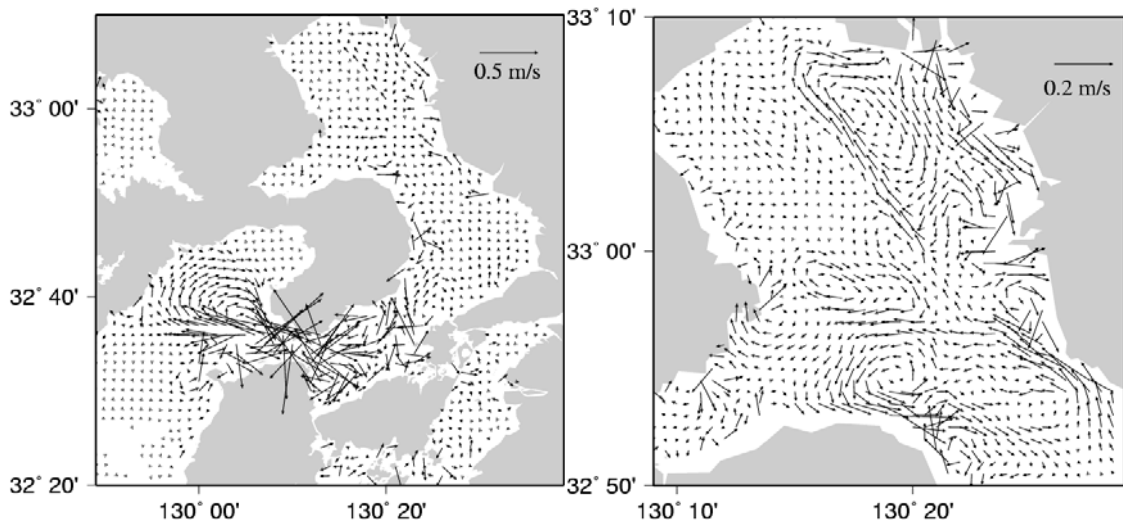
Fig. 6.7 Depth-averaged tidal residual current vectors (left: Ariake Sea, right: inner Ariake Sea; by Kim, 2005).
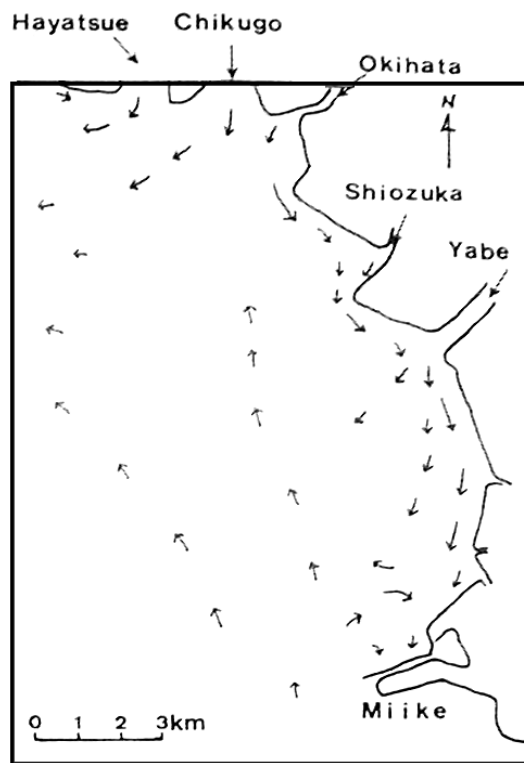
Fig. 6.8 Mean surface current pattern inferred from the drifter track observations made in July 1992. Cited from "A report on tidal analysis in Ariake Kai fishing grounds" by Sanyo Techno Marine Inc. (1993).

Tidal residual currents in Ariake sea
Event : 1979–t7920

10 cm/s

(a) One day (1979)

Tidal residual currents in Ariake sea
Event : 1991–t9109

10 cm/s

(b) One day (1991)

Tidal residual currents in Ariake sea
Event : 2001–06

10 cm/s

(c) Seven days (2001)

Tidal residual currents in Ariake sea
Event : 2004–t0423

10 cm/s

(d) Three days (2004)

Fig. 6.9 Simulated depth-averaged tidal residual currents velocities. The simulation periods were different (see Table 6.1).

Next, the wind-induced residual current velocities were evaluated as following procedures.

1) Simulations with real-time tidal water level open boundary conditions were first performed

for all listed storm events.

2) Simulations with the tidal boundary conditions were conducted with the external meteorological forcing such as momentum flux by reanalyzed wind and atmospheric pressure.

3) Wind-induced currents were calculated by subtracting the tidal residual currents from the second simulation results.

Four examples of the calculated wind-induced currents from the all reanalyzed data were presented in Fig. 6.10 for the same storm events of tidal residual current simulations shown in Fig. 6.9. It was interesting to note that the wind-induced currents showed their flow patterns depending on the track of typhoons. The strong southeastward wind-induced currents along the Ariake Sea channel were found when the typhoon passed through the south of Ariake Sea whereas the northwestward currents were revealed when the typhoon passed through the north of Ariake Sea. The small embedded upper right images show the track of typhoons. The magnitudes of almost all wind-induced currents were much larger than those of tidal residual currents implying that the wind-induced currents play crucial roles in the material transport in typhoon and storm conditions. In contrast to the currents situations inside Ariake Sea under the storm events, the wind-induced current in the mouth, Kuchinotsu (Fig. 6.6) showed that the strong tidal residual currents prevail determining the circulation in the narrow channel.

From these simulation results, one can deduce the interesting consequence that when a typhoon passes through the south of Ariake Sea in the peak of flood tide, the highly feasible energy focusing by currents and wind waves in south of the Sea can be expected, while when a typhoon passes through the north of Ariake Sea in flood tide, the energy could reach to the north of the Sea. These energy focusing could end up with physical storm surge events in the coastal area. The noticeable thing when a typhoon passes through the north of Ariake Sea in the peak of ebb tide, is that there might be reproduced a strong velocity shear between the southward ebb tidal currents and the strong northward wind-induced currents synoptically, which could induce the considerable turbulent mixing process in the south of Ariake Sea.
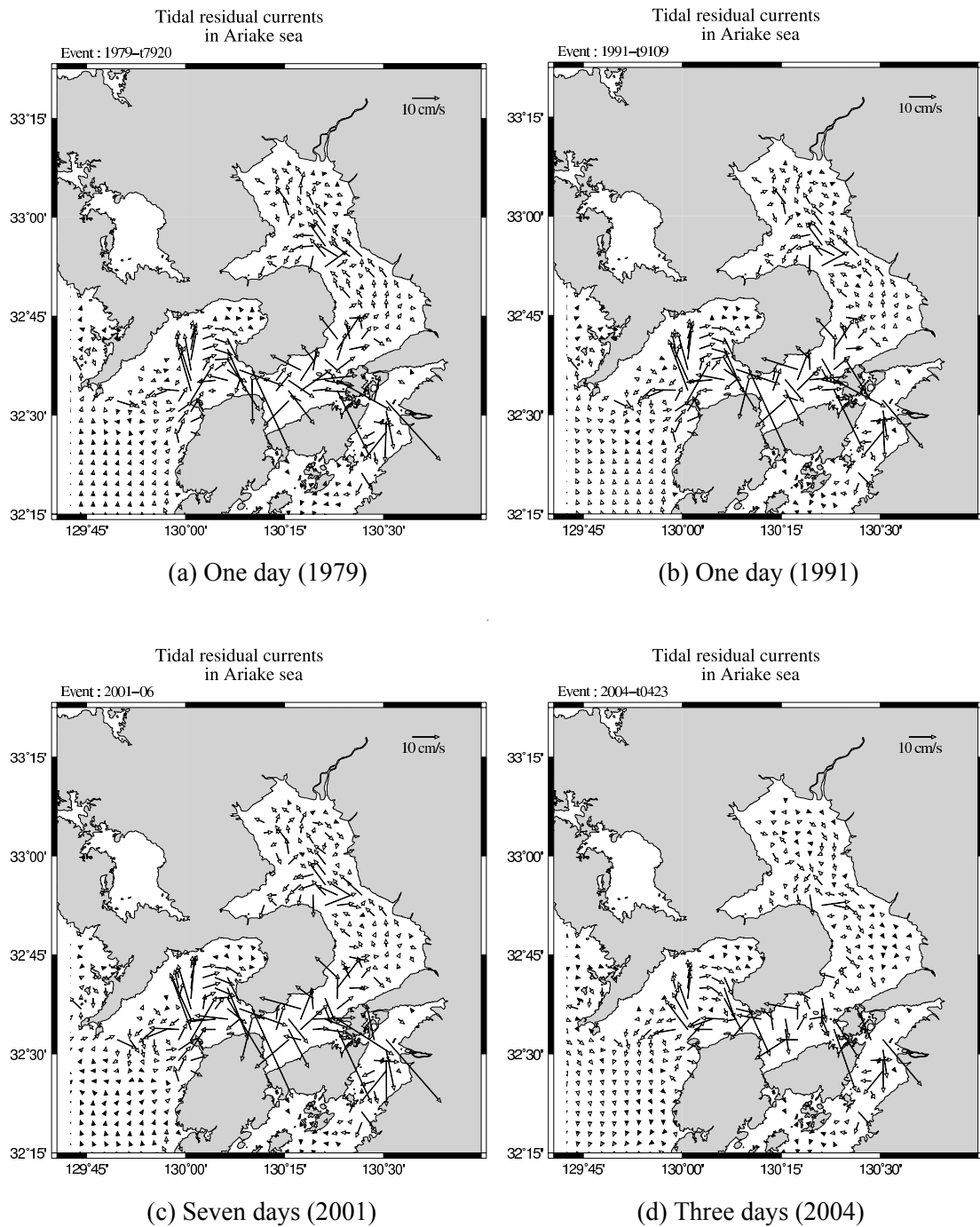
Fig. 6.11 shows the water discharge rate by wind-induced currents with the typhoon tracks. As the Ariake Sea has large tidal flats in its inner parts (Fig. 6.6), the water discharge rate in most tidal flats in Ariake Sea is relatively small compared to that in rather deep water region in the south of the Sea.

Fig.6.12 shows the long-term depth-averaged wind-induced residual currents in Ariake Sea and its vicinity which was derived from the reanalized water circulations of 47 storms in the sea. The overall current velocities remained weak less than 5 cm/s and the rather strong current in the vicinity became smaller in velocities. A clear counter-clockwise circulation was reproduced in the inner shallower area of the bay, that was linked to the northward residual currents in the central part of the sea off Kumamoto. However, clockwise tidal residual

circulation in the northeast inner bay was not reproced in the case of wind-driven residual currets.

Wind-driven residual currents in Ariake sea
Event : 1979-t7920

(a) T7920

Wind-driven residual currents in Ariake sea
Event : 1991-t9109

(b) T9109

Wind-driven residual currents in Ariake sea
Event : 1998-t9810

(b) T9810

Wind-driven residual currents in Ariake sea
Event : 2004-t0423

(b) T0423

Fig. 6.10 Simulated depth-averaged wind-induced residual current velocities computed by using atmospheric reanalysis data.

(a) T7920 (1 day)

(b) T9109 (1 day)

(c) T9810 (3 days)

(d) T0423 (3 days)
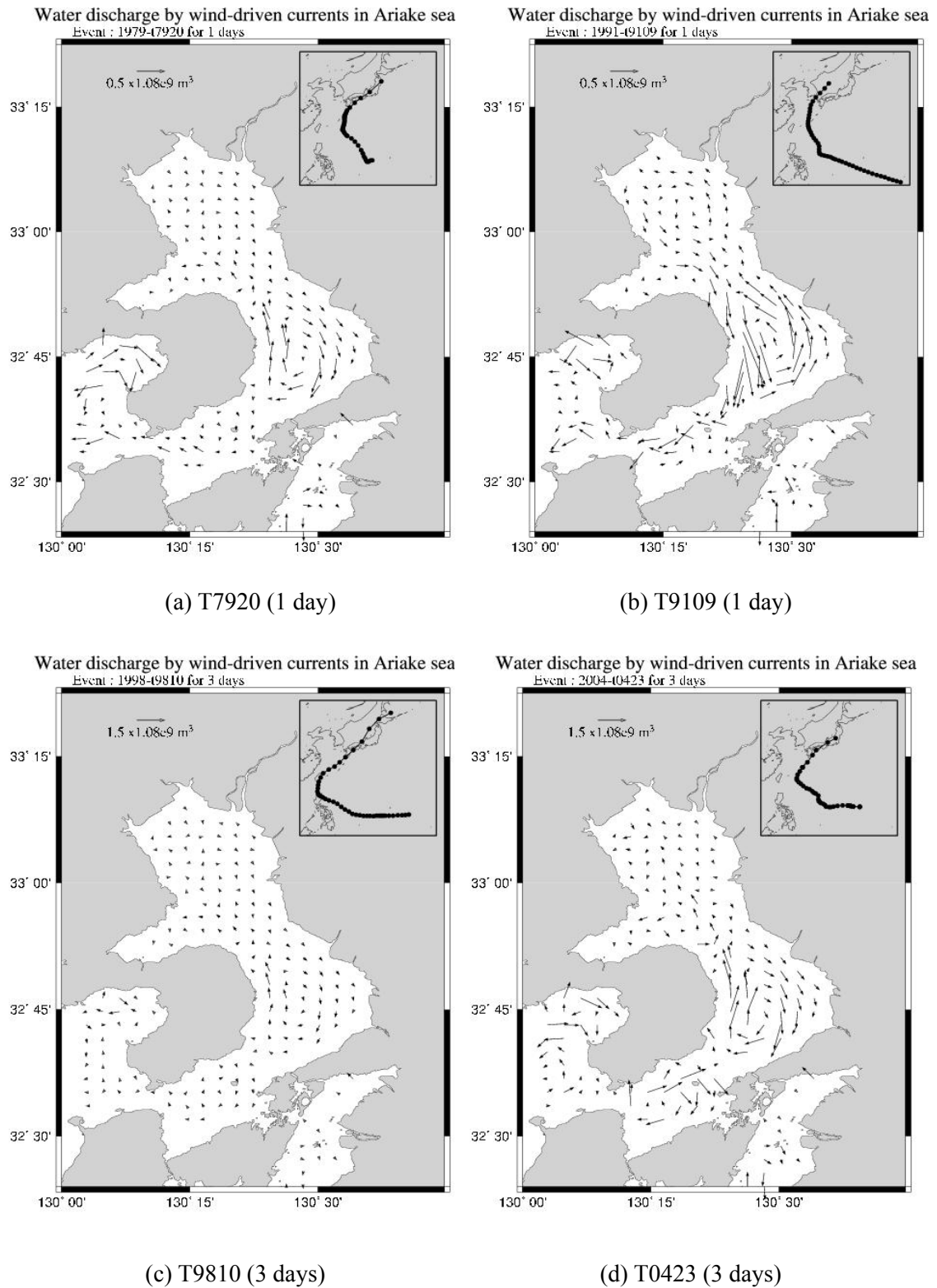
Fig. 6.11 Simulated water discharge rate by depth-averaged wind-induced residual (integrated) currents from the atmospheric reanalysis data. The upper-right embedded chart shows the track of typhoon.

Wind-driven residual currents
in Ariake sea

Event : 50typhoons
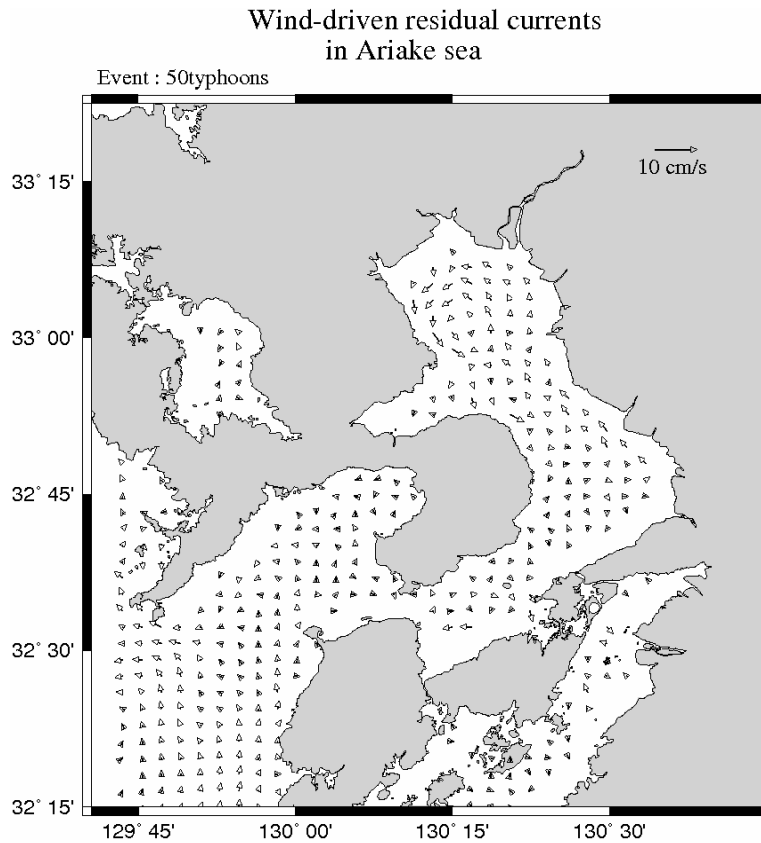
Fig. 6.12 Wind-induced residual current reproduced by 47 past major storms in Ariake Sea.

6.2.4 Summary

Mesoscale meteorological model, MM5 was used for the reanalysis of the 47 past major storms since 1959 including 42 typhoons that caused disasters in West Kyushu, Japan to consider the topographical influences on wind fields. The inventory of reanalysis results of the 47 storm events was constructed as a database including the 2D and 3D meteorological elements and now is available upon request with read-in FORTRAN code.

From the reanalysis results, the results of Typhoon 0416 and 0418 were presented and validated with the wind observations at Nagasaki, Sasebo and Omura (Nagasaki airport) stations. The screening effects by mountains and topographical obstacles at specific wind direction in the observed wind field were made clear and reproduced well in reanalysis results. Statistical analysis of extreme wind in 30 years return period in Omura Bay was also performed with the inventory of reanalysis data.

Study on wind-induced currents in Ariake Sea was carried out by using the primitive ocean model, POM, with the external forcing such as wind and atmospheric pressure from the reanalysis inventory. Tidal water level variations in time were imposed as an open boundary

condition in POM simulations. The results of these simulations can be summarized below.

1) The simulated tidal residual currents agreed well with previous numerical study by Kim, (2005) and field observation by Sanyo Techno Marine Inc. (1993). The clockwise circulation in northeast inner area of the bay is well reproduced in the simulation results.

2) Wind-induced currents in the Ariake Sea depend on the track of typhoons that pass through the north or south of the sea. From these wind-induced currents, the potential storm surge events in coastal area of the sea are deduced in combination with the tidal currents under storm conditions.

3) A clear counter-clockwise circulation was reproduced in the inner shallower area of the bay, that was linked to the northward residual currents in the central part of the sea off Kumamoto. However, clockwise tidal residual circulation in the northeast inner bay was not reproced in the case of wind-driven residual currets.
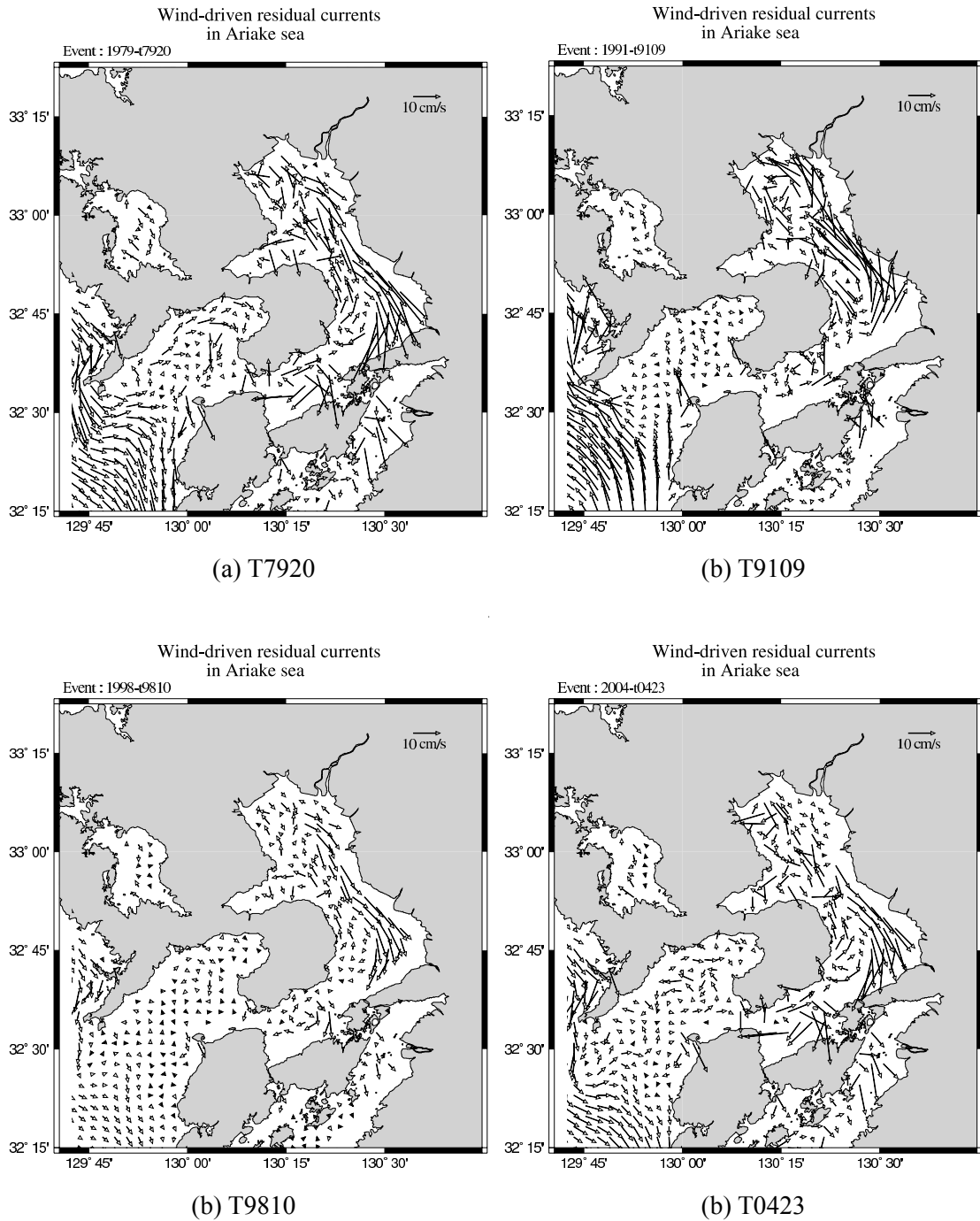
6.3 Wave breaking and overtopping

Results of ocean wave and circulation simulation initiate the connecting simulations of waves and currents in the nearshore. However, wave deformation in this nearshore region is so complicated because of depth-limited wave breaking that is the three-dimensional wave-turbulence mixture water motion with free surface boundary. So many nearshore hydrodynamic models have been developed to simplify this complex phenomenon for simulation of nearshore current and wave deformation (wave breaking) in the surf zone which are the main external forces of sediment transport, wave forces acting on the coastal structures, and overtopping water body crossing over the seawalls into the land. To simulate such water motions which may cause disasters in coastal area, we have to introduce another simulation model that can describe large scale turbulent motion including wave breaking, three-dimensional motion including both wave set-up and undertow. Unless small scale turbulent motions are concerned, a direct simulation method of Navier-Stokes equation system may be able to use for this purpose. VOF which was developed in 1980's is one of possible numerical schemes. CADMAS_FURF which was employed in REDES was developed based on VOF scheme as explained in Chapter 2.

6.3.1 Wave breaking

Surface wave breaking in shallow water is a phenomenon of momentum transfer from the waves to the ocean currents and turbulence. It generally occurs when the amplitude reaches the point that the crest of the wave actually overturns after wave crests got steepened as the amplitude increases. Breaking of surface water waves may occur anywhere that the amplitude is sufficient, including in mid-ocean. However, it is particularly common on beaches because waves are refracted towards the region of shallower water (because the phase velocity is lower there), and the shallow water also means that the same wave energy density gives rise to a greater surface amplitude.

There are four basic types of breaking water waves. They are spilling, plunging, collapsing, and surging (Sorensen, 1993). Those are,

Spilling : In this type of wave, the crest undergoes deformation and destabilizes, resulting in it spilling over the front of the wave. This wave tends to create a frothy appearance. It occurs most often on gentle beaches.

Plunging : Purportedly a rather dramatic form of break. The crest of the wave curls over and crashes into the base of the wave, creating a sizable splash. It tends to happen most often on steep beaches.

Surging : On steeper beaches, a wave might advance up without breaking at all. It deforms and flattens from the bottom. The front of the wave advances up towards the crest, creating reflection.

Collapsing : Collapsing waves are a cross between plunging and surging, in which the crest never fully breaks, yet the bottom face of the wave gets steeper and collapses, resulting in foam.

After the tip of the wave overturns and the jet collapses, it creates a very coherent and defined horizontal vertex. The plunging breakers create secondary eddies down the face of the wave. Small horizontal random eddides that form on the sides of the wave suggest that prior to breaking, the water motion is more or less two dimensional. This becomes three dimensional upon breaking. The main vortex along the front of the wave diffuses rapidly into the interior of the wave after breaking, as the eddies on the surface become more viscous. Advection and molecular diffusion play a part in stretching the vortex and redistributing the vorticity, as well as the formation of turbulence cascades. The energy of the large vortices is transferred to much smaller isotropic vortices (turbulence) and mean currents. These characteristics of wave breaking including momentum transfer from wave motion down to the large and small eddies can not be simulated well by the numerical models based on the potential wave theory.

6.3.2 Wave overtopping

For the design and maintenance works of coastal structures, reliable predictions of wave overtopping are required. Wave overtopping (usually the mean overtopping discharge) has been estimated by empirical or simplified numerical models. The mean overtopping discharge varies with the shaper of seawall, crest level of seawall, water level and wave conditions.

Empirical models or formulae use relatively simple equations to describe wave overtopping discharges in relation to defined wave and structure parameters. Empirical equations and coefficients are, however, limited to a relatively small number of simplified structure configurations. Their use out of range, or for other structure types, may require extrapolation, or may indeed not be valid.

Numerical models of wave overtopping may be less restricted, in that any validated numerical model can (in theory) be configured for any structure within the overall range covered (see Figs. 6.13(a) and (b)). In REDES, 2D VOF (Volume of Fluid) scheme model, CADMAS-SURF developed by the Coastal Development Institute of Technology (see Chapter 2), was employed for the wave overtopping simulations. This model can compute a free water surface deformation together with air entrainment into water and overtopping onto the land over through the seawalls with an arbitrary cross section.

(a) Wave overtopping over the seawall in UK

(b) Wave overtopping over the seawall in Hokkaido, Japan

Fig. 6.13 Pictures of sea water splash caused by wave overtopping

6.3.2.1 Overtopping simulation method by CADMAS-SURF

The severe storms cause the wave overtopping over through coastal structures such as breakwaters and seawalls resulting in inundation disasters in the hinterland. In this study, overtopping simulation methods was conducted by using 2D CADMAS-SURF which was connected to offshore waves and sea levels (surges) conditions simulated by atmosphere-ocean coupled model. Incident waves in the surf zone simulation are assumed to be regular waves in this study. Three cases of preliminary numerical experiments were conducted by assuming computational cross-sections of nearshore topography and seawall which are presented in Figs. 6.14(a) and (b) with installed wave gauges. Case 1 is the case of original cross-section. Case 2 is the case of 2m rising of seawall crest level. Case 3 is the case of submerged offshore breakwater

construction on Case 2 cross- section. The computational domain was discretized as $\Delta x \approx (\Delta L/300)$ and $\Delta z = (\Delta H/20)$ where Δx is the grid interval in x-direction and Δz is in z-direction, ΔL is the wave length and ΔH is the wave height. The incident wave generation was imposed by Stokes wave theory with 5m in height and 8sec in period for all experiments (Fig.6.15). Sommerfeld's radiation condition was employed at the open boundary where the incident wave generation condition is imposed. Experimental conditions of overtopping simulation were summarized in Table 6.4.

Table 6.4 Experimental conditions of overtopping simulation.

Cross Sections	Wave generation
Case 1 (original cross-section)	H:5m,T:8sec,Stokes wave
Case 2 (2m rising of seawall crest)	H:5m,T:8sec,Stokes wave
Case 3 (Case 2 + submerged offshore breakwater construction)	H:5m,T:8sec,Stokes wave
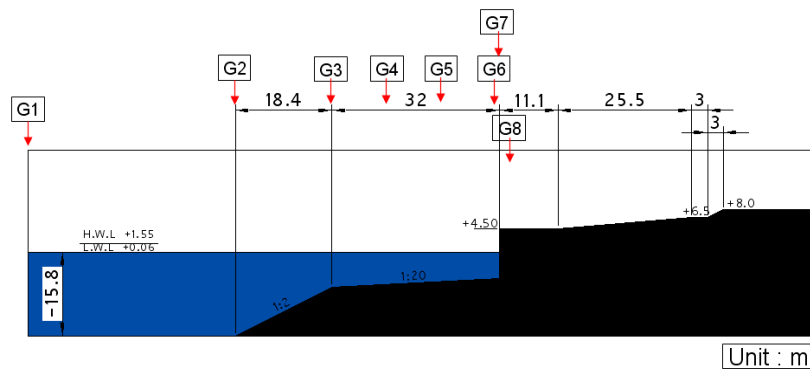
(a) Case 1 (Original)
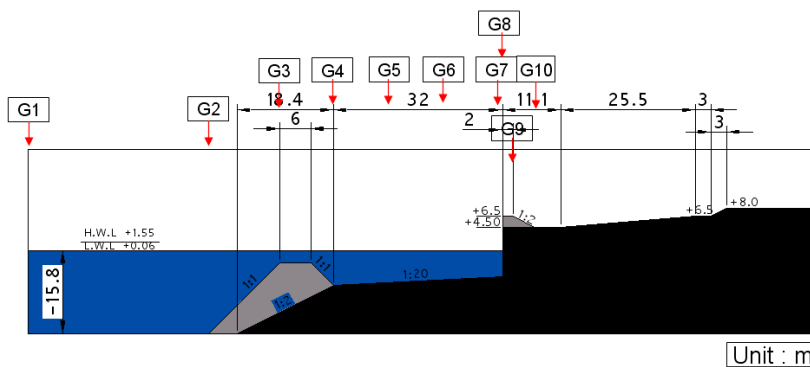
(b) Case 2 (2m rising of seawall crest) and
Case 3 (+submerged offshore breakwater construction)

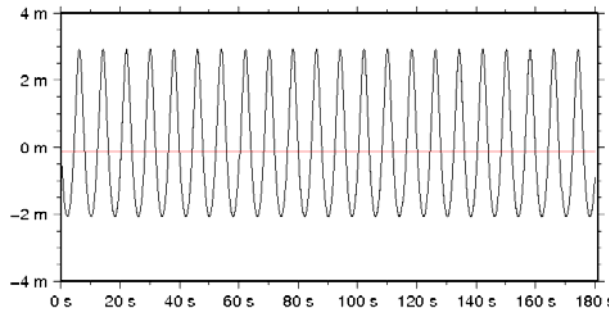Fig. 6.14 Three cases of assumed cross sections of seawall

Fig. 6.15 Incident wave profile given by Stokes wave theory.

6.3.2.2 Simulation results

Computed wave profiles at gauges G1 through G8 for Case 1 are shown in Fig. 6.16, and wave profiles at wave gauges G1 through G10 for Case 3 are in Fig. 6.17. Wave profiles in these figures are defined as the water surface variations in time that were detected by CADMAS_SURF including splashes and air entrainments. The red line in the figure is the mean water level computed by time-averaging of the wave profiles. The transient discharge per unit width was calculated by Eq. 6.1 after assuming that the inner crest area behind seawalls is filled with water up to the water level measured at wave gauges (G9 in Case 2 and G10 in Case 3).

$$q = \left(\frac{\partial h}{\partial t} \right) b \qquad (6.1)$$

where h is the water level measured by gauge G9 or G10, t is simulation time, and b is the length of upper side of water-filled trapezoid which is formed by the assumption. Therefore, it is obvious that the calculated cumulative discharge (total water volume) is a little overestimated since the inner crest area behind the seawall is never filled completely with water at transient time. The cumulative discharge rate by these simulations, however, helps us estimate the effects of enhanced seawall and submerged offshore breakwater on wave overtopping, synoptically.

(1) In Case 1, the water level variation at G7 and G8 shows the constant overtopping after the first overtopping about 15s after starting the simulation because the water levels at G6 are continuously higher than the initial level that is the height of seawall crest.

(2) In Case 3, the effect of submerged offshore breakwater can be seen in the water level variation at G5 which shows constant dissipation of incident wave energy just after the breakwater. The overtopping frequency at G8 seems to be increasing due to the breakwater, however the water level variation got remained same as the initial level at several times from 30~40sec, 75~80sec, 155~160sec and 170~180sec. The water level variation at G9 and G10 showed further reduction of overtopping water volume due to construction of offshore submerged breakwater.

(3) Cumulative curve of computed overtopping discharge in Case 2, measurement at G9 is shown in Fig. 6.18 that depicts the overtopping discharge rate increases gradually in the initial stage and then becomes increased after equilibrium stage. Its rate is about 1.625 $m^3/s/m$.

(4) The cumulative wave overtopping discharge per unit width in Case 3 shown in Fig 6.19 is reduced about 50 m^3/m compared to the value of enhanced seawall design (Case 2). The discharge rate increases rapidly before 40s and then becomes lower after the equilibrium state. Its rate is about 0.625 $m^3/s/m$.
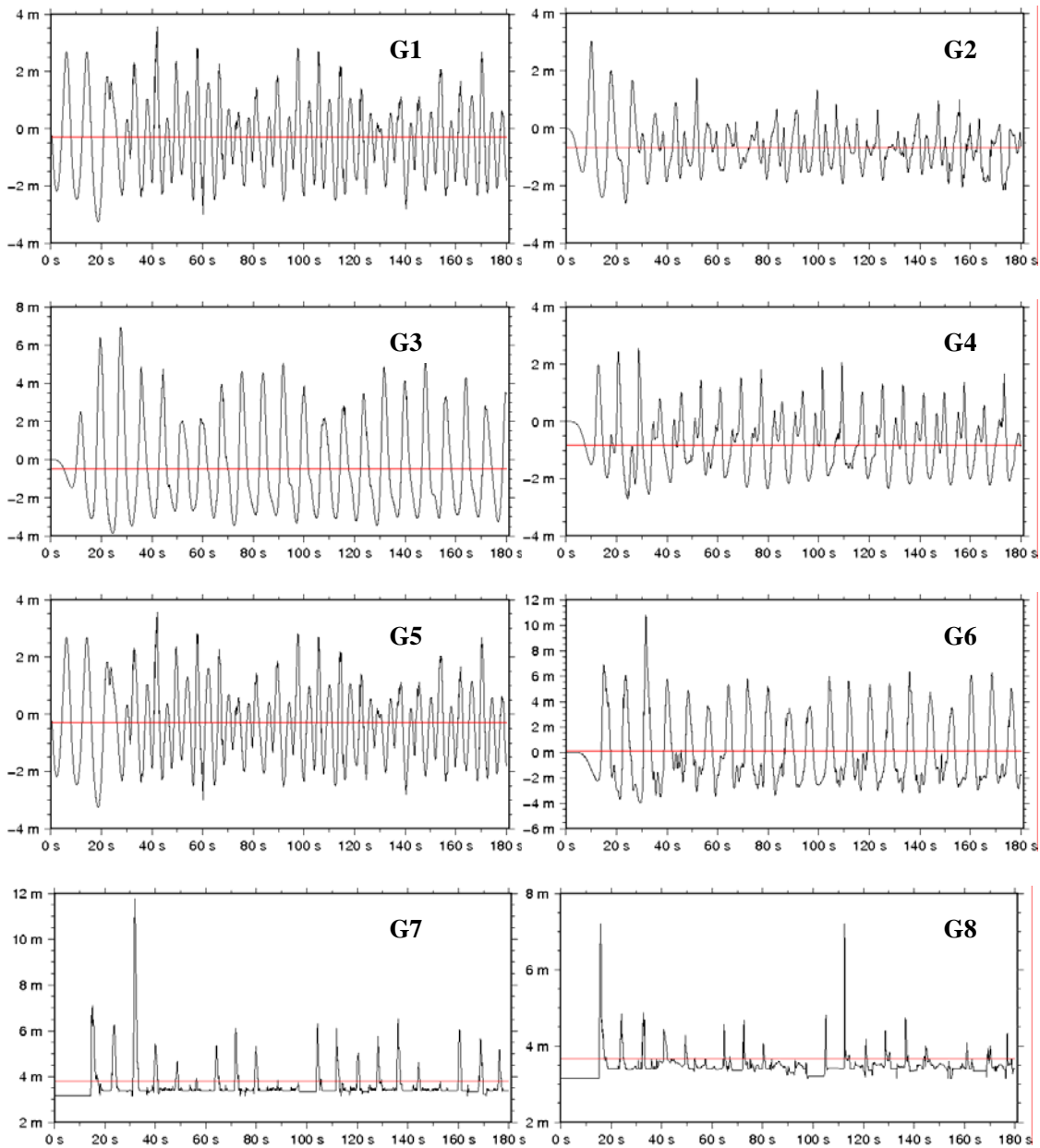
Fig. 6.16 Computed wave profiles at gauges G1 through G8 for Case 1
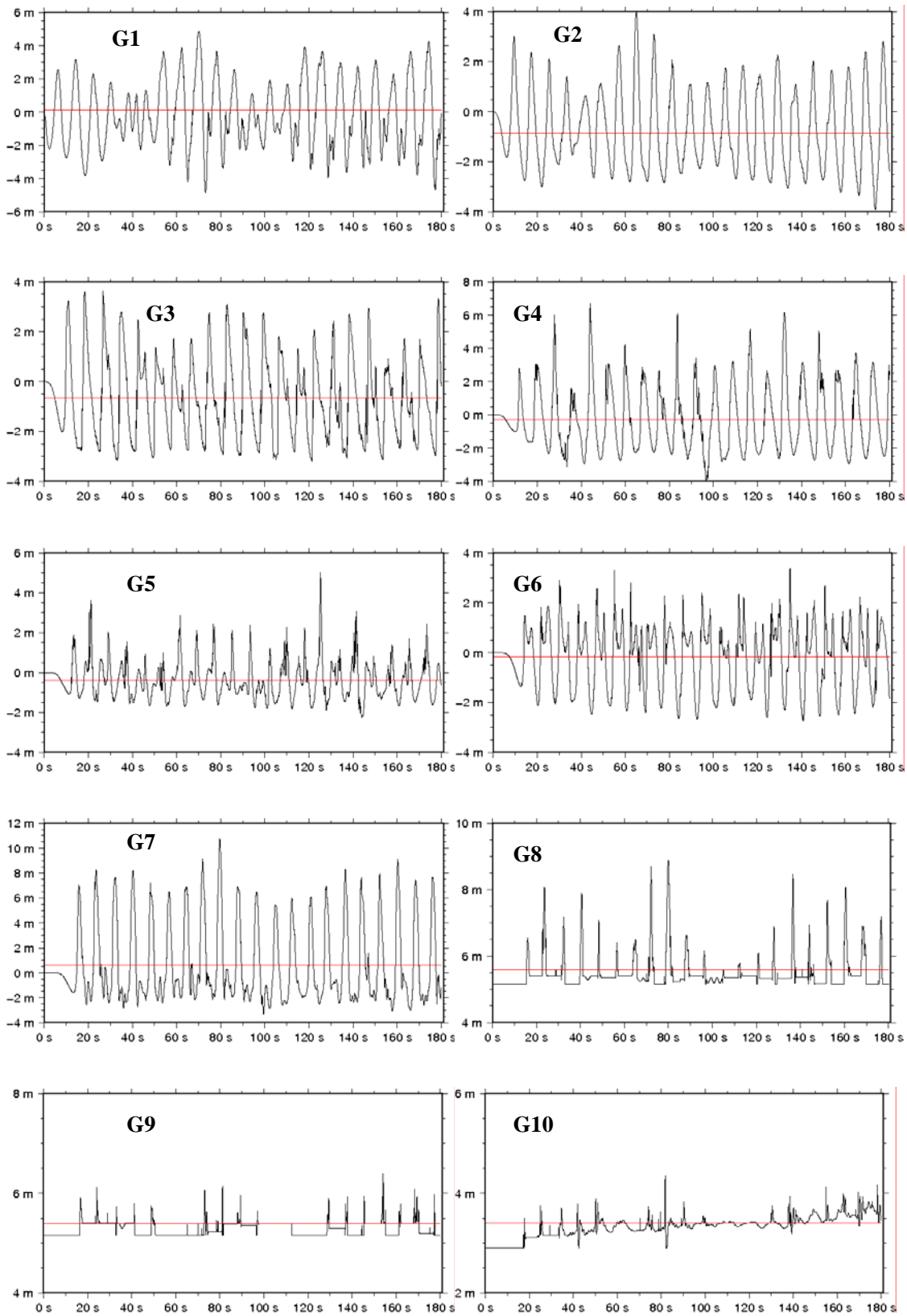
Fig. 6.17 Computed wave profiles at wave gauges G1 through G10 for Case 3

161
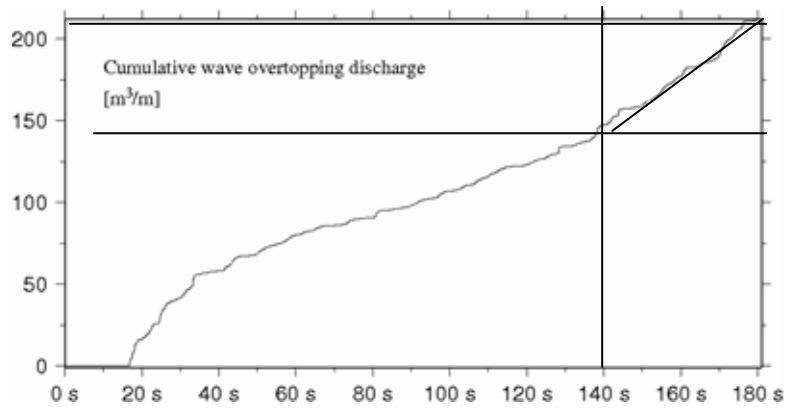
Fig. 6.18 Cumulative curve of computed overtopping discharge in Case 2
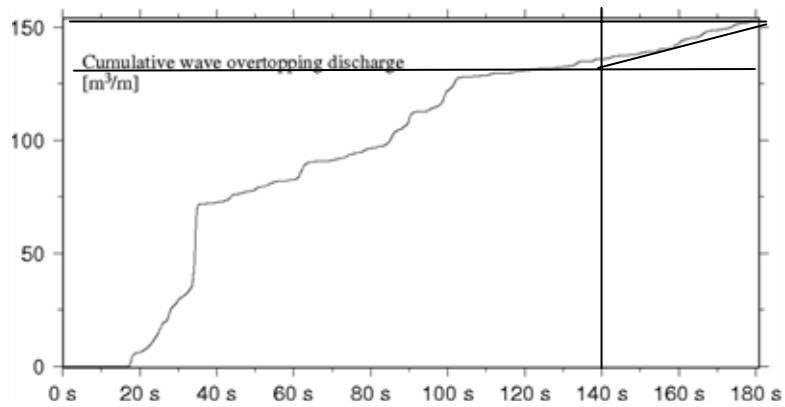
Fig. 6.19 Cumulative curve of computed overtopping discharge in Case 3

6.3.3 Summary and discussion

Results of ocean wave and circulation simulation initiate the connecting simulations of waves and currents in the nearshore. To fulfill the connecting simulations of water waves and currents in shallow water which may cause disasters in coastal area, 2D CADMAS-SURF which was developed based on VOF scheme was employed in REDES.

Three cases of preliminary numerical experiments were conducted by assuming computational cross-sections of submerged offshore breakwater and enhanced seawall with installed wave gauges. From the water level profiles at gauges and derived cumulative discharge rates, it is found that the submerged breakwater construction and enhance seawall reduce the frequency of wave overtopping occurrence and overtopping discharge rate. The submerged breakwater is effective to reduce the wave overtopping discharge.

By extending this preliminary experiment of CADMAS-SURF, it will be connected to

offshore waves and sea levels (surges) conditions simulated by atmosphere-ocean coupled model.

6.4 Conclusions

The conclusions from the reanalysis of the past major storms are as follows.

1) Atmospheric mesoscale model, MM5 was applied to past storm events in West Kyushu, Japan to take into account the topographical influences on wind fields. The storm events were comprised of 47 storms including 42 typhoons, low-pressure system with fronts and atmospheric developed low-pressure in winter since 1959.

2) The inventory of reanalysis results of the 47 storm events was made as a database including the 2D and 3D meteorological elements and now is available upon request with read-in Fortran code.

3) The results in case of Typhoon 0416 and 0418 were presented and validated in comparison with the wind observations at Nagasaki, Sasebo and Omura (Nagasaki airport) stations. The screening effect by mountains and topographical obstacles was made clear by analyzing the observed winds and this effect was reproduced well in reanalysis results.

4) The wind-induced currents estimated by using the reanalyzed data were proven to be important in the water circulation and material transport in the Ariake sea. The possible storm surge regions by the interaction of tidal residual currents and wind-induced currents were deduced from the simulation results of wind-induced currents.

To extend the applicability of REDES to nearshore wave deformation and coastal problem such as wave overtopping and the consequential inundation, preliminary experiments on wave overtopping had been made by 2D CADMAS-SURF with regular incident waves by Stokes wave theory.

1) Three cases of wave overtopping simulation were carried out by assuming computational cross-sections of submerged offshore breakwater and enhanced seawall. The effect of enhanced seawall and submerged breakwater was clearly shown in water level profiles measured at wave gauges and cumulative wave overtopping discharge rate. The submerged breakwater is very effective to reduce the wave overtopping discharge inferred from the results of preliminary experiments.

References

Araki, H., Sato, K., Koga, K., Yamanishi, H. Ohgushi, K. and Liengcharernsit, W., (2001): Study on environmental change and peculiarity of Ariake Sea, Japan, *Water Resources Management*, 341-350.

Hiramatsu, K., S. Shikasho and K. Mori, (2005): Numerical prediction of suspended sediment concentrations in the Ariake Sea, Japan, using a time-dependent sediment esuspension and deposition model, *Paddy and Water Environment*, **3(1)**, 13-19.

Kim, K. (2005): Coastal ocean model with consideration of meteorological-oceanographic mesoscale interaction, Ph.D dissertation, Kyoto University, Japan.

Kim, K., H. S. Lee, and T.Yamashita, (2005): Winter Huge Wave Simulation in Japan Sea by MM5 and WW3 Coupled Model Using Depression Bogussing, *Annual Journal of Coastal Engineering, JSCE*, Vol.52, pp.176-180. (in Japanese)

Ohtsuka, T., (2005): Epipelic diatoms blooming in Isahaya Tidal Flat in the Ariake Sea, Japan, before the drainage following the Isahaya-Bay Reclamation Project, *Phycological Research*, **53 (2)**, 138–148.

Sorensen, R. M., (1993): Basic wave mechanics: For coastal and ocean engineers, Wiley-Interscience Pub., 304pp.

Yamaguchi, K., T.Yamashita, and K.Kim, (2005): SST Effects of Kuroshio Warm Current on Precipitation and Surface Wind Fields by the Simulation of Meso-Scale Meteorological Model (MM5), *Annual Journal of Coastal Engineering, JSCE*, Vol.52, pp.366-370. (in Japanese)

Chapter 7

Concluding Remarks

The Regional Environment and Disaster Prevention Simulator was proposed and constructed in this study of which objective was improvement of the numerical assessment method to disaster events and environment problems by introducing the coupling effects between different systems. Its applications were conducted to various scale processes from local air-sea interaction such as typhoon-ocean interaction, storm surge and extreme high waves to small scale processes in thermal circulation in inland lake. Concluding remarks in this chapter summarize the section conclusions and summaries that were found by the numerical studies.

Regional Environment and Disaster Prevention Simulator (REDES)

An atmosphere (MM5) and ocean (MITgcm) coupled model with surface wave interface (WW3/SWAN) was developed in this study. The idea of "simulator" was proposed in which interaction can be investigated as coupling effects between different systems through the existing interactions and to enhance our understanding of the physical processes of natural disasters and environmental factors.

The Regional Environment and Disaster Prevention Simulator (REDES) was established in this study, that consists of public domain models mainly for atmospheric and oceanic circulation, ocean wind waves which have been constructed by integrating scientific basic knowledge and technological new findings in many research communities all over the world. The two types of regional coupled simulations (combination of modules of REDES) were conducted in this study. Their model structure and objectives are;

1) Wind(MM5)-wave(WW3)-current(POM) coupled model uses the specially-designed coupler for exchanging data such as wind, pressure, current and water level. This wind-wave-current model has been extensively used for storm surge simulations.

2) The atmosphere (MM5) and ocean (MITgcm) coupled model was developed by using special coupler based on the state-of-the-art coupling library called OASIS3 for controlling the coupled model, transferring and regridding the data between the component models. The ocean state is

simulated in baroclinic condition in this atmosphere and ocean coupled model, while the ocean is treated in barotropic condition in wind-wave-current coupled model.

3) REDES has been developed to improve the numerical assessment method to disaster events and environment problems by introducing the coupling effects between different systems through the existing interactions and to enhance our understanding of the physical processes of natural disasters and environmental issues.

Storm surge caused by Hurricane Katrina

Bogus scheme is necessary to reproduce the wind field and typhoon intensity for the storm surge simulation in barotropic condition. However, special care is needed for the R_{MX} values, grid size of the domain and the baroclinic simulation of ocean when the bogus scheme is applied.

One of the additional stresses from waves to ocean currents in the coupling process computation, the stress by wave breaking (whitecapping), plays very important role in storm surge in shallow region where the wide continental shelf is developed. The water level variation in time at Ocean Springs depicts well the significance of the breaking stress (τ_{br}) by whitecapping dissipation in the coupling process for storm surge simulation. The computed water level shows good agreement with the observations in wave-current coupled run while the water level in uncoupled run shows considerable discrepancy.

Extreme high waves by Typhoon 7920

Typhoon TIP which is the strongest typhoon that human have ever recorded, caused huge damages in the coastal region in Suruga Bay by accompanied storm surge, high waves, wave overtopping. The extreme high waves observed at Hara (inner station in the Suruga Bay) were discussed by means of the simulation results with wind-wave-current coupled model. The results of numerical simulation showed that the estimated wave climate around Suruga Bay depicted general agreement with the observed values except at Hara.

Some possibilities to explain the high waves at Hara are discussed. Those are typhoon bogus scheme employed in mesoscale meteorological model, MM5, wave-current interaction, and the resonance of seiche in the Suruga Bay. From these results, it would be carefully summarized that the high waves observed at Hara might actually occur in the Suruga Bay. It may be reproduced by the simulator if the shortcoming of typhoon bogus scheme (smoothed maximum wind near the radius of maximum winds) is made clear. Bogus scheme need special care as revealed by storm surge simulation by Hurricane Katrina when applied.

Numerical Experiment of Typhoon-Ocean Interaction

A 3D non-hydrostatic atmosphere and ocean coupled model of REDES was used to investigate the typhoon-ocean interaction over the baroclinic ocean state including Kuroshio Warm Current (KWC). The two-way typhoon-ocean interaction experiments were performed under the real Typhoon 0310 (ETAU) from 00:00 UTC 5th Aug. to 18:00 UTC 8th Aug., 2003. The following three cases were conducted as; 1) the atmosphere-alone (uncoupled) run, 2) the ocean-alone (uncoupled) run and 3) last, the atmosphere-ocean (coupled) run. The important initial condition for ocean state was imposed from a regional high-resolution (1/12° deg and 45 vertical levels) ocean reanalysis data by Japan Coastal Ocean Predictability Experiment (JCOPE) for the day of the 3rd Aug. 2003 and two-days spin-up had been performed until the start of coupled run.

1) The ocean responses to Typhoon ETAU in the coupled run were presented in terms of the currents in ocean mixed layer, sea surface temperature (SST) cooling and changes of vertical temperature profile. The asymmetric divergent currents in ocean mixed layer that result from the wind stress acting on the inertially rotating flow were clearly revealed. Interestingly, the asymmetric divergent patterns of mixed layer currents were maintained well after the passage of typhoon, which were generally over 1.5m/s and induced the consequential continuous SST cooling behind the typhoon. The mixed layer currents changed their direction from the northeastward to southeastward about one day after the passage of typhoon. The ambient flow in the real ocean played an important role that limits the spatial scale of divergent mixed layer currents less than about 300km in its radius.

2) In the vertical temperature profile changes, the SST cooling due to the cool thermocline water brought by the velocity shear between ocean mixed layer currents and thermocline currents was shown. Simulated SST reductions were validated with the SST observation by Tropical Rainfall measuring mission (TRMM) satellite.

3) In typhoon response in the coupled run, the net heat flux (sensible plus latent) was reduced about 350-400W/m^2 in the cold wake of typhoon and its distribution well coincided with the distribution of SST anomaly mainly due to the decrease of latent heat flux. Accompanied by the decrease of net heat flux, the total precipitation and the equivalent potential temperature were reduced with 5% (about 300mm) and 6°-7° in maximum locations, respectively.

4) The influence of KWC which produces large horizontal SST gradient was evaluated with respect to typhoon intensity when Typhoon 0310 moved onto KWC. After typhoon moved on KWC until it made landfall, the typhoon maintained its intensity for about one day due to the constant heat supply from KWC. In the coupled run, however, the influence of KWC just before the landfall was not able to be captured due to the lager decrease of SST (2-3℃) than the observed value. It is partially explained that the horizontal mixing processes might also important in SST cooling in high horizontal SST gradient condition of ocean. The boundary

condition with 2-days temporal resolution of JCOPE data is not sufficient to supply the persistent heat budget from KWC.

5) Initial condition is very significant for ocean computation. JCOPE data used for the initial ocean states in the present study rather underestimated in SST in wide region below the KWC such that resulted in significant changes in typhoon intensity. Although surface waves may play crucial roles in air-sea interaction such as heat flux exchanges, SST changes, momentum flux transfer, etc, the surface wave is not taken into account in this coupling model.

Dam Lake Hydrodynamics

The wind induced currents, thermal structure and its evolution, and the internal waves in Yachiyo Lake, Hiroshima were investigated by REDES of 3D non-hydrostatic model system of meteorological (MM5) and oceanic (MITgcm) circulation models.

1) The thermal structure of Yachiyo Lake and its evolution simulated for one month, July in 2006, with the meteorological forcing of the surface heat flux transfer showed good agreements with the observations. The diurnal cycle of heating and cooling in clear days and the local convection in rainy days in response to the surface cooling were clearly identified.

2) The internal gravity waves below the thin surface layer are sometimes depicted in large displacement of isotherms up to 2m in the lake in the direct response to the wind stress.

3) As identified by non-dimensional gradient Richardson number, the Yachiyo Lake is under control of strong stratification in summer. Therefore the wind stress plays important role in lake circulations.

Reanalysis of past major storms in West Kyushu

The reanalysis of the past major storms were performed with wind-wave-current coupled model of REDES.

1) Atmospheric mesoscale model, MM5 was applied to past storm events in West Kyushu, Japan to take into account the topographical influences on wind fields. The storm events were comprised of 47 storms including 42 typhoons, low-pressure system with fronts and atmospheric developed low-pressure in winter since 1959.

2) The inventory of reanalysis results of the 47 storm events was made as a database including the 2D and 3D meteorological elements and now is available upon request with read-in Fortran code.

3) The results in case of Typhoon 0416 and 0418 were presented and validated in comparison with the wind observations at Nagasaki, Sasebo and Omura (Nagasaki airport) stations. The screening effect by mountains and topographical obstacles was made clear by analyzing the observed winds and this effect was reproduced well in reanalysis results.

4) The wind-induced currents estimated by using the reanalyzed data were proven to be important in the water circulation and material transport in the Ariake sea. The possible storm surge regions by the interaction of tidal residual currents and wind-induced currents were deduced from the simulation results of wind-induced currents.

Wave overtopping simulation

To extend the applicability of REDES to nearshore wave deformation and coastal problem such as wave overtopping and the consequential inundation, preliminary experiments on wave overtopping were made by 2D CADMAS-SURF with regular incident waves by Stokes wave theory.

1) Three cases of wave overtopping simulation were carried out by assuming computational cross-sections of submerged offshore breakwater and enhanced seawall. The effect of enhanced seawall and submerged breakwater was clearly shown in water level profiles measured at wave gauges and cumulative wave overtopping discharge rate. The submerged breakwater is very effective to reduce the wave overtopping discharge inferred from the results of preliminary experiments.

For future studies

It can be confirmed that REDES is effective in simulation of disaster events and regional environment assessment. However it still has many possibilities of extension and parts to be improved. I would like to summarize the works that need for further development of REDES.

The interaction between element systems of REDES and our understating of physical processes in boundary layer are very limited. The role of ocean waves between air and sea and the behavior of ocean waves under typhoon condition are still in veil in many parts.

Those are (1) the storm surge simulation generally considers only the momentum flux transfer from wind to wave and from wave to current with barotropic ocean condition. In the mean time, the simulation for prediction of typhoon intensity and track considers the air-sea interaction with baroclinic ocean state generally neglecting the effects of ocean waves in the coupling processes. Therefore incorporating the ocean waves in atmosphere and ocean coupled model of REDES will help us understand the interactions between the systems and improve the assessment method of regional environment and disaster events.

(2) During the application of REDES to inland lake circulation problem, it is found that the land surface processes are very important in the simulation of meteorological condition. Thus it is necessary to include the land surface processes in REDES when apply to inland environmental problems.

(3) All the hindcasting simulations conducted in this study have their appropriate initial and boundary conditions. Especially in baroclinic simulation in the ocean, the initial and boundary conditions become the main concern. When we conduct the prediction we need the appropriate initial and boundary condition. For a forecasting studies and tasks, we have to consider connecting REDES with the global prediction projects or their forecasting data.

As REDES consists of many complicated and state-of-the-art models, complete understanding of each model is prerequisite for REDES users. To understand each model (=event) is a very good chance to study its nature and related science. From this point of view, it can be said that the simulator is in connection with education and further progress in science.

APPENDIX A

OASIS3 coupler and coupling procedure

The coupler used for the regional atmosphere and ocean coupled model in this thesis based on the coupler library called OASIS3 developed for coupling the General Circulation Models (GCMs) in CERFACS (European Centre for Research and Advanced Training in Scientific Computation; http://www.cerfacs.fr/PRISM/prism.html) at Toulouse, France. The OASIS3 coupler is written in Fortran and C language and becomes an independent executable in the modeling. The coupler process that exchanges the coupling variables between the component models is based on the Massage Passing Interface (MPI) and file I/O using mpp_io library from GFDL (Geophysical Fluid Dynamics Laboratory).

A.1 Interfacing models through OASIS3 coupler

To adapt the coupler to connect the component models, specific calls that invoke and conduct coupling procedure have to be implemented in the component models as follows:

1) Initialization of the coupler

`USE mod_prism_proto`

: Declare the module to be used by the component models

`CALL prism_init_comp_proto (compid, model_name, ierror)`

: Routine for initializing the coupling

- `compid` : component model ID

- `model_name` : name of calling component model

- `ierror` : returned error code

`CALL prism_get_localcomm_proto (local_comm, ierror)`

: Routine to get the value of a local communicator if the component model is parallelized internally.

- `local_comm` : value of local communicator

- `ierror` : returned error code

2) Grid data file definition of component models

```
USE mod_prism_grids_writing
```

: Declare the module to be used by the component models to call grid writing routines

```
CALL prism_start_grids_writing (flag)
```

: Routine for initializing of grid writing

- flag : returns 1 or 0 if grids writing is needed or not needed

```
CALL prism_write_grid (cgrid, nx, ny, lon, lat)
```

: Routine for writing of the component models grid longitudes and latitudes

- cgrid : grid name prefix
- nx : grid dimension in x-direction
- ny : grid dimension in y-direction
- lon : array of longitudes (nx, ny)
- lat : array of latitudes (nx, ny)

```
CALL prism_write_corner (cgrid, nx, ny, nc, clon, clat)
```

: Routine for writing of the component models grid cell corner longitudes and latitudes

- cgrid : grid name prefix
- nx : grid dimension in x-direction
- ny : grid dimension in y-direction
- nc : number of corners per grid cell (4)
- clon : array of corner longitudes (nx, ny, nc)
- clat : array of corner latitudes (nx, ny, nc)

```
CALL prism_write_mask (cgrid, nx, ny, mask)
```

: Routine for writing of the component models grid mask

- cgrid : grid name prefix
- nx : grid dimension in x-direction
- ny : grid dimension in y-direction
- mask : mask array (0 : not masked, 1 : masked)

```
CALL prism_write_area (cgrid, nx, ny, area)
```

: Routine for writing of the component models grid cell area

- cgrid : grid name prefix
- nx : grid dimension in x-direction
- ny : grid dimension in y-direction
- area : array of grid cell area (nx, ny)

```
CALL prism_terminate_grids_writing ()
```

: Routine for closing of the component models grid writing

3) Partition definition of component models

```
USE mod_prism_def_partition_proto
```

: Declare the module to be used by the component models to call

```
CALL prism_def_partition_proto (il_part_id, ig_paral, ierror)
```

: Routine for defining the local partitions if the component model is parallelized itself

- `il_part_id` : partition ID
- `ig_paral` : vector of integers describing the local partition in the global index space
- `ierror` : returned error code

4) I/O coupling variable declaration

```
CALL prism_def_var_proto (var_id, name, il_part_id, var_nodims,
kinout, var_actual_shape, var_type, ierror)
```

: Routine for declaration of the coupling variables that will be sent or received during the simulation

- `var_id` : coupling variable ID
- `name` : variable symbolic name
- `il_part_id` : partition ID
- `var_nodims` : rank of variable array
- `kinout` : PRISM_IN for variables received by component models, or PRISM_OUT for variables sent by component models
- `var_actual_shape` : vector of integers giving the minimum and maximum index for each dimension of the coupling field array; the minimum index has to be 1 and the maximum index has to be the extent of the dimension.
- `var_type` : type of coupling variable array (single or double precision real array)
- `ierror` : returned error code

5) Closing the definition phase of component models

```
CALL prism_enddef_proto (ierror)
```

: Routine for closing the definition phase

- `ierror` : returned error code

6) Sending and receiving process

```
USE mod_prism_put_proto
USE mod_prism_get_proto
```

: Declare the module to be used by the component models to send and receive the coupling variables

```
CALL prism_put_proto (var_id, date, field_array, info)
```

: Routine for sending the defined coupling variable

- `var_id` : variable ID from I/O coupling varibale declaration
- `date` : number of seconds in the run at the beginning of the timestep

173

- `field_array` : I/O or coupling variable array

- `info` : returned info code corresponding to the action of sending variable

CALL `prism_get_proto (var_id, date, field_array, info)`

: Routine for receiving the defined coupling variable

- `var_id` : variable ID from I/O coupling varibale declaration

- `date` : number of seconds in the run at the beginning of the timestep

- `field_array` : I/O or coupling variable array

- `info` : returned info code corresponding to the action of receiving variable

7) End of coupling

CALL `prism_terminate_proto (ierror)`

: Routine for terminating the coupling process

- `ierror` : returned error code

CALL `prism_abort_proto (compid, routine_name, abort_message)`

: Routine for aborting the process if needed

- `compid` : component model ID from initialization

- `routine_name` : name of calling routine

- `abort_message` : message to be written out

A.2 Coupling procedure of atmosphere and ocean models

The coupling procedure of atmosphere mesoscale model (MM5) and ocean general circulation model (MITgcm) were first implemented by initializing the OASIS3 coupler with CALL `prism_init_comp_proto` in both models. In the initialization, this call must be placed after the `MPI_Init` of both models since MM5 and MITgcm are parallel codes. After initialization, the grid data file of both MM5 and MITgcm are generated by the CALLs for grid writing. In the typhoon-ocean interaction simulation, the coupling between the first domain (27km grid size) of MM5 and the domain (1/6° horizontal resolution) of MITgcm was performed. As their partitioning of domains in MM5 and MITgcm are different, the local partitions are defined by the CALL `prism_def_partition_proto`. The coupling variables defined by CALL `prism_def_var_proto` in MM5 and MITgcm were the sea surface temperature (SST), surface heat flux, surface wind and atmospheric pressure. The variable, SST in MM5 was defined for receiving and the others were for sending variables and vice versa in MITgcm. In MM5, simple calculation codes for Q_{net} ($Q_{net} = Q_{swd} - (Q_{lhf} + Q_{shf})$) and momentum flux by wind were implemented since MITgcm receives them in net surface heat flux and momentum flux for external forcing. During the simulation in typhoon-ocean interaction, the coupling processes (sending/receiving) of variables were taken place every 900 sec which was the multiple common time step between MM5 and MITgcm by CALLs `prism_put_proto` and

`prism_get_proto`. MM5 and MITgcm had their time steps 90 and 15 sec for their coupling domains, respectively. As initialization was set after `MPI_Init` of the models, the termination of coupling by CALL `prism_terminate_proto` must be placed before calling `MPI_Finalize` in both models.
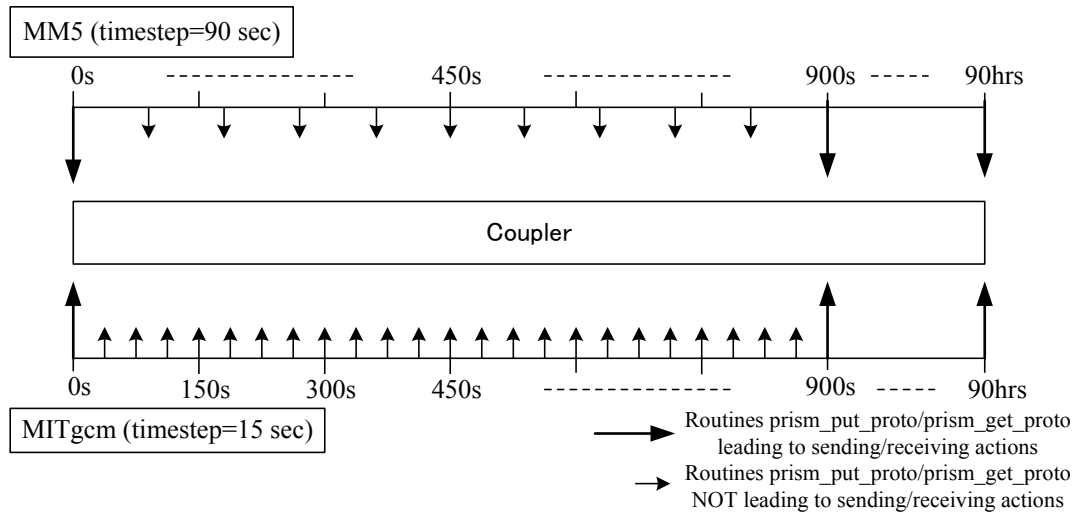

Fig. A.1 The coupling procedure in case of typhoon-ocean interaction simulation